

**Muon Antineutrino Disappearance and  
Non-standard Interactions at the T2K Experiment**

by

**Stephen Dennis**

**Thesis**

Submitted to the University of Warwick

for the degree of

**Doctor of Philosophy**

**Physics**

October 2015

THE UNIVERSITY OF  
**WARWICK**

# Abstract

T2K is a long-baseline neutrino oscillation experiment, which studies the changing flavour composition of a  $\nu_\mu$  beam over a 295 km baseline from an accelerator at J-PARC to Super-Kamiokande, a 50 kt water Čerenkov detector. The T2K neutrino beam has an energy peak at 0.6 GeV which gives strong sensitivity to oscillations at the atmospheric mass squared splitting. The beam can be run in two modes, producing a beam either dominated by neutrinos or by antineutrinos. Collecting data in antineutrino-mode allows the measurement of the neutrino mixing parameters on antineutrinos only. In the first analysis of T2K antineutrino-mode data, we use beam data collected up to June 2015 to measure  $\sin^2\overline{\theta_{23}}$  and  $|\overline{\Delta m_{32}^2}|$ . The 90% CL allowed values for mixing angle are  $0.327 < \sin^2\overline{\theta_{23}} < 0.692$  (normal hierarchy) and  $0.332 < \sin^2\overline{\theta_{23}} < 0.697$  (inverted hierarchy). The 90% CL allowed values for mass splitting are  $2.03 \times 10^{-3} \text{ eV}^2 < |\overline{\Delta m_{32}^2}| < 2.92 \times 10^{-3} \text{ eV}^2$  (normal hierarchy) and  $2.03 \times 10^{-3} \text{ eV}^2 < |\overline{\Delta m_{31}^2}| < 2.92 \times 10^{-3} \text{ eV}^2$  (inverted hierarchy). This is the world's best measurement in  $\sin^2\overline{\theta_{23}}$ .

A difference between neutrino and antineutrino survival probabilities could result from physics beyond the Standard Model, known as non-standard interactions. A simultaneous fit to the T2K neutrino-mode and antineutrino-mode datasets allows for a direct search for such interactions. We see no evidence for this hypothesis.

# Contents

<b>Abstract</b>	i
<b>Abbreviations</b>	xiii
<b>Acknowledgments</b>	xvi
<b>Declarations</b>	xvii
<b>Chapter 1 Introduction</b>	1
<b>Chapter 2 An Overview of Neutrino Physics</b>	2
2.1 The History of the Neutrino . . . . .	2
2.1.1 Prediction and Discovery . . . . .	2
2.1.2 Neutrino Mixing . . . . .	4
2.1.2.1 The Solar Neutrino Problem . . . . .	4
2.1.2.2 The Atmospheric Neutrino Anomaly . . . . .	5
2.1.2.3 Confirmation of Neutrino Oscillation . . . . .	6
2.1.2.4 The LSND Anomaly . . . . .	6
2.2 Neutrino Theory . . . . .	7
2.2.1 The Weak Interaction . . . . .	7
2.2.2 CP Violation . . . . .	8
2.2.3 V-A Structure . . . . .	9
2.2.4 Neutrino Mass . . . . .	10
2.2.5 Neutrino Oscillation . . . . .	11
2.2.6 Maximality in Neutrino Oscillation . . . . .	14
2.2.7 Matter Interactions in Oscillation Physics . . . . .	15
2.2.7.1 Neutrino Mixing in Matter . . . . .	15
2.2.7.2 The MSW Resonance . . . . .	17
2.3 Current Status of Neutrino Oscillation Research . . . . .	19
2.3.1 Atmospheric Neutrino Experiments . . . . .	19
2.3.2 Reactor Experiments . . . . .	19

2.3.3	Long Baseline Accelerator Neutrino Experiments . . . . .	21
2.3.4	Short Baseline Neutrino Oscillation Experiments . . . . .	23
2.3.5	Global Fits . . . . .	23
2.3.6	Measurement of Oscillation Parameters on Antineutrinos . . . . .	24
<b>Chapter 3</b>	<b>The T2K Experiment</b>	<b>26</b>
3.1	The J-PARC Neutrino Beam . . . . .	26
3.2	Near Detector Complex . . . . .	31
3.2.1	Simulation at ND280 . . . . .	36
3.3	Super-Kamiokande . . . . .	36
3.3.1	Super-Kamiokande Event Reconstruction . . . . .	37
3.4	T2K Physics Results . . . . .	40
<b>Chapter 4</b>	<b>Inputs to the Oscillation Analysis</b>	<b>42</b>
4.1	Flux Prediction . . . . .	43
4.2	NEUT Monte Carlo . . . . .	47
4.2.1	Neutrino Interaction Modes . . . . .	47
4.2.1.1	Charged Current Quasi-Elastic (CCQE) . . . . .	47
4.2.1.2	Meson Exchange Currents (MEC) . . . . .	49
4.2.1.3	Resonance (RES) . . . . .	49
4.2.1.4	Coherent Pion Production (COH) . . . . .	50
4.2.1.5	Deep Inelastic Scattering (DIS) . . . . .	51
4.2.2	Interaction Modes . . . . .	52
4.3	CCQE External Data Tuning . . . . .	53
4.4	Near Detector Flux and Cross-Section Constraints . . . . .	60
4.4.1	Near Detector Samples . . . . .	60
4.4.2	Near Detector Binning . . . . .	61
4.4.3	Near Detector Analysis Strategy . . . . .	62
4.5	Super-Kamiokande Samples . . . . .	77
4.6	Super-Kamiokande Detector and Final State Interaction Systematics . . . . .	80
4.6.1	Final State Interactions and Secondary Interactions . . . . .	81
4.6.2	Detector Efficiency Systematics . . . . .	83
4.6.3	Super-K Energy Scale . . . . .	84
<b>Chapter 5</b>	<b>Muon Antineutrino Disappearance Measurement</b>	<b>86</b>
5.1	Hypothesis . . . . .	86
5.2	Fit Method . . . . .	88
5.2.1	Profiled Systematics . . . . .	90
5.2.2	Marginalised Systematics . . . . .	91

5.3	Predicted Event Rates and Spectra . . . . .	91
5.4	Effects of Systematics on the Spectrum . . . . .	97
5.5	Method for Goodness-of-fit Tests . . . . .	103
5.6	Validation of the Oscillation Fitter . . . . .	103
5.6.1	Oscillation Parameter Biases . . . . .	105
5.6.2	Systematic Parameter Biases . . . . .	105
5.7	Method for Construction of Confidence Regions . . . . .	115
5.8	Expected Sensitivity . . . . .	115
5.9	Results of the $\bar{\nu}_\mu$ Disappearance Analysis . . . . .	117
5.9.1	Best-fit Oscillation Parameters and Spectra . . . . .	117
5.9.2	Goodness-of-fit Tests . . . . .	117
5.9.3	Confidence Regions . . . . .	118
5.10	Summary . . . . .	127
<b>Chapter 6</b>	<b>Non-standard Neutrino-Matter Interactions</b>	<b>128</b>
6.1	Introduction . . . . .	128
6.2	Analysis Strategy . . . . .	131
6.3	Predicted Event Rates and Spectra . . . . .	131
6.4	Effects of Systematics on the Neutrino-Mode Spectrum . . . . .	137
6.5	Validation of the Oscillation Fitter for the NSI Hypothesis . . . . .	141
6.6	Method for Construction of Confidence Regions . . . . .	144
6.7	Expected Sensitivity for Current and Future Datasets . . . . .	145
6.8	Results of the Non-standard Matter Interactions Analysis . . . . .	147
6.8.1	Best-fit Oscillation Parameters . . . . .	147
6.8.2	Goodness-of-fit Tests . . . . .	147
6.8.3	Confidence regions . . . . .	147
6.9	Summary . . . . .	148
<b>Chapter 7</b>	<b>Conclusions and Outlook</b>	<b>153</b>
<b>Appendix A</b>	<b>Interaction Modes in the Analysis</b>	<b>154</b>
<b>Appendix B</b>	<b>Effects of Systematics on the Spectrum</b>	<b>157</b>
<b>Bibliography</b>		<b>164</b>

# List of Figures

2.1	The beta-decay spectrum for Carbon-14. . . . .	3
2.2	The energies and relative fluxes of the neutrinos produced by different solar processes. . . . .	5
2.3	Example weak interaction vertices. . . . .	7
2.4	The two possible hierarchies of neutrino mass states. . . . .	15
2.5	Probabilities of observing a given neutrino flavour in a beam generated as pure $\nu_\mu$ at varying baselines. . . . .	16
2.6	The muon survival probability as a function of $\sin^2 \theta_{23}$ , with dashed lines marking the position of maximum disappearance. . . . .	17
2.7	The RENO reactor antineutrino spectrum, demonstrating the 5 MeV excess. .	20
3.1	Diagram of the T2K long-baseline setup. . . . .	26
3.2	Diagram of the J-PARC Accelerator Complex. . . . .	27
3.3	The T2K beam's bunch and spill structure . . . . .	28
3.4	T2K delivered POT, broken down into individual T2K running periods. .	28
3.5	Diagram of the primary and secondary beamlines of the T2K neutrino beam. . . . .	28
3.6	The T2K muon monitor (MUMON). . . . .	29
3.7	Neutrino energy as a function of pion momentum for decays as a function of outgoing neutrino angle. . . . .	30
3.8	T2K flux predictions for different angles from the beam central axis. . .	31
3.9	T2K FHC flux predictions at Super-Kamiokande. . . . .	32
3.10	T2K RHC flux predictions at Super-Kamiokande. . . . .	32
3.11	The layout of the modules in the on-axis near detector (INGRID). . . .	34
3.12	A schematic of the arrangement of detectors in the off-axis near detector (ND280). . . . .	35
3.13	A simplified diagram showing the main elements of a TPC module. . . .	35
3.14	A photograph of the Super-Kamiokande inner detector, before it was filled.	37
3.15	A diagram of the Super-Kamiokande detector. . . . .	37
3.16	PID discriminator between $\mu$ -like and e-like rings at Super-K. . . . .	39

3.17	Examples of a single ring muon-like, and a single ring electron-like event at Super-K.	39
3.18	Projected T2K $\delta_{CP}$ sensitivity at $7.8 \times 10^{21}$ POT.	41
4.1	A flowchart demonstrating the stages of the T2K oscillation analysis.	43
4.2	The detector layout of the NA61 detector.	44
4.3	The phase space of pions and kaons contributing to the predicted neutrino flux at SK, and the regions covered by NA61/SHINE measurements.	44
4.4	The pion multiplicity observed by NA61 in bins of angle and momentum.	45
4.5	$\nu_\mu$ Run 5c-6e RHC flux tuning weights	46
4.6	$\overline{\nu}_\mu$ Run 5c-6e RHC flux tuning weights	46
4.7	$\nu_e$ Run 5c-6e flux tuning weights	46
4.8	$\overline{\nu}_e$ Run 5c-6e RHC flux tuning weights	46
4.9	Feynman diagram of a neutrino CCQE process.	48
4.10	Feynman diagram of an antineutrino CCQE process.	48
4.11	Electron-nucleus scattering data from the JUPITER experiment.	50
4.12	Feynman diagram of an example MEC process.	51
4.13	Feynman diagram of single pion production via a charged-current delta resonance.	51
4.14	Feynman diagrams of coherent pion production.	51
4.15	MiniBooNE CCQE data for neutrino beam-mode running.	54
4.16	MiniBooNE CCQE data for antineutrino beam-mode running.	55
4.17	MINER $\nu$ A CCQE dataset for neutrino beam-mode running.	55
4.18	MINER $\nu$ A CCQE dataset for antineutrino beam-mode running.	55
4.19	CCQE best-fit distributions compared with the MINER $\nu$ A neutrino dataset used in the CCQE fit.	57
4.20	CCQE best-fit distributions compared with the MINER $\nu$ A antineutrino dataset used in the CCQE fit.	57
4.21	CCQE best-fit distributions compared with the MiniBooNE double-differential neutrino dataset used in the CCQE fit.	59
4.22	CCQE best-fit distributions compared with the MiniBooNE double-differential antineutrino dataset used in the CCQE fit.	59
4.23	Example data event displays for the neutrino beam mode ND280 fit samples.	63
4.24	Example event displays for the antineutrino beam mode ND280 fit samples.	64
4.25	Correlations between flux and cross-section parameters for antineutrino beam mode.	66
4.26	BANFF data spectra for the FHC $\nu_\mu$ CC0 $\pi$ selection	72
4.27	BANFF data spectra for the FHC $\nu_\mu$ CC1 $\pi$ selection	73

4.28	BANFF data spectra for the FHC $\nu_\mu$ CC other selection . . . . .	74
4.29	BANFF data spectra for the RHC $\overline{\nu}_\mu$ CC 1-track selection . . . . .	75
4.30	BANFF data spectra for the RHC $\overline{\nu}_\mu$ CC N-tracks selection . . . . .	75
4.31	BANFF data spectra for the RHC $\nu_\mu$ CC 1-track selection . . . . .	76
4.32	BANFF data spectra for the RHC $\nu_\mu$ CC N-tracks selection . . . . .	76
4.33	Distributions of $\Delta T_0$ at Super-K from T2K runs 1-6, for events by selection.	78
4.34	Distributions of $\Delta T_0$ at Super-K for FC events in runs 1-5 and run 6. . .	78
4.35	Super-K PID distributions for run 6 event numbers. . . . .	79
4.36	Cumulative effects of Super-K PID cuts on run 6 event numbers. . . . .	80
4.37	True vs. reconstructed neutrino energy for simulated $\overline{\nu}_\mu$ events by mode. .	81
4.38	Correlations in the Super-K detector and FSI/SI errors. . . . .	83
4.39	$\pi^+$ -carbon scattering cross-sections used to tune FSI systematics. . . . .	84
4.40	$\pi^-$ -carbon scattering cross-sections used to tune FSI systematics. . . . .	84
5.1	Effects of flux tuning on reconstructed-energy spectra of antineutrino beam mode 1 $\mu$ -like ring events at Super-K. . . . .	92
5.2	Effects of BANFF tuning on reconstructed-energy spectra of antineutrino beam mode 1 $\mu$ -like ring events at Super-K. . . . .	95
5.3	Predicted RHC Super-K $E_{reco}$ spectrum, with BANFF prefit systematics and no oscillations. . . . .	96
5.4	Predicted RHC Super-K $E_{reco}$ spectrum, with BANFF postfit systematics and no oscillations. . . . .	96
5.5	Predicted RHC Super-K $E_{reco}$ spectrum, with BANFF prefit systematics and typical oscillations. . . . .	96
5.6	Predicted RHC Super-K $E_{reco}$ spectrum, with BANFF postfit systematics and typical oscillations. . . . .	96
5.7	Error envelopes for the RHC energy spectrum as a result of all systematic parameters, without oscillations. . . . .	100
5.8	Error envelopes for the RHC energy spectrum as a result of all systematic parameters, with oscillations. . . . .	100
5.9	Antineutrino mode prefit and postfit error envelopes, expressed as an event-count ratio, as a result of Super-K detector and FSI/SI systematics, with oscillations. . . . .	101
5.10	Antineutrino mode prefit and postfit error envelopes, expressed as an event-count ratio, as a result of the BANFF flux systematics, with oscillations. . . . .	101

5.11	Antineutrino mode prefit and postfit error envelopes, expressed as an event-count ratio, as a result of the BANFF cross-section systematics, with oscillations. . . . .	101
5.12	Antineutrino mode prefit and postfit error envelopes, expressed as an event-count ratio, as a result of all systematics, with oscillations. . . . .	101
5.13	Predicted RHC Super-K $E_{reco}$ spectrum, using the goodness-of-fit binning and typical oscillations . . . . .	104
5.14	Distributions of the pulls of $ \overline{\Delta m_{32}^2} $ at a true value $ \overline{\Delta m_{32}^2}  = 2.51 \times 10^{-3}$ eV <sup>2</sup> .105	
5.15	Distributions of the pulls of $\sin^2 \overline{\theta_{23}}$ at a true value $\sin^2 \overline{\theta_{23}} = 0.527$ . . . . .	106
5.16	Distributions of the best-fit values of $\sin^2 \overline{\theta_{23}}$ at a true value $\sin^2 \overline{\theta_{23}} = 0.35$ .106	
5.17	Distributions of the pulls of $\sin^2 \overline{\theta_{23}}$ at a true value $\sin^2 \overline{\theta_{23}} = 0.35$ . . . . .	107
5.18	Summary of systematic pull distributions, with true systematic values allowed to be unphysical (normal hierarchy). . . . .	110
5.19	Summary of systematic pull distributions, with true systematic values allowed to be unphysical (inverted hierarchy). . . . .	111
5.20	Summary of systematic pull distributions, with true systematic values not allowed to be unphysical (normal hierarchy). . . . .	112
5.21	Summary of systematic pull distributions, with true systematic values not allowed to be unphysical (inverted hierarchy). . . . .	113
5.22	Distributions of pulls for four systematic parameters that have small biases.114	
5.23	The chi-square distribution when varying Super-K energy scale for a single randomised toy experiment. . . . .	114
5.24	T2K $\overline{\nu_\mu}$ expected sensitivity at T2K run-4 and MINOS $\overline{\nu_\mu}$ best-fit points. . 116	
5.25	The Run 5+6 single $\mu$ -like ring $4.011 \times 10^{20}$ POT dataset and the best-fit reconstructed energy spectrum. The normal mass hierarchy result is shown, and is compared with the event rate prediction in the absence of oscillation. . . . .	119
5.26	The Run 5+6 single $\mu$ -like ring $4.011 \times 10^{20}$ POT dataset and the best-fit reconstructed energy spectrum. The inverted mass hierarchy result is shown, and is compared with the event rate prediction in the absence of oscillation. . . . .	119
5.27	The Run 5+6 single $\mu$ -like ring $4.011 \times 10^{20}$ POT dataset and the best-fit spectrum, compared with the T2K neutrino mode result (normal hierarchy).120	
5.28	The Run 5+6 single $\mu$ -like ring $4.011 \times 10^{20}$ POT dataset and the best-fit spectrum, compared with the T2K neutrino mode result (inverted hierarchy). . . . .	120
5.29	Goodness-of-fit for the $\overline{\nu_\mu}$ disappearance fit (normal hierarchy). . . . .	121
5.30	Goodness-of-fit for the $\overline{\nu_\mu}$ disappearance fit (inverted hierarchy). . . . .	121

5.31	$\Delta\chi^2$ surface from the fit of the $4.011 \times 10^{20}$ POT run 5+6 dataset (normal hierarchy) . . . . .	122
5.32	$\Delta\chi^2$ surface from the fit of the $4.011 \times 10^{20}$ POT run 5+6 dataset (inverted hierarchy) . . . . .	122
5.33	Confidence regions for the $4.011 \times 10^{20}$ POT Run 5+6 dataset, comparing fits with no systematics and profiled systematics. . . . .	123
5.34	Confidence regions for the $4.011 \times 10^{20}$ POT Run 5+6 dataset, comparing the data result with expected sensitivity. . . . .	123
5.35	Confidence regions for the $4.011 \times 10^{20}$ POT Run 5+6 dataset, comparing the T2K result with MINOS. . . . .	124
5.36	Confidence regions for the $4.011 \times 10^{20}$ POT Run 5+6 dataset, comparing with the T2K neutrino mode contour. . . . .	124
5.37	Confidence regions for the $4.011 \times 10^{20}$ POT Run 5+6 dataset, comparing profiled systematics with marginalised systematics. . . . .	125
5.38	Confidence regions in $\sin^2\overline{\theta_{23}}$ only for the fit to the $4.011 \times 10^{20}$ POT Run 5+6 dataset. . . . .	126
5.39	Confidence regions in $ \Delta m_{32}^2 $ only for the fit to the $4.011 \times 10^{20}$ POT Run 5+6 dataset. . . . .	126
6.1	Survival probabilities of muon neutrinos for different values of the NSI parameter $\varepsilon_{\mu\tau}$ . . . . .	130
6.2	Effects of flux tuning on reconstructed-energy spectra of neutrino beam mode 1 $\mu$ -like ring events at Super-K. . . . .	132
6.3	Effects of BANFF tuning on reconstructed-energy spectra of neutrino beam mode 1 $\mu$ -like ring events at Super-K. . . . .	135
6.4	Predicted FHC Super-K $E_{reco}$ spectrum, with BANFF prefit systematics and no oscillations. . . . .	136
6.5	Predicted FHC Super-K $E_{reco}$ spectrum, with BANFF postfit systematics and no oscillations. . . . .	136
6.6	Predicted FHC Super-K $E_{reco}$ spectrum, with BANFF prefit systematics and typical oscillations. . . . .	136
6.7	Predicted FHC Super-K $E_{reco}$ spectrum, with BANFF postfit systematics and typical oscillations. . . . .	136
6.8	Error envelopes for the FHC energy spectrum as a result of all systematic parameters, without oscillations. . . . .	139
6.9	Error envelopes for the FHC energy spectrum as a result of all systematic parameters, with oscillations. . . . .	139

6.10	Neutrino mode prefit and postfit error envelopes, expressed as an event-count ratio, as a result of Super-K detector and FSI/SI systematics, with oscillations. . . . .	140
6.11	Neutrino mode prefit and postfit error envelopes, expressed as an event-count ratio, as a result of the BANFF flux systematics, with oscillations. . . . .	140
6.12	Neutrino mode prefit and postfit error envelopes, expressed as an event-count ratio, as a result of the BANFF cross-section systematics, with oscillations. . . . .	140
6.13	Neutrino mode prefit and postfit error envelopes, expressed as an event-count ratio, as a result of all systematics, with oscillations. . . . .	140
6.14	Best-fit values of the NSI parameter $\varepsilon_{\mu\tau}$ for toy experiments with various true values. . . . .	142
6.15	Pulls of the NSI parameter $\varepsilon_{\mu\tau}$ for toy experiments with various true values.	142
6.16	Summary of FHC-specific systematic pull values. . . . .	143
6.17	T2K expected $\varepsilon_{\mu\tau}$ sensitivity with current POT. . . . .	146
6.18	T2K expected $\varepsilon_{\mu\tau}$ sensitivity with T2K’s final projected POT. . . . .	146
6.19	The neutrino-mode data compared with the best-fit spectrum from the NSI fit. . . . .	149
6.20	The antineutrino-mode data compared with the best-fit spectrum from the NSI fit. . . . .	149
6.21	Goodness-of-fit for the NSI fit using the MINOS constraint (normal hierarchy). . . . .	150
6.22	Goodness-of-fit for the NSI fit using the MINOS constraint (normal hierarchy). . . . .	150
6.23	Results of the T2K Run 1 to 6 data fit for NSI (normal hierarchy). . . . .	151
6.24	Results of the T2K Run 1 to 6 data fit for NSI (inverted hierarchy). . . . .	151
6.25	Results of the T2K Run 1 to 6 data fit for NSI compared to expected sensitivity (flat prior). . . . .	152
6.26	Results of the T2K Run 1 to 6 data fit for NSI compared to expected sensitivity (MINOS prior). . . . .	152

# List of Tables

2.1	Global oscillation parameter best-fit values from the Particle Data Group.	24
2.2	Best measurements of mixing parameters on antineutrinos.	25
3.1	The T2K running periods and their accumulated POT.	30
3.2	Summary of the T2K ND280 ECal module design.	33
4.1	The versions of the software and productions used in this analysis.	42
4.2	POT normalisation of input Super-K MC samples for antineutrino beam mode.	53
4.3	Results of the CCQE external data fit.	56
4.4	BANFF cross-section parameters with their prefit and post-fit values and uncertainties.	67
4.5	BANFF FHC flux parameters with their prefit and post-fit values and uncertainties.	68
4.6	BANFF RHC flux parameters with their prefit and post-fit values and uncertainties.	69
4.7	Actual and predicted event rates for the different ND280 samples in the BANFF fit.	69
4.8	Summary of which systematics are applied to which MC interaction modes.	71
4.9	Numbers of Monte Carlo events passing each stage of the SK PID, for $4.011 \times 10^{20}$ with standard oscillations applied.	78
4.10	Super-K selection efficiency and FSI+SI systematic parameters.	82
5.1	The T2K run 1-4 oscillation parameter results, with the reactor constraint.	87
5.2	Effects of tuning on the RHC 1-ring $\mu$ -like SuperK spectrum, without oscillations.	93
5.3	Effects of tuning on the RHC 1-ring $\mu$ -like SuperK spectrum, with oscillations.	94
5.4	Summary of the size of effects of systematic groups on SuperK event rate.	98
5.5	$\pm 1\sigma$ effect of the systematic parameters on the total number of SuperK events.	99

5.6	Relative size of effect of each systematic parameter on oscillation measurements, sorted by effect on $\sin^2\overline{\theta_{23}}$	102
5.7	The T2K run 1-4 oscillation parameter results, without the reactor constraint	104
5.8	The binning used for the calculation of confidence regions	115
5.9	The critical values $\Delta\chi^2_{crit}$ used for construction of confidence regions using the constant- $\Delta\chi^2$ method	116
5.10	Summary of best-fit oscillation parameters from the fits of the combined T2K Run 5+6 dataset	117
6.1	Effects of tuning on the FHC 1-ring $\mu$ -like SuperK spectrum, without oscillations	133
6.2	Effects of tuning on the FHC 1-ring $\mu$ -like SuperK spectrum, with oscillations	134
6.3	$\pm 1\sigma$ effect of the systematic parameters on the total number of FHC SuperK events	138
6.4	Summary of the size of effects of systematic groups on the neutrino beam mode SuperK event rate	139
6.5	Summary of best-fit oscillation parameters from the fits of the combined T2K Run 5+6 dataset	147

# Abbreviations

- **BANFF** : Beam And Nd280 Flux extrapolation task Force: the name given to the near detector constraint.
- **CC** : Charged Current.
- **CCQE** : Charged Current Quasi-Elastic.
- **CL** : Confidence Level.
- **COH** : Coherent pion production.
- **DIS** : Deep Inelastic Scattering.
- **DOF** : Degrees of Freedom.
- **DUNE** : Deep Underground Neutrino Experiment.
- **ECal** : Electromagnetic Calorimeter.
- **FC** : Fully Contained
- **FCFV** : Fully Contained, in Fiducial Volume.
- **FGD** : Fine-Grained Detector: an ND280 component detector, one of which provides the interaction mass for the BANFF fits.
- **FHC** : Forward Horn Current: the T2K beam mode with a predominantly neutrino beam.
- **FSI** : Final State Interactions.
- **FV** : Fiducial Volume.

- **GENIE** : A neutrino Monte Carlo generator.
- **IH** : Inverted Hierarchy.
- **INGRID** : Interactive Neutrino GRID. The T2K on-axis near detector.
- **J-PARC** : Japan Proton Accelerator Research Complex.
- **MC** : Monte Carlo.
- **MEC** : Meson Exchange Currents.
- **MINOS** : Main Injector Neutrino Oscillation Search, another long baseline neutrino experiment.
- **MPPC** : Multi-Pixel Photon Counter, a photo-sensitive in the near detector.
- **MSW effect**: Mikheyev–Smirnov–Wolfenstein effect: a matter oscillation effect.
- **MUMON** : Muon Monitor: a T2K near detector used for monitoring the beam.
- **NA61** : Experiment at CERN used for flux tuning.
- **NC** : Neutral Current.
- **ND280** : Near Detector (at) 280m. The T2K off-axis near detector.
- **NEUT** : The neutrino Monte Carlo event generator used.
- **NH** : Normal Hierarchy.
- **NIWG** : Neutrino Interactions Working Group: a T2K subgroup.
- **OD** : Outer Detector.
- **OOFV** : Out of Fiducial Volume.
- **PDG** : Particle Data Group: a group who provide summaries of current physics knowledge.
- **PID** : Particle identification.

- **PMT** : Photomultiplier Tube, a photosensitive used at Super-K.
- **POT** : Protons on Target: the measure of delivered beam.
- **RC** : Ring Counting.
- **RES** : Resonance.
- **RFG** : Relativistic Fermi Gas: the main nuclear model for interaction simulation in this thesis.
- **RHC** : Reverse Horn Current: the T2K beam mode with a predominantly antineutrino beam.
- **RPA** : Random Phase Approximation.
- **SF** : Spectral Function: a possible nuclear model for interaction simulation.
- **SHINE** : SPS Heavy Ion and Neutrino Experiment, also known as NA61.
- **SK** : Super-Kamiokande: the T2K far detector.
- **Super-K** : Super-Kamiokande: the T2K far detector.
- **T2K** : Tokai-to-Kamioka.
- **TOF** : Time of Flight.
- **TPC** : Time Projection Chamber: used in the ND280 as a detector volume.
- **WLS** : Wavelength Shifting (fibre).

# Acknowledgments

I'd like to thank my supervisors, Gary Barker, Steve Boyd and Costas Andreopoulos for the training and support that made these four years both possible and productive. The T2K experiment both produced the data used, and gave valuable feedback and experience. It has been a great environment to begin my career.

The VALOR group, and the wider T2K oscillation analysis group have been invaluable in developing the analysis described in this document.

To the inhabitants of office P450, past and present, over the course of these four years you've provided advice, help and entertainment whenever necessary. It's been a pleasure.

Finally, I'd like to thank my friends, family and pub quiz teams. Your support made this all worthwhile.

# Declarations

Chapter 2 of this work is a historical and theoretical background to the field. It is a summary of the research of my forebears, and is constructed from a review of the literature. Chapter 3 is a description of the T2K experiment and its constituent parts, the source of the data analysed. This chapter is derived from T2K documentation, published both internally and externally to the collaboration. Chapter 4 is a description of the analysed data used as input to my physics analyses, as developed and validated by members of the T2K collaboration. This includes evaluations of beam fluxes, detector performance and physics model uncertainties. Chapters 5 and 6 contain physics analyses that are my original work, which rely on the information from Chapter 4. This work was performed as part of the ‘VALOR’ analysis group, which was actively developed by myself, Costas Andreopoulos, Thomas Dealtry, Lorena Escudero, Nick Grant, Davide Sgalaberna and Raj Shah during my studies. Chapter 7 is a short summary of the work done and insights gained.

# Chapter 1

## Introduction

Since its development in the 1960s, The Standard Model of Particle Physics has had an impressive record of predictions, including the gluon, W and Z bosons and most recently the Higgs boson. It has also made many precision predictions of many physical observables which have been verified by the best possible experimental measurements. However, the theory is not complete with open questions remaining about the origin of gravity, dark matter and the matter-dominated universe itself.

This thesis covers two topics which are not in the Standard Model. The first is neutrino oscillation, which was experimentally confirmed in the early 2000s. Neutrino oscillation demonstrates that the neutrino is massive, requiring physics beyond the Standard Model. Oscillations also add the possibility of CP violation in the lepton sector, which could help to explain the matter-antimatter asymmetry in the universe. T2K is a powerful experiment designed to use an accelerator neutrino source to study oscillation phenomena. This thesis contains the first analysis of T2K data taken in the antineutrino beam mode, which shows strong evidence for muon antineutrino disappearance.

The second analysis topic concerns a search for evidence of new forms of neutrino oscillation outside of the standard framework that has developed from the results of many experiments stretching back to the pioneering measurements of Ray Davies in the 1950s. The hypothesis tested is the addition of novel flavour-changing neutral current interactions with matter occurring along the experiment's baseline. Evidence for these new interactions would influence future attempts to measure CP violation in neutrinos, as well as requiring major additions to our theories. Current and future limits for these hypothetical phenomena are included, offering no evidence for their existence.

## Chapter 2

# An Overview of Neutrino Physics

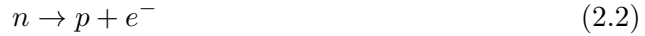
### 2.1 The History of the Neutrino

#### 2.1.1 Prediction and Discovery

In 1930, a key issue in physics was the shape of the beta decay electron energy spectrum. At the time, a normal beta decay was believed to be:



In terms of nucleons, this is:



With only two outgoing particles, conservation of energy and momentum required that the electron emission energy was uniquely specified and should have appeared as sharp peak. Empirically, however, the spectrum had a distinctive, wide pattern which did not fit with a two-particle final state. The shape of the beta decay spectrum can be seen in Figure 2.1. The existence of spin makes this problem even worse: the single spin  $\frac{1}{2}$  neutron cannot produce a final state with exactly two spin  $\frac{1}{2}$  outgoing particles, implying that the suggested beta decay process violates conservation of angular momentum as well.

In order to resolve this tension, in 1930 Wolfgang Pauli proposed the neutrino: beta decays would also emit a neutral fermion, although the shape of spectrum and the particle's previously undetected nature made clear that the new particle was both light and reluctant to interact. With three decay products, the conservation issues were resolved. Pauli referred to this particle as a ‘neutron’ but in 1932, before his theory became accepted, that name was given to the neutral nucleon. Pauli’s particle became known as the neutrino.

Orders of magnitude lighter than any other known fermion, and incapable of

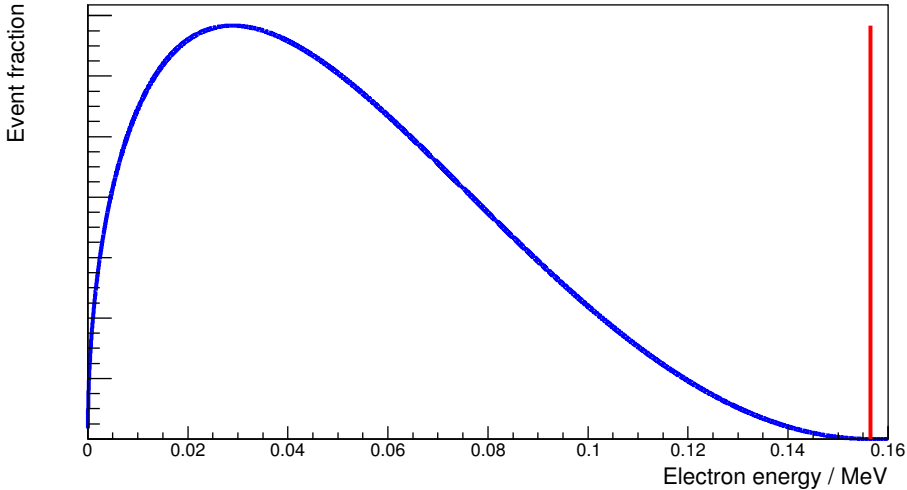


Figure 2.1: The beta-decay spectrum for Carbon-14. The blue line shows the spectrum with a neutrino, while the red line shows the prediction for a two-body decay (not to scale).

interacting with the electromagnetic or strong forces, neutrinos were not detected directly until the work of Reines and Cowan, published in 1956 [1]. The advent of fission reactors gave mankind a new, high flux source of neutrinos, which made direct neutrino detection a more feasible task. Reines and Cowan built their experiment 11 m from the Savannah River nuclear reactor in South Carolina. They used water tanks, with dissolved cadmium chloride, surrounded by scintillator layers. The neutrinos underwent the inverse beta decay interaction:

$$\bar{\nu}_e + p \rightarrow e^+ + n \quad (2.3)$$

The positron produced would then annihilate with an electron from the material, producing a pair of photons, which would be detected in the scintillator. To better constrain the signal, the neutron could also be captured by the cadmium solute:

$$n + {}^{108}\text{Cd} \rightarrow {}^{109}\text{Cd} + \gamma \quad (2.4)$$

Thus, the signal was a coincidence of detection of the pair production photons, followed by detection of the gamma ray from the neutron capture. The experiment discovered a significantly increased signal when the reactor was running than when it was dormant: the first convincing observation of the neutrino. In 1995, after the death of Clyde Cowan, Frederick Reines received the Nobel Prize in Physics, in large part due to this experiment.

Discovery of a single neutrino type was a huge step, but the story did not end there. Reines-Cowan had seen the electron antineutrino ( $\bar{\nu}_e$ ) as produced by a fission reactor, but it did not remain unique for long.

The muon neutrino was discovered in 1962 at Brookhaven National Laboratory, in New York state [2]. The experiment used a proton beam to produce pions, which decayed to produce muons and their associated neutrinos:

$$\pi^\pm \rightarrow \mu^\pm + \bar{\nu}_\mu \quad (2.5)$$

The resulting neutrinos were detected using an aluminium spark chamber. They produced only muons, rather than electrons, demonstrating that the muon and electron neutrino flavour states are distinct. This work resulted in Lederman, Schwartz and Steinberger receiving the 1988 Nobel Prize in Physics.

At this point in the timeline, we had observed three charged leptons, but only two neutrino flavours. The existence of a neutrino partner to the heavy tau lepton was inferred, yet it took many more years to be experimentally verified due to the tau's high mass and short lifetime.

In the 1990s, experiments at the Large Electron Positron collider (LEP) at CERN demonstrated that there were three light active neutrinos [3]. This third neutrino was finally directly observed by the DONUT (Direct Observation of NU Tau) experiment at Fermilab, published in 2000 [4]. Using photographic emulsion sheets to get fine grained observations of neutrino interactions, DONUT observed neutrino-induced interactions with a muon-like track containing a kink shortly after the vertex, indicating the decay of a tau to a muon and finally confirming the existence of the tau neutrino.

### 2.1.2 Neutrino Mixing

There exist three discovered neutrino flavour states, each associated with a charged lepton flavour ( $\nu_e$ ,  $\nu_\mu$  and  $\nu_\tau$ ). Neutrino oscillation is the phenomenon by which the flavour composition of a neutrino flux changes as it propagates. Several sets of experimental evidence led toward the ultimate acceptance of oscillation as a theory.

#### 2.1.2.1 The Solar Neutrino Problem

Neutrino oscillations were first hinted at by the Homestake Experiment in the late 1960s [5]. Homestake used a radiochemical method to detect solar electron neutrinos: a large tank of pure  $\text{C}_2\text{Cl}_4$  was used as a target. An inverse beta decay mechanism was again used:



Roughly monthly, the argon atoms were removed by bubbling helium through the volume, and were then counted as they decayed giving a measurement of electron neutrino flux. These electron neutrinos were produced in the Sun, and their rates were lower than

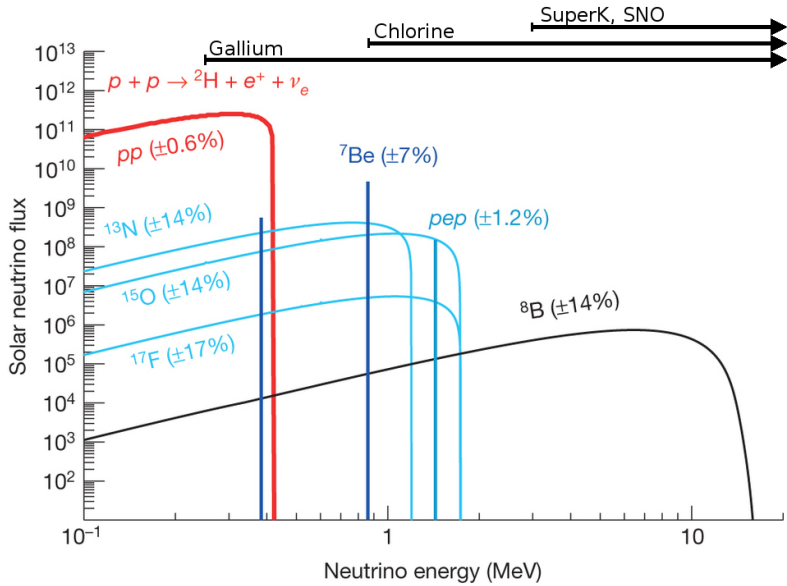


Figure 2.2: The energies and relative fluxes of the neutrinos produced by different solar processes. The energy thresholds for various solar neutrino experiments are shown along the top of the figure. Adapted from [9].

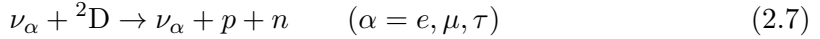
solar models predicted, by a factor of 2-3 [6]. Other experiments such as SAGE [7] and GALLEX [8] used gallium to detect higher flux, lower energy solar neutrinos. These experiments observed a smaller deficit, suggesting an energy dependence. These discrepancies became known as the ‘solar neutrino problem’. The vast majority of solar neutrinos being studied were below the energy threshold required for  $\nu_\mu$  or  $\nu_\tau$  charged current (CC) interactions, so any oscillated flux could not be seen in these experiments. The solar reactions that produce neutrinos, the energies of those neutrinos and thresholds for detection methods can be seen in Figure 2.2.

### 2.1.2.2 The Atmospheric Neutrino Anomaly

Studies were also performed of neutrinos produced by muon decays in the atmosphere; these measured the ratio of  $\nu_\mu$  to  $\nu_e$  events as a function of zenith angle (a proxy for baseline). In order to cancel systematic uncertainties, a double ratio of the predicted rate to the expected rate for each of  $\nu_\mu$  and  $\nu_e$  was used. The ratios measured were lower than predicted - an indication of either  $\nu_\mu$  disappearance or  $\nu_e$  appearance. This result became known as the ‘atmospheric neutrino anomaly’. Importantly, Super-Kamiokande demonstrated that the observed neutrino flux varied as a function of zenith angle (and thus distance travelled) [10]. Neutrino oscillations were proposed as the cause of this [11]. More information on Super-Kamiokande and the water Čerenkov method can be found in Section 3.3.

### 2.1.2.3 Confirmation of Neutrino Oscillation

The Sudbury Neutrino Observatory (SNO) used heavy water in a Čerenkov detector to detect solar neutrinos. Due to the use of heavy water, it could also detect neutral current (NC) neutrino interactions on deuterium [12]:



The neutrons produced in this interaction can interact with another deuteron, producing tritium and a 6.3 MeV photon.



Detecting the coincidence of these two interactions allowed the identification of NC events. Later phases of SNO detected the neutrons using techniques with a higher capture rate, first with a NaCl solute, then with Helium-3 proportional counters. Since these neutral current interactions do not produce charged leptons, they are flavour-independent. The rate matched the solar predictions, showing that the ‘missing’ solar neutrinos were still there, and had only changed flavour state. SNO also observed charged current events from solar neutrinos, and observed a deficit [13]. Taken together, these results can be considered proof of flavour-changing neutrino oscillation.

The Standard Model was constructed with massless neutrinos for reasons that will be explained in Section 2.2.4, but the evidence of neutrino oscillations demonstrated that at least two neutrinos are massive, as explained in Section 2.2.5. While their absolute mass is unknown, it has been experimentally confirmed that the neutrino masses are  $< 2$  eV using tritium decay [14]. Some cosmological experiments claim even more stringent limits, like  $\Sigma m_\nu < 0.6$  eV [15], although these are highly model dependent.

### 2.1.2.4 The LSND Anomaly

The neutrino oscillation story has one more major twist: the LSND anomaly [16]. LSND (the Liquid Scintillator Neutrino Detector) was a short baseline (30 m) accelerator neutrino experiment at Fermilab designed to search for  $\bar{\nu}_e$  appearance in a  $\bar{\nu}_\mu$  beam using inverse beta decay:  $p + \bar{\nu}_e \rightarrow e^+ + n$ . As will be seen in Section 2.2.5, oscillations depend on the splitting of neutrino mass states:

$$\Delta m_{kj}^2 = m_k^2 - m_j^2 \quad (2.9)$$

Previously, studies of oscillation in the atmospheric and solar sectors had measured values of  $|\Delta m_{32}^2| \approx 2.3 \times 10^{-3}$  eV<sup>2</sup> and  $\Delta m_{21}^2 \approx 8 \times 10^{-5}$  eV<sup>2</sup> respectively. In a three-

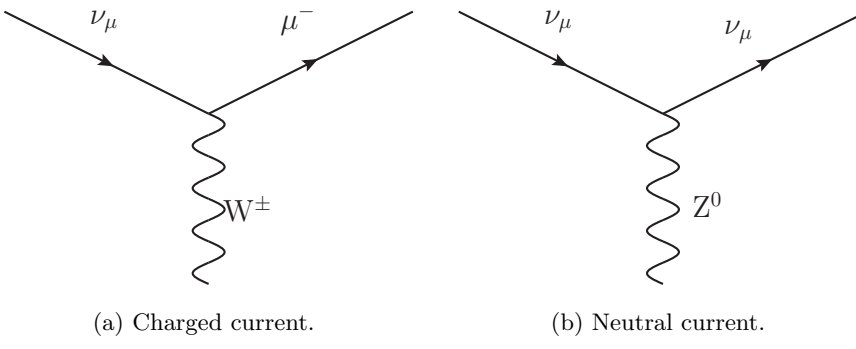


Figure 2.3: Example weak interaction vertices.

flavour oscillation system, there are only two free mass splittings  $\Delta m_{21}^2$  and  $|\Delta m_{32}^2|$  since  $\Delta m_{13}^2 + \Delta m_{21}^2 + \Delta m_{32}^2 = 0$ . However, LSND found a splitting  $\Delta m_{LSND}^2 \approx 1.2 \text{ eV}^2$  which is inconsistent with the solar and atmospheric results in a three-flavour model. The LEP experiment had confirmed that there are only three weakly interacting neutrinos lighter than half the  $Z^0$  boson mass [3], while the LSND result needed a fourth neutrino. This neutrino would thus have to be unable to couple to the weak force: it must be *sterile*. Subsequent experiments have provided incompatible results in sterile studies, which have yet to be reconciled.

## 2.2 Neutrino Theory

### 2.2.1 The Weak Interaction

The weak force is so named because the electromagnetic and strong interactions tend to dominate it when they are allowed. However, neutrinos interact only via the weak force. This results in neutrino interactions having very small cross sections. This is a major reason that neutrinos evaded detection for so long, and is crucial to the design of neutrino experiments: experiments must be designed to study very high neutrino fluxes, and have large detector masses in order to accumulate usable event numbers. The weak force is mediated by massive gauge bosons: the electrically charged  $W^\pm$  bosons and the neutral  $Z^0$  boson. It is the fact that the gauge bosons are massive ( $\sim 80$  and  $\sim 91$  GeV) that leads to the suppression of weak interactions, and thus the observed weakness of the force. The charged and neutral bosons lead to two categories of weak interactions: charged current (CC) and neutral current (NC) respectively. CC interactions respect flavour, and produce the appropriate charged leptons. NC interactions have no dependence on the (non-sterile) flavour state of the neutrino, and do not make charged leptons directly. Feynman diagrams of the two types of weak vertex can be seen in Figures 2.3a and 2.3b.

For the analyses in this thesis, the main signal mode will be Charged Current

Quasi-Elastic (CCQE), in which a neutrino interacts with a nucleon to produce only a charged lepton and a daughter nucleon. This, and other neutrino interaction modes will be explained in much greater detail in Section 4.2.1.

A key aspect of the weak interaction is its relationship with two linked concepts: *helicity* and *chirality*. We define the helicity of a particle to be the dot product of its spin and its direction of motion. This helicity commutes with the Hamiltonian, and is thus conserved. For massless particles this is clearly defined, but for massive particles a Lorentz boost can reverse the direction of motion without affecting the spin, switching the helicity. Neutrinos are nearly massless, which means experimentally we observe neutrinos with a well-defined helicity. In 1957, it was observed that neutrinos only appear with left-handed helicity [17].

However, we now know that neutrinos have mass. For massive particles we must define a rather more abstract quantity which is Lorentz invariant, at the expense of its commutation with the Hamiltonian. This is the chirality, and we define the chiral projection operators which break a Dirac spinor  $\psi$  into left-handed and right-handed chiral components:

$$\psi_L = \hat{P}_L \psi = \frac{1 - \gamma^5}{2} \psi \quad ; \quad \psi_R = \hat{P}_R \psi = \frac{1 + \gamma^5}{2} \psi \quad (2.10)$$

where  $\gamma^5$  is the  $i$  times the product of the 4 gamma matrices in the Dirac equation [18]. Clearly, we see  $\psi = \psi_L + \psi_R$ . Since  $\gamma^5$  is Hermitian and  $\{\gamma^5, \gamma^\mu\} = 0$ , it also follows:

$$\overline{\psi_L} \psi_L = \overline{\psi_R} \psi_R = 0 \quad (2.11)$$

The weak force is a chiral interaction, and in the Standard Model only left-handed particles and right-handed antiparticles couple to the weak bosons.

### 2.2.2 CP Violation

One of the great questions of modern physics is the matter-antimatter asymmetry in the universe. In order to explain why we do not see a universe with equal parts matter and antimatter, three conditions must be met: Baryon number must be violated, C and CP-symmetry must be violated and these processes must occur outside of thermal equilibrium [19]. Neutrino physics could provide evidence for violation of CP-symmetry beyond that already observed in the quark sector.

To explain this in a more useful fashion, a little more detail is required. We can define a quantum mechanical charge conjugation operator  $\hat{C}$  which replaces particles with their antiparticles:

$$q \rightarrow -q \quad (2.12)$$

where  $q$  represents each charge carried by the particle. We also define a parity operator  $\hat{P}$  which reverses the sign of spatial dimensions:

$$t \rightarrow t \quad x \rightarrow -x \quad y \rightarrow -y \quad z \rightarrow -z \quad (2.13)$$

Since applying either of these operators twice gives the original input,  $\hat{P}^2 = \hat{C}^2 = 1$  and so the eigenvalues of these operators can have the values  $\pm 1$ . The parity of a system is the product of the parities of its components. Similarly, the  $\hat{C}$  eigenvalue of a system (henceforth called C-parity) is the product of the C-parities of its components. By convention, we give fermions a parity of  $+1$  and anti-fermions a parity of  $-1$ .

Parity and C-parity are, to our knowledge, conserved in strong and EM interactions. In 1956, however, it was demonstrated using beta decays from cobalt atoms with aligned spins that parity is maximally violated by the weak interaction [20]. CP, the product of parity and C-parity, appeared to be conserved until it was demonstrated using kaon decays that CP is violated in a minority of weak interactions. Measuring CP violation in the lepton sector remains a major goal of particle physicists. So far, evidence suggests that we do reach a fully conserved quantity if we apply a third transformation - time reversal ( $\hat{T}$ ):

$$t \rightarrow -t \quad (2.14)$$

The property that applying these three transformations leaves physics unchanged is known as CPT symmetry, and is an essential property of many physics models. CPT violation would require a reinterpretation of most of modern physics, and CPT symmetry will be considered to be true for the remainder of this work.

### 2.2.3 V-A Structure

The requirement that any given matrix element for an interaction must be Lorentz invariant puts strict constraints on the possible form of the interaction vertex. There are sixteen combinations of the gamma matrices and spinors that produce Lorentz invariant currents. These form 5 categories according to the way they transform under parity: scalar, pseudoscalar, vector, axial vector and tensor. Under a parity transformation, the scalar and axial vector components remain the same, while the pseudoscalar and vector are transformed.

Experimentally, it was determined that the structure of the charged current weak interaction is Vector-Axial, in which a spin-1 particle is exchanged [21]:

$$J_{CC} \propto \gamma^\mu (1 - \gamma^5) \quad (2.15)$$

In this way, the vector and axial components both conserve parity on their own, but the

difference V-A does not. The neutral current weak interaction follows a similar structure, modified by a correction for the each of the vector ( $C_V^f$ ) and axial ( $C_A^f$ ) components, dependent on the type of fermion  $f$  interacting [22]:

$$J_{NC} \propto \gamma^\mu (C_V^f - C_A^f \gamma^5) \quad (2.16)$$

In the Standard Model,  $C_V^\nu = C_A^\nu = \frac{1}{2}$  [21]. The contributions from the vector and axial currents must be calculated separately, and will lead to different systematics in our cross-section models.

#### 2.2.4 Neutrino Mass

The non-zero neutrino mass raises an additional puzzle. In the Standard Model Lagrangian, particle masses are included by a Dirac mass term:

$$\begin{aligned} \mathcal{L}_D &= m\bar{\psi}\psi \\ &= m\overline{(\psi_L + \psi_R)}(\psi_L + \psi_R) \\ &= m(\overline{\psi_L}\psi_R + \overline{\psi_R}\psi_L) \end{aligned} \quad (2.17)$$

Equation 2.11 was used for the final step here. As such, a Dirac mass appears in the Lagrangian as a coupling of a left-handed to a right-handed chiral state. However, if the neutrino has no right-handed state (and similarly the antineutrino has no left-handed state), this term disappears. Thus, unless there exists a right-handed neutrino, the neutrino cannot have a Dirac mass.

Since we know that the neutrino does have mass but have not observed a right-handed state, we introduce an alternative mechanism. We can introduce a right-handed neutrino field that does not couple to the weak interaction and carries no gauge quantum numbers. Majorana proposed that we manufacture this right-handed field from the charge conjugate of the left-handed field:

$$\hat{C} = i\gamma^2\gamma^0 \quad (2.18)$$

$$\psi_L^C = \hat{C}\overline{\psi_L} \quad (2.19)$$

$$\mathcal{L}_M = -\frac{1}{2}M(\overline{\psi_L}\psi_L^C + \overline{\psi_L^C}\psi_L) \quad (2.20)$$

Under this hypothesis, the right-handed component is accessed by the charge conjugation operator applied to the left-handed state: the neutrino and the antineutrino are the same particle. The two states are coupled by the Majorana mass  $M$ . The

interactions of this single neutrino are dependent on which chiral state interacts with the W boson. Thus the mass is included by the coupling of the left-handed state (which interacts to produce negative leptons) to the right-handed state (which interacts to produce positive leptons). Neutrinos are the only Standard Model fermions for which this is possible since the others have electromagnetic charge, which would reverse under the charge conjugation. This construction adds a number of interactions that violate lepton number by  $\pm 2$ , such as neutrinoless double beta decay. Experimental searches for these interactions are ongoing.

### 2.2.5 Neutrino Oscillation

The major topic of this thesis is the study of neutrino oscillation: a phenomenon in which the flavour composition of a neutrino flux changes as it propagates. We will consider neutrinos with three flavour states ( $\nu_e$ ,  $\nu_\mu$  and  $\nu_\tau$ ) and three mass states ( $\nu_1$ ,  $\nu_2$  and  $\nu_3$ ). The empirical observation of oscillation indicates that the neutrino flavour eigenstates are not identical to the mass eigenstates. We produce and detect neutrinos in definite flavour eigenstates, and they propagate according to their mass states. Each neutrino flavour state is a different quantum mechanical superposition of the mass states. Flavour oscillation is a direct consequence of this: the differing mass states propagate at slightly different velocities. In the context of a coherent neutrino beam, this results in the mass states having different relative phases at different points in the beam. When an interaction occurs, we have a neutrino with a set of mass states which yields a superposition of different flavour states. The result is that neutrino beam can contain flavour eigenstates which were not present in the beam when it was generated. This explains the experimental data from solar and atmospheric neutrinos described in Section 2.1.2.

In order to calculate oscillation probabilities, we must consider the transformations between mass ( $k$ ) and flavour ( $\alpha$ ) states. This transformation can be expressed as a unitary rotation matrix  $U$ :

$$|\nu_\alpha\rangle = \sum_k U_{\alpha k} |\nu_k\rangle \quad (2.21)$$

$$|\nu_k\rangle = \sum_\alpha U_{\alpha k}^* |\nu_\alpha\rangle \quad (2.22)$$

Here, the matrix  $U$  for three flavour oscillation is known as the Pontecorvo-Maki-Nakagawa-Sakata (PMNS) matrix, and is parameterised in terms of three mixing angles

$(\theta_{12}, \theta_{23}$  and  $\theta_{13}$ ) and a phase which describes CP violation ( $\delta_{cp}$ ) [14]:

$$\begin{aligned}
U &= \begin{pmatrix} U_{e1} & U_{e2} & U_{e3} \\ U_{\mu 1} & U_{\mu 2} & U_{\mu 3} \\ U_{\tau 1} & U_{\tau 2} & U_{\tau 3} \end{pmatrix} \\
&= \begin{pmatrix} 1 & 0 & 0 \\ 0 & c_{23} & s_{23} \\ 0 & -s_{23} & c_{23} \end{pmatrix} \begin{pmatrix} c_{13} & 0 & s_{13}e^{-i\delta_{cp}} \\ 0 & 1 & 0 \\ -s_{13}e^{i\delta_{cp}} & 0 & c_{13} \end{pmatrix} \begin{pmatrix} c_{12} & s_{12} & 0 \\ -s_{12} & c_{12} & 0 \\ 0 & 0 & 1 \end{pmatrix} \quad (2.23) \\
&= \begin{pmatrix} c_{12}c_{13} & s_{12}c_{13} & s_{13}e^{-i\delta_{cp}} \\ -s_{12}c_{23} - c_{12}s_{23}s_{13}e^{i\delta_{cp}} & c_{12}c_{23} - s_{12}s_{23}s_{13}e^{i\delta_{cp}} & s_{23}c_{13} \\ s_{12}s_{23} - c_{12}c_{23}s_{13}e^{i\delta_{cp}} & -c_{12}s_{23} - s_{12}c_{23}s_{13}e^{i\delta_{cp}} & c_{23}c_{13} \end{pmatrix}
\end{aligned}$$

For conciseness, the notation convention:

$$c_{kj} = \cos(\theta_{kj}) \quad ; \quad s_{kj} = \sin(\theta_{kj}) \quad (2.24)$$

has been used. The three flavour framework offers only one free physical phase, and its association with  $\theta_{13}$  in the above equation is an arbitrary choice made in the parameterisation. The time development of the mass eigenstates can be written:

$$i \frac{d}{dt} \begin{pmatrix} \nu_1 \\ \nu_2 \\ \nu_3 \end{pmatrix} = H \begin{pmatrix} \nu_1 \\ \nu_2 \\ \nu_3 \end{pmatrix} \quad (2.25)$$

Here,  $H$  is the Hamiltonian operator. In vacuum:

$$H_{vacuum} = \frac{1}{2E} \begin{pmatrix} m_1^2 & 0 & 0 \\ 0 & m_2^2 & 0 \\ 0 & 0 & m_3^2 \end{pmatrix} \quad (2.26)$$

The total Hamiltonian will contain this vacuum Hamiltonian, but may contain other terms from matter interaction, as will be explained in Section 2.2.7. Transforming to the flavour states using the PMNS matrix  $U$ , we get:

$$i \frac{d}{dt} \begin{pmatrix} \nu_e \\ \nu_\mu \\ \nu_\tau \end{pmatrix} = U H_{total} U^\dagger \begin{pmatrix} \nu_e \\ \nu_\mu \\ \nu_\tau \end{pmatrix} \quad (2.27)$$

To calculate probabilities, we treat the evolving mass states as plane waves [18]:

$$|\nu_k(t)\rangle = e^{-iE_k t} |\nu_k\rangle \quad (2.28)$$

This means that a neutrino created at  $t = 0$  with definite flavour  $\alpha$  has a flavour component at time  $t$ :

$$|\nu_\alpha(t)\rangle = \sum_k U_{\alpha k}^* e^{-iE_k t} |\nu_k\rangle \quad (2.29)$$

Combining equations 2.21 and 2.29, we get the flavour state at  $t$  as a superposition of flavour states:

$$|\nu_\alpha(t)\rangle = \sum_\beta \left( \sum_k U_{\alpha k}^* e^{-iE_k t} U_{\beta k} \right) |\nu_k\rangle \quad (2.30)$$

From here, we get the amplitude of  $\nu_\alpha$  oscillating to  $\nu_\beta$ :

$$A_{\nu_\alpha \rightarrow \nu_\beta}(t) \equiv \langle \nu_\beta | \nu_\alpha(t) \rangle = \sum_k U_{\alpha k}^* U_{\beta k} e^{-iE_k t} \quad (2.31)$$

with the oscillation probability:

$$P_{\nu_\alpha \rightarrow \nu_\beta}(t) \equiv |A_{\nu_\alpha \rightarrow \nu_\beta}(t)|^2 = \sum_{k,j} U_{\alpha k}^* U_{\beta k} U_{\alpha j}^* U_{\beta j} e^{-i(E_k - E_j)t} \quad (2.32)$$

For a neutrino of extremely small mass, the energies of different components of a neutrino with energy  $E$  are:

$$E_k \simeq E + \frac{m_k^2}{2E} \quad (2.33)$$

This gives a difference of:

$$E_k - E_j \simeq \frac{\Delta m_{kj}^2}{2E} \quad (2.34)$$

The mass splittings here are defined as:

$$\Delta m_{kj}^2 = m_k^2 - m_j^2 \quad (2.35)$$

For an accelerator neutrino experiment like T2K, we know the baseline  $L$ , and since our neutrinos are ultra-relativistic we can approximate  $t = L$  for the purposes of equation 2.32. This gives us oscillations as such:

$$P_{\nu_\alpha \rightarrow \nu_\beta}(L, E) = \sum_{k,j} U_{\alpha k}^* U_{\beta k} U_{\alpha j}^* U_{\beta j} e^{-i \frac{\Delta m_{kj}^2 L}{2E}} \quad (2.36)$$

As such, we have oscillations of an amplitude specified by the mixing angles, and a phase specified by mass splitting  $\Delta m_{kj}^2$  and the ratio  $L/E$ .

We can calculate a disappearance or appearance probability in a vacuum [23]:

$$P(\nu_\alpha \rightarrow \nu_\beta) = \delta_{\alpha\beta} - 4 \sum_{k>j} Re(U_{\alpha k}^* U_{\beta k} U_{\alpha j} U_{\beta j}^*) \sin^2 \left( \frac{\Delta m_{kj}^2 L}{4E} \right) + 2 \sum_{k>j} Im(U_{\alpha k}^* U_{\beta k} U_{\alpha j} U_{\beta j}^*) \sin \left( \frac{\Delta m_{kj}^2 L}{2E} \right) \quad (2.37)$$

This probability is a function of baseline ( $L$ ), neutrino energy ( $E$ ) and the mass squared splittings ( $\Delta m_{21}^2$  and  $|\Delta m_{32}^2|$ ) as well as the mixing angles. If we simplify this into a two-flavour disappearance probability, and use a convenient unit convention, it looks like this:

$$P(\nu_x \rightarrow \nu_y) = \sin^2(2\theta) \sin^2(1.27\Delta m^2(\text{eV}^2) \frac{L(\text{km})}{E(\text{GeV})}) \quad (2.38)$$

The dimensionless factor 1.27 here corrects for the units involved, and it is important to note that for  $\Delta m^2 = 0$ , no oscillations would be seen. As such, the observation of oscillation requires massive neutrinos. It should also be noted that this probability is dependent on the absolute value of  $\Delta m^2$  and to first order, long-baseline experiments provide no information about its sign or absolute magnitude.

In three-flavour oscillation, the fact that only the differences in squared mass have an effect leads to an ambiguity in the ordering of the mass states. Matter effects on oscillation in the sun allow determination that the sign of  $\Delta m_{21}^2$  is positive.  $\Delta m_{21}^2$  is of order  $10^{-5}$  eV $^2$  while  $|\Delta m_{32}^2|$  is of order  $10^{-3}$  eV $^2$ . This could be caused by either two light neutrinos and one heavier one, or two heavier neutrinos and one lighter one. The two options are respectively known as the *normal hierarchy* (NH) and the *inverted hierarchy* (IH). A diagram of this can be seen in Figure 2.4. Oscillation results in this document will generally be quoted for each of these two distinct hierarchies, and will be calculated using a full three-flavour calculation. Figure 2.5 shows the flavour makeup of an initially pure  $\nu_\mu$  beam at various values of  $L/E$ .

## 2.2.6 Maximality in Neutrino Oscillation

As trigonometric rotations, the mixing angles and complex phase are inherently periodic, and their effects on the mixing matrix are bounded. For example, the value of  $\sin^2(\theta)$  can only take values between 0 and 1, as can the matrix elements  $U_{\alpha i}$ . In an oscillation measurement, these boundaries can be important: if a disappearance experiment has a statistical fluctuation downwards, this can lead to a dataset whose ‘true’ best-fit point lies at greater than maximal disappearance. As such, it is important to recognise the position of the maxima and minima of the oscillation probabilities, and how these can affect confidence regions. In particular, a dataset closer to maximum disappearance will

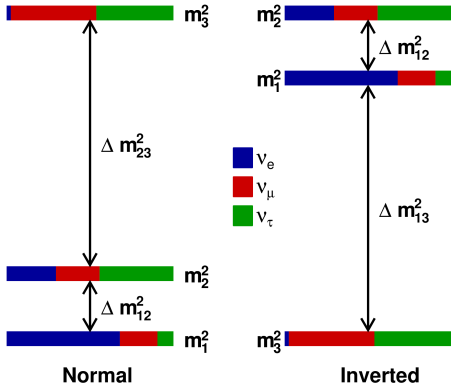


Figure 2.4: The two possible hierarchies of neutrino mass states. Fractions of flavours here are drawn with mixings  $\sin^2(\theta_{23}) = 0.527$ ,  $\sin^2(\theta_{12}) = 0.304$  and  $\sin^2(\theta_{13}) = 0.0248$ .

have a smaller confidence region. Additionally, as one moves away from maximal mixing, one can travel in either direction, toward either octant. Now that it has been empirically demonstrated that  $\sin^2(\theta_{13}) \neq 0$ , the two octants for a muon neutrino disappearance experiment are guaranteed to be different. For off-maximal mixing, we expect to see two different local minima, and the oscillation analysis must take this into account. Maximum  $\nu_\mu$  disappearance occurs at:

$$\sin^2(\theta_{23}) = \frac{1}{2 \cos(\theta_{13})} \quad (2.39)$$

A plot of the muon survival probability, demonstrating the shift in the position of maximal mixing can be seen in Figure 2.6.

## 2.2.7 Matter Interactions in Oscillation Physics

### 2.2.7.1 Neutrino Mixing in Matter

In the previous section, we covered the mixing of neutrinos due to mass differences, which can occur in a vacuum. In practice, our neutrinos propagate through matter with high electron densities, although no muons or tau leptons. As a result, they undergo additional effects due to their interactions with this medium. These interactions are coherent elastic weak CC and NC scatterings, which each add an effective potential to the Hamiltonian. If the potential  $V_{CC}$  varies with neutrino flavour, then an additional phase difference can be introduced making the neutrino oscillate as a result of matter effects. With neutrino energy  $E_\nu$ , electron density  $N_e$  and Fermi constant  $G_F$ , the

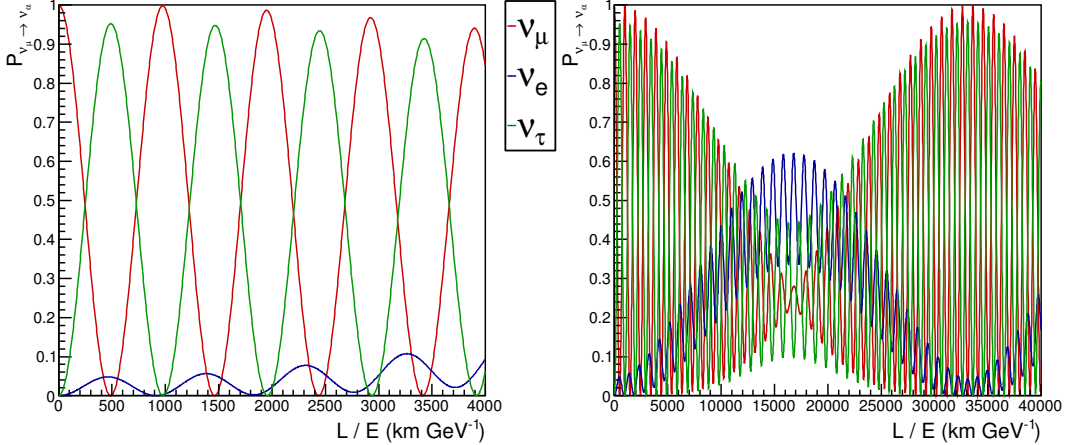


Figure 2.5: Probabilities of observing a given neutrino flavour in a beam generated as pure  $\nu_\mu$  at varying baselines. The oscillation parameters here are  $\sin^2 \theta_{23} = 0.527$ ,  $\sin^2(\theta_{12}) = 0.304$ ,  $\sin^2(\theta_{13}) = 0.0248$ ,  $|\Delta m_{32}^2| = 2.51 \times 10^{-3}$  eV $^2$ ,  $\Delta m_{21}^2 = 7.53 \times 10^{-5}$  eV $^2$  and  $\delta_{CP} = -1.55$ .

potential due to charged current effects has the following dependence [18]:

$$V_{CC} = \pm \sqrt{2} G_F N_e \quad (2.40)$$

The coefficient is positive for neutrinos, and negative for antineutrinos. There are also neutral current matter interactions, depending on the density of neutrons  $N_n$  in the matter. Contributions from protons and electrons cancel each other out in neutral matter.

$$V_{NC} = \pm \frac{1}{2} \sqrt{2} G_F N_n \quad (2.41)$$

Since these interactions are neutral current, they are flavour independent. This means that each flavour's potential is altered by the same amount, leaving no net phase difference. As such, NC matter effects have no effect on an oscillation signal unless there exist sterile neutrinos, and for the purposes of this thesis, they will not be considered further.

This result gives us an effective Hamiltonian for flavour states of:

$$H_F = \frac{1}{2E_\nu} (U \mathbf{M}^2 U^\dagger + \mathbf{A}) \quad (2.42)$$

For the case of three neutrino mixing, the matrices here are the mass splittings:

$$\mathbf{M}^2 = \begin{pmatrix} 0 & 0 & 0 \\ 0 & \Delta m_{21}^2 & 0 \\ 0 & 0 & \Delta m_{31}^2 \end{pmatrix} \quad (2.43)$$

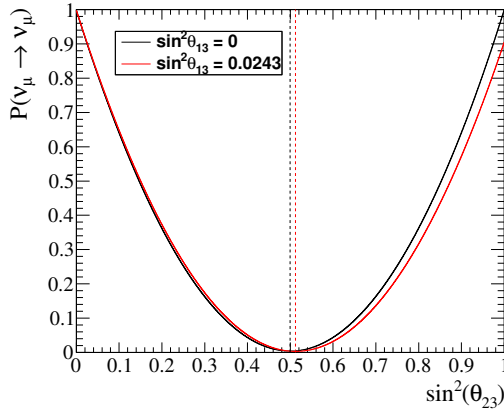


Figure 2.6: The muon survival probability as a function of  $\sin^2 \theta_{23}$ , with dashed lines marking the position of maximum disappearance.

And the contributions of matter:

$$\mathbf{A} = 2E_\nu V_{CC} \begin{pmatrix} 1 & 0 & 0 \\ 0 & 0 & 0 \\ 0 & 0 & 0 \end{pmatrix} \quad (2.44)$$

### 2.2.7.2 The MSW Resonance

One of the most striking consequences of matter effects is the Mikheyev-Smirnov-Wolfenstein (MSW) resonance, which can be observed in the sun [24, 25]. The sun produces electron neutrinos, and has an extremely high electron density ( $N_e$ ) near the centre, which smoothly decreases as the neutrinos propagate outwards. There exists a resonance point in electron density ( $N_e^R$ ) which leads to maximal mixing for neutrinos of a given energy. The electron density in the sun is very high, such that for sufficiently high energy neutrinos,  $N_e \gg N_e^R$ , and the neutrinos must pass through this resonance point on their way out of the sun towards space.

In order to understand where this resonance point comes from, let us consider a two flavour approximation with matter effects. With the two-flavour approximation, we have one mixing angle  $\vartheta$  and one mass splitting  $\Delta m^2$ , with a mixing matrix:

$$U = \frac{1}{4E_\nu} \begin{pmatrix} \cos \vartheta & \sin \vartheta \\ -\sin \vartheta & \cos \vartheta \end{pmatrix} \quad (2.45)$$

The Hamiltonian for flavour states takes the form:

$$H_F = \frac{1}{4E_\nu} \begin{pmatrix} -\Delta m^2 \cos 2\vartheta + 2E_\nu V_{CC} & \Delta m^2 \sin 2\vartheta \\ \Delta m^2 \sin 2\vartheta & \Delta m^2 \cos 2\vartheta - 2E_\nu V_{CC} \end{pmatrix} \quad (2.46)$$

To get an effective Hamiltonian in matter for the mass states  $H_M$ , we must diagonalise using a rotation matrix  $U_M$ :

$$U_M^T H_F U_M = H_M \quad (2.47)$$

which has an effective mixing angle  $\vartheta_M$ :

$$U_M = \begin{pmatrix} \cos \vartheta_M & \sin \vartheta_M \\ -\sin \vartheta_M & \cos \vartheta_M \end{pmatrix} \quad (2.48)$$

$H_M$  is a diagonal matrix parameterised with an effective mass splitting  $\Delta m_M^2$ :

$$H_M = \frac{1}{4E_\nu} \begin{pmatrix} -\Delta m_M^2 & 0 \\ 0 & \Delta m_M^2 \end{pmatrix} \quad (2.49)$$

It can be shown that the effective mixing angle and mass splitting are [18]:

$$\Delta m_M^2 = \sqrt{(\Delta m^2 \cos 2\vartheta - 2E_\nu V_{CC})^2 + (\Delta m^2 \sin 2\vartheta)^2} \quad (2.50)$$

$$\tan 2\vartheta_M = \frac{\tan 2\vartheta}{1 - \frac{2E_\nu V_{CC}}{\Delta m^2 \cos 2\vartheta}} \quad (2.51)$$

It is clear that this equation diverges for a matter potential contribution:

$$V_{CC}^R = \frac{\Delta m^2 \cos 2\vartheta}{2E_\nu} \quad (2.52)$$

Using equation 2.40, we can see that this is equivalent to an electron density of:

$$N_e^R = \frac{\Delta m^2 \cos 2\vartheta}{2\sqrt{2}E_\nu G_F} \quad (2.53)$$

When  $\tan 2\vartheta$  diverges, the value of  $\vartheta$  is  $\pi/4$ , leading to maximal mixing. Using equation 2.50, we can see that the effective mass splitting reaches a minimum at this point:

$$\Delta m_{M,R}^2 = \Delta m^2 \sin 2\vartheta \quad (2.54)$$

It can be seen from equation 2.53 that the resonance electron density depends on neutrino energy. For the sun, the threshold neutrino energy is approximately 6 MeV [26]. For neutrinos above this energy deep inside the sun, the electron density vastly exceeds the resonance density  $N_e^R$ . Thus the mixing angle is effectively  $\pi/2$  and thus the electron neutrino is created as nearly pure  $\nu_2$ . As the neutrino propagates out of the sun, it crosses the resonance point adiabatically, remaining in the  $\nu_2$  state. Once it has exited

the sun, its flavour makeup is:

$$\nu_2 = \sin \vartheta \nu_e + \cos \vartheta \nu_\mu \quad (2.55)$$

In the case of a minimal mixing angle  $\vartheta \simeq 0$ , this leads to effectively all the electron neutrinos having oscillated to muon neutrinos, despite a near-zero mixing angle.

## 2.3 Current Status of Neutrino Oscillation Research

### 2.3.1 Atmospheric Neutrino Experiments

The muon neutrino disappearance observed in atmospheric experiments is used to measure  $\sin^2 \theta_{23}$  and  $|\Delta m_{32}^2|$ . More recently, atmospheric measurements have been used to constrain the mass hierarchy and sterile signal. Super-K atmospheric analyses express a weak ( $1\sigma$ ) preference for the normal mass hierarchy, and have constrained sterile PMNS matrix elements ( $|U_{\mu 4}|^2 < 0.041$  and  $|U_{\tau 4}|^2 < 0.18$  at 90% C.L) [27].

IceCube is a cubic kilometre of ice at the South Pole, instrumented with PMTs to detect Čerenkov light. While primarily designed to study cosmic neutrino signals, the detector can also detect atmospheric neutrinos, particularly using the more densely instrumented section of the detector known as DeepCore. IceCube's best measurement of atmospheric  $\nu_\mu$  disappearance gives limits of  $|\Delta m_{32}^2| = 2.72^{+0.19}_{-0.20} \times 10^{-3}$  eV<sup>2</sup> and  $\sin^2 \theta_{23} = 0.53^{+0.09}_{-0.12}$  [28]. A future upgrade named PINGU (Precision IceCube Next Generation Upgrade) aims to determine the mass hierarchy using atmospheric neutrino data with as little as three years running [29].

### 2.3.2 Reactor Experiments

Nuclear reactors produce a significant flux of electron antineutrinos, and these are analysed at a variety of baselines. These experiments often use a near detector at a short baseline to evaluate the produced neutrino flux and a far detector to observe the effects of oscillation at a longer baseline. This is a powerful technique for reducing experimental uncertainties, and is also used in long-baseline experiments. The contemporary reactor oscillation experiments are Double Chooz, Daya Bay and RENO (Reactor Experiment for Neutrino Oscillations). All of these search for electron antineutrino disappearance, which allows for measurement of  $\theta_{13}$ , but does not offer any information about  $\delta_{CP}$ . One open question in reactor experiments is the observation of an excess of events around 5 MeV in all three of these experiments. This excess has been postulated as an oscillation signal, although is more likely to be related to modelling of reactor flux [30]. The RENO 5 MeV excess can be seen in Figure 2.7.

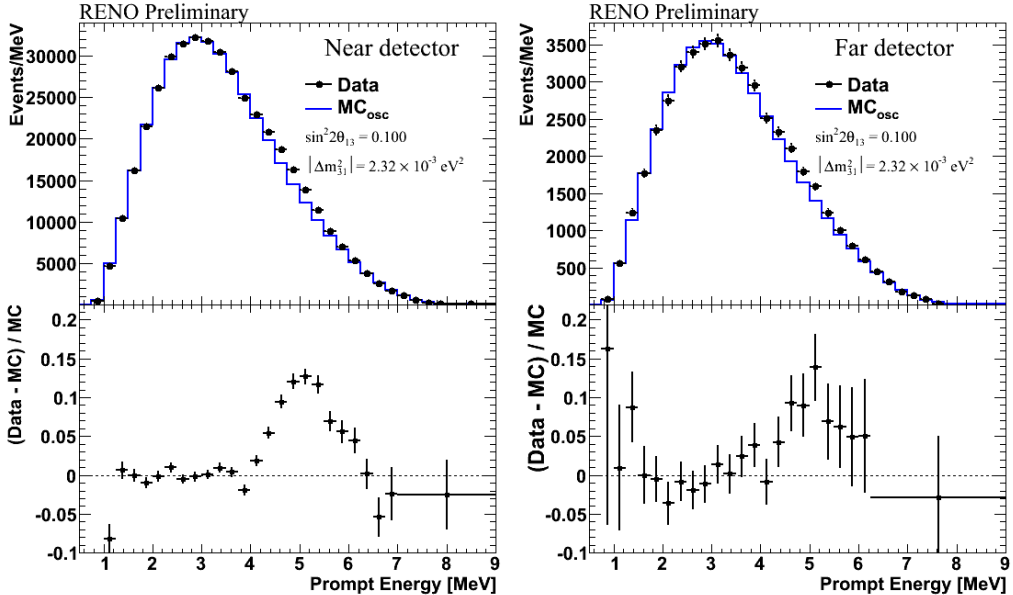


Figure 2.7: The RENO reactor antineutrino spectrum, demonstrating the 5 MeV excess. Reproduced from [31].

Double Chooz studies neutrinos from the Chooz nuclear power plant in France. It uses two identical detectors: a near detector at 400 m and a far detector at 1050 m. Double Chooz is the successor experiment to CHOOZ, which used only the far detector site and was responsible for demonstrating that  $\theta_{13}$  is small and thus the atmospheric neutrino anomaly could not be caused by  $\nu_\mu \rightarrow \nu_e$  oscillation [32]. Each detector contains 8.8 t of gadolinium-doped liquid scintillator, surrounded non-doped scintillator in order to capture photons. Double Chooz began collecting far detector data in 2009, and its near detector was finally completely in September 2014. Double Chooz has measured  $\sin^2 2\theta_{13} = 0.090^{+0.032}_{-0.029}$  [33].

Daya Bay consists of six identical antineutrino detectors, each with an interaction mass of 20 t of gadolinium-doped liquid scintillator. These detectors are all within 2 km of six nuclear reactors, giving the experiment a number of available baselines. This experimental design means that all measurements of event rate are relative and systematic errors can be cancelled effectively. This allowed Daya Bay to release the first definitive evidence of non-zero  $\theta_{13}$  with a  $5.2\sigma$  significance result published in 2012 [34]. The current Daya Bay best measurement is  $\sin^2 2\theta_{13} = 0.084 \pm 0.005$  and  $|\Delta m^2_{ee}| = 2.42 \pm 0.11 \times 10^{-3} \text{ eV}^2$  [35].  $|\Delta m^2_{ee}|$  is an effective parameter, defined by:

$$\sin^2(\Delta m^2_{ee} \frac{L}{4E}) = \cos^2 \theta_{12} \sin^2(\Delta m^2_{31} \frac{L}{4E}) + \sin^2 \theta_{12} \sin^2(\Delta m^2_{32} \frac{L}{4E}) \quad (2.56)$$

RENO is a reactor experiment in South Korea, which uses the antineutrino flux from six nuclear reactors. RENO uses two identical gadolinium-doped liquid scintillator detectors at a flux weighted average baseline of 410 m and 1440 m. The current RENO measurement is  $\sin^2 2\theta_{13} = 0.101 \pm 0.008(\text{stat.}) \pm 0.010(\text{syst.})$  [36].

KamLAND (Kamioka Liquid Scintillator Anti-Neutrino Detector) was a 1 kt liquid scintillator detector in the same mine as Super-K. It primarily observed electron antineutrinos from 56 Japanese nuclear reactors at a mean baseline of 180 km, but also performed measurements of solar neutrinos and geoneutrinos. The final three-flavour KamLAND measurements yield limits of  $\tan^2 \theta_{12} = 0.452^{+0.035}_{-0.033}$ ,  $\Delta m_{21}^2 = 7.50^{+0.19}_{-0.20} \times 10^{-5} \text{ eV}^2$  and  $\sin^2 2\theta_{13} = 0.020^{+0.016}_{-0.016}$  [37]. In 2011, the KamLAND tank had a balloon of Xenon-doped liquid scintillator installed, becoming a neutrinoless double beta decay experiment known as KamLAND-Zen.

The next generation of reactor experiments will include JUNO (Jiangmen Underground Neutrino Observatory) and RENO-50, which are successors to Daya Bay and RENO respectively. Both will use a baseline of approximately 50 km. Each will a large liquid scintillator detector (20 kt for JUNO, 18 kt for RENO-50) instrumented by approximately 15000 PMTs. The  $L/E$  for RENO and JUNO is optimised for the mass splitting  $\Delta m_{21}^2$ , but the wide range of energies produced by a reactor mean that if these experiments achieve an energy resolution of approximately 3% for 1 MeV events, they could observe the interference pattern between oscillations caused by  $\Delta m_{32}^2$  and  $\Delta m_{21}^2$ , allowing them to determine the mass hierarchy.

### 2.3.3 Long Baseline Accelerator Neutrino Experiments

Long-baseline neutrino beam experiments like T2K use a proton accelerator to produce a high-energy beam of muon neutrinos. These experiments are good for precision measurements of neutrino disappearance, and can observe  $\delta_{CP}$  by studying electron neutrino appearance in the beam. The comparatively small value of  $\sin^2 \theta_{13}$  makes electron neutrino appearance rare, which renders measurement of  $\delta_{CP}$  difficult. The baseline and peak beam energy are normally chosen such that the far detector lies at the first oscillation maximum:

$$\frac{L(\text{km})}{E(\text{GeV})} = \frac{\pi}{2} \frac{1}{1.27 \Delta m^2(\text{eV}^2)} \quad (2.57)$$

For  $|\Delta m_{32}^2| \approx 2.5 \times 10^{-3} \text{ eV}^2$ , the appropriate ratio is approximately  $L/E = 500 \text{ km GeV}^{-1}$ . Future experiments should be able to probe the second and even higher oscillation maxima. Long-baseline experiments allow good control over the beam energy, and relatively accurate flux prediction. Use of beam timing triggers can reduce backgrounds greatly. Muon neutrinos are made by firing a proton beam onto a target, and then using magnets to select a specific charge from the resulting meson (pion and kaon) flux. Selecting

for positive pions allows creation of a muon neutrino beam with a purity of over 90%. Selecting for negative pions allows creation of a beam with an enhanced muon antineutrino component, although the purities are lower (approximately 80%  $\bar{\nu}_\mu$  at T2K’s near detector). There is a fuller discussion of T2K’s beam composition in Section 4.1.

K2K (KEK to Kamioka) was the predecessor to T2K, and was the first long baseline accelerator neutrino experiment, running between 1999 and 2004. The beam was produced at KEK in Tsukuba, Japan. As with T2K, the far detector was Super-Kamiokande. The baseline was 250 km and an on-axis neutrino beam was used with a peak energy of around 1 GeV. K2K observed a  $4.2\sigma$  result confirming muon neutrino disappearance, and placed limits on  $\sin^2 2\theta_{23}$  and  $|\Delta m_{32}^2|$  [38]. K2K’s two-flavour fit results indicated maximal muon neutrino disappearance ( $\sin^2 2\theta_{23} = 1$ ) and a 90% confidence region of  $1.9 \times 10^{-3} \text{ eV}^2 < |\Delta m_{32}^2| < 3.5 \times 10^{-3} \text{ eV}^2$ .

MINOS (Main Injector Neutrino Oscillation Search) was the next long-baseline experiment, and used a 735 km baseline. The beam is produced at Fermilab’s NuMI beamline, with the far detector in the Soudan Underground Laboratory in Minnesota. The 5.4 kt MINOS far detector was turned on in 2003, and began taking NuMI beam data in 2005. The neutrino beam used is on-axis, with energies of a few GeV. Magnetised steel-scintillator detectors are used for both the near and far detectors. MINOS performed measurements with a neutrino mode and an antineutrino mode beam. The MINOS neutrino-mode dataset disfavoured maximal mixing at 86% confidence [39]. MINOS has continued to run under the name MINOS+, using the upgraded NuMI beam line designed for NO $\nu$ A.

T2K is the subject of this thesis, and is described in more detail in Chapter 3. It turned on in 2010, and is running to this day. T2K’s most important oscillation result is the first  $> 5\sigma$  demonstration of electron neutrino appearance in a muon neutrino beam [40], announced in 2013. The collaboration has also published precision measurements of  $\sin^2 \theta_{23}$  and  $|\Delta m_{32}^2|$  in a disappearance-only analysis, and joint fits of electron and muon data which, when combined with reactor constraints on  $\sin^2 \theta_{13}$  can place a 90% exclusion region  $\delta_{CP}$  [41].

NO $\nu$ A (NuMI Off-axis  $\nu_e$  Appearance experiment) is a newer experiment using the Fermilab NuMI beamline, with a 14 kt far detector at Ash River, Minnesota - a baseline of 810 km. Both the near and far detectors use a similar design, with liquid scintillator stored in PVC cells, and these detectors are positioned off-axis. The detectors are modular, and began taking some data in early 2014, with full operation using the completed detector beginning in October 2014.

The future of the long-baseline field is currently likely to be one or both of DUNE and T2HK. T2HK is an upgrade to T2K using a 1 Mt water off-axis far detector known as HyperKamiokande (HK). It would also include a beam upgrade to the T2K beam and

a new water Čerenkov near detector.

DUNE (Deep Underground Neutrino Experiment), formerly known as LBNE (Long Baseline Neutrino Experiment), is a proposed 1300 km baseline experiment in the USA. DUNE would use a beam from Fermilab, and would have an on-axis far detector in the Sanford Underground Research Facility near Lead, South Dakota. The far detector is intended to be a 40 kt liquid argon TPC, nearly 1.5 km underground. The wide-band beam allows DUNE access to the second oscillation maximum, which offers a new source of sensitivity to  $\delta_{CP}$ .

### 2.3.4 Short Baseline Neutrino Oscillation Experiments

As well as the long-baseline accelerator experiments, we also perform short baseline neutrino oscillation experiments. The LSND (Liquid Scintillator Neutrino Detector) experiment ran at Los Alamos National Laboratory from 1993 to 1998. An accelerator was used to produce muon antineutrinos in the energy range 0 to 53 MeV, which were detected at a 31 m baseline. It famously observed a small but significant excess of  $\overline{\nu}_e$  events, which is consistent with a sterile neutrino with  $\Delta m^2_{sterile} \approx 1 \text{ eV}^2$  [16].

A number of experiments were subsequently designed to confirm or refute this result. MiniBooNE used a mineral oil based Čerenkov detector at a baseline of approximately 500 m from the Fermilab Booster neutrino beamline. It used a typical neutrino beam energy of 500 MeV, meaning that it had a similar  $L/E$  to LSND, but a very different set of systematics. MiniBooNE was capable of running in both neutrino and antineutrino beam mode, and ran from 2002 to 2012. It observed a significant excess at low energy in both the  $\nu_\mu$  ( $3.4\sigma$ ) and  $\overline{\nu}_\mu$  ( $2.8\sigma$ ) beam modes [42]. The  $\overline{\nu}_\mu$  data agrees well with the LSND result, but there is tension with the  $\nu_\mu$  result. MicroBooNE is a new liquid argon detector in the same beamline which is intended to test the signal further, using a liquid argon TPC. The liquid argon TPC will allow the detector to better reject  $\nu_\mu$  NC $\gamma$  events which could be causing the excess.

### 2.3.5 Global Fits

The world's best knowledge of neutrino fit parameters can be determined by global fits, including data from many experiments. The Particle Data Group (PDG) typically selects one of these to be used as reference values. The current (2014) PDG recommendation was performed by F. Capozzi et al. [43], using the data available up until the end of 2013 from MINOS, T2K, KamLAND, Super-K, Daya Bay and RENO. The best-fit parameters from this global fit can be seen in Table 2.1.

Parameter	Best-fit ( $\pm 1\sigma$ )
$\Delta m_{21}^2$	$7.54^{+0.26}_{-0.22} \times 10^{-5}$ eV $^2$
$ \Delta m^2 $	$2.43 \pm 0.06 (2.38 \pm 0.06) \times 10^{-3}$ eV $^2$
$\sin^2 \theta_{12}$	$0.308 \pm 0.017$
$\sin^2 \theta_{23}$	$0.437^{+0.033}_{-0.023} (0.455^{+0.039}_{-0.031})$
$\sin^2 \theta_{13}$	$0.0234^{+0.0020}_{-0.0019} (0.0240^{+0.0019}_{-0.0022})$
$\delta_{CP}$ ( $2\sigma$ range)	$1.39^{+0.38}_{-0.27} (1.31^{+0.29}_{-0.33})\pi$

Table 2.1: Current knowledge of neutrino oscillation parameters from a global fit [43], via the Particle Data Group’s 2014 release [44]. Values in brackets are for the inverted hierarchy. For parity between the hierarchies, the definition of atmospheric mass splitting used here is  $\Delta m^2 = m_3^2 - (m_2^2 + m_1^2)/2$ .

### 2.3.6 Measurement of Oscillation Parameters on Antineutrinos

In the standard three-flavour neutrino oscillation framework, the neutrino masses and PMNS matrix parameters are shared between neutrinos and antineutrinos. The global fits described in the previous section make this assumption. However, in order to interpret the antineutrino-specific data contained within this thesis, it is important to separate the measurements made on neutrinos from those made on antineutrinos.

The precision of parameters measured on neutrinos is dominated by the long-baseline accelerator experiments for  $\theta_{13}$ ,  $\theta_{23}$  and  $|\Delta m_{32}^2|$ . T2K has the most precise measurement of these parameters. For  $\theta_{12}$  and  $\Delta m_{21}^2$ , the neutrino measurement is dominated by solar neutrino experiments, although these are generally analysed in conjunction with antineutrino data from KamLAND.

On antineutrinos, short baseline reactor experiments produce the most accurate measurement of  $\theta_{13}$  and via a measurement of the effective parameter  $|\Delta m_{ee}^2|$ , the most accurate measurement of  $|\Delta m_{32}^2|$ . KamLAND provides the best measurement of  $\theta_{12}$  and  $\Delta m_{21}^2$ . Prior to this analysis, the strongest constraint on  $\theta_{23}$  measured on antineutrinos was provided by a combined measurement of accelerator and atmospheric data at MINOS. A summary of the antineutrino-only constraints and their source can be seen in Table 2.2.

Parameter	Best-fit ( $\pm 1\sigma$ ) Antineutrino-only	Source
$\Delta m_{21}^2$	$7.50 \pm 0.20 \times 10^{-5}$ eV <sup>2</sup>	KamLAND[37]
$ \Delta m_{32}^2 $	$2.37 \pm 0.11$ eV <sup>2</sup>	Daya Bay[35]
$\sin^2 \theta_{12}$	$0.330^{+0.037}_{-0.041}$	KamLAND[37]
$\sin^2 2\theta_{23}$	$0.97^{+0.03}_{-0.07}$	MINOS[39]
$\sin^2 2\theta_{13}$	$0.089 \pm 0.005$	Daya Bay[35]

Table 2.2: Best measurements of mixing parameters on neutrinos and antineutrinos.

# Chapter 3

## The T2K Experiment

T2K is a long-baseline accelerator neutrino experiment consisting of three main components: the beam source, the near detectors and the far detector. A beam of muon neutrinos is generated at the Japan Particle Accelerator Complex (J-PARC) in Tokai, Ibaraki. The near detector complex is 280 m away, also at J-PARC. The far detector is the Super-Kamiokande (Super-K) water Čerenkov detector, 295 km away in Kamioka. T2K uses an ‘off-axis’ beam to produce neutrinos with a smaller spread of energies in order to allow precision measurements of oscillation parameters. A graphical representation of the T2K experiment can be seen in Figure 3.1.

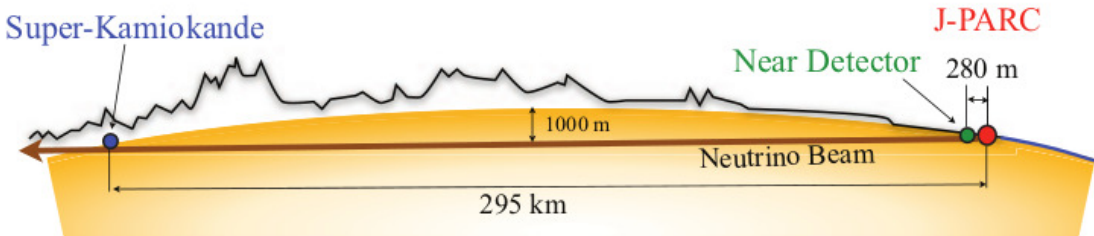


Figure 3.1: The T2K Experiment. Reproduced from [45].

### 3.1 The J-PARC Neutrino Beam

The first step in the production of the neutrino beam is a proton beam produced by a series of three accelerators, whose layout can be seen in Figure 3.2. First, a linear accelerator (LINAC) is used to accelerate a beam of  $H^-$  ions up to 400 MeV. These ions are then injected into a rapid-cycling synchrotron (RCS), stripped of electrons and then further accelerated up to 3 GeV. The RCS cycles at 25 Hz with two bunches per cycle. From the RCS, the protons are directed to either the J-PARC Materials and Life Science Facility or the main ring (MR) accelerator. Several cycles of the LINAC and RCS are

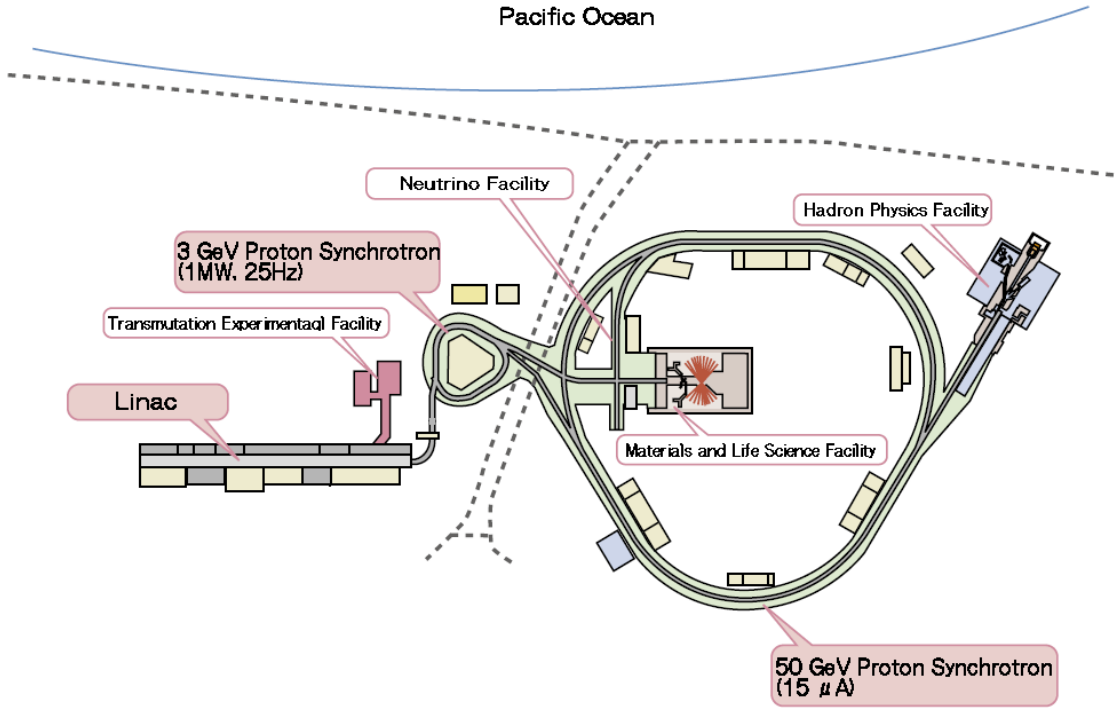


Figure 3.2: The J-PARC Accelerator Complex. Reproduced from the J-PARC public website.

used to fill the MR. Each MR cycle has 8 bunches of protons. Inside the main ring, the protons are accelerated to their final energy of 30 GeV, with the ring cycling at a rate of 0.3 Hz. The bunch structure and timings can be seen in Figure 3.3. The T2K design specified a beam power of 750 kW [45]. At the time of writing, the stable beam power is around 340 kW, having ramped up steadily over time as can be seen in Figure 3.4. The neutrino beamline at J-PARC uses a series of 5 kicker magnets to perform ‘fast extraction’ in which all 8 proton bunches are extracted in one cycle.

The neutrino beamline consists of two sections, which can be seen in Figure 3.5. The kicker magnets in the main ring direct the protons into the primary beamline in which the beam is steered to point toward Kamioka, focused and directed into the target station. The proton beam is monitored in a number of ways, including 21 electrostatic monitors (ESMs) to measure beam position, 19 segmented secondary emission monitors (SSEMs) to measure beam profile and 50 beam loss monitors (BLMs). Beam intensity is measured by 5 current transformers (CTs), which allows calculation of delivered POT.

In the target station, the proton beam impinges on a 91.4 cm long, 2.6 cm diameter graphite target. This corresponds to 1.9 interaction lengths, so approximately 85% of protons interact. Additionally, inside the target station, there is the Optical Transition

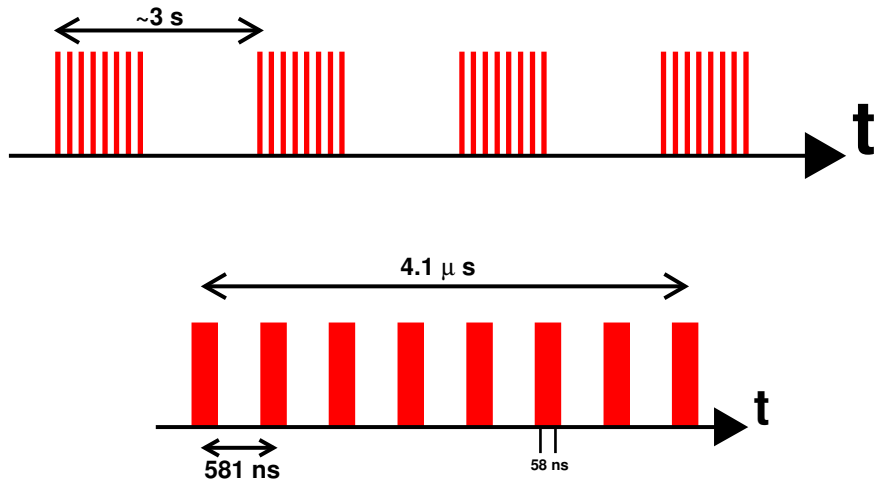


Figure 3.3: The T2K bunch structure. Each spill consists of 8 bunches of protons, each with a length of 58 ns. There is a bunch every 581 ns, giving the entire spill a duration of 4.1  $\mu$ s. The spill repetition rate is approximately once every 3 s.

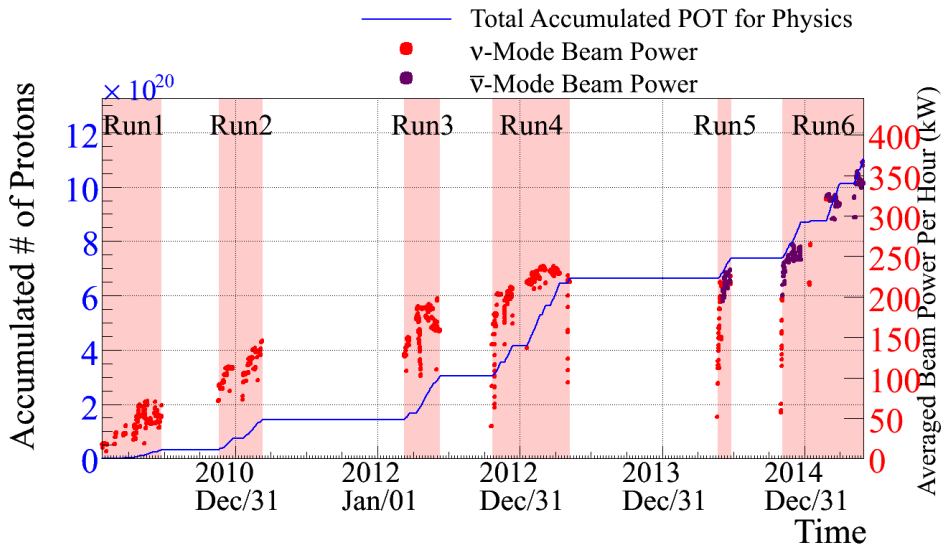


Figure 3.4: T2K delivered POT, broken down into individual T2K running periods.

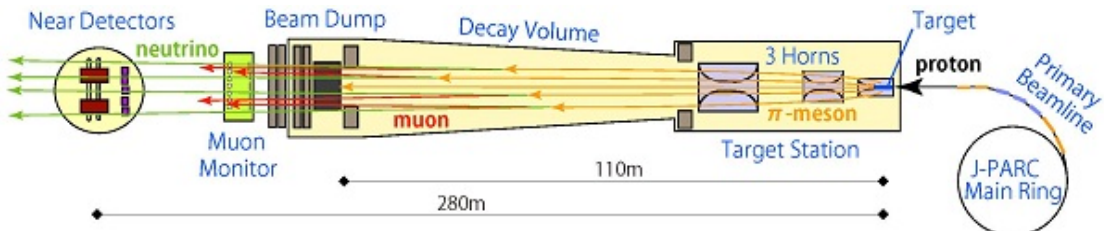


Figure 3.5: The primary and secondary beamlines of the T2K neutrino beam. Reproduced from J-PARC public website.

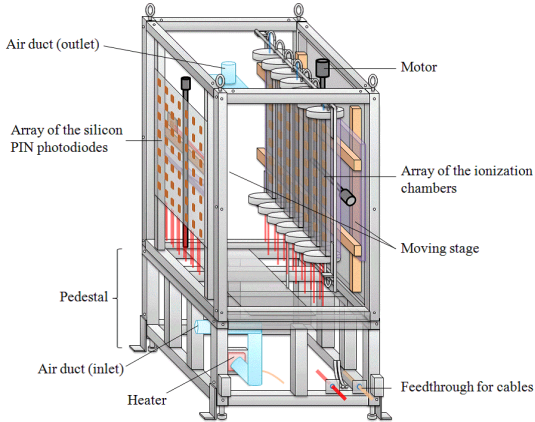


Figure 3.6: The T2K muon monitor (MUMON). Reproduced from [46].

Radiation (OTR) monitor, which is used to measure beam direction and intensity. The proton-carbon interactions produce a large number of pions and kaons which enter the secondary beamline.

In the secondary beam line, three magnetic horns with a current of  $\pm 250$  kA are used to focus the mesons. The three-horn design was designed to optimise the focusing efficiency for T2K's low energy, high emittance meson production. The magnetic horns have an opposite effect on positive and negative particles, so by reversing the current, one can move between a mostly  $\nu_\mu$  beam called Forward Horn Current (FHC), and a beam with an enhanced fraction of  $\bar{\nu}_\mu$  known as Reversed Horn Current (RHC). The primary analysis in this thesis is performed on data taken during RHC running. More information on the beam composition with different horn currents can be seen in Section 4.1.

After the 96 m long decay pipe, there is a cooled 75 tonne graphite beam dump to absorb most components of the remaining beam. The neutrino beam is hardly attenuated, and the high energy ( $\gtrsim 5$  GeV) muons pass through the beam dump. These muons are detected on a bunch-by-bunch basis by the muon monitor (MUMON), which is located after the beam dump, 118 m from the target. The flux is approximately  $1 \times 10^7$  charged particles per  $\text{cm}^2$  per spill, with muons making up 87% of this flux and the rest being mainly delta rays. MUMON is made up of ionisation chambers and silicon photodiodes. An image of MUMON can be seen in Figure 3.6. The MUMON allows measurement of the muon beam direction to a precision of  $0.014^\circ$  [46].

T2K running times are measured in terms of the number of incident protons on the target (POT). A plot of the collected POT over time can be seen in Figure 3.4, while the exact numbers of POT collected per T2K running period can be seen in Table 3.1.

Since oscillation has a neutrino energy dependence and neutrino energy reconstruction is imperfect, it is desirable to have a neutrino flux with a sharp peak in energy around the point of maximum oscillation. T2K achieves this goal using the off-axis

T2K Run Number	Begin Date	End Date	FHC POT ( $\times 10^{20}$ )	RHC POT ( $\times 10^{20}$ )
Run 1	23 Jan. 2010	26 Jun. 2010	0.323	N/A
Run 2	18 Nov. 2010	11 Mar. 2011	1.108	N/A
Run 3	08 Mar. 2012	09 Jun. 2012	1.579	N/A
Run 4	19 Oct. 2012	08 May. 2013	3.560	N/A
Run 5	16 May. 2014	24 Jun. 2014	0.242	0.506
Run 6	30 Oct. 2014	01 Jun. 2015	0.102	3.505

Table 3.1: The T2K running periods and their accumulated POT.

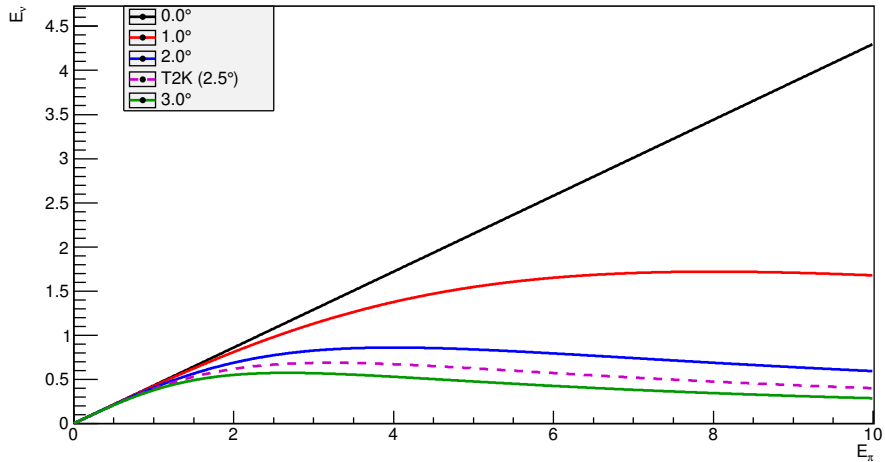


Figure 3.7: Neutrino energy as a function of pion momentum for decays with a selected angle between pion direction and neutrino direction. Note that at the T2K off-axis angle, a large range of pion momenta give similar neutrino energies.

technique. For small angles, the energy ( $E_\nu$ ) of neutrinos produced by pion decay as a function of pion energy ( $E_\pi$ ) and the angle between neutrino and pion ( $\theta$ ) is [47]:

$$E_\nu \approx \frac{0.43E_\pi}{1 + \gamma^2\theta^2} \quad (3.1)$$

where  $\gamma = \frac{E_\pi}{m_\pi}$ . As such,  $E_\nu \propto E_\pi$  for  $\theta = 0$  but as one moves away from the forward-going axis, the neutrino energy varies less. Figure 3.7 shows outgoing neutrino energy as a function of pion energy at different angles from the beam centre, and it should be noticed that at the T2K off-axis angle of  $2.5^\circ$ , the neutrino energy distribution is nearly flat. Figure 3.8 shows that this concentrates the neutrino beam flux at the first point of maximum oscillation. T2K has its main detectors  $2.5^\circ$  away from the central axis of the neutrino beam, which results in a neutrino beam with a peak energy of around 0.6 GeV. A plot of the unoscillated on-axis and off-axis neutrino fluxes this produces can be seen in Figures 3.9 and 3.10.

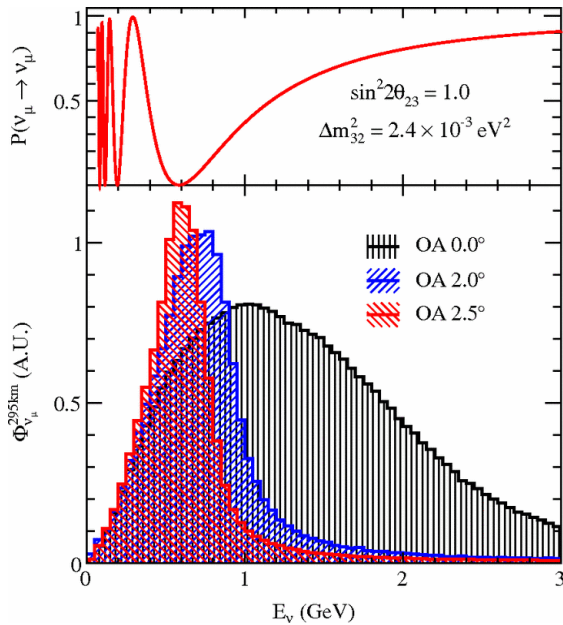


Figure 3.8: T2K flux predictions for different angles from the beam central axis. Reproduced from [45].

### 3.2 Near Detector Complex

T2K has two near detectors: an on-axis detector known as INGRID (Interactive Neutrino GRID) and an off-axis detector which will be referred to as ND280 (Near Detector, 280 m). INGRID is designed to measure the beam centre with enough statistics to provide a daily measurement to a precision of 10 cm at 280 m (equivalent to 0.4 mrad). It also produces a measurement of beam intensity to a 4% precision during normal running.

INGRID consists of 14 identical modules arranged in the cross pattern shown in Figure 3.11, with a full span of 10 m in both X and Y. The neutrino beam centre lies at the centre of the INGRID cross. Additionally, there are two shoulder modules which can also be seen in Figure 3.11, used to evaluate the axial symmetry of the beam.

Each module is constructed from alternating layers of iron (the interaction mass) and tracking scintillator planes (the detector). There are 9 layers of iron per module, with dimensions  $1240 \times 1240 \times 65$  mm, producing an iron interaction mass of 7.1 tonnes. Between these are the 11 scintillator planes, which each consist of 24 vertical bars and 24 horizontal bars. The scintillator bars used have dimensions  $10 \times 50 \times 1203$  mm. The whole module is surrounded by additional scintillator planes to veto events which occurred outside the module. Finally, at the centre of the INGRID cross, between the modules in the vertical line and the horizontal line lies the Proton Module, which is similar to the INGRID modules, but without the iron interaction mass, and with smaller scintillator bars to allow more finely grained tracking. The goal of the Proton Module is

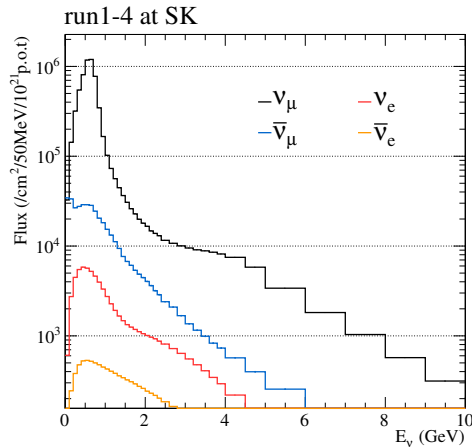


Figure 3.9: T2K FHC flux predictions at Super-Kamiokande.

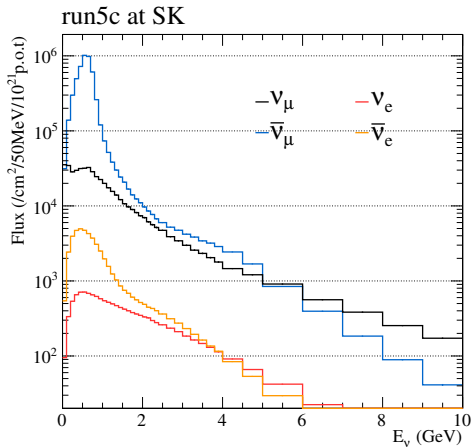


Figure 3.10: T2K RHC flux predictions at Super-Kamiokande.

to identify both the muon and the proton from CCQE events, and use this to evaluate and improve Monte Carlo modelling of these interactions.

ND280 has different objectives, and uses a number of different subdetector types in order to allow many types of measurement. In order to perform precision oscillation measurements, ND280 must measure accurately the energy spectrum and flavour composition of the neutrino beam. It also seeks to measure cross-sections for different neutrino interaction modes, which are important to optimise measurement precision, in addition to being interesting in their own right. It consists of a  $\pi^0$  detector (P0D) followed by a tracker module made up of three gas time projection chambers (TPCs) interleaved with a pair of fine-grained detectors (FGDs). These modules are surrounded by several electromagnetic calorimeters (ECals) which are known as the P0D ECAL (around the P0D), the Barrel ECAL (around the tracker) and the downstream (DS) ECAL (downstream of the tracker). All of this lies within the SMRD (Side Muon Range Detector), and a 0.2 T magnet to allow the measurement of momentum and charge identification. A schematic can be seen in Figure 3.12.

Each ECAL consists of layers of plastic scintillator and lead. The purpose of the ECals is to detect and measure the energies of particles escaping the inner detector. The information recorded by the ECals can be essential to particle identification (PID), and its detection of photons is key to recognising  $\pi^0$  events. Each T2K ECAL scintillator bar has a hit efficiency of 97-99%, and is 4 cm wide. Alternating layers of vertical and horizontal bars allow for 3D reconstruction. A summary of the different types of ECAL module and their construction is shown in Table 3.2. The time resolution of a typical ECAL track or shower is approximately 1 ns, which can allow determination of particle direction, while the energy resolution is  $7.5\%/\sqrt{E \text{ (GeV)}}$  [48].

	DS Ecal	Barrel ECal	P0D ECal
Length (mm)	2300	4140	2454
Width (mm)	2300	1676 top/bottom 2500 side	1584 top/bottom 2898 side
Depth (mm)	500	462	155
Weight (kg)	6500	8000 top/bottom 10000 side	1500 top/bottom 3000 side
Num. of layers	34	31	6
Bar orientation	$x/y$	Longitudinal and Perpendicular	Longitudinal
Num. of bars	1700	2280 Longitudinal top/bottom 1710 Longitudinal sides 6144 Perp top/bottom 3072 Perp sides	912 Longitudinal top/bottom 828 Longitudinal sides
Bars per layer	50	38 Longitudinal top/bottom 57 Longitudinal side 96 Perp top/bottom/sides	38 Longitudinal top/bottom 69 Longitudinal sides
Bar length (mm)	2000	3840 Longitudinal 1520 Perp top/bottom 2280 Perp sides	2340 Longitudinal
Pb thickness (mm)	1.75	1.75	4.0

Table 3.2: Summary of the different ECal modules showing the overall dimensions, numbers of layers, length and orientation of scintillator bars, numbers of bars, and lead thickness for each module. The dimensions and weights apply to the complete module, including the bulkheads. Reproduced from [48]

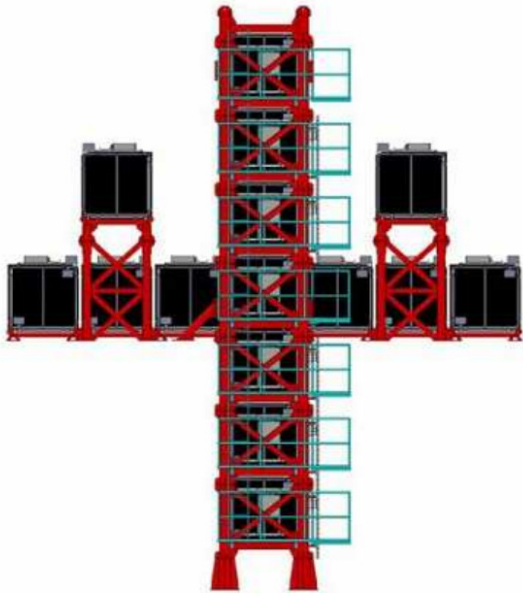


Figure 3.11: The layout of the modules in the on-axis near detector (INGRID). In this image, the neutrino beam is travelling directly into the page. The modules in the vertical line are upstream, followed by the Proton Module (not visible here) and then the modules in the horizontal line. Reproduced from [45].

The P0D also consists of layers of scintillator and layers of interaction mass. It starts and finishes with ECals as described above, but in the middle the interaction targets are sheets of brass and optionally pouches of water. It was intended that by comparing runs with the pouches empty to runs with them filled with water, subtraction could be used to measure neutrino interaction cross sections on water. This would constrain systematics for observations at Super-K. In the most recent NC1 $\pi^0$  cross-section analysis, the P0D reported a  $\pi^0$  vertex position resolution of approximately 8 cm and a  $\pi^0$  energy resolution of approximately 20% over the  $\pi^0$  momentum range [49].

The two FGDs have slightly different construction from one another. The first FGD (FGD1) is entirely constructed of plastic scintillator, with 30 alternating layers of vertical and horizontal bars, each 9.61 mm thick. The second FGD (FGD2) is the same size, but has approximately half of the scintillator replaced by water, for the purpose of constraining neutrino-Oxygen cross-sections. It has seven pairs of scintillator layers, interleaved with six 2.5 cm layers containing water. FGD1 is the interaction target for the ND samples used to constrain systematics for the analysis in this thesis. Future T2K analyses will use near detector samples from both FGD1 and FGD2. The FGDs have a timing resolution of 1.5 ns for a cluster [50].

The SMRD is made up of 440 modules which are attached to the magnet return yokes. The SMRD modules are made of plastic scintillator, and are used to record high-angle escaping muons, as well as serving as part of the cosmic ray trigger, and allowing

some characterisation of events which occur in the magnet.

In all the scintillator detectors (INGRID, ECals, P0D, FGDs and the SMRD), the scintillator bars are threaded with a wavelength-shifting fibre (WLS), and the emitted light is read out using Multi-Pixel Photon Counters (MPPCs). The wavelength-shifting fibres absorb light peaked at 430 nm, close to the emission peak of the scintillator at 420 nm (blue light). The WLS reemits the photons at 476 nm, in the green part of the spectrum. The emitted light is partially contained by total internal reflection, allowing a fraction to be detected by the MPPC. PMTs were unsuitable for ND280 readout due to the strong (0.2 T) magnetic field which would disrupt PMT operation. MPPCs are a novel form of photodiode which function reliably in a magnetic field, as well as being compact and well-suited to the WLS wavelength [51]. T2K uses custom MPPCs, which have 667-pixel readout in a  $1.3 \times 1.3 \text{ mm}^2$  area. Over the entire ND280 and INGRID, approximately 64,000 MPPCs are used. T2K was the first experiment to use large numbers of MPPCs in this fashion.

The three TPCs use a drift gas made up of 95% Argon, 3% tetrafluoromethane ( $\text{CF}_4$ ) and 2% isobutane ( $\text{iC}_4\text{H}_{10}$ ). Charged particles cause ionisation of the gas, and the resulting electrons drift away from the central cathode toward readout planes. The inner volume of each TPC has exterior dimensions of  $1808 \times 2230 \times 854 \text{ mm}$ , and is surrounded by an insulation volume of  $\text{CO}_2$ . A simplified diagram of a TPC module can be seen in Figure 3.13. The TPCs have a momentum resolution of approximately  $0.1/p_{\perp}$ , and a spatial resolution of better than 1 mm, although the exact spatial resolution depends on track angle and drift distance [52].

Information on the use of these detectors to constrain systematic uncertainties on the oscillation result is available in Section 4.4.

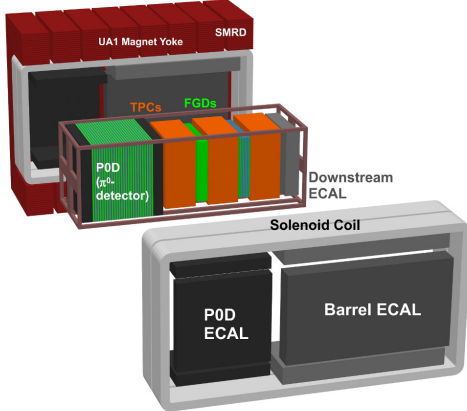


Figure 3.12: A schematic of the arrangement of detectors in the off-axis near detector (ND280). Reproduced from [45].

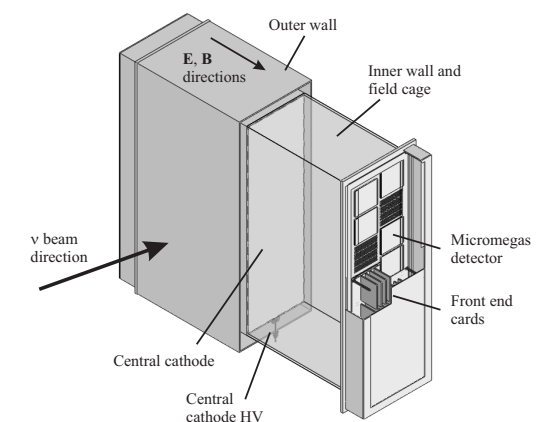


Figure 3.13: A simplified diagram showing the main elements of a TPC module. Reproduced from [52].

### 3.2.1 Simulation at ND280

The NEUT [53] Monte Carlo generator is used to simulate interactions in the INGRID and ND280 detectors. The GENIE [54] MC generator can also be used with the ND280 software, although the constraints in this thesis are produced solely with NEUT. Interactions inside the detector are simulated using the GEANT4 [55] package, and a custom software package named elecSim (electronics Simulation) is used to simulate the detector response. In the scintillator detectors, elecSim is responsible for simulating the scintillation light and the fibre transmission, as well as the MPPC readout and other electronics. In the TPCs, elecSim calculates the numbers of ionised electrons, and then simulates their drift trajectories and readout.

This produces calibration-level files similar to those produced by the first steps of processing real data output. From here, the processing of data and Monte Carlo through the reconstruction stages are very similar. Following the reconstruction stage, the data is reformatted into a reduced format that allows fast and powerful access to the information needed for a physics analysis.

## 3.3 Super-Kamiokande

The far detector is the Super-K water Čerenkov detector located in a mine below Mount Ikenoyama at Kamioka in Gifu, Japan. The detector is a stainless steel tank containing 50,000 tonnes of ultra-pure water instrumented with 13,000 photomultiplier tubes (PMTs), and it is positioned under a kilometre of rock to limit backgrounds from cosmic-ray muons. The cosmic muon rate in Super-K is 2 Hz, a reduction of 5 orders of magnitude from the cosmic rate it would experience on the surface [56]. Neutrinos interact in the large water target mass, and produce leptons.

The tank is separated into two volumes. The inner detector (ID) is a cylinder 33.8 m in diameter and 36.2 m in height. The outer detector (OD) volume is the 2 m of water surrounding the inner detector structure. The ID and OD are separated by a large stainless steel frame, upon which the PMTs are mounted. On the OD side, this frame is hung with sheets of a white reflective plastic known by the trademark Tyvek. This material helps reflect light back into the OD, making greater light collection likely. On the ID side, black sheets of polyethylene terephthalate (PET) are used to optically isolate the inner detector. A photograph taken inside the T2K inner detector before filling can be seen in Figure 3.14.

The outer detector is instrumented with 1,885 PMTs with a 20 cm diameter, mounted facing outwards in order to veto charged particles which entered from outside the detector (either cosmic muons or radioactive background from the surrounding rock). On the inner surface, there are 11,129 PMTs of diameter 50 cm covering 40% of the total

area. 26 pairs of Helmholtz coils are used to cancel out the earth’s magnetic field which may otherwise interfere with PMT functionality. The inner detector has a mass of 32 kilotonnes, of which 25 kt are part of the fiducial volume. A diagram of Super-K can be seen in Figure 3.15. Beam bunch timing is used to identify events caused by the T2K beam using GPS modules at both J-PARC and Super-K.

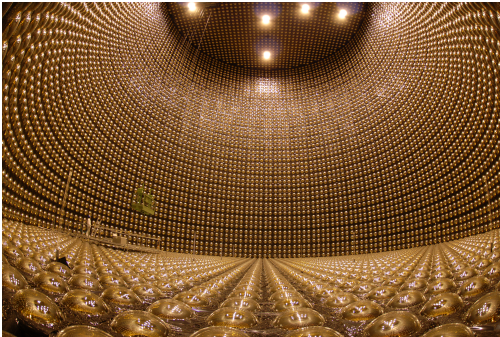


Figure 3.14: A photograph of the Super-Kamiokande inner detector, before it was filled. Reproduced from Super-Kamiokande public website.

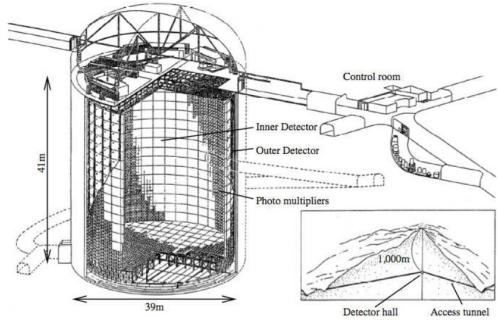


Figure 3.15: A diagram of the Super-Kamiokande detector. Reproduced from [45].

### 3.3.1 Super-Kamiokande Event Reconstruction

When a charged particle travels through an insulating medium at faster than phase velocity of light in that medium, it emits light. This ‘Čerenkov’ light is a result of a polarisation of the medium due to the particle’s electric field. For a particle travelling fast enough, the medium does not relax rapidly, and the disruption remains. The energy stored in this is released as a coherent ‘shock wave’ of light, which appears as a ring around the direction of motion of the charged particle. This ring appears at an angle of [18]:

$$\cos \theta = \frac{1}{\beta n} \quad (3.2)$$

Note that the opening angle is dependent on the momentum of the observed particle. For water, the refractive index  $n$  is  $\simeq 4/3$ , so the Čerenkov threshold is  $\beta \gtrsim 0.75$ . At T2K energies, the primary electron or muon from a CC event will usually be above this threshold, but emitted nucleons and secondary hadrons will not be visible.

Super-K began collecting data in 1996, and as such its performance is well understood. Mature algorithms have been developed to accurately reconstruct and identify events with low ring multiplicity. First, PMT timing information is used to reconstruct an initial estimate of the neutrino interaction vertex. After this, Hough transformations [57] are used to reconstruct rings based on the detected photoelectrons in the

PMTs. After a ring is identified, the hits involved are subtracted and the algorithm attempts to construct another new ring with the remaining hits.

After the ring fitting stage, there is a PID stage. Super-K aims to detect and differentiate between electron and muon rings, and these are distinguished primarily by measuring the ‘sharpness’ of the ring: electrons interact far more often in the water than muons, producing many secondary particles, and thus the rings appear more fuzzy. An example of a Super-K single ring muon and electron event can be seen in Figure 3.17. Super-K’s reconstruction also looks for an electron-like ring shortly after a muon-like ring, indicative of Michel decay.

Following this, there is a stage where all the ring candidates are refitted to redistribute the observed photoelectrons into all the ring candidates according to the best estimate of their actual source. Additionally, at this stage, the vertex position is refitted using the new PID information. Particle momentum can then be reconstructed using the observed number of photoelectrons per ring, as well as information about expected detector effects (such as PMT coverage area, PMT acceptance and water attenuation). The SuperK momentum ( $p$ ) and angle resolutions are estimated to be  $1.7 + 0.7\sqrt{p[\text{GeV}/c]}$  and  $1.8^\circ$  respectively for single ring muon-like events. For electron-like events, the resolutions are  $0.6 + 2.6\sqrt{p[\text{GeV}/c]}$  and  $3^\circ$ [41]. For a typical muon-like CCQE event at T2K energies, these resolutions together smear neutrino energy by approximately 3%.

The final vertex position resolution is approximately 24 cm for muon-like events and 35 cm for electron-like events. The PID is highly accurate, giving only an approximately 1% chance of confusing an electron and a muon [58]. A plot of the PID variable which separates electron-like and muon-like rings can be seen in Figure 3.16. The energy scale relative error is estimated as 2.4%[59].

Recently, optimised algorithms have been developed, based on code from Mini-BooNE [61] which use both charge and timing information to form likelihood ratios between different particle hypotheses. These offer much greater rejection of NC  $\pi^0$  events, which are a major background in the electron neutrino appearance analysis [41]. However, the analysis in this thesis uses only the muon sample, calculated using the long-established SK reconstruction. More information on how the SK selection is performed can be found in Section 4.5.

Super-K is well-suited to T2K’s 0.6 GeV neutrino beam, where the majority of events are charged-current quasi-elastic (CCQE). This allows reconstruction of the neutrino energy without observing the hadronic system, which will be explained in more detail in Section 4.5. In a higher energy beam, Super-K’s PID efficiency and energy resolution would suffer.

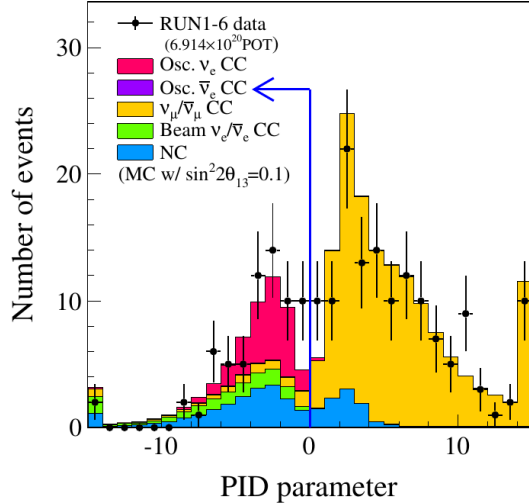


Figure 3.16: The distribution of the Super-K PID variable for determining between  $\mu$ -like and  $e$ -like rings, for neutrino mode T2K data. Reproduced from [60].

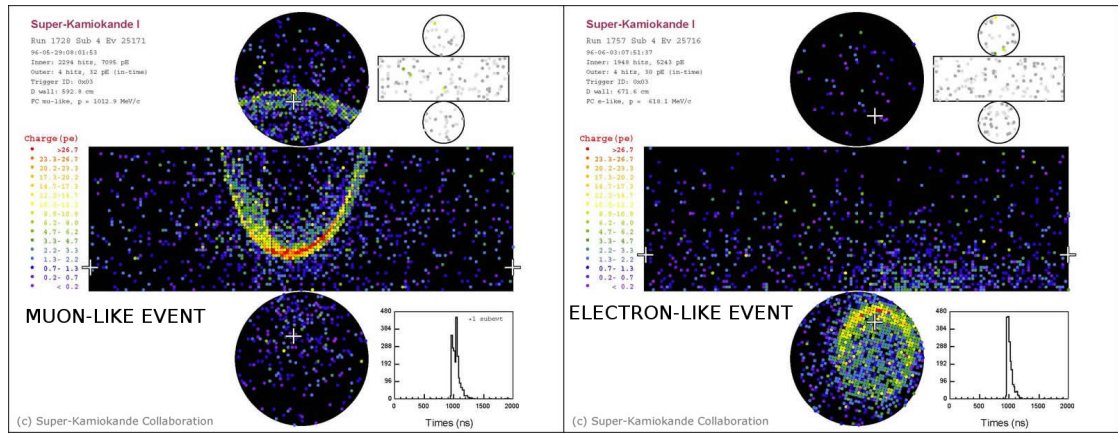


Figure 3.17: Examples of a single ring muon-like, and a single ring electron-like event at Super-K. Lepton flavours are primarily differentiated by the sharpness of the ring, which indicates whether or not the particle showered. Reproduced from Super-Kamiokande public website.

### 3.4 T2K Physics Results

T2K was initially designed to characterise neutrino oscillation. The primary goals were precision measurements of  $\sin^2 \theta_{23}$  and  $|\Delta m_{32}^2|$  through muon neutrino disappearance, and direct observation of non-zero  $\theta_{13}$  through electron neutrino appearance. These objectives have been achieved, with T2K’s neutrino-mode data yielding a  $7.3\sigma$  discovery of electron neutrino appearance [40], and a world-best precision measurement of the disappearance parameters [62]. The two results have been combined into a joint fit of the neutrino oscillation parameters, and the combination of T2K data with the reactor constraints from Daya Bay, Double Chooz and RENO can exclude a small region of  $\delta_{CP}$  space [41]. Using combined  $\nu$ - $\bar{\nu}$  mode running, T2K will be able to increase its sensitivity to  $\delta_{CP}$ , and set stronger constraints on that parameter. The projected sensitivity to  $\delta_{CP}$  at T2K’s expected final POT can be seen in Figure 3.18.

In addition to these results T2K has performed non-standard oscillation studies such as a sterile neutrino search at the ND280 looking for short baseline electron neutrino disappearance [64], and a measurement searching for Lorentz Violation using sidereal variations in neutrino event rate in the INGRID.

A key secondary goal of T2K was measurements of neutrino interaction cross-sections, and T2K has a strong record of publishing results in this area. Cross-section results already published from the ND280 include the CC inclusive cross-sections for both  $\nu_\mu - C^{12}$  interactions [65] and for  $\nu_e - C^{12}$  interactions [66]. Measurements of the  $\nu_\mu$  CCQE cross-section have been performed on carbon in the ND280 [67] as well as on both carbon and iron in the INGRID [68, 69]. T2K has also published a measurement of the  $\nu_e$  CC inclusive interaction on water in the ND280 P0D [70]. A measurement of the NC interaction cross-sections on water was performed at Super-K [71].

Upcoming T2K neutrino-mode cross-section publications include measurements of CC coherent pion production at both the ND280 and INGRID, CC  $1\pi$  on water in the ND280 and CC inclusive on scintillator and iron in the INGRID.

Now that T2K has accumulated a useful amount of POT in antineutrino beam-mode, the experiment will begin publishing further antineutrino studies, including the CC inclusive  $\bar{\nu}_\mu$  and the  $\bar{\nu}_\mu$  CC zero  $\pi$  cross-section. T2K will also soon publish additional oscillation results showing electron antineutrino appearance in the muon antineutrino beam mode, and a constraint on  $\delta_{CP}$  using a combined fit to neutrino and antineutrino beam mode data.

Up to the end of Run 6 (June 2015), the T2K integrated POT in FHC mode is  $6.91 \times 10^{20}$ , while the integrated POT in RHC mode is  $4.011 \times 10^{20}$ . The final target POT for both horn currents combined is  $7.8 \times 10^{21}$ .

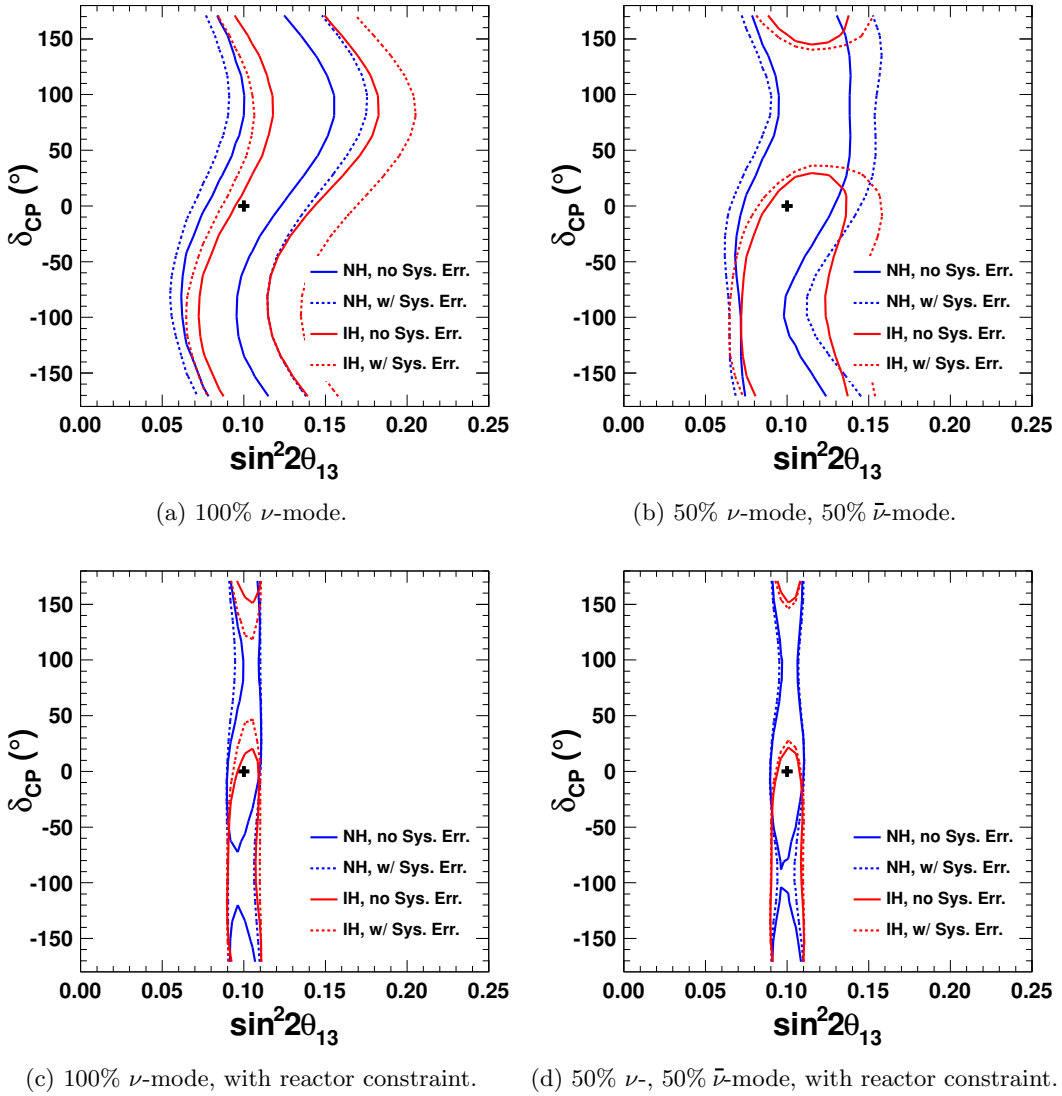


Figure 3.18: Projected T2K  $\delta_{CP}$  vs.  $\sin^2 2\theta_{13}$  90% confidence level intervals for  $7.8 \times 10^{21}$  POT. Contours are plotted for the case of true  $\delta_{CP} = 0^\circ$  and NH. The solid contours are with statistical error only, while the dashed contours include the 2012 systematic errors fully correlated between  $\nu$ - and  $\bar{\nu}$ -mode. Reproduced from [63].

## Chapter 4

# Inputs to the Oscillation Analysis

The analysis method used in this thesis relies on several sets of inputs. There is Monte Carlo simulation of the beam, tuned on hadron production data, described in Section 4.1. Neutrino interactions are simulated in both the near and far detectors using the methods outlined in Section 4.2. Section 4.3 describes the use of external data to tune the cross-section models. Section 4.4 discusses analysis of the T2K near detector data in order to produce a tuning and covariance matrix for flux and cross-section parameters. The data selection at Super-K is documented in Section 4.5, and the methods used to calculate uncertainties at Super-K are discussed in Section 4.6.

A flowchart showing how these inputs feed into the final analysis can be seen in Figure 4.1. A summary of all the inputs and the relevant versions used can be seen in Table 4.1.

Input	Version
JNUBEAM flux	13av1.1
NEUT	5.3.2
SKDETSIM	v13p90
Super-K Software and MC	14a
Super-K Detector Systematics	2015v4
Super-K FSI Systematics	2015v1
External CCQE Fitter	TNv2.1
ND280 Software	v11r31
BANFF Fitter	v3r15

Table 4.1: The versions of the software and productions used in this analysis.

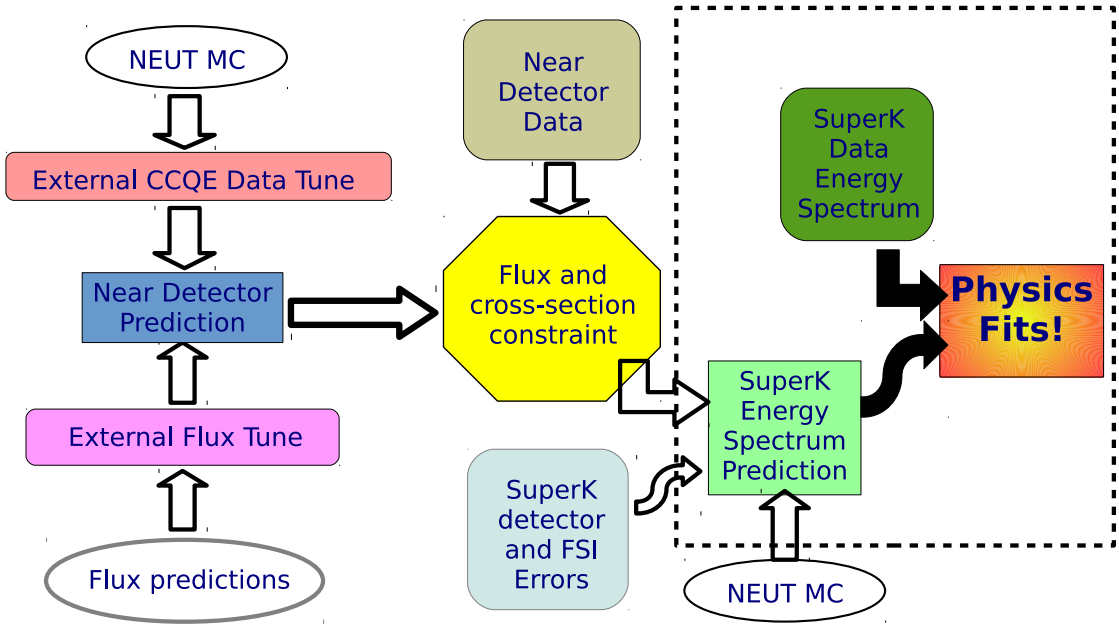


Figure 4.1: A flowchart demonstrating the stages of the T2K oscillation analysis. The dashed box contains the section of the analysis performed as original work in this thesis.

## 4.1 Flux Prediction

The T2K flux is predicted using a simulation which is then tuned on both external and T2K data. FLUKA2008 [72] is used to simulate the 30 GeV proton beam interacting in the target and baffle, producing secondary pions and other particles. FLUKA was selected as it showed the best agreement with hadron production data. The propagation of these secondary particles through the rest of the T2K beam line is performed using a GEANT3-based package known as JNUBEAM. This package simulates the secondary particles through the entire beamline as displayed in Figure 3.5, including the baffle, target, horn magnets, helium vessel, decay volume, beam dump, and muon monitor. JNUBEAM also predicts the neutrino spectrum in the near and far detectors. Within JNUBEAM, hadronic interactions are modelled with GCALOR [73].

The models in both GCALOR and FLUKA are tuned on hadron production data, predominantly from the NA61/SHINE (SPS Heavy Ion and Neutrino Experiment) experiment at CERN, henceforth referred to as simply NA61 [74, 75]. A schematic layout of NA61 can be seen in Figure 4.2. It consists of five TPCs, of which two are magnetised, and several ToF (time of flight) detectors. Measurements of  $\frac{dE}{dx}$  and ToF are used for particle identification. Charge and momentum are reconstructed using the track curvature in the magnetised TPCs.

For the data used in the T2K tune, NA61 uses the same proton beam energy as T2K (30 GeV), and graphite target which is 2 cm long in the beam direction (ap-

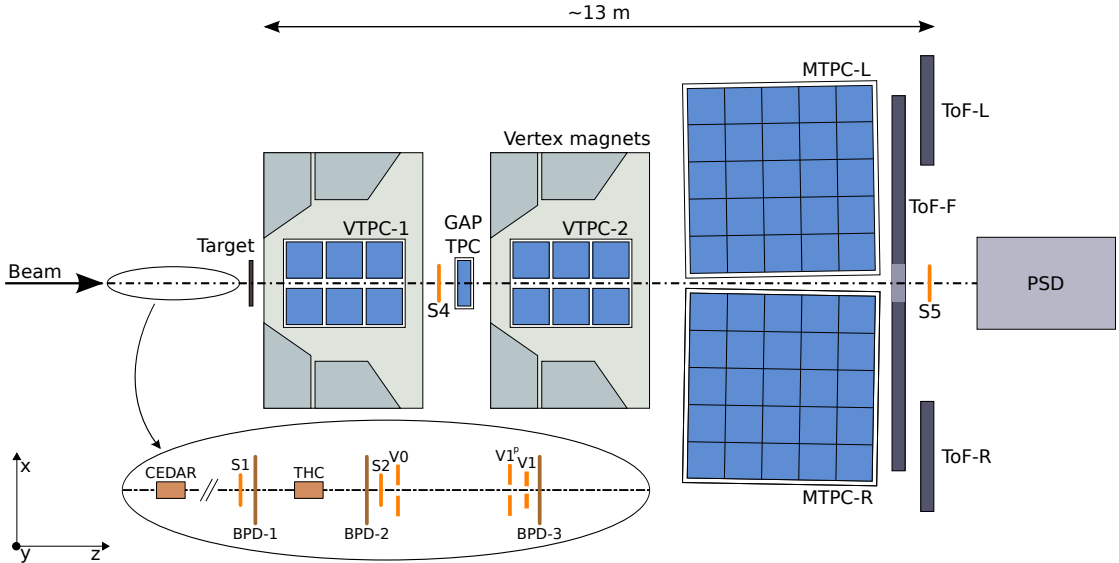


Figure 4.2: The detector layout of the NA61 detector. Reproduced from [76].

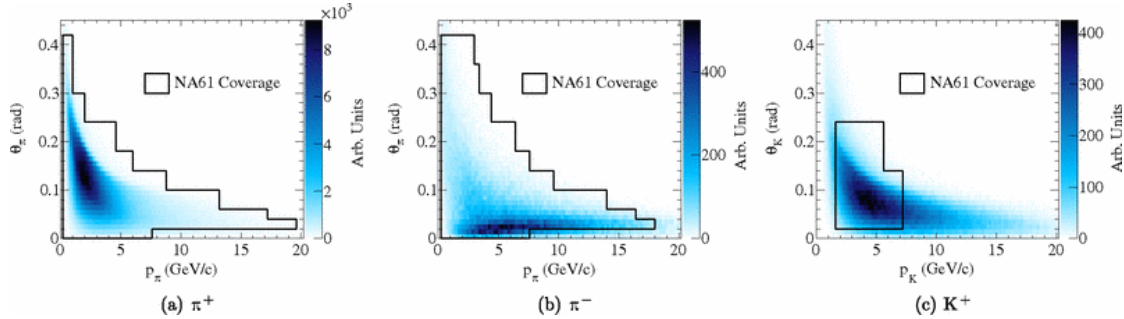


Figure 4.3: The phase space of pions and kaons contributing to the predicted neutrino flux at SK, and the regions covered by NA61/SHINE measurements. Reproduced from [81].

proximately 4% of the interaction length). NA61 covers more than 90% of the pion phase space relevant to T2K, as well as 60% of the kaon phase space, as can be seen in Figure 4.3. In the regions of phase space which are not covered by the NA61 data, alternative data is used from several other experiments [77–79]. In the future, NA61 data collected using a replica of the T2K target (90 cm or 1.9 interaction lengths long) will be used in order to better characterise the effects of meson reinteractions in the target[80].

The observed pion multiplicities can be seen in Figure 4.4, where they are compared with the FLUKA predictions, showing good agreement. Kaon production data also agree well with the FLUKA predictions. The NA61 data for proton multiplicity exhibit a deficit compared to the FLUKA model[81].

Each neutrino in the flux prediction is associated with information about its hadronic ancestor particles, the kinematics of these interactions and the distances trav-

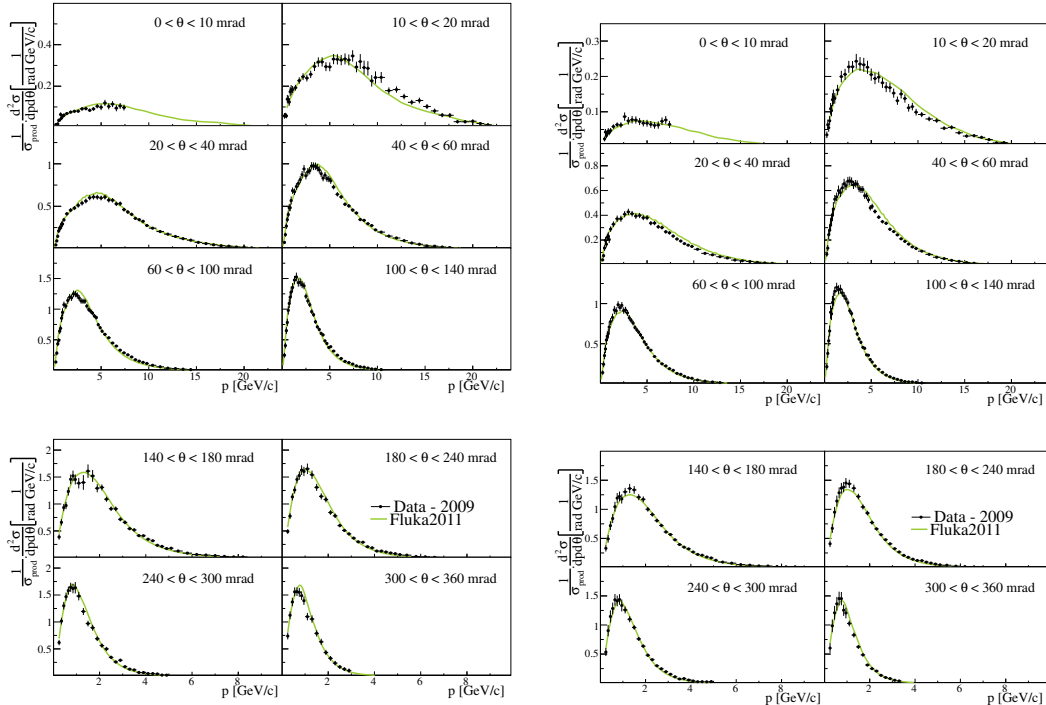


Figure 4.4: The observed multiplicity for  $\pi^+$  (left) and  $\pi^-$  (right) production in bins of angle and momentum using the NA61 thin target. The FLUKA 2011.2.8 prediction is shown in green. Reproduced from [81].

elled by each ancestor. This information can be used to reweight the neutrino MC to agree with the data collected by NA61. Total weights are calculated in two parts. First, weights are calculated for the likelihood of an incident proton with momentum  $p_{in}$  undergoing a hadronic interaction in the target of density  $\rho$  with a nucleus of atomic mass  $A$  at a distance  $d_0$  from the point of entry, producing a daughter with momentum  $p_{out}$  which travels another distance  $d_1$  before exiting the target:

$$W_1(p_{in}, p_{out}, A, d_0, d_1) = \frac{\sigma_p^{data}(p_{in}, A)}{\sigma_p^{MC}(p_{in}, A)} \times \exp\left(\rho d_0 [\sigma_p^{data}(p_{in}, A) - \sigma_p^{MC}(p_{in}, A)]\right) \times \exp\left(\rho d_1 [\sigma_p^{data}(p_{out}, A) - \sigma_p^{MC}(p_{out}, A)]\right) \quad (4.1)$$

where  $\sigma_p^{data}$  and  $\sigma_p^{MC}$  are the momentum and target dependent production cross-sections from the data and the Monte Carlo prediction respectively. Most daughter hadrons exit the target through the sides rather than the downstream end, and are focused along the beamline (or defocused) by the first magnetic horn.

The second set of weights are calculated for all hadronic daughter particles in a

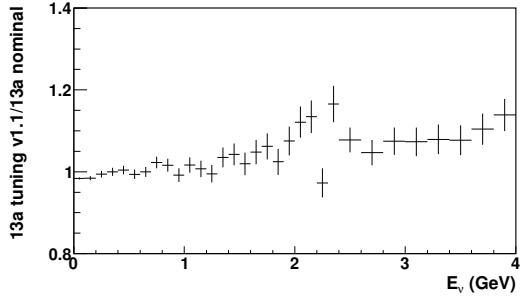


Figure 4.5:  $\nu_\mu$  Run 5c-6e RHC flux tuning weights applied to nominal  $\nu_\mu$  and oscillated- $\nu_e$  MC templates (T2K flux version 13av1.1) [82].

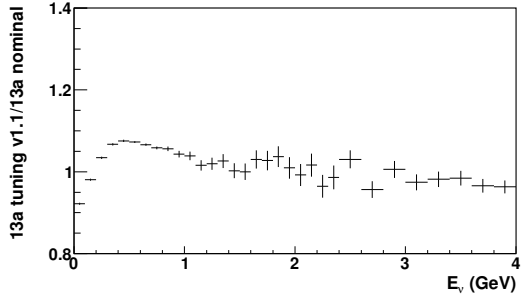


Figure 4.6:  $\bar{\nu}_\mu$  Run 5c-6e RHC flux tuning weights applied to nominal  $\bar{\nu}_\mu$  and oscillated- $\bar{\nu}_e$  MC templates (T2K flux version 13av1.1) [82].

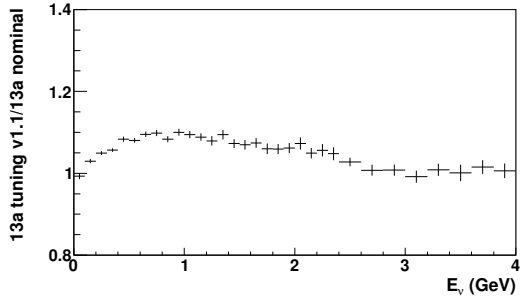


Figure 4.7:  $\nu_e$  Run 5c-6e RHC flux tuning weights applied to nominal  $\nu_e$  MC templates (T2K flux version 13av1.1) [82].

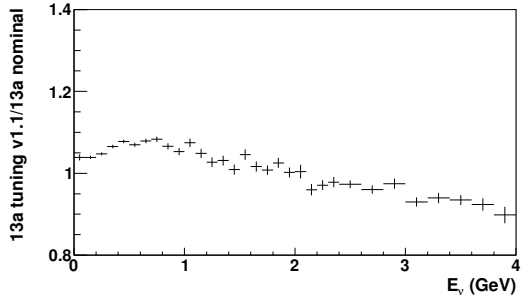


Figure 4.8:  $\bar{\nu}_e$  Run 5c-6e RHC flux tuning weights applied to nominal  $\bar{\nu}_e$  MC templates (T2K flux version 13av1.1) [82].

given angle  $\theta$  and momentum  $p$  bin, based on the final state particle multiplicity ( $n$ ) in that bin over all events:

$$\frac{d^2n(p, \theta)}{dpd\theta} = \frac{1}{\sigma_p} \frac{d^2\sigma_p(p, \theta)}{dpd\theta} \quad (4.2)$$

$$W_2(p, \theta) = \left[ \frac{d^2n(p, \theta)}{dpd\theta} \right]_{data} / \left[ \frac{d^2n(p, \theta)}{dpd\theta} \right]_{MC} \quad (4.3)$$

The total weight for the simulated neutrino is the product of the appropriate weights  $W_1$  and  $W_2$  given that particle's ancestors. The resulting flux tuning for T2K antineutrino beam mode for the data used in this analysis can be seen in Figures 4.5, 4.6, 4.7 and 4.8. The tuning increases the  $\bar{\nu}_\mu$ ,  $\nu_e$  and  $\bar{\nu}_e$  event rates around the T2K beam peak, and suppresses the number of high energy  $\bar{\nu}_e$  events.

The final predicted flux at Super-K, without oscillations or detector effects is 90%  $\bar{\nu}_\mu$  for RHC mode, with a contamination of 9%  $\nu_\mu$  and 1%  $\bar{\nu}_e$ . For FHC mode, the beam is 93%  $\nu_\mu$  with a contamination of 6%  $\bar{\nu}_\mu$  and 1%  $\nu_e$ . The shape of these fluxes can be seen in Figures 3.9 and 3.10.

## 4.2 NEUT Monte Carlo

For an experiment to observe the chargeless neutrino, we require it to interact in the detector, and observe the resultant particles. We calculate the cross-sections of these interactions according to various interaction models, leading to several categories of final states. For this analysis, the NEUT [53] neutrino Monte Carlo generator is used, both to produce the near detector inputs and to simulate expected far detector data. The simulation of neutrino interactions is a major source of uncertainty in neutrino oscillation experiments, and care must be taken to parameterise and constrain these uncertainties. The NEUT software version used is NEUT 5.3.2, for both the Super-K and ND280 datasets.

### 4.2.1 Neutrino Interaction Modes

#### 4.2.1.1 Charged Current Quasi-Elastic (CCQE)

The main signal interaction mode for the studies described in this thesis is CCQE. In this interaction, a neutrino interacts with a neutron, producing a proton and a negatively charged lepton. Alternatively, an antineutrino interacts with a proton, producing a neutron and a positively charged lepton. Feynman diagrams of these processes can be seen in Figures 4.9 and 4.10. The free-nucleon CCQE interaction cross-section is calculated using the model of Llewellyn Smith: [83]. The differential cross-section from this model is:

$$\frac{d\sigma}{dQ^2} = \frac{M^2 G_F^2 \cos^2 \theta_c}{8\pi E_\nu^2} \left[ A(Q^2) \pm B(Q^2) \frac{(s-u)}{M^2} + C(Q^2) \frac{(s-u)^2}{M^4} \right] \quad (4.4)$$

where  $M$  is the nucleon mass,  $G_F$  is the Fermi coupling constant,  $\theta_c$  is the Cabibbo angle,  $E_\nu$  is the neutrino energy and  $s$  and  $u$  are the Lorentz invariant Mandelstam kinematic variables. For an outgoing lepton of mass  $m$ ,  $(s-u) = 4ME_\nu - Q^2 - m^2$ . A, B and C are functions of the four momentum transfer to the nucleus  $Q^2$ , and in turn depend on six  $Q^2$ -dependent form factors  $F_1$ ,  $F_2$ ,  $F_A$ ,  $F_P$ ,  $F_{3V}$  and  $F_{3A}$  which represent the nucleon charge distribution.  $F_1$  and  $F_2$  are vector form factors which are well constrained by electron scattering experiments.  $F_{3V}$  and  $F_{3A}$  have a very small effect on the  $\nu_\mu$  cross-section, and their effect depends on the lepton mass. In this analysis, the uncertainties on these form factors is folded into the  $\nu_\mu/\nu_e$  cross-section normalisation.  $F_A$  and  $F_P$  are axial form factors which introduce the largest uncertainty. For a given  $Q^2$ ,  $F_P$  is a multiple of  $F_A$ , which is treated as a dipole:

$$F_A(Q^2) = \frac{F_A(0)}{(1 + Q^2/(M_A^{QE})^2)^2} \quad (4.5)$$

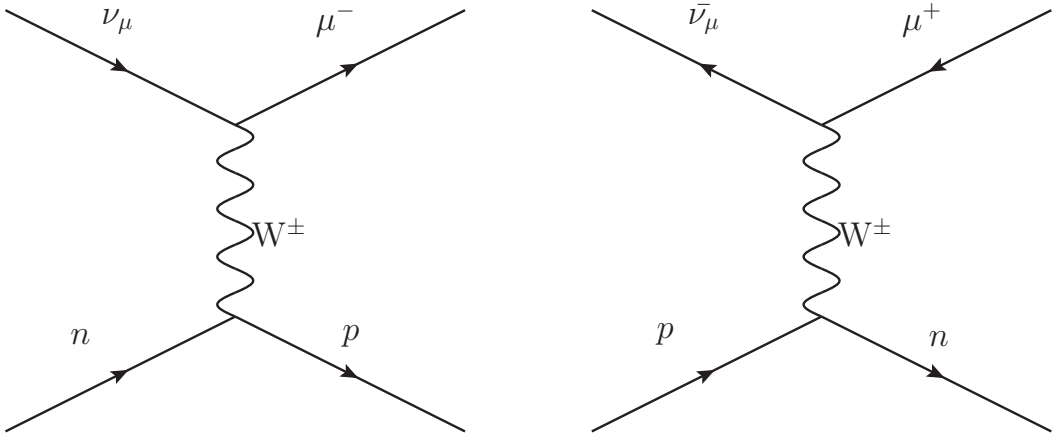


Figure 4.9: Feynman diagram of a neutrino CCQE process.

Figure 4.10: Feynman diagram of an antineutrino CCQE process.

The value of  $F_A$  at  $Q^2 = 0$  can be measured from beta decay, and does not provide a significant uncertainty on the cross-section. The dipole form factor is parameterised with the axial mass  $M_A^{QE}$ , which would be expected to be around 1 GeV, similar to the equivalent vector mass which can be measured by electron scattering experiments. Since it can only be measured in neutrino scattering experiments, the uncertainty on  $M_A^{QE}$  is significant. There is some tension between published results for CCQE cross-sections on deuterium and heavier targets, as well as a function of  $Q^2$  where the differences are often interpreted as inconsistent values of  $M_A^{QE}$  [84].

T2K does not use free nucleons as a target - the signal modes are interactions on carbon (ND280) and oxygen (Super-K) nuclei. In this analysis, the nuclear model used to calculate the cross-section for scattering off nucleons bound in a nucleus is the Relativistic Fermi Gas (RFG) model of Smith and Moniz [85]. The nuclear model parameterisation adds two systematic parameters: the Fermi momentum and the binding energy. For oxygen, these parameters have prior values of 225 MeV and 27 MeV respectively [86]. Before being used for T2K fits, the CCQE model parameters and the underlying nuclear model were tuned on external data, which is explained further in Section 4.3.

In a CCQE interaction, the energy of the initial neutrino can be reconstructed from the momentum  $p_l$ , energy  $E_l$  and angle  $\cos \theta_l$  of the final state lepton:

$$E_{reco} = \frac{(M_n - V)E_l - \frac{M_l^2}{2} + M_n V - \frac{V^2}{2} + \frac{M_p^2 - M_n^2}{2}}{M_n - V - E_l + p_l \cos \theta_l} \quad (4.6)$$

$M_n$ ,  $M_p$  and  $M_l$  are the neutron, proton and lepton masses respectively.  $V$  is the binding energy of the target nucleus.

#### 4.2.1.2 Meson Exchange Currents (MEC)

For a muon antineutrino disappearance analysis, we expect to see a significant number of events from ‘meson exchange current’ (MEC) interactions. This is motivated by electron scattering measurements, which measure inclusive electron-nucleus cross-sections as a function of electron energy loss [87]. These experiments see the QE peak, as well as a delta resonance peak, and a growing contribution from inelastic interactions at higher energies. However, without modelling MEC, one would expect to see a deep dip between the QE and RES peaks. As can be seen in Figure 4.11, this dip is far less pronounced in data. The extra events in this region are believed to be contributed by MEC interactions.

In an MEC event, the lepton interacts with more than a single nucleon, and a meson is exchanged between the nucleons. An example of one type of MEC event can be seen in Figure 4.12. All MEC events simulated are charged current, as neutral current interactions of this type are effectively elastic neutrino-nucleus scatters and would not be visible in Super-K. The NEUT Monte Carlo generator uses a model developed by J. Nieves et al., which considers 49 separate Feynman diagrams known as ‘2p2h’, or two-particle, two hole [88]. These can cause multiple nucleons to be ejected from the nucleus, but since these will generally not be seen by Super-Kamiokande, MEC events appear CCQE-like in our oscillation samples. However, the formula used for reconstructing the neutrino energy (based on CCQE kinematics) is less accurate for MEC events, and this results in them having a somewhat lower oscillation sensitivity.

The MEC cross-section uncertainties are implemented as a unique MEC normalisation parameter, in addition to all of the parameters which apply to the CCQE events. MEC events appear CCQE-like at Super-K, and have the detector efficiency uncertainty for CCQE events applied rather than the CCnonQE uncertainty.

#### 4.2.1.3 Resonance (RES)

For neutrinos interacting with higher energies, it is possible to produce heavier intermediate particles. The neutrino interacts with a nucleon, producing a lepton and a heavier baryon. This intermediate baryon then decays to a nucleon and another outgoing particle. The outgoing particle can be a photon or one of the heavier mesons, but is most likely to be a pion.

NEUT considers 18 different resonances, up to a limit of hadronic invariant mass  $W < 2$  GeV. This upper limit is placed in order to prevent double-counting with deep inelastic scattering events. The model is based on the work of Rein and Seghal [90].

In this study, we treat resonances that produce a single pion as an individual mode (CC $1\pi$  and NC $1\pi$ ). All other resonances are classified into the ‘CC other’ or ‘NC other’ samples. A Feynman diagram of one possible CC $1\pi$  event from a delta resonance

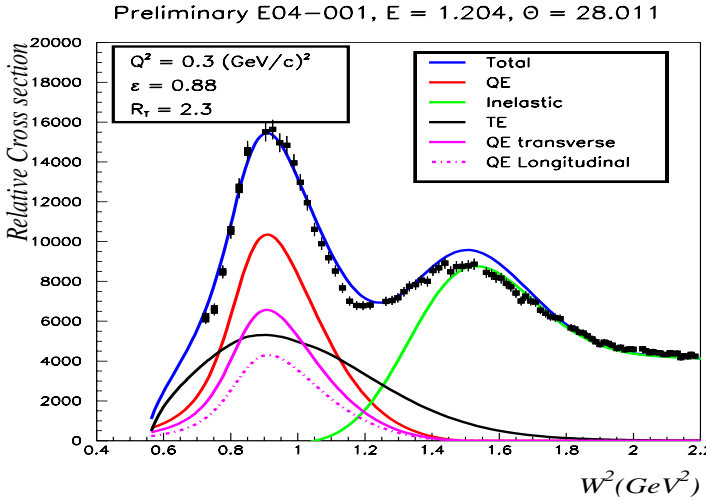


Figure 4.11: Electron-nucleus scattering data from the JUPITER experiment, as a function of  $W^2$ , the squared invariant mass of the final state hadronic system. MEC here is shown as the black line, labelled TE (transverse enhancement). Note the longer tail of the MEC cross-section than the CCQE cross-section, reducing the depth of the dip between the QE and resonance peaks. This data is measured at  $Q^2 = 0.3$  GeV $^2$ , while T2K's zero  $\pi$  sample peaks at around  $Q^2 = 0.1$  GeV $^2$  so the MEC tail length for T2K would be even more pronounced. Reproduced from [89].

can be seen in Figure 4.13.

Like the QE interactions, resonance interactions can be parameterised using a number of form factors [91]. As in CCQE, the vector form factors are accurately constrained by electron scattering data. This leaves two parameters for the axial dipole form factor which must be considered for a neutrino experiment. First, there is another axial mass ( $M_A^{RES}$ ) analogous to  $M_A^{QE}$ . Since beta decay cannot be used to constrain the resonance form factors, there is also additional form factor scaling parameter  $C_5^A$ .

The Rein-Seghal quark model describes the final single-pion state entirely in terms of resonances. However, both theory and data suggest the need for a non-resonant contribution to single pion production. Rein and Seghal implement such a background by modelling it as a resonance nucleon, controlled by an adjustable constant [90]. This leads to an additional contribution to the single pion production cross-section which rises smoothly with energy. The uncertainty on the constant controlling nonresonant pion production is parameterised in this analysis as the isospin  $\frac{1}{2}$  background uncertainty.

#### 4.2.1.4 Coherent Pion Production (COH)

Instead of interacting with individual nucleons, a neutrino can interact with an entire nucleus. These interactions tend to produce very forward-going pions due to the increased target mass. In NEUT, these interactions are modelled using the model of Rein

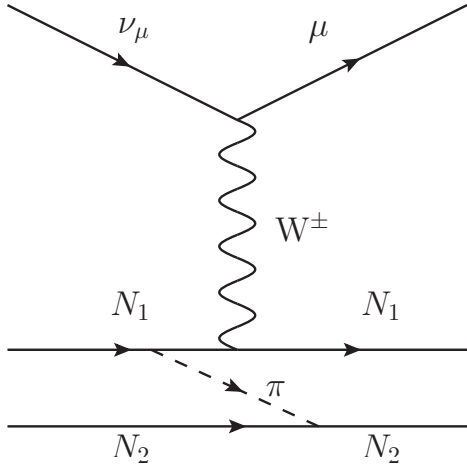


Figure 4.12: Feynman diagram of an example MEC process. In practice, 49 separate diagrams are simulated by the NEUT generator.

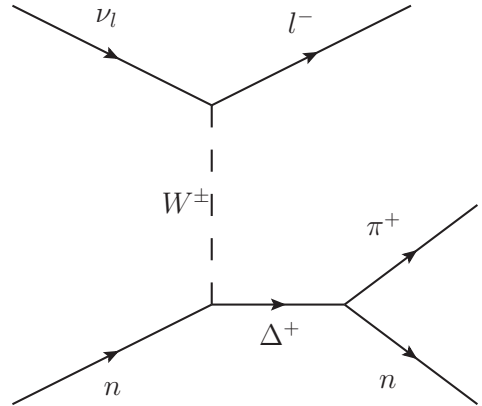


Figure 4.13: Feynman diagram of single pion production via a charged-current delta resonance.

and Seghal [92], with an additional correction for the lepton mass in charged current interactions [93]. Feynman diagrams of these processes can be seen in Figure 4.14.

In this analysis, the coherent models are treated with a single normalisation parameter each for CC and NC interactions.

#### 4.2.1.5 Deep Inelastic Scattering (DIS)

At higher neutrino energies, the struck nucleon breaks up. The hadronisation is modelled in two separate ways, depending on the energy of hadronic system ( $W$ ). For  $1.3 \text{ GeV} < W < 2 \text{ GeV}$ , a bespoke piece of NEUT code is used to estimate pion multiplicities,

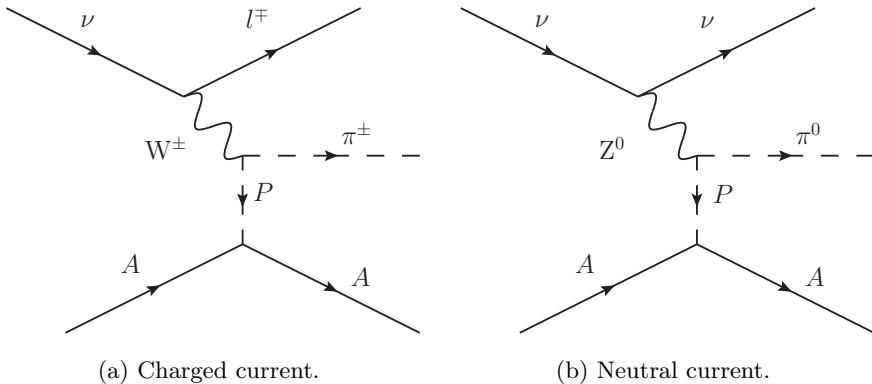


Figure 4.14: Feynman diagrams of coherent pion production.  $P$  represents a pomeron carrying four-momentum to the nucleus.

and only multiple-pion events are used in order to avoid double-counting of single-pion events from RES interactions. Nucleon structure functions are determined using the GRV98 parton distribution function [94], with some corrections calculated by Bodek and Yang [95] to improve agreement with charged lepton-hydrogen scattering data. Pion multiplicities are tuned using data from antineutrino-proton scattering data collected in a hydrogen bubble chamber [96]. For  $W > 2$  GeV, the PYTHIA [97] simulation package is used, and single pion events are not cut out. Neutral current cross-sections are determined using empirical measurements of CC/NC branching ratios [98, 99].

These events form part of the CC other and NC other templates. In this analysis, a fit parameter is associated with the uncertainty on the DIS CC pion multiplicity, and a normalisation for NC events.

#### 4.2.2 Interaction Modes

The NEUT Monte Carlo is used as an input to SKDETSIM, a GEANT3 based package designed to simulate the response of Super-K to these neutrino interactions. GCALOR [73] is used to simulate hadronic interactions in water, with the exception of pions with momenta below 500 MeV, for which bespoke KamiokaNDE code is used [100].

Six separate samples of Monte Carlo are generated, of which two are oscillated samples:

- $\nu_\mu$  MC generated with the  $\nu_\mu$  neutrino flux.
- $\overline{\nu}_\mu$  MC generated with the  $\overline{\nu}_\mu$  neutrino flux.
- $\nu_e$  MC generated with the  $\nu_e$  neutrino flux.
- $\overline{\nu}_e$  MC generated with the  $\overline{\nu}_e$  neutrino flux.
- $\nu_e$  MC generated with the  $\nu_\mu$  neutrino flux.
- $\overline{\nu}_e$  MC generated with the  $\overline{\nu}_\mu$  neutrino flux.

The numbers of events generated and the POT normalisation used can be seen in Table 4.2.

These neutrinos can interact with matter in a number of ways, producing different final states. For the purposes of this analysis, we simulate and analyse 46 of these. These vary by initial neutrino flavour, the underlying physics model and the particles in the final state. More detail on the processes involved can be seen in Section 4.2. The 46 modes used are explicitly listed in Appendix A.

Sample	Number of events per 22.5 kt fiducial per $10^{21}$ POT	Number of generated events in true fiducial volume in all available MC
$\bar{\nu}_\mu$	353.789	633988
$\nu_\mu$	208.369	634659
$\bar{\nu}_e$	6.811	127013
$\nu_e$	8.941	127262
<i>Oscillated</i> $\bar{\nu}_e$	376.420	126812
<i>Oscillated</i> $\nu_e$	215.099	127278

Table 4.2: POT normalisation of input Super-K MC samples for antineutrino beam mode.

### 4.3 CCQE External Data Tuning

In order to improve the input prediction, the T2K Neutrino Interactions Working Group (NIWG) performed fits to external data from the MiniBooNE [101, 102] and MINER $\nu$ A [103, 104] experiments. For each experiment, one neutrino and one antineutrino dataset was fitted. These fits affect the CCQE and MEC modes only.

The version of NEUT used for this analysis (5.3.2) uses the ‘spectral function’ (SF) model of Benhar [105]. Cross-section values for an alternative nuclear model, the Relativistic Fermi gas (RFG) model of Smith and Moniz [85] are also calculated. This allows event-by-event reweighting to produce a Monte Carlo prediction based on the RFG model.

The RFG is a comparatively simple model, where all states in momentum space are filled up to a certain level (the Fermi momentum), and above this no states are filled. The particle distribution in momentum space is thus a step function. When the RFG is used in this analysis, it is modified using a calculation known as the Random Phase Approximation (RPA). RPA is a screening effect calculated from long-ranged correlations between nucleons [88]. The authors of the RPA model provided two separate calculations - relativistic RPA and non-relativistic RPA, which were initially considered equally credible. The RPA calculations have only been calculated with the RFG model, so no RPA contribution is used in conjunction with SF.

As a result, the external CCQE fits provided three options for the CCQE model to be used as the default for the T2K oscillation analysis.

- Relativistic Fermi Gas and relativistic RPA.
- Relativistic Fermi Gas and non-relativistic RPA.
- Spectral Function

The MiniBooNE dataset fits were done using the cross-sections released as a

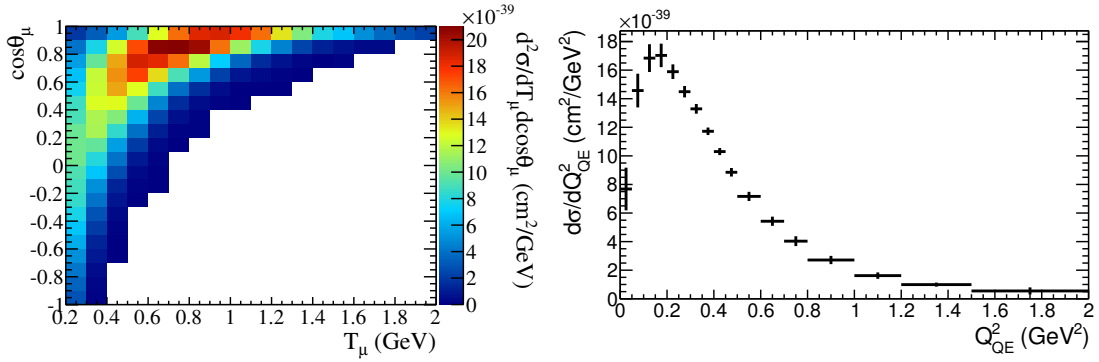


Figure 4.15: MiniBooNE CCQE data for neutrino beam-mode running. Reproduced from [86].

double-differential with respect to  $T_\mu$ , the kinetic energy of the muon and  $\cos \theta_\mu$ , the angle between the muon direction and the beam.

In the MiniBooNE neutrino dataset [101], events were selected as CCQE-like if a single muon was detected but no pions above threshold. No cut was made on the detection of the proton. The signal (CCQE+MEC) purity was 77%, with the majority of the background coming from CC1 $\pi^+$ , and the overall flux normalisation uncertainty was 10.7%. The distributions released can be seen in Figure 4.15.

The MiniBooNE antineutrino dataset [102] had significant  $\nu_\mu$  contamination in the  $\bar{\nu}_\mu$  beam. MiniBooNE was not magnetised and was thus unable to separate  $\nu_\mu$  and  $\bar{\nu}_\mu$  events based on lepton charge, so an additional correction was applied to reduce this background. The background is characterised using the fact that 8% of  $\nu_\mu$  CC interactions produce no decay electron, and most  $\pi^-$  mesons are absorbed, allowing a separate measurement of  $\nu_\mu$  CC $\pi^+$ . With this background subtraction, the CCQE-like signal has a purity of 61% and an overall flux normalisation uncertainty of 13.0%. The cross-section distributions can be seen in Figure 4.16.

MINER $\nu$ A released cross sections measured as a single-differential function of  $Q_{QE}^2$ , defined for a muon with energy  $E_\mu$  and angle  $\cos \theta_\mu$  as:

$$Q_{QE}^2 = -m_\mu^2 + 2E_\nu^{QE}(E_\mu - \sqrt{E_\mu^2 - m_\mu^2 \cos \theta_\mu}) \quad (4.7)$$

using the reconstructed neutrino energy  $E_\nu^{QE}$  calculated using Equation 4.6. Here  $E_\mu$  is the reconstructed muon energy,  $M_n$ ,  $M_p$  and  $m_\mu$  are the neutron, proton and muon masses respectively and  $V_C$  is the binding energy on carbon. The binding energy on Carbon  $V_C$  is assumed to be 30 MeV for the MINER $\nu$ A antineutrino dataset, and 34 MeV for the other analyses.

Both the neutrino [103] and antineutrino [104] MINER $\nu$ A datasets follow the

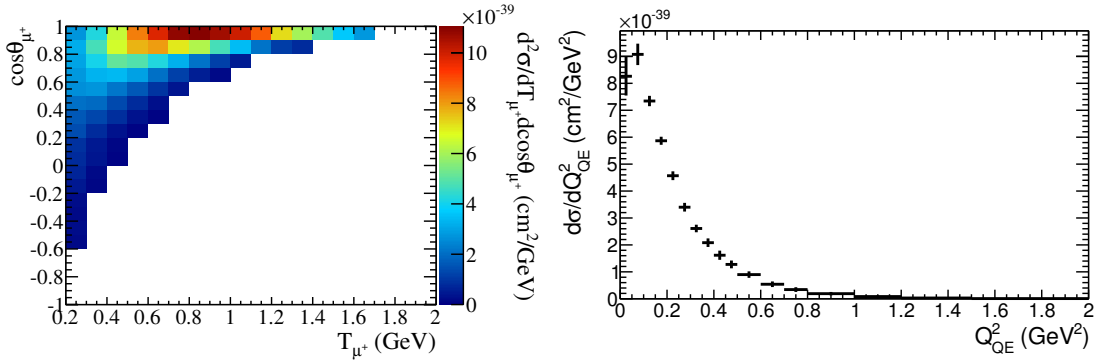


Figure 4.16: MiniBooNE CCQE data for antineutrino beam-mode running. Reproduced from [86].

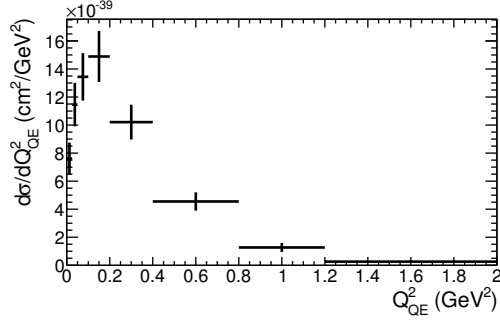


Figure 4.17: MINERνA CCQE dataset for neutrino beam-mode running. Reproduced from [86].

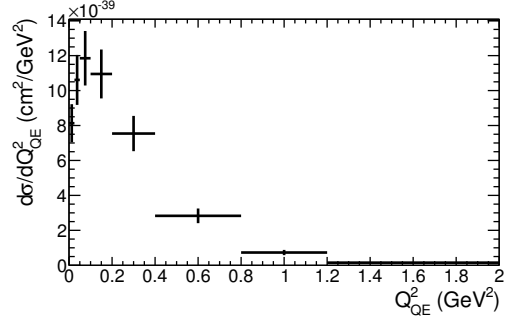


Figure 4.18: MINERνA CCQE dataset for antineutrino beam-mode running. Reproduced from [86].

same method. Data was released in the form of a flux averaged cross-section over the region  $1.5 \text{ GeV} \leq E_\nu^{QE} \leq 10 \text{ GeV}$ . Background corrections are applied by fitting simulated background distributions to the data in terms of energy deposited outside the vertex (recoil energy). The purity of the neutrino sample is given as 49%, and the antineutrino sample purity as 77%. The MINERνA datasets used can be seen in Figures 4.17 and 4.18.

The CC0π systematic parameters ( $M_A$ , Fermi momentum, binding energy and MEC normalisation) are fitted. MiniBooNE also has normalisation parameters  $\lambda_\nu^{MB}$  and  $\lambda_{\bar{\nu}}^{MB}$  for the neutrino and antineutrino datasets respectively, which have published uncertainties of  $\varepsilon = 10.7\%$  and  $\bar{\varepsilon} = 13.0\%$ . MINUIT [106] is used to minimise the  $\chi^2$  for

Fit type	$\chi^2/\text{DOF}$	$M_A^{QE}$ (GeV)	MEC (%)	$p_F$ (GeV)	$\lambda_\nu^{MB}$	$\lambda_{\bar{\nu}}^{MB}$
Rel. RPA + MEC	97.84/195	$1.15 \pm 0.03$	$27 \pm 12$	$223 \pm 5$	$0.79 \pm 0.03$	$0.78 \pm 0.03$
Non-rel. RPA + MEC	117.87/195	$1.07 \pm 0.03$	$34 \pm 12$	$225 \pm 5$	$0.80 \pm 0.04$	$0.75 \pm 0.03$
SF + MEC	97.46/196	$1.33 \pm 0.02$	0 (at limit)	$234 \pm 4$	$0.81 \pm 0.02$	$0.86 \pm 0.02$

Table 4.3: Best fit parameter values for the fits to all four datasets simultaneously for the CCQE RFG+RPA+MEC and SF+MEC fits. The parameters  $\lambda_\nu^{MB}$  and  $\lambda_{\bar{\nu}}^{MB}$  are the MiniBooNE normalisations. Note that the  $\chi^2/\text{DOF}$  is low due to issues related to the use of multiple independent datasets, and the lack of correlation between data points in the MiniBooNE datasets. This is discussed in greater detail in [107]. Table reproduced from [86].

the four datasets together, with the following definition:

$$\begin{aligned} \chi^2(\theta) = & \left[ \sum_{k=0}^M \left( \frac{N_k^{DATA} - (\lambda_\nu^{MB})^{-1} N_k^{MC}(\theta)}{\sigma_k} \right)^2 + \left( \frac{\lambda_\nu^{MB} - 1}{\varepsilon} \right)^2 \right] \rightarrow \text{MiniBooNE } \nu \\ & + \left[ \sum_{l=0}^{\bar{M}} \left( \frac{N_l^{DATA} - (\lambda_{\bar{\nu}}^{MB})^{-1} N_l^{MC}(\theta)}{\sigma_l} \right)^2 + \left( \frac{\lambda_{\bar{\nu}}^{MB} - 1}{\bar{\varepsilon}} \right)^2 \right] \rightarrow \text{MiniBooNE } \bar{\nu} \\ & + \left[ \sum_{i=0}^{16} \sum_{j=0}^{16} (N_i^{DATA} - N_i^{MC}(\theta)) V_{ij}^{-1} (\nu_j^{DATA} - \nu_j^{MC}(\theta)) \right] \rightarrow \text{MINER}\nu\text{A} \end{aligned}$$

where  $\theta$  represents the physics parameters,  $V_{ij}$  is the MINER $\nu$ A covariance matrix and  $N_x$  is the number of events in bin  $x$ .  $M$  and  $\bar{M}$  represent the number of bins in the MiniBooNE neutrino and antineutrino samples respectively.

The results can be seen in Table 4.3, and the best-fit distributions can be seen in Figures 4.19, 4.20, 4.21 and 4.22.

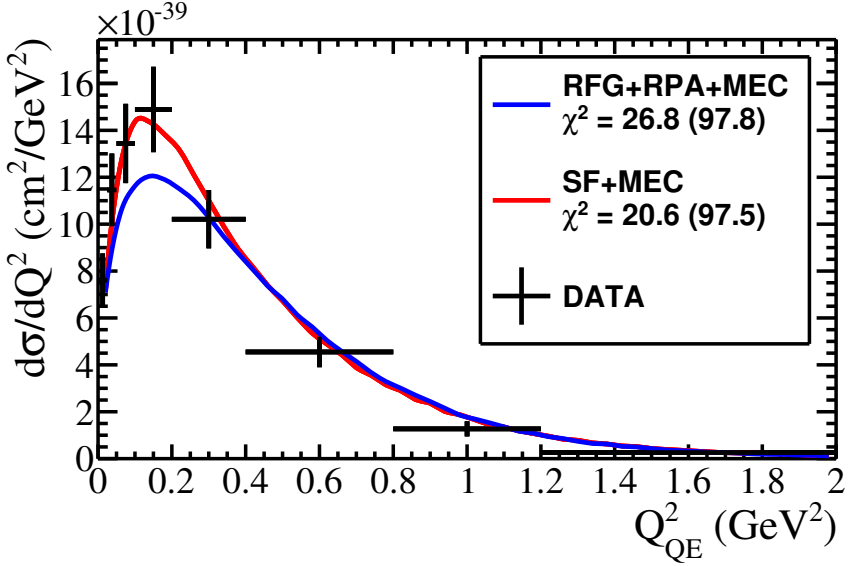


Figure 4.19: CCQE best-fit distributions compared with the MINER $\nu$ A neutrino dataset used in the CCQE fit. The legend shows the  $\chi^2$  contribution from this dataset only, with the total  $\chi^2$  for the combined four dataset fit in brackets. The RPA lines use the relativistic calculation. Reproduced from [86].

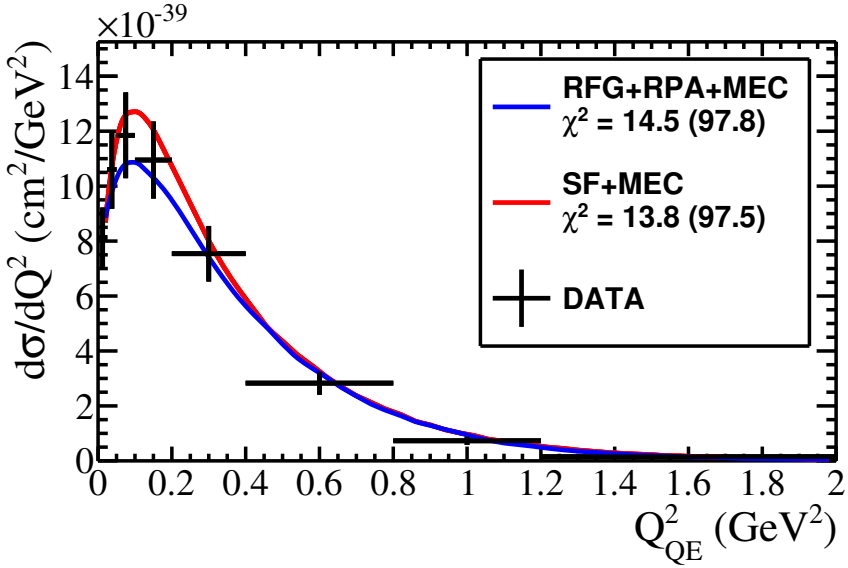


Figure 4.20: CCQE best-fit distributions compared with the MINER $\nu$ A antineutrino dataset used in the CCQE fit. The legend shows the  $\chi^2$  contribution from this dataset only, with the total  $\chi^2$  for the combined four dataset fit in brackets. The RPA lines use the relativistic calculation. Reproduced from [86].

The fits disfavour the RFG model with non-relativistic RPA, and provide a limited distinction between the SF model and the RFG model with relativistic RPA. The Spectral Function model fit suggested an MEC value at the limit of zero, and the RFG model contains an appropriate treatment of the RPA correction. The RFG model with relativistic RPA was selected as the nuclear model for the oscillation analysis. As such, all Monte Carlo events used in the analysis have two weights initially applied for the nuclear model. The first reweights the MC from Spectral Function to Relativistic Fermi Gas, while the second reweights from the RFG to RFG with relativistic RPA.

It can also be seen in Table 4.3 that the best-fit point of  $M_A^{QE}$  was tuned down from its nominal value of 1.2 GeV to 1.15 GeV. This tune reduces the total predicted ND280 event rate by about 20% from flux-tuned Monte Carlo. This effect can be seen in the third column of Tables 5.2 and 5.3.

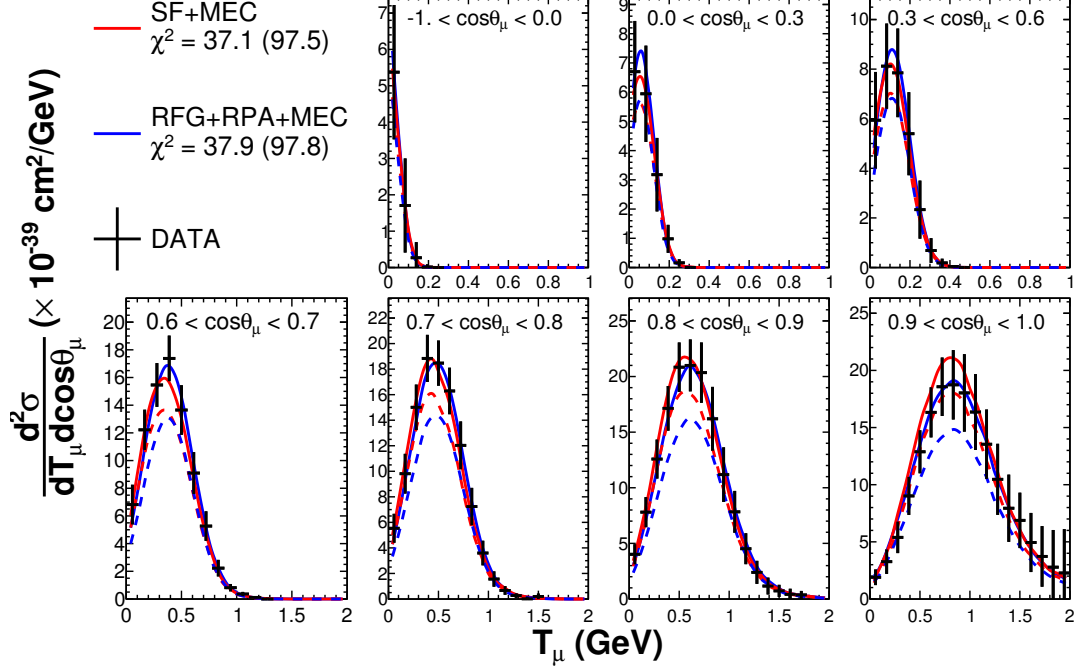


Figure 4.21: CCQE best-fit distributions compared with the MiniBooNE double-differential neutrino dataset used in the CCQE fit. The legend shows the  $\chi^2$  contribution from this dataset only, with the total  $\chi^2$  for the combined four dataset fit in brackets. The RPA lines use the relativistic calculation. The solid lines include the MiniBooNE normalisation terms, the dashed lines are without. Reproduced from [86].

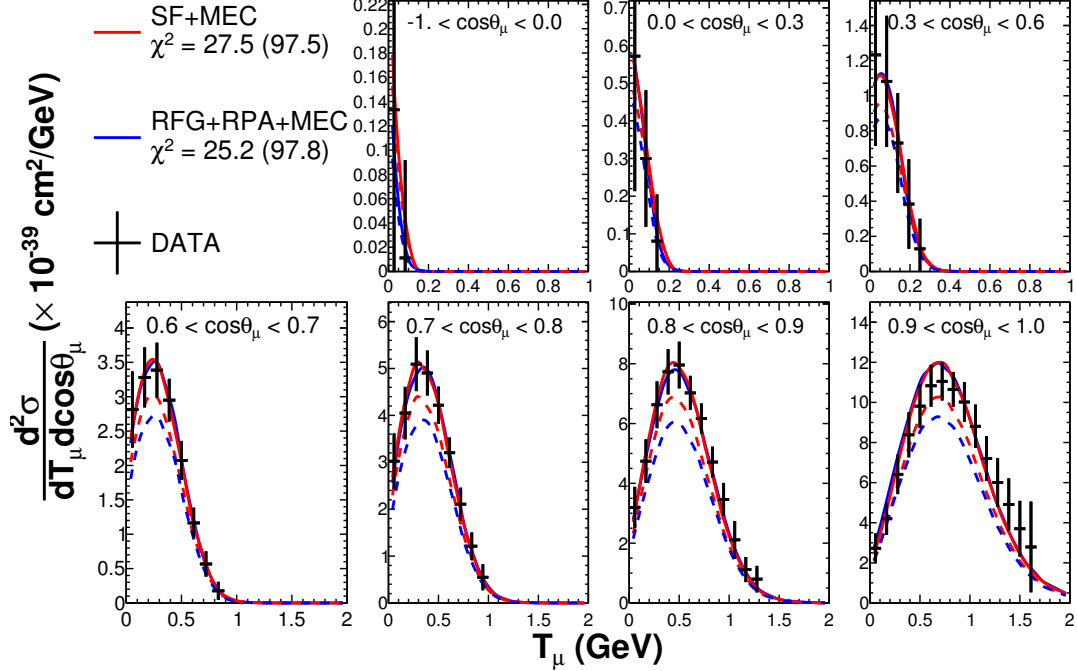


Figure 4.22: CCQE best-fit distributions compared with the MiniBooNE double-differential antineutrino dataset used in the CCQE fit. The legend shows the  $\chi^2$  contribution from this dataset only, with the total  $\chi^2$  for the combined four dataset fit in brackets. The RPA lines use the relativistic calculation. The solid lines include the MiniBooNE normalisation terms, the dashed lines are without. Reproduced from [86].

## 4.4 Near Detector Flux and Cross-Section Constraints

For the oscillation analysis, the spectrum predictions used as input are tuned based on an analysis of the near detector data in order to constrain the J-PARC neutrino beam flux and neutrino interaction models. These parameters are fitted at the ND280 independent of the Super-K data, producing a tuned central value for each parameter, and a covariance matrix representing the uncertainties on, and correlations between, each flux and cross-section parameter.

### 4.4.1 Near Detector Samples

The ND280 systematic fits use events selected to form three samples for neutrino beam mode, and four samples for antineutrino beam mode. The interaction target used is FGD1, and we select for events with a single muon. For each beam mode, first a CC inclusive sample is formed. In neutrino beam mode, this uses the following cuts[108]:

- Data quality: all ND280 systems working correctly, good beam spill.
- Total multiplicity: at least one track reconstructed in TPC2.
- Quality and fiducial volume: there must be one reconstructed track inside the FGD1 fiducial volume, and it must be associated with a TPC object with more than 18 clusters.
- Upstream background veto: veto events in which the second highest momentum track starts 150 mm upstream of the muon candidate, in order to avoid selecting muons created in the P0D where the reconstruction has created two tracks.
- Broken tracks: if there is at least one FGD-only track, require that the muon candidate track starts less than 425 mm away from the FGD upstream edge, in order to reject events where the reconstruction has split the track inside the FGD.
- Muon PID cut: TPC PID, which uses  $dE/dx$  information and track curvature, identifies the highest momentum track as a negative muon.

The events passing this selection are subdivided into CC0 $\pi$ , CC1 $\pi$  and CC other by reconstructing secondary tracks starting in FGD1. If the track is visible in the TPC, the TPC PID algorithm is used. For positive tracks, a likelihood is calculated for three different hypotheses:  $\pi^+$ , proton and positron. For negative tracks, only the  $\pi^-$  and electron hypotheses are considered. Neutral pions are identified using the observation of the electron and positron pair produced by a decay photon. For tracks not visible in the TPC, charged pions can be identified either by observing the pion track itself in the FGD, or observing the Michel electron from a muon produced by pion decay at rest.

Events with no identified pions are selected as CC0 $\pi$ . Events with a single positive pion identified in either the TPC or FGD, and no negative pions, electrons or positrons are selected as CC1 $\pi$ . All other events which pass the CC inclusive selection are classified as CC other.

In antineutrino beam mode, the same cuts are used to form two different CC inclusive samples, differentiated by the identified charge of the muon candidate [109, 110]. These two samples are each further subdivided into CC 1-track and CC N-track. The CC 1-track sample consists of events with an identified muon and no identified pions. All other events passing the CC inclusive selection are placed into the CC N-track sample. The charge selection provides strong separation of neutrino and antineutrino events, with approximately 5% of the selected negative-charge events resulting from  $\overline{\nu}_\mu$ , and 1.7% of selected positive-charge events resulting from  $\nu_\mu$  interactions.

#### 4.4.2 Near Detector Binning

All ND280 samples are binned in observed lepton momentum ( $p$ ) and the cosine of the angle between the neutrino beam and the observed lepton ( $\cos \theta$ ). For neutrino beam mode ND280 data, the sample binning is as follows:

- CC0 $\pi$  in 14  $p$  bins, and 11  $\cos \theta$  bins.
- CC1 $\pi$  in 13  $p$  bins, and 11  $\cos \theta$  bins.
- CC other in 14  $p$  bins, and 11  $\cos \theta$  bins.

The binning was selected to maximise signal over signal plus background per bin, summed over all bins while maintaining a minimum of 25 expected MC events per bin. Minimum bin sizes are set based on detector resolution. A more detailed description of the optimisation process for this binning is given in [111]. For the purposes of detector uncertainties, these are rebinned more coarsely in order to reduce the number of parameters in the fit, and thus the computation time. The detector uncertainties use 10 bins in  $p$  and 7 bins in  $\cos \theta$ , for a total of 210 bins over the three samples.

For the antineutrino beam mode ND280 data, coarser binning was used due to the low data statistics. Once again, the binning was optimised in order to have a similar number of events per bin and an acceptable minimum number of events per bin. Each of the four samples using the same binning:

- $\overline{\nu}_\mu$  CC 1-track, in 5  $p$  bins, and 4  $\cos \theta$  bins.
- $\overline{\nu}_\mu$  CC N-track, in 5  $p$  bins, and 4  $\cos \theta$  bins.
- $\nu_\mu$  CC 1-track, in 5  $p$  bins, and 4  $\cos \theta$  bins.
- $\nu_\mu$  CC N-track, in 5  $p$  bins, and 4  $\cos \theta$  bins.

#### 4.4.3 Near Detector Analysis Strategy

The software used to generate these inputs is known as the BANFF (Beam And Nd280 Flux extrapolation task Force) fitter. In the BANFF fit, both T2K’s neutrino beam mode (FHC) and antineutrino beam mode (RHC) ND280 datasets are fitted simultaneously.  $5.82 \times 10^{20}$  POT of FHC data and  $0.43 \times 10^{20}$  POT of RHC data are used. Flux parameters are treated separately for each beam mode, while the cross-section parameters are shared between both modes.

Detector uncertainties for these parameters use the same binning, for a total of 80 bins over the four RHC samples and a combined a total of 290 detector uncertainty bins for the entire fit. Figures 4.23 and 4.24 show representative event displays for each of these samples.

A binned likelihood is formed, and twice the negative logarithm of this likelihood behaves as a  $\chi^2$  distribution:

$$\begin{aligned} \chi^2_{ND280} = & 2 \sum_i^{Nbins} \left( N_i^p(\vec{b}, \vec{x}, \vec{d}) - N_i^d + N_i^d \ln[N_i^d / N_i^p(\vec{b}, \vec{x}, \vec{d})] \right) + \\ & \sum_i^{N_b} \sum_j^{N_b} \Delta b_i (\mathbf{V}_b^{-1})_{i,j} \Delta b_j + \sum_i^{N_x} \sum_j^{N_x} \Delta x_i (\mathbf{V}_x^{-1})_{i,j} \Delta x_j + \\ & \sum_i^{N_d} \sum_j^{N_d} \Delta d_i (\mathbf{V}_d^{-1})_{i,j} \Delta d_j \end{aligned} \quad (4.8)$$

Here,  $N_i^d$  is the numbers of events observed in each bin ( $i$ ) of the analysis.  $N_i^p$  is the predicted number of events for the  $i^{\text{th}}$  bin and depends on the flux ( $\vec{b}$ ), cross section ( $\vec{x}$ ) and detector ( $\vec{d}$ ) systematic parameters. The first term of the equation represents the difference between prediction and data, while the following three terms add a penalty term as the fitted parameters move further from their prior value.  $\mathbf{V}_b$ ,  $\mathbf{V}_x$  and  $\mathbf{V}_d$  represent the covariance matrices for the flux, cross section and detector parameters respectively, while  $\Delta b$ ,  $\Delta x$  and  $\Delta d$  are the deviations of these parameters away from their prior central values.  $N_x$  is the total number of cross-section parameters in the fit, and  $N_b$  is the total number of parameters controlling normalisations of the flux bins.  $N_d = 290$ , which is the previously mentioned number of detector uncertainty normalisation parameters. The uncertainties on these normalisations and their correlations are determined by evaluating the effect on number of events per bin by tweaking the ND280 detector systematic parameters [112].

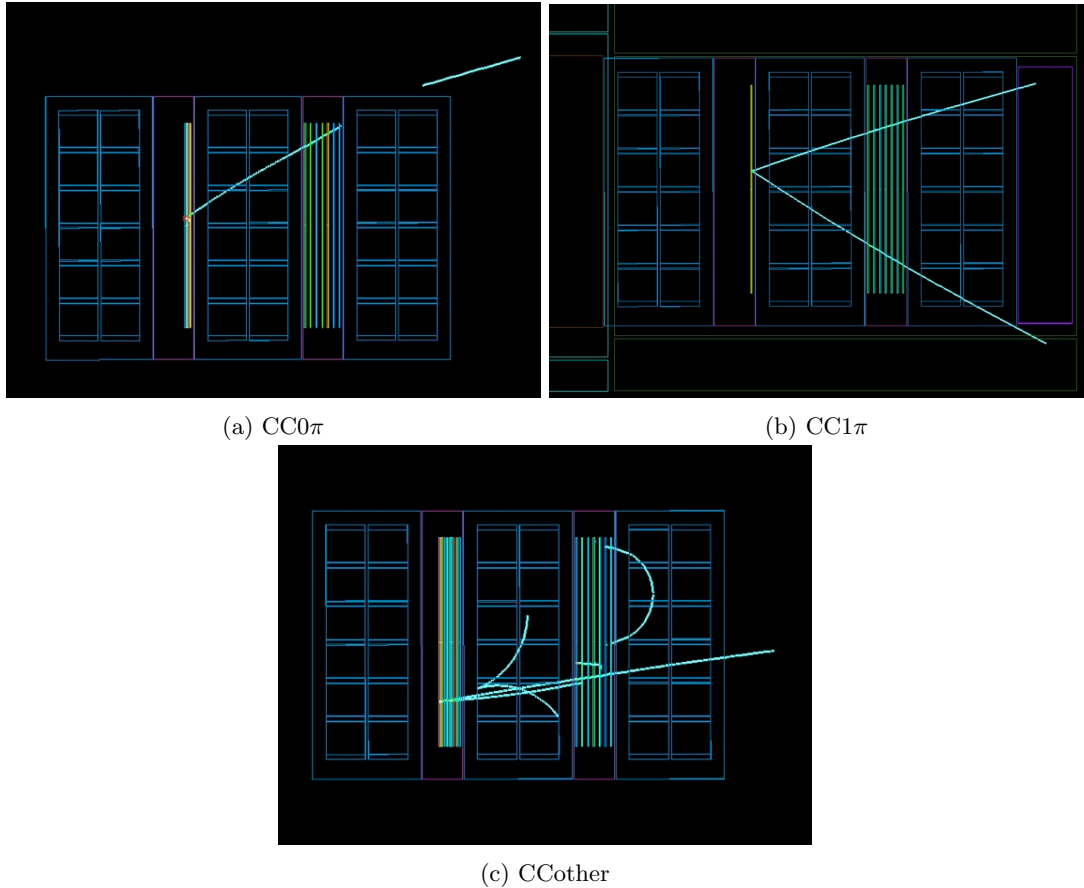


Figure 4.23: Example data event displays for the neutrino beam mode ND280 fit samples. The CC $0\pi$  event contains a single muon-like track, from a CCQE (or possibly MEC) event. The CC $1\pi$  event contains a muon-like track (top) and a pion-like track (below), probably from a resonance event. The CC other event contains a muon-like track and a number of other particles including pair produced electrons.

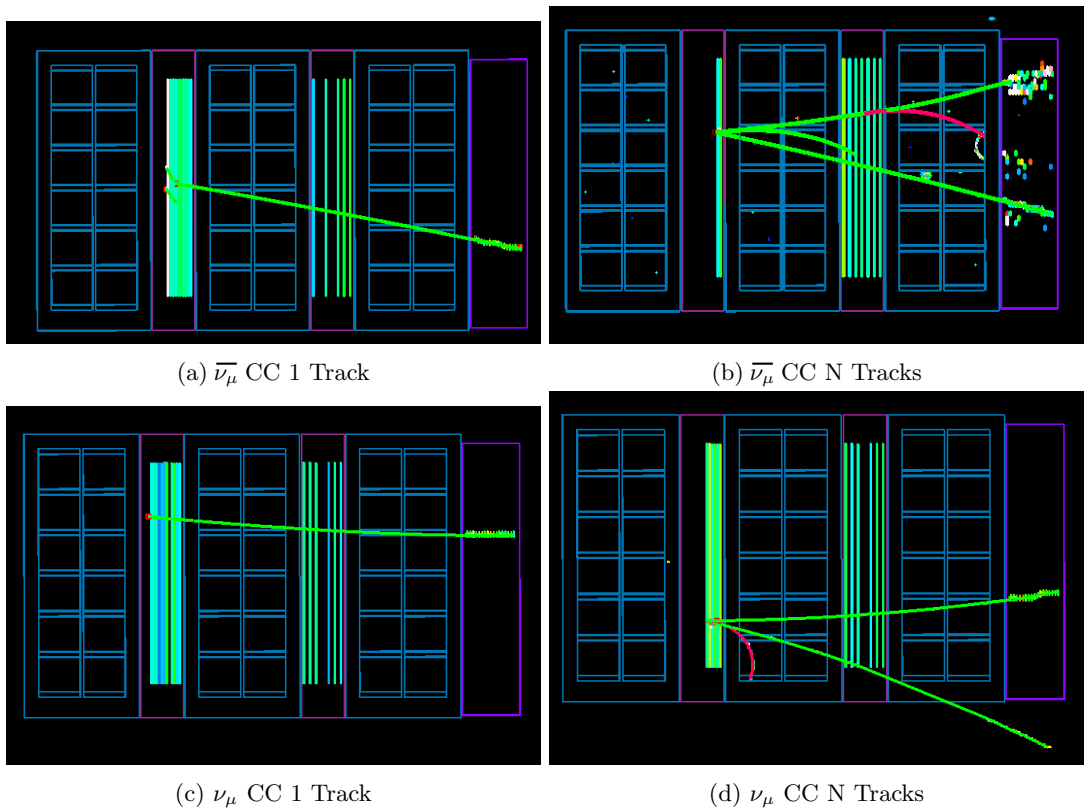


Figure 4.24: Example event displays for the antineutrino beam mode ND280 fit samples. Direction of curvature of the muon-like track is used to separate  $\nu_\mu$  from  $\overline{\nu_\mu}$ .

The BANFF fit contains 25 flux parameters each for ND280 FHC, ND280 RHC, SK FHC and SK RHC fluxes, binned in true neutrino energy. For the purposes of this analysis, only the 25 RHC flux parameters are used at Super-K. 16 cross-section parameters are used, as well as 6 ND280 FSI parameters. The four carbon-specific cross-section parameters as well as the 6 FSI parameters are marginalised away by performing a numerical integration according to their postfit distribution, before the matrix is propagated to SK leaving the oscillation analysis with 12 cross-section parameters. This gives a total of 37 systematic parameters constrained by the near detector.

The main interaction mass of FGD1 is carbon, while the main nuclear target at SuperK is Oxygen. The BANFF sample contains very few events on oxygen (approximately 0.5%), reducing our ability to constrain the errors on oxygen-specific cross-section parameters. While it is not possible to significantly reduce the uncertainty on oxygen using the ND280 data, the best-fit parameters from the fit to carbon are used as a tune. For example, the CCQE tune suggests a prior central value of 0.27 for the MEC normalisation on both nuclei with a prior error on oxygen of 1.04. The ND280 data fit to carbon suggests a postfit central value of 1.031 for the MEC normalisation. This result is used as the central value for the systematic on oxygen at Super-K, but the uncertainty on oxygen is not reduced by the data collected on carbon, giving a final value for MEC on oxygen of  $1.031 \pm 1.015$ . The cross-section and ND280 FSI parameters and whether or not they are propagated to SK are shown in Table 4.4.

The fit results for cross-section, FHC flux errors and RHC flux errors can be seen in Table 4.4, Table 4.5 and Table 4.6 respectively. The numbers of events predicted before and after fitting the near detector data can be seen in Table 4.7. The exact set of which systematics are applied to which interaction modes can be seen in Table 4.8. The BANFF correlation matrix can be seen in Figure 4.25. Fitted distributions of ND280 data can be seen in Figures 4.26 to 4.32. It should be observed that the ND280 data event rates exceed the prediction from the external data CCQE tuning. As a result, the BANFF fit results increase the predicted signal event rate at ND280 by approximately 15%. The largest change is applied to the MEC normalisation parameter, which the CCQE tune from its initial prediction (1) down to 0.27. The results of the T2K near detector fit returned this parameter to close to its pre-tune value (at 103%). The corresponding increase in Super-K event rate will be demonstrated in Tables 5.2 and 5.3.

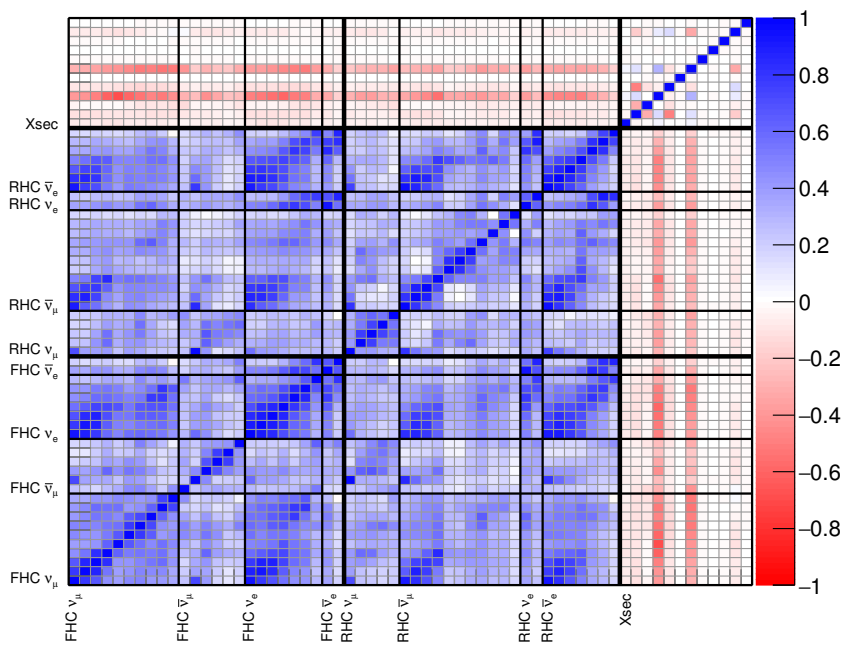


Figure 4.25: Correlations between flux and cross-section parameters from the ND280 fit. Absolute error sizes can be seen in Table 4.4 for cross-section parameters and Tables 4.5 and 4.6 for flux parameters. The parameters are shown in the order of those tables.

Cross Section Parameter	Prefit	BANFF postfit	Type	Used at SK
$M_A^{QE}$ (GeV/c <sup>2</sup> )	$1.15 \pm 0.069607$	$1.1371 \pm 0.033559$	Shape	✓
$p_F$ <sup>12</sup> C (MeV/c)	$223.0 \pm 12.301$	$222.67 \pm 8.8333$	Shape	
MEC <sup>12</sup> C	$27.0 \pm 29.053$	$103.11 \pm 17.245$	Norm	
$E_B$ <sup>12</sup> C (MeV)	$25.0 \pm 9.0$	$23.903 \pm 7.3458$	Shape	
$p_F$ <sup>16</sup> O (MeV/c)	$225.0 \pm 12.301$	$224.43 \pm 12.152$	Shape	✓
MEC <sup>16</sup> O	$27.0 \pm 104.13$	$103.11 \pm 101.49$	Norm	✓
$E_B$ <sup>16</sup> O (MeV)	$27.0 \pm 9.0$	$27.045 \pm 8.8047$	Shape	✓
$CA5^{RES}$	$1.01 \pm 0.12$	$0.86234 \pm 0.074094$	Shape	✓
$M_A^{RES}$ (GeV/c <sup>2</sup> )	$0.95 \pm 0.15$	$0.72437 \pm 0.052156$	Shape	✓
Isospin=½ Background	$1.3 \pm 0.2$	$1.4853 \pm 0.19014$	Shape	✓
$\nu_e/\nu_\mu$	$1.0 \pm 0.02$	$1.0008 \pm 0.019997$	Norm	✓
CC Other Shape	$0.0 \pm 0.4$	$0.023024 \pm 0.1928$	Shape	✓
CC Coh <sup>12</sup> C	$1.0 \pm 1.0$	$0.021658 \pm 0.16037$	Norm	
CC Coh <sup>16</sup> O	$1.0 \pm 1.0$	$1.0764 \pm 0.97171$	Norm	✓
NC Coh	$1.0 \pm 0.3$	$0.98 \pm 0.29922$	Norm	✓
NC Other	$1.0 \pm 0.3$	$1.4128 \pm 0.1858$	Norm	✓
FSI Inel. Low E	$0.0 \pm 0.41231$	$-0.30957 \pm 0.15282$	Norm	
FSI Inel. High E	$0.0 \pm 0.33793$	$0.12113 \pm 0.23671$	Norm	
FSI Pion Prod.	$0.0 \pm 0.5$	$-0.17671 \pm 0.34675$	Norm	
FSI Pion Abs.	$0.0 \pm 0.41161$	$-0.06842 \pm 0.23702$	Norm	
FSI Ch. Exch. Low E	$0.0 \pm 0.56679$	$0.66502 \pm 0.43203$	Norm	
FSI Ch. Exch. High E	$0.0 \pm 0.27778$	$-0.098172 \pm 0.19264$	Norm	

Table 4.4: BANFF cross-section parameters with their prefit and post-fit values and uncertainties. Reproduced from [112].

FHC Flux parameter	Prefit	Postfit
SK $\nu_\mu$ (0.0 - 0.4 GeV)	$1.0 \pm 0.09873$	$1.2038 \pm 0.05919$
SK $\nu_\mu$ (0.4 - 0.5 GeV)	$1.0 \pm 0.10349$	$1.2329 \pm 0.05535$
SK $\nu_\mu$ (0.5 - 0.6 GeV)	$1.0 \pm 0.09644$	$1.1997 \pm 0.04533$
SK $\nu_\mu$ (0.6 - 0.7 GeV)	$1.0 \pm 0.08670$	$1.1244 \pm 0.03798$
SK $\nu_\mu$ (0.7 - 1.0 GeV)	$1.0 \pm 0.11305$	$1.0555 \pm 0.04110$
SK $\nu_\mu$ (1.0 - 1.5 GeV)	$1.0 \pm 0.09175$	$1.0751 \pm 0.04202$
SK $\nu_\mu$ (1.5 - 2.5 GeV)	$1.0 \pm 0.07017$	$1.1095 \pm 0.04024$
SK $\nu_\mu$ (2.5 - 3.5 GeV)	$1.0 \pm 0.07368$	$1.1200 \pm 0.04272$
SK $\nu_\mu$ (3.5 - 5.0 GeV)	$1.0 \pm 0.08737$	$1.1062 \pm 0.04227$
SK $\nu_\mu$ (5.0 - 7.0 GeV)	$1.0 \pm 0.09794$	$1.0465 \pm 0.04247$
SK $\nu_\mu$ (7.0 - 30.0 GeV)	$1.0 \pm 0.11436$	$1.0072 \pm 0.05272$
SK $\bar{\nu}_\mu$ (0.0 - 0.7 GeV)	$1.0 \pm 0.10258$	$1.1561 \pm 0.08070$
SK $\bar{\nu}_\mu$ (0.7 - 1.0 GeV)	$1.0 \pm 0.07853$	$1.0818 \pm 0.04748$
SK $\bar{\nu}_\mu$ (1.0 - 1.5 GeV)	$1.0 \pm 0.08445$	$1.0564 \pm 0.06033$
SK $\bar{\nu}_\mu$ (1.5 - 2.5 GeV)	$1.0 \pm 0.08557$	$1.0566 \pm 0.07216$
SK $\bar{\nu}_\mu$ (2.5 - 30.0 GeV)	$1.0 \pm 0.08643$	$1.1097 \pm 0.07022$
SK $\nu_e$ (0.0 - 0.5 GeV)	$1.0 \pm 0.08970$	$1.1903 \pm 0.04718$
SK $\nu_e$ (0.5 - 0.7 GeV)	$1.0 \pm 0.08995$	$1.1804 \pm 0.04356$
SK $\nu_e$ (0.7 - 0.8 GeV)	$1.0 \pm 0.08597$	$1.1697 \pm 0.04152$
SK $\nu_e$ (0.8 - 1.5 GeV)	$1.0 \pm 0.080912$	$1.1233 \pm 0.03713$
SK $\nu_e$ (1.5 - 2.5 GeV)	$1.0 \pm 0.07897$	$1.1117 \pm 0.04086$
SK $\nu_e$ (2.5 - 4.0 GeV)	$1.0 \pm 0.08385$	$1.0961 \pm 0.04203$
SK $\nu_e$ (4.0 - 30.0 GeV)	$1.0 \pm 0.09390$	$1.0903 \pm 0.06037$
SK $\bar{\nu}_e$ (0.0 - 2.5 GeV)	$1.0 \pm 0.07403$	$1.1303 \pm 0.05463$
SK $\bar{\nu}_e$ (2.5 - 30.0 GeV)	$1.0 \pm 0.12842$	$1.1559 \pm 0.11855$

Table 4.5: Prefit and postfit values for the Super-K FHC flux parameters. Reproduced from [112].

RHC Flux parameter	Prefit	Postfit
SK $\nu_\mu$ (0.0 - 0.7 GeV)	$1.0 \pm 0.09368$	$1.1424 \pm 0.07101$
SK $\nu_\mu$ (0.7 - 1.0 GeV)	$1.0 \pm 0.07934$	$1.0907 \pm 0.05294$
SK $\nu_\mu$ (1.0 - 1.5 GeV)	$1.0 \pm 0.07673$	$1.0791 \pm 0.05176$
SK $\nu_\mu$ (1.5 - 2.5 GeV)	$1.0 \pm 0.08056$	$1.0740 \pm 0.05976$
SK $\nu_\mu$ (2.5 - 30.0 GeV)	$1.0 \pm 0.08029$	$1.0497 \pm 0.05277$
SK $\bar{\nu}_\mu$ (0.0 - 0.4 GeV)	$1.0 \pm 0.10448$	$1.2044 \pm 0.06858$
SK $\bar{\nu}_\mu$ (0.4 - 0.5 GeV)	$1.0 \pm 0.10153$	$1.2104 \pm 0.05785$
SK $\bar{\nu}_\mu$ (0.5 - 0.6 GeV)	$1.0 \pm 0.09617$	$1.1801 \pm 0.05066$
SK $\bar{\nu}_\mu$ (0.6 - 0.7 GeV)	$1.0 \pm 0.08464$	$1.1282 \pm 0.04076$
SK $\bar{\nu}_\mu$ (0.7 - 1.0 GeV)	$1.0 \pm 0.12509$	$1.1232 \pm 0.07706$
SK $\bar{\nu}_\mu$ (1.0 - 1.5 GeV)	$1.0 \pm 0.10529$	$1.1177 \pm 0.06761$
SK $\bar{\nu}_\mu$ (1.5 - 2.5 GeV)	$1.0 \pm 0.07999$	$1.1206 \pm 0.05296$
SK $\bar{\nu}_\mu$ (2.5 - 3.5 GeV)	$1.0 \pm 0.07394$	$1.1215 \pm 0.04904$
SK $\bar{\nu}_\mu$ (3.5 - 5.0 GeV)	$1.0 \pm 0.09399$	$1.1224 \pm 0.06676$
SK $\bar{\nu}_\mu$ (5.0 - 7.0 GeV)	$1.0 \pm 0.09251$	$1.1122 \pm 0.06375$
SK $\bar{\nu}_\mu$ (7.0 - 30.0 GeV)	$1.0 \pm 0.13031$	$1.0930 \pm 0.10825$
SK $\nu_e$ (0.0 - 2.5 GeV)	$1.0 \pm 0.06888$	$1.1091 \pm 0.04721$
SK $\nu_e$ (2.5 - 30.0 GeV)	$1.0 \pm 0.08495$	$1.0898 \pm 0.06720$
SK $\bar{\nu}_e$ (0.0 - 0.5 GeV)	$1.0 \pm 0.09470$	$1.1926 \pm 0.05406$
SK $\bar{\nu}_e$ (0.5 - 0.7 GeV)	$1.0 \pm 0.09104$	$1.1842 \pm 0.04732$
SK $\bar{\nu}_e$ (0.7 - 0.8 GeV)	$1.0 \pm 0.09101$	$1.1670 \pm 0.04876$
SK $\bar{\nu}_e$ (0.8 - 1.5 GeV)	$1.0 \pm 0.08386$	$1.1411 \pm 0.04436$
SK $\bar{\nu}_e$ (1.5 - 2.5 GeV)	$1.0 \pm 0.07958$	$1.1195 \pm 0.05398$
SK $\bar{\nu}_e$ (2.5 - 4.0 GeV)	$1.0 \pm 0.08901$	$1.1231 \pm 0.06779$
SK $\bar{\nu}_e$ (4.0 - 30.0 GeV)	$1.0 \pm 0.15581$	$1.1796 \pm 0.14381$

Table 4.6: Prefit and postfit values for the Super-K RHC flux parameters. Reproduced from [112].

Sample	Data	BANFF prefit MC	BANFF postfit MC
$\nu_\mu$ CC Inclusive (FHC mode)	25569	24145.26	25517.17
$\nu_\mu$ CC0 $\pi$ (FHC mode)	17362	15624.99	17248.24
$\nu_\mu$ CC1 $\pi$ (FHC mode)	3988	4748.21	4189.69
$\nu_\mu$ CC Other (FHC mode)	4219	3772.06	4079.24
$\bar{\nu}_\mu$ CC Inclusive (RHC mode)	571	515.63	566.28
$\bar{\nu}_\mu$ CC 1-Track (RHC mode)	435	387.37	437.72
$\bar{\nu}_\mu$ CC N-Tracks (RHC mode)	136	128.26	128.56
$\nu_\mu$ CC Inclusive (RHC mode)	276	288.73	291.33
$\nu_\mu$ CC 1-Track (RHC mode)	131	141.42	147.31
$\nu_\mu$ CC N-Tracks (RHC mode)	145	147.31	144.02

Table 4.7: Actual and predicted event rates for the different ND280 samples in the BANFF fit. The MC predictions are shown both before and after the BANFF fit. Reproduced from [112].



Table 4.8 – *Continued from previous page*

	$\nu_\mu$ CCQE	$\nu_\mu$ CC $1\pi^-$	$\nu_\mu$ CC coherent	$\nu_\mu$ CC MEC	$\nu_\mu$ CC other	$\nu_\mu/\nu_\tau$ NC $1\pi^+/-$	$\nu_\mu/\nu_\tau$ NC $1\pi^0$	$\nu_\mu/\nu_\tau$ NC coherent	$\nu_\mu/\nu_\tau$ NC other	$\overline{\nu}_\mu$ CCQE	$\overline{\nu}_\mu$ CC $1\pi^-$	$\overline{\nu}_\mu$ CC coherent	$\overline{\nu}_\mu$ CC MEC	$\overline{\nu}_\mu$ CC other	$\overline{\nu}_\mu/\overline{\nu}_\tau$ NC $1\pi^+/-$	$\overline{\nu}_\mu/\overline{\nu}_\tau$ NC $1\pi^0$	$\overline{\nu}_\mu/\overline{\nu}_\tau$ NC coherent	$\overline{\nu}_\mu/\overline{\nu}_\tau$ NC other	$\nu_e$ CCQE	$\nu_e$ CC $1\pi^-$	$\nu_e$ CC coherent	$\nu_e$ CC MEC	$\nu_e$ CC other	$\overline{\nu}_e$ CCQE	$\overline{\nu}_e$ CC $1\pi^-$	$\overline{\nu}_e$ CC coherent	$\overline{\nu}_e$ CC MEC	$\overline{\nu}_e$ CC other	Osc. $\nu_e$ CCQE	Osc. $\nu_e$ CC $1\pi^-$	Osc. $\nu_e$ CC coherent	Osc. $\nu_e$ CC MEC	Osc. $\nu_e$ CC other			
$f_{M_A^{QE}}^{BANFF}$	✓																																			
$f_{M_A^{RES}}^{BANFF}$		✓				✓	✓																													
$J_{NormMEC}^{BANFF}$			✓																																	
$f_{C_5^A}^{BANFF}$	✓					✓																														
$f_{B_{gRES}}^{BANFF}$	✓					✓																														
$f_{pf}^{BANFF}$	✓																																			
$f_{ShapeCCoth}^{BANFF}$				✓																																
$f_{E_B}^{BANFF}$	✓																																			
$f_{NormCCcoh}^{BANFF}$			✓																																	
$f_{NormNCother}^{BANFF}$						✓	✓	✓																												
$f_{Norm(-)}^{BANFF} \nu_e \rightarrow \nu_\mu^{(-)}$																																				
$f_{E_{ir}^{SK}}$	✓	✓	✓	✓	✓	✓	✓	✓	✓	✓	✓	✓	✓	✓	✓	✓	✓	✓	✓	✓	✓	✓	✓	✓	✓	✓	✓	✓	✓	✓	✓	✓	✓	✓	✓	✓
$f_{0;t,r}^{SK+FSI} RHC$	✓																																			
$f_{1;t,r}^{SK+FSI} RHC$	✓																																			
$f_{2;t,r}^{SK+FSI} RHC$	✓																																			
$f_{3;t,r}^{SK+FSI} RHC$	✓	✓		✓																																
$f_{4;t,r}^{SK+FSI} RHC$		✓	✓		✓																															
$f_{5;t,r}^{SK+FSI} RHC$						✓	✓	✓	✓																											

Table 4.8: Each row of this table represents one of the 44 systematic parameters considered in the  $\overline{\nu}_\mu$  disappearance analysis and each column represents one of the 46 MC templates used to construct the single  $\mu$ -like ring reconstructed energy spectrum p.d.f. A ✓ symbol denotes that the given MC template is modified when the given systematic parameter is tweaked.

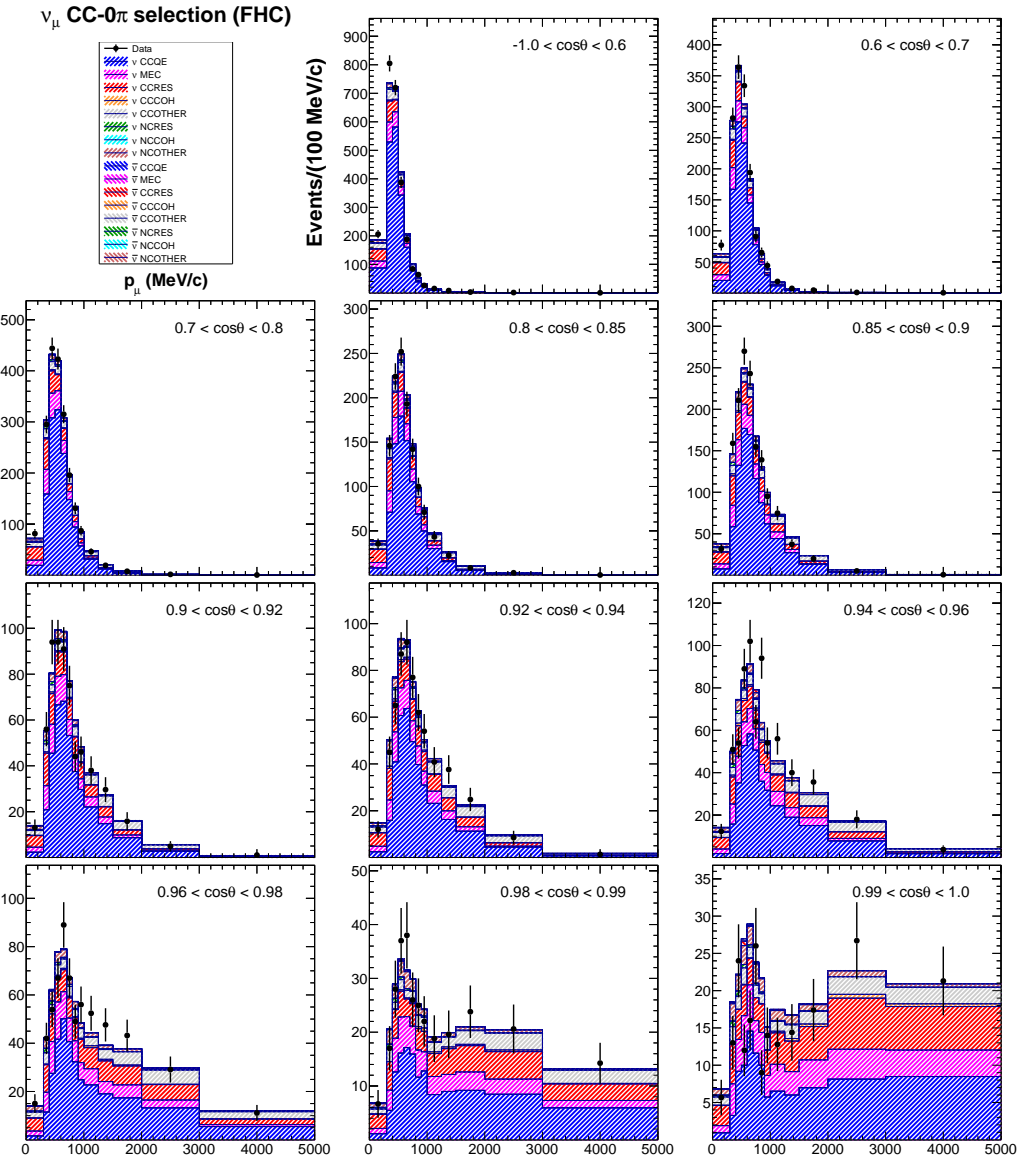


Figure 4.26: Overlays of the data and the fitted MC prediction for the  $\nu_\mu$  CC0 $\pi$  selection (FHC). Reproduced from [112].

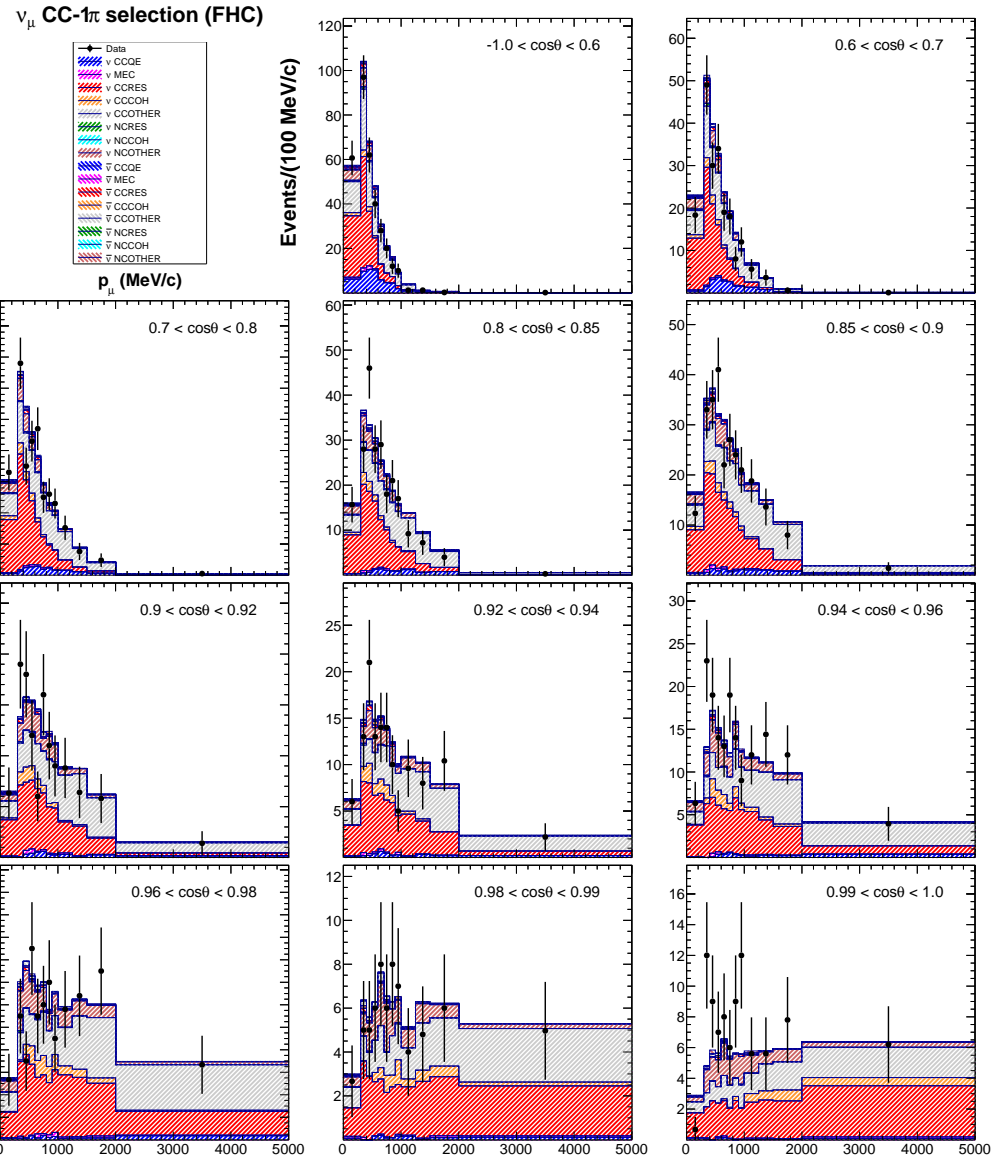


Figure 4.27: Overlays of the data and the fitted MC prediction for the  $\nu_\mu$  CC1 $\pi$  selection (FHC). Reproduced from [112].

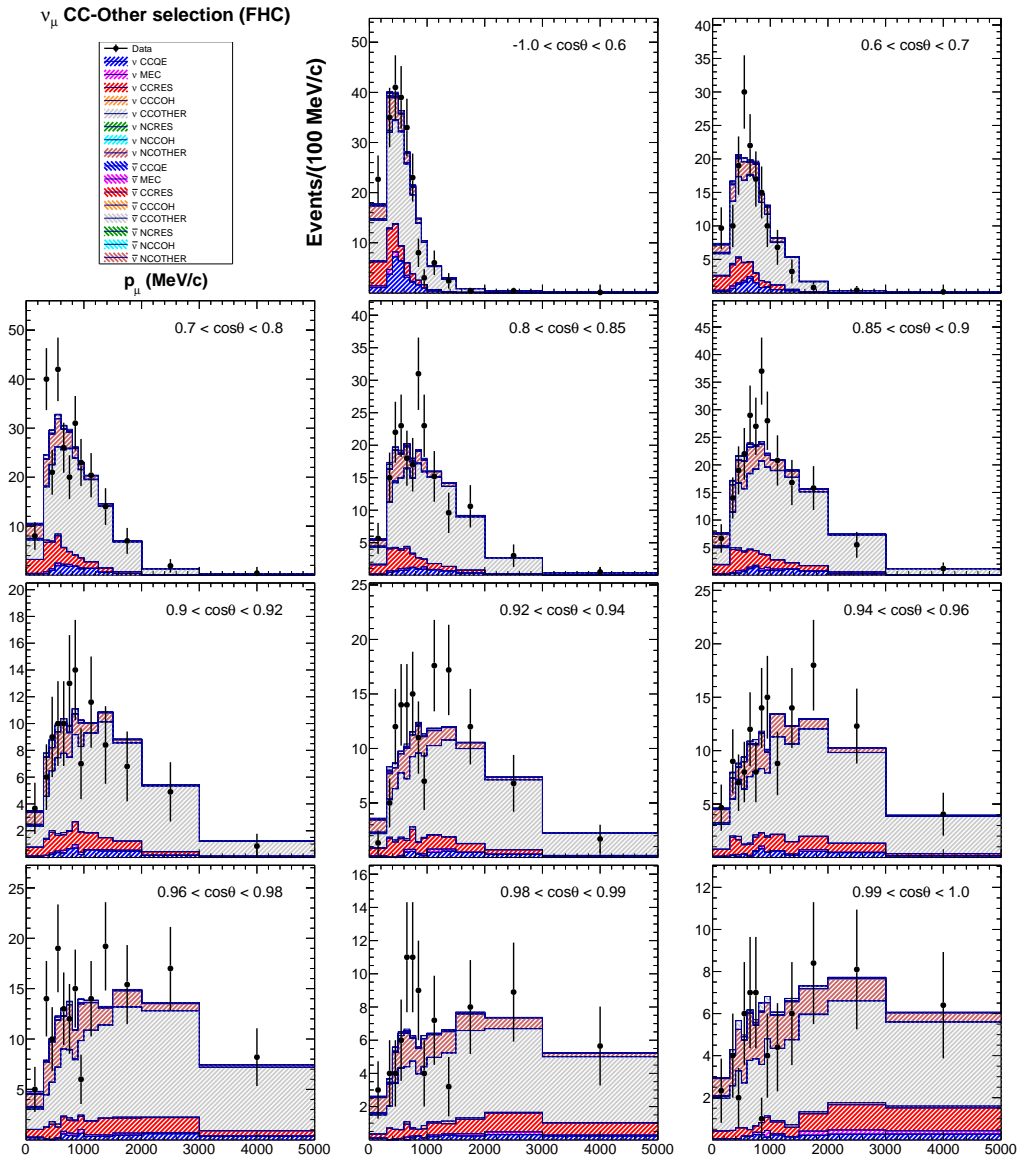


Figure 4.28: Overlays of the data and the fitted MC prediction for the  $\nu_\mu$  CC other selection (FHC). Reproduced from [112].

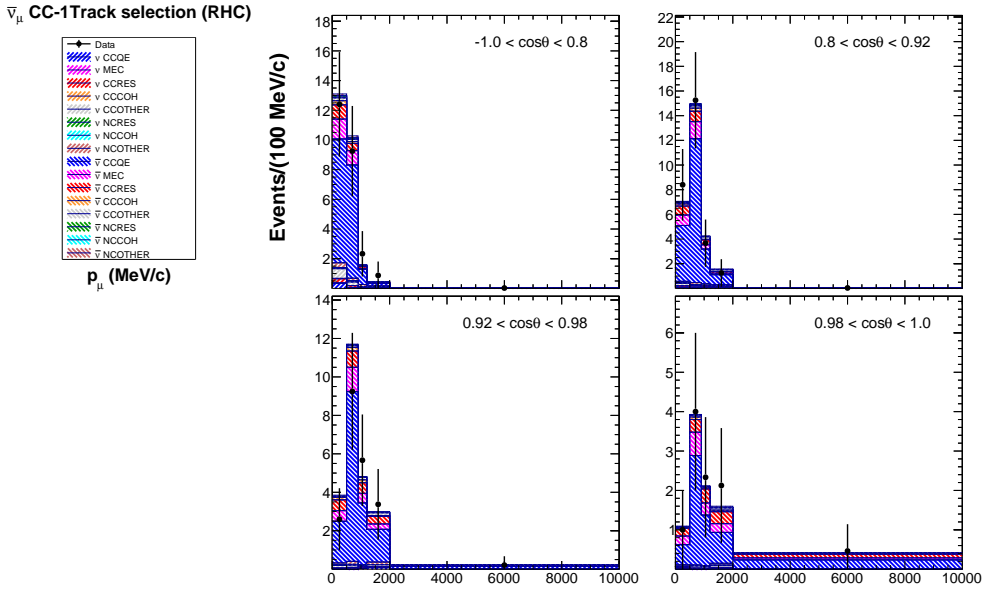


Figure 4.29: Overlays of the data and the fitted MC prediction for the  $\bar{\nu}_\mu$  CC 1-track selection (RHC). Reproduced from [112].

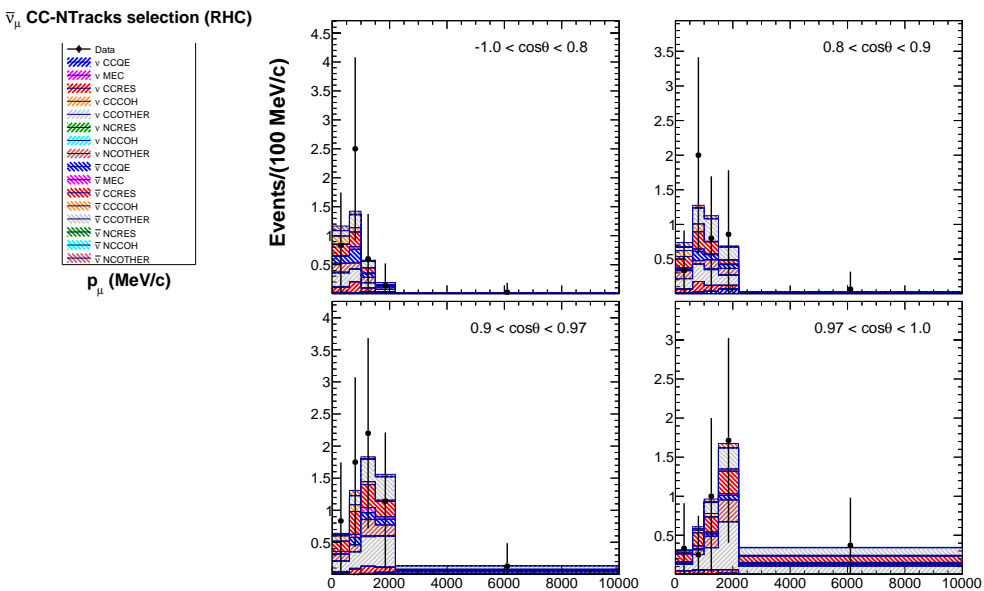


Figure 4.30: Overlays of the data and the fitted MC prediction for the  $\bar{\nu}_\mu$  CC N-tracks selection (RHC). Reproduced from [112].

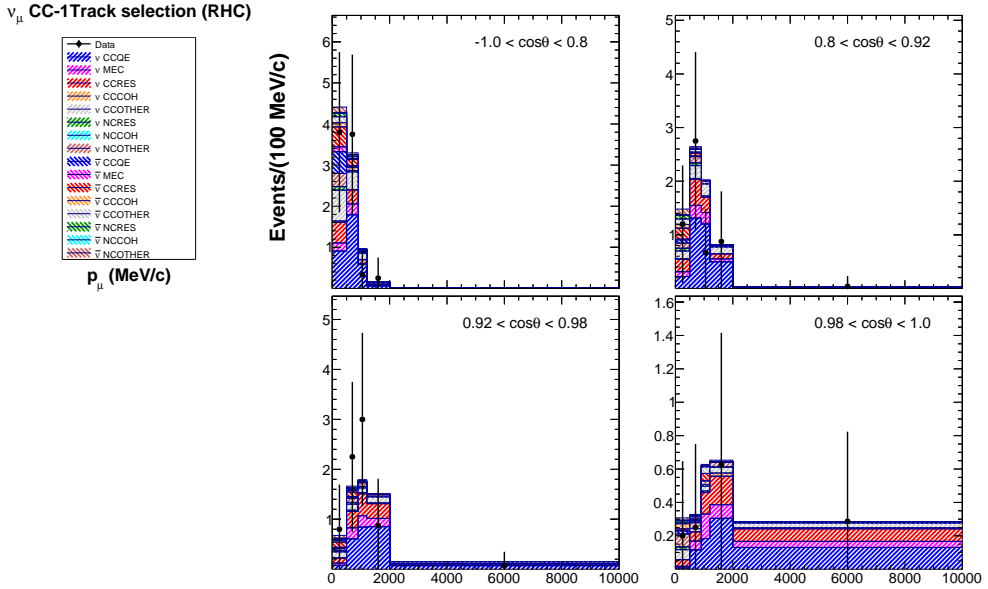


Figure 4.31: Overlays of the data and the fitted MC prediction for the  $\nu_\mu$  CC 1-track selection (RHC). Reproduced from [112].

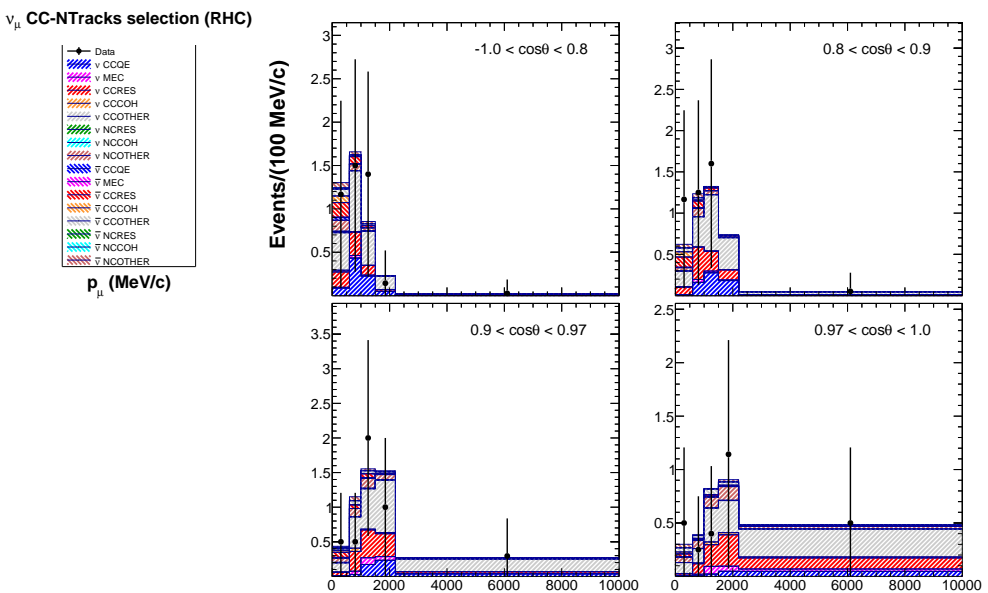


Figure 4.32: Overlays of the data and the fitted MC prediction for the  $\nu_\mu$  CC N-tracks selection (RHC). Reproduced from [112].

## 4.5 Super-Kamiokande Samples

Events are selected at Super-K with the intention of getting a pure sample of  $\nu_\mu$  or  $\overline{\nu}_\mu$  CCQE-like interactions. First, cuts are applied to select good fully contained (FC) events:

- **Data Quality Cuts.** Check for good beam spill, Super-K data quality flag, no trigger activity in the  $100 \mu\text{s}$  before the beam spill and the SK DAQ is fully functional. Sometimes, due to a malfunction a PMT produces light itself, which Super-K detects as a so-called ‘flasher’ event. Flasher events have a distinctive spatial and timing distribution of PMT hits, which can be used to accurately identify them. If 25 or more flasher events are seen in a 30 minute window, that entire subrun is assumed to be bad.
- **Timing Cuts.** The event time relative to the beginning of the beam spill  $\Delta T_0$  is measured. In order to cut out background events not caused by the beam spill, a cut of  $-2 \mu\text{s} < \Delta T_0 < 10 \mu\text{s}$  is used. The distributions of this variable can be seen in Figure 4.33.
- **Containment Cuts.** In order to reject events that are not fully contained, only events for which the highest charge outer-detector cluster has less than 16 hits are used.

In previous T2K analyses, there was also a cut to reject flasher events separate from the data quality cut, but this was removed for the 2015 T2K oscillation analysis because the accuracy of the beam trigger makes the likelihood of coincidence between a beam spill and a flasher event extremely small. The following cuts are applied to the FC sample in order to get the fully-contained fiducial-volume (FCFV) sample:

- **Fiducial volume cut.** The reconstructed vertex must be at least 2 metres from any edge of the inner detector.
- **Visible energy cut.** The observed amount of Čerenkov light must be greater than the amount that would be produced by an electron with an energy of 30 MeV.

After we have the FCFV sample, PID cuts are applied to get a sample of  $\nu_\mu$  or  $\overline{\nu}_\mu$  CCQE events:

- **Single Ring Cut.** There must be exactly one reconstructed ring in the event according to the SK ring-counting algorithm, in order to reject events with an additional visible charged particle. This rejects visible particles like a pion or additional charged lepton. The proton from a  $\nu$  CCQE event is not affected by this cut as it will not be above the Čerenkov threshold.

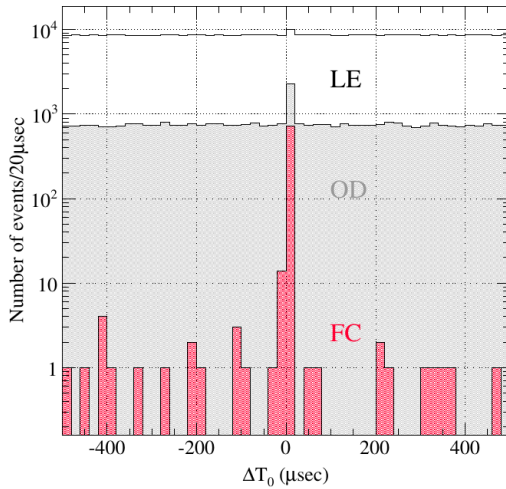


Figure 4.33: Distributions of  $\Delta T_0$  at Super-K for events in the Low Energy (LE), Outer Detector (OD) and Fully Contained (FC) events at SK from T2K runs 1-6. Reproduced from [60].

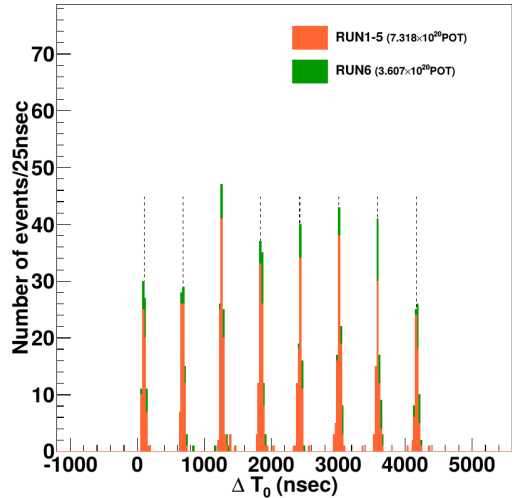


Figure 4.34: Distributions of  $\Delta T_0$  at Super-K for FC events in runs 1-5 and run 6. Bunch centres are labelled with dotted lines. Reproduced from [60].

	Total MC	$\nu_\mu$ CCQE	$\bar{\nu}_\mu$ CCQE	$(-) \nu_\mu$ CCnonQE	$(-) \nu_e$ CC	NC
Interacted in FV	108.7	6.58	10.32	32.75	5.48	53.05
Single-ring	30.30	4.44	8.11	9.74	3.95	4.06
Muon-like PID	22.85	4.40	8.00	9.19	0.04	1.23
$p_\mu > 200 \text{ MeV}/c$	22.81	4.40	7.99	9.18	0.04	1.22
$N_{decay} \leq 1$	20.97	4.32	7.96	7.48	0.03	1.17
Efficiency from Interaction in FV [%]	19.4	65.7	77.1	22.9	0.6	2.2

Table 4.9: Numbers of Monte Carlo events passing each stage of the SK PID, for  $4.011 \times 10^{20}$  with standard oscillations applied.

- **Muon-like PID cut.** The reconstructed event must appear muon-like, according to the SK PID separator, which is described in Section 3.3.1.
- **Muon momentum cut.** The reconstructed muon momentum must be above 200 MeV, in order to reject charged pions and misidentified electrons.
- **Decay electron cut.** The number of observed electrons from muon decay must be zero or one, in order to reject events with charged pions below the Čerenkov threshold. Electrons originating from these decays are identified using timing information.

The effects of these cuts on event count can be seen in Figures 4.35 and 4.36 as well as Table 4.9.

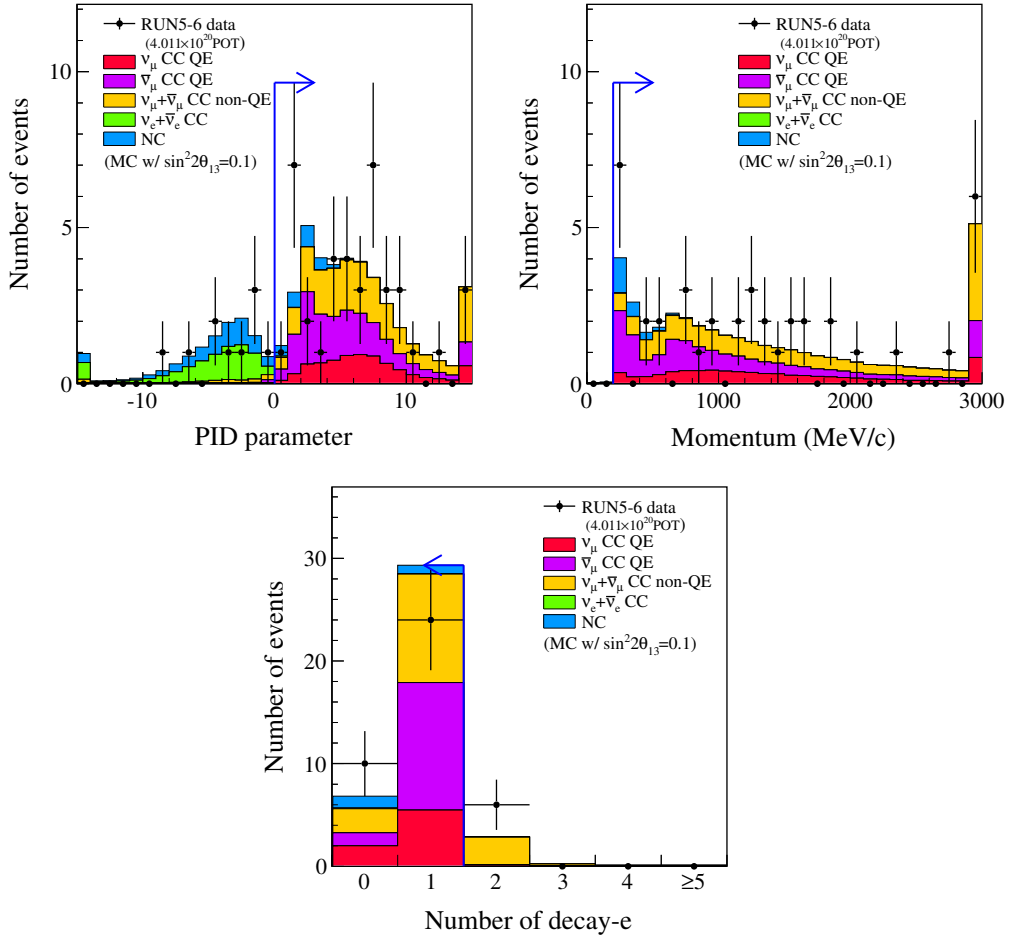


Figure 4.35: Super-K PID distributions for run 5 and 6 ( $4.011 \times 10^{20}$  POT). Reproduced from [60].

The kinematics of a CCQE interaction are used to reconstruct the neutrino energy ( $E_{reco}$ ) using the momentum and angle of the outgoing muon according to Equation 4.6. The binding energy of oxygen,  $V_O$ , is taken to be 27 MeV. This formula is accurate for a CCQE interaction, but biased for the other interaction modes we observe in SK. The relationship between true and reconstructed neutrino energy for different interaction modes can be seen in Figures 4.37a, 4.37b and 4.37c.

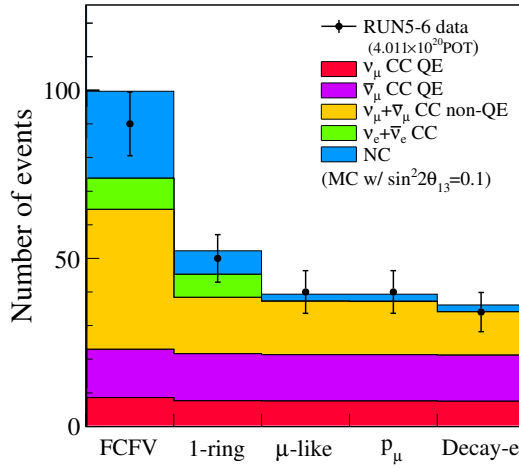


Figure 4.36: Cumulative effects of Super-K PID cuts on run 5 and 6 event numbers ( $4.011 \times 10^{20}$  POT). Reproduced from [60].

## 4.6 Super-Kamiokande Detector and Final State Interaction Systematics

Finally, there is a group of systematics which are unique to Super-Kamiokande but are clearly correlated with one another. These represent the uncertainties in Super-K's detection efficiency, in the nuclear final state interactions (FSI) and in secondary interactions (SI), the likelihood of pions interacting with a different nucleus to the one they were produced in. Covariance matrices are produced independently which account for detector efficiency uncertainties, and for FSI/SI. Both sets of uncertainties are calculated using the same binning:

- $\nu_\mu^{(-)}$  CCQE and MEC with  $E_{reco} < 0.4$  GeV.
- $\nu_\mu^{(-)}$  CCQE and MEC with  $0.4 \text{ GeV} < E_{reco} < 1.1 \text{ GeV}$ .
- $\nu_\mu^{(-)}$  CCQE and MEC with  $E_{reco} > 1.1 \text{ GeV}$ .
- $\nu_\mu^{(-)}$  CCnonQE.
- $\nu_e^{(-)}$  CC.
- All NC.

The CCQE bins were divided in order to have one bin covering the region of maximum oscillation, and a bin each below and above this energy. Since the detector and FSI

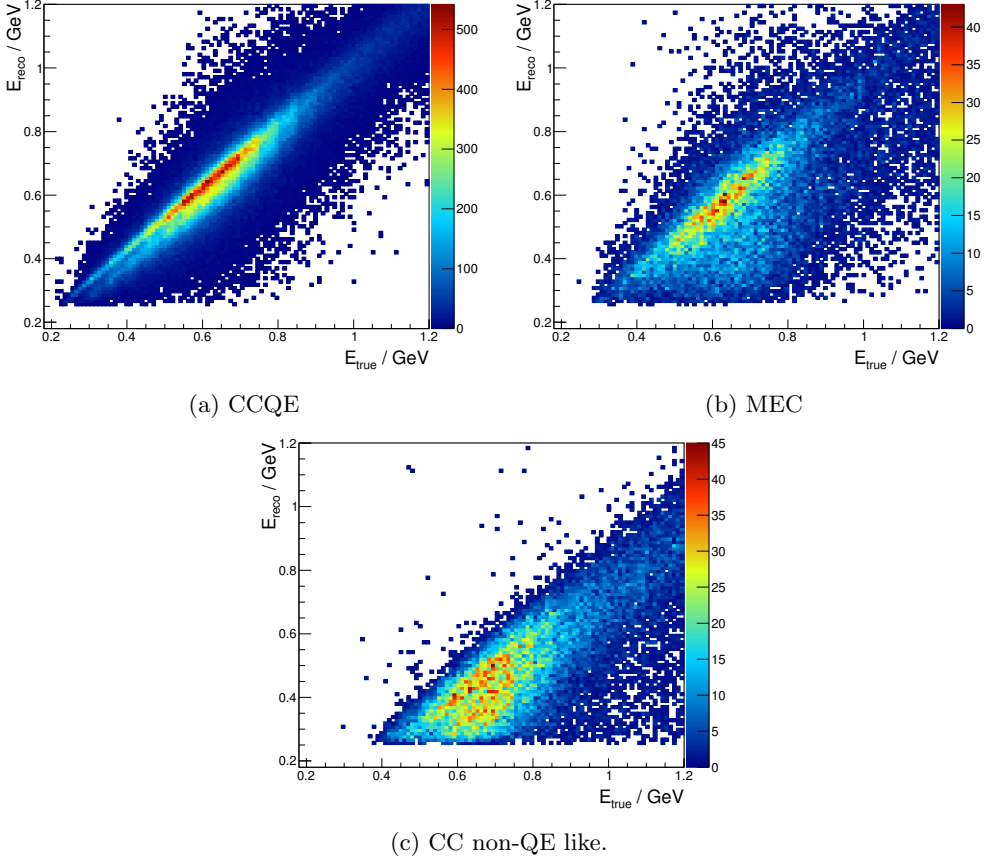


Figure 4.37: True vs. reconstructed neutrino energy for simulated  $\bar{\nu}_\mu$  events by mode.

systematics use the same binning, the covariance matrices can be summed and the fit can treat each detector+FSI bin as a single parameter. Each of these parameters is evaluated for both neutrino beam mode and antineutrino beam mode. The correlated detector/FSI parameters and their errors can be seen in Table 4.10. The correlation matrix for antineutrino beam mode can be seen in Figure 4.38.

#### 4.6.1 Final State Interactions and Secondary Interactions

FSI can cause issues for the oscillation analysis since pion absorption will cause a CC event with emitted pions to appear in Super-K as a CCQE event with the wrong reconstructed energy, which can cause background events to be reconstructed in the disappearance region. T2K FSI effects are simulated using a cascade model in NEUT, with the pion propagated through the nuclear medium in finite steps. At each point, the pion can interact in a number of ways dependent on cross-section, allowing the initial particle and any products to interact multiple times on the way out of the nucleus.

Parameter	Definition	$1\sigma$ error	SK Det	FSI/SI
FHC 1	$\bar{\nu}_\mu^{(-)}$ CCQE, $E_{reco} < 0.4$ GeV	0.018	0.018	0.000
FHC 2	$\bar{\nu}_\mu^{(-)}$ CCQE, $0.4 \text{ GeV} \leq E_{reco} \leq 1.1 \text{ GeV}$	0.017	0.017	0.000
FHC 3	$\bar{\nu}_\mu^{(-)}$ CCQE, $E_{reco} > 1.1 \text{ GeV}$	0.018	0.018	0.001
FHC 4	$\bar{\nu}_\mu^{(-)}$ CCnonQE	0.077	0.046	0.062
FHC 5	$\bar{\nu}_e^{(-)}$ CC	1.003	1.003	0.023
FHC 6	All NC	0.598	0.592	0.079
RHC 1	$\bar{\nu}_\mu^{(-)}$ CCQE, $E_{reco} < 0.4$ GeV	0.018	0.018	0.000
RHC 2	$\bar{\nu}_\mu^{(-)}$ CCQE, $0.4 \text{ GeV} \leq E_{reco} \leq 1.1 \text{ GeV}$	0.016	0.016	0.000
RHC 3	$\bar{\nu}_\mu^{(-)}$ CCQE, $E_{reco} > 1.1 \text{ GeV}$	0.016	0.016	0.001
RHC 4	$\bar{\nu}_\mu^{(-)}$ CCnonQE	0.089	0.034	0.082
RHC 5	$\bar{\nu}_e^{(-)}$ CC	1.003	1.003	0.022
RHC 6	All NC	0.597	0.593	0.073

Table 4.10: Super-K selection efficiency and FSI+SI systematic parameters for neutrino beam mode (FHC) and antineutrino beam mode (RHC). The SK detector errors and the FSI+SI errors are added in quadrature to give the total  $1\sigma$  error. The correlations between these parameters can be seen in Figure 4.38.

In order to evaluate the FSI model uncertainty, the simulation was compared to data from pion-nucleus scattering experiments. Twenty-three datasets were used, over a wide range of pion energies and nuclear targets. The datasets used and nuclear targets are described in [113]. The events were split into five categories, based on their observable final state.

- **Absorption:** No pion appears in the final state.
- **Inelastic Scattering:** Only one pion in the final state with the same charge as the pion beam.
- **Single Charge Exchange:** Only 1  $\pi^0$  in the final state.
- **Double Charge Exchange:** Only one pion in the final state with the opposite charge to the pion beam.
- **Hadron Production:** 2 or more pions in the final state.

Three parameters were varied in the fits: the mean free path, QE scattering probability and charge exchange probability, and these were varied separately for low energy ( $p_\pi < 500$  MeV) and high energy ( $p_\pi > 500$  MeV). Data fits to pion-carbon data in these modes can be seen in Figures 4.39 and 4.40.

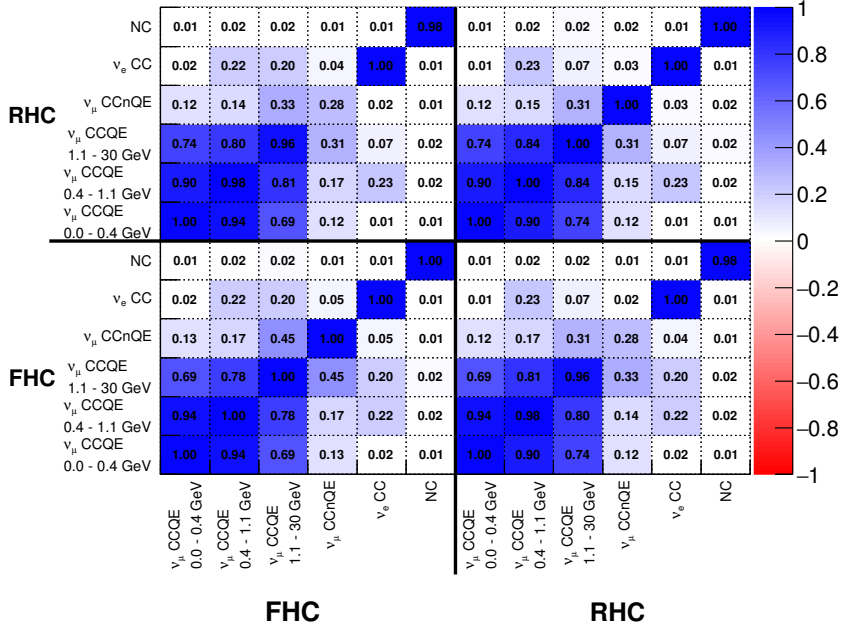


Figure 4.38: Correlations in the Super-K detector and FSI/SI errors. Absolute error sizes can be seen in Table 4.10. It should be observed that neutrino beam mode (FHC) and antineutrino beam mode (RHC) systematics are highly correlated with one another for CCQE-like and NC events.

Pion secondary interactions (SI) are modelled in a similar fashion, using the pion-nucleus interaction cross-sections but with the pion beginning outside the nucleus rather than inside as in FSI. SKDETSIM propagates the pion through Super-K simulating the possibility of a pion reinteraction. Since the same interaction probabilities are used, the secondary interaction and FSI systematics are evaluated simultaneously, and produce a single uncertainty matrix. Full details can be found in [113].

#### 4.6.2 Detector Efficiency Systematics

The Super-K detection efficiency systematics are evaluated using atmospheric neutrino data from the Super-K Run IV period, between October 20th 2008 and September 20th 2014. Atmospheric data is used regardless of T2K beam mode. The uncertainties are evaluated separately for each of the event selection cuts:

- Fiducial Volume (FV) selection.
- Ring Counting (RC).
- Outer detector (OD) activity.
- Particle identification (PID).

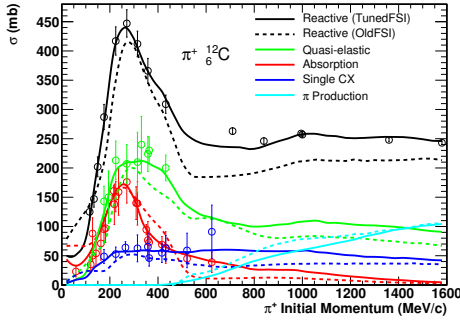


Figure 4.39:  $\pi^+$ -carbon scattering cross-sections used to tune FSI systematics. ‘Reactive’ here describes the inclusive interaction cross-section, and the plot contains both the prior distribution (OldFSI) and the fitted distribution (TunedFSI). Reproduced from [113].

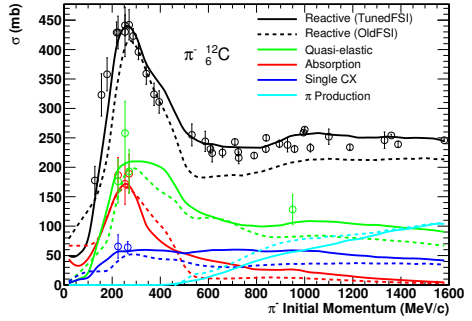


Figure 4.40:  $\pi^-$ -carbon scattering cross-sections used to tune FSI. ‘Reactive’ here describes the inclusive interaction cross-section, and the plot contains both the prior distribution (OldFSI) and the fitted distribution (TunedFSI). Reproduced from [113].

- Momentum cuts.
- Decay electron cuts.

Control samples are produced from the atmospheric data in each of the systematic bins without the cut being studied applied. The distribution of the variable being cut on is compared between data and Monte Carlo, and the difference treated as a  $1\sigma$  error. The cut is then varied by this amount and the effect on the number of events passing the full 1-ring muon selection is evaluated. The systematics from each of these effects are then combined to produce a single uncertainty for Super-K detector selection efficiency in each bin.

The OD cut and momentum cut have a negligible effect on the uncertainty. The decay electron and FV cuts yield an uncertainty of 1% each. The PID cuts add a 0.3% uncertainty on CC events and a 55% uncertainty on NC events due to a large uncertainty on the misidentification of the pion in  $\text{NC}1\pi^\pm$  events. The ring-counting cuts have an uncertainty of 1.84%, 2.21% and 3.25% for the CCQE-like bins, 8.1% for the CCnonQE bin and 21.8% for the NC bin [114].

#### 4.6.3 Super-K Energy Scale

The final Super-K systematic is a parameter controlling the absolute Super-Kamiokande reconstructed energy scale. While clearly a Super-K detector systematic, it is not correlated with the others and is thus fitted independently.

To evaluate the size of this systematic, four Super-K control samples are used which cover different energy ranges. A Gaussian is fitted to the energy distribution of each sample, and the difference between data and Monte Carlo peak positions is treated as the uncertainty [59]. The four samples are:

- Decay electrons from stopping cosmic muons provide an estimate of the low-energy uncertainty of  $0.7\pm0.2\%$ .
- NC atmospheric events with 2 rings and a reconstructed  $\pi^0$  invariant mass between 85 MeV and 185 MeV provide an estimated uncertainty of  $0.5\pm0.7\%$ .
- Cosmic stopping muons with a momentum between 200 MeV and 440 MeV provide an estimated uncertainty around the T2K beam energy of up to 2.4%.
- Cosmic stopping muons with momenta greater than 1 GeV provide an estimated uncertainty of up to 1.3% at higher energies.

The largest of these errors, from the lower energy cosmic stopping muon sample, is used as the absolute uncertainty size (2.4%). The Super-K  $E_{reco}$  binning of detector efficiencies and FSI listed in Section 4.6 apply to the initial  $E_{reco}$  values before the application of this systematic parameter. The Super-K energy scaling systematic is applied to binned data, assuming that events are distributed uniformly across each bin.

## Chapter 5

# Muon Antineutrino Disappearance Measurement

In 2014, T2K began collecting data in reverse horn current (RHC, or antineutrino) beam mode. This chapter describes the first oscillation analysis performed with that data. This dataset was collected in two run periods: Run 5, in May - June 2014 ( $0.506 \times 10^{20}$  RHC POT) and Run 6 from November 2014 - June 2015 ( $3.505 \times 10^{20}$  RHC POT) making a total POT of  $4.011 \times 10^{20}$ . The pattern of the accumulation of this POT can be seen in Figure 3.4.

Section 5.1 describes the hypothesis being tested, in which separate oscillation parameters ( $\sin^2 \overline{\theta_{23}}$  and  $|\Delta m_{32}^2|$ ) are fitted for antineutrinos. A likelihood ratio was used to fit the reconstructed energy spectrum for muon-like events in the T2K RHC sample, as described in Section 5.2. The predicted event rates and spectra are shown in Section 5.3. The effects of the systematic parameters are quantified in Section 5.4. Goodness-of-fit tests are described in Section 5.5 and the analysis is validated in Section 5.6.

The observed T2K data and best-fit spectra are presented in Section 5.9.1. Section 5.9.2 contains the results of the goodness-of-fit tests which indicate that the data is consistent with the hypothesis used.

Confidence regions were produced for the  $\sin^2 \overline{\theta_{23}}$  and  $|\Delta m_{32}^2|$  for the full Run 5 and 6 dataset. These contours are presented in Section 5.9.3. where they are also compared to T2K's neutrino-mode measurements as well as results from MINOS.

### 5.1 Hypothesis

In the past, T2K has performed precision measurements of  $\sin^2 \theta_{23}$  and  $|\Delta m_{32}^2|$  in a full three-flavour oscillation framework using a neutrino mode (FHC) beam [41]. The goal of this analysis is to provide the first T2K measurement of  $\overline{\nu_\mu}$  disappearance parameters

Parameter(s)	Fixed value in fits (NH)	Fixed value in fits (IH)
$\sin^2 \theta_{23}$	0.527	0.533
$\sin^2 \bar{\theta}_{13}$ and $\sin^2 \theta_{13}$	0.0248	0.0252
$\sin^2 \bar{\theta}_{12}$ and $\sin^2 \theta_{12}$	0.304	0.304
$ \Delta m_{32}^2 $ (NH only)	$2.51 \times 10^{-3}$ eV <sup>2</sup>	-
$ \Delta m_{31}^2 $ (IH only)	-	$2.48 \times 10^{-3}$ eV <sup>2</sup>
$\overline{\Delta m_{21}^2}$ and $\Delta m_{21}^2$	$7.53 \times 10^{-5}$ eV <sup>2</sup>	$7.53 \times 10^{-5}$ eV <sup>2</sup>
$\delta_{CP}$	-1.55	-1.56

Table 5.1: Values of oscillation parameters that are fixed in fits (NH = normal mass hierarchy, IH = inverted mass hierarchy). These are the results of the T2K Run1-4 oscillation fit performed with the reactor constraint [41], and used are for real data fits.

in an antineutrino beam, and to evaluate if there is any difference between the squared mass splittings and PMNS matrices as extrapolated from  $\nu_\mu$  and  $\overline{\nu}_\mu$  disappearance measurements. As such, we introduce an additional pair of parameters  $\sin^2 \overline{\theta}_{23}$  and  $|\Delta m_{32}^2|$  which takes the place of  $\sin^2 \theta_{23}$  and  $|\Delta m_{32}^2|$  in the calculation of oscillation probabilities for the beam  $\overline{\nu}_\mu$ ,  $\overline{\nu}_e$  and oscillated  $\overline{\nu}_e$  samples. It is these two parameters that this analysis measures. The other oscillation parameters use the same values for neutrino and antineutrino mixing.

For a  $\overline{\nu}_\mu$  disappearance study,  $\sin^2 \theta_{12}$ ,  $\sin^2 \theta_{13}$  and  $\Delta m_{12}^2$  have a small effect, and their values are well constrained by the experiments as described in Section 2.3.  $\delta_{CP}$  is not well constrained, but produces a negligible effect on a statistics-dominated  $\nu_\mu$  disappearance experiment. As a result, for the purposes of this analysis, these will be fixed at the values shown in Table 5.1. Since the effects of the mixing angles are as a rotation matrix, they only appear in the probability calculation in their trigonometric forms. Measurements of mixing are usually performed in terms of either  $\sin^2(\theta)$  or  $\sin^2(2\theta)$ . The double-angle version of the formula loses octant information, and is a natural choice for analyses performed using a two-flavour approximation since only these terms appear in equation 2.38. However, this analysis is performed using a full three flavour oscillation calculation and has some sensitivity to distinguish which octant the true value is in, so all mixing angles will be used in their single-angle ( $\sin^2 \theta$ ) form. The mass splitting parameter is often described as  $|\Delta m_{32}^2|$ , but this parameter is only used for the normal hierarchy (NH) fits. The inverted hierarchy fits instead use the parameter  $|\Delta m_{31}^2|$ , which differs from  $|\Delta m_{32}^2|$  by the value of  $\Delta m_{12}^2$ . As can be seen in Figure 2.4, this uses the second-largest mass-splitting each time, making the results for the two hierarchies more directly comparable.

## 5.2 Fit Method

For a given set of input parameter values, a prediction for the Super-Kamiokande 1-ring muon-like spectrum in reconstructed neutrino energy is calculated. This is carried out using Monte Carlo templates constructed from the outputs of the full Super-K simulation, reconstruction and data reduction chain.

The templates used for the prediction are binned in true neutrino energy ( $E_{true}$ ) and reconstructed neutrino energy  $E_{reco}$ . Oscillation probabilities are calculated and applied for each  $E_{true}$  bin, using the energy at the bin centre. For example, at T2K when a typical set of oscillation parameters are applied, the  $\overline{\nu}_\mu$  templates (described in Section 4.2.2) are weighted down by  $\overline{\nu}_\mu$  disappearance, while the oscillated  $\overline{\nu}_e$  templates are weighted up representing  $\overline{\nu}_e$  appearance.

The binning regime was selected to optimise T2K's sensitivity while ensuring a reasonable number of expected events per reconstructed bin. The spectrum is most finely binned near the beam energy peak (and oscillation maximum). The binning scheme in  $E_{true}$  has 84 bins total, and is as follows:

- 50 MeV bins from 0 to 0.3 GeV (6 bins).
- 25 MeV bins from 0.3 to 1 GeV (28 bins).
- 50 MeV bins from 1 GeV to 3 GeV (40 bins).
- 100 MeV bins from 3 GeV to 3.5 GeV (5 bins).
- One bin from 3.5 to 4 GeV.
- One bin from 4 to 5 GeV.
- One bin from 5 to 7 GeV.
- One bin from 7 to 10 GeV.
- One bin for events  $> 10$  GeV.

Oscillation probabilities for these bins are calculated at the bin centre. For this purpose, the last bin stops at 30 GeV. However, this bin is designed to also include any events generated above this energy, although no such events exist in the current SK MC production.

The  $E_{reco}$  binning scheme consists of 73 bins and is as follows:

- 50 MeV bins from 0 to 3 GeV (60 bins).
- 250 MeV bins from 3 GeV to 4 GeV (4 bins).

- 500 MeV bins from 4 GeV to 6 GeV (4 bins).
- 1000 MeV bins from 6 GeV to 10 GeV (4 bins).
- One bin for events  $> 10$  GeV.

The last bin is treated as having an upper limit at 30 GeV. An event being reconstructed above 30 GeV is extremely unlikely: in the approximately two million Monte Carlo events used for the analysis, there are two events reconstructed above 30 GeV. No such events exist in the data.

These bins are filled with the Monte Carlo described in Section 4.2, and weighted for the appropriate POT ( $4.011 \times 10^{20}$ ) using the normalisation factors in Table 4.2.

By summing over all of the interaction modes and all of the  $E_{true}$  bins, a predicted  $E_{reco}$  spectrum is produced for a given set of parameter values. The agreement between this prediction and the true data can thus be calculated and used for a likelihood fit. The expected number of events in a given Super-K reconstructed energy bin  $N_r^{exp}$  is given by:

$$N_r^{exp} = \sum_{m=\text{mode}} \sum_{t=\text{true}} \sum_{r'=\text{reco}} P_{m;t;\vec{p}}^{osc} T_{r;r';f_E} W_{m;r';t;\vec{f}} N_{m;r';t}^{exp} \quad (5.1)$$

Here,  $P_{m;t;\vec{p}}^{osc}$  represents the oscillation probability for mode  $m$  given a set of physics parameters  $\vec{p}$  and  $W_{m;r';t;\vec{f}}$  represents a bin weight calculated given the current values of systematic parameters ( $\vec{f}$ ).  $T_{r;r';f_E}$  represents a transfer matrix which migrates fractional events to neighbouring  $E_{reco}$  bins given the current value of the SK energy scale systematic  $f_E$ .  $N_{m;r';t}^{exp}$  is the number of events from the POT-weighted Monte Carlo prediction for mode  $m$ , reconstructed energy bin  $r'$  and true energy bin  $t$ . For the purposes of this, ‘mode’ refers to the 46 templates listed in Appendix A.

The three-flavour oscillation probability  $P$  is calculated using a bespoke piece of code, which calculates the oscillation probability in constant density matter. The diagonalisation of the matter matrix was implemented using the method of Cardano, as described by Kopp [115]. The accuracy of the probability calculation was verified against the Prob3++ library [116].

The matter density used is  $2.6 \text{ g cm}^{-3}$ , based on a geological survey of the T2K baseline [117]. For the  $\overset{(-)}{\nu_\mu}$  and non-oscillated  $\overset{(-)}{\nu_e}$  CC modes, the probabilities used are for particle survival. For the oscillated  $\overset{(-)}{\nu_e}$  modes, the probabilities calculated are for  $\overset{(-)}{\nu_\mu} \rightarrow \overset{(-)}{\nu_e}$ . No oscillations are applied to the NC modes.

Two different methods are used in order to eliminate the nuisance parameters allowing a final confidence region in terms of only  $\sin^2 \theta_{23}$  and  $|\Delta m_{32}^2|$ . The first is ‘profiling’ in which the likelihood is minimised with respect to all nuisance parameters,

and is described in Section 5.2.1. The second method is ‘marginalisation’, in which the likelihood is integrated over the possible values of the nuisance parameters according to their prior probability distributions. For continuity with published T2K neutrino-mode results, the profiled result will be considered the primary result of this thesis, with the marginalised results treated as a cross-check.

### 5.2.1 Profiled Systematics

In this analysis, the parameters being measured are  $\sin^2 \overline{\theta_{23}}$  and  $|\overline{\Delta m_{32}^2}|$ . The parameters  $\sin^2 \theta_{23}$  and  $|\Delta m_{32}^2|$  are applied to neutrinos only, while  $\sin \theta_{12}$ ,  $\sin \theta_{13}$ ,  $\Delta m_{12}^2$  and  $\delta_{CP}$  are applied as normal to both neutrinos and antineutrinos. These remain fixed at their values in Table 5.1. Applying an uncertainty to these parameters was demonstrated to have a negligible effect on the final contour size in this statistics-dominated analysis, and it was decided that the analysis use fixed values rather than an uncertainty based on measurements made with the standard three-flavour oscillation hypothesis. The 44 systematic parameters are treated as ‘nuisance’ parameters.

Given a spectrum for Super-K sample  $s$  with an expected number of events  $N_{r,s}^{exp}$  and an observed number of events  $N_{r,s}^{obs}$  in each reconstructed energy bin  $r$ , the likelihood ratio function that is minimised for a fit with profiled systematics is as follows:

$$\begin{aligned}\chi_{prof}^2 &= -2 \ln \mathcal{L}_{prof}(\sin^2 \overline{\theta_{23}}, |\overline{\Delta m_{32}^2}|, \vec{f}) \\ &= 2 \sum_s \sum_{r=0}^{N_s-1} \left( N_{r,s}^{obs} \cdot \ln \left( \frac{N_{r,s}^{obs}}{N_{r,s}^{exp}} \right) + N_{r,s}^{exp} - N_{r,s}^{obs} \right) + \chi_{penalty}^2(\vec{f})\end{aligned}\quad (5.2)$$

This likelihood ratio function is designed to be able to fit many Super-K samples simultaneously, but in this analysis only the RHC muon-like sample is used ( $N_s = 1$ ). The function tends to a  $\chi^2$  distribution when there are many events per bin, and will be referred to as  $\chi^2$  for the remainder of this document. The MIGRAD algorithm from the software package MINUIT is used to find the minimum of this function [106]. In the fit with profiled systematics, when the nuisance parameters are varied away from their central values, a penalty term is added to the likelihood in order to represent that these values are considered less likely.

Given a vector of current nuisance parameter values  $\vec{f}$ , a vector of central nuisance parameter values  $\vec{f}_0$  and a covariance matrix containing their uncertainties  $\mathbf{C}$ , this penalty term is as follows:

$$\chi_{penalty}^2(\vec{f}) = (\vec{f} - \vec{f}_0)^T \cdot \mathbf{C}^{-1} \cdot (\vec{f} - \vec{f}_0) \quad (5.3)$$

In the case of uncorrelated parameters with a central value ( $\mu_p$ ) and an uncer-

tainty ( $\sigma_p$ ), this would simplify to:

$$\chi^2_{penalty}(\vec{f}) = \sum_{p=\text{nuisance}} \left( \frac{f_p - \mu_p}{\sigma_p} \right)^2 \quad (5.4)$$

### 5.2.2 Marginalised Systematics

The alternative method used to eliminate the systematics is Bayesian marginalisation. In this method, the likelihood distribution is integrated over the prior distribution ( $\pi$ ) of the nuisance parameters. This integral is approximated by summing over 10000 toy experiments generated according to their prior parameter distribution.

$$\begin{aligned} \mathcal{L}_{marg}(\sin^2 \overline{\theta_{23}}, |\overline{\Delta m_{32}^2}|) &= \int_F \mathcal{L}(\sin^2 \overline{\theta_{23}}, |\overline{\Delta m_{32}^2}|, \vec{f}) \pi(\vec{f}) d\vec{f} \\ &\approx \sum_i^{10000} \mathcal{L}_i(\sin^2 \overline{\theta_{23}}, |\overline{\Delta m_{32}^2}|, \vec{f}_i) \pi(\vec{f}_i) \end{aligned} \quad (5.5)$$

The likelihood ratio function used for each evaluation is:

$$-2\mathcal{L}_i(\sin^2 \overline{\theta_{23}}, |\overline{\Delta m_{32}^2}|, \mathbf{f}_i) = 2 \sum_s \sum_{r=0}^{N_s-1} \left( N_{r,s}^{obs} \cdot \ln \left( \frac{N_{r,s}^{obs}}{N_{r,s}^{exp}} \right) + N_{r,s}^{exp} - N_{r,s}^{obs} \right) \quad (5.6)$$

Once again, we use the fact that this likelihood behaves like a  $\chi^2$  distribution:

$$\chi^2_{marg} = -2 \ln \mathcal{L}_{marg} \quad (5.7)$$

The prior used for each parameter is a Gaussian with the mean and  $1\sigma$  errors listed in Tables 4.4, 4.6 and 4.10. The 10000 toy experiments are generated by randomising all of the systematic parameters according to their priors. The random parameter variations are generated with correlations using the Cholesky decomposition [118] of the BANFF and Super-K covariance matrices. If any of the randomised systematic parameters lie outside of the physically allowed range for that parameter the toy experiment is discarded and another generated in its place.

## 5.3 Predicted Event Rates and Spectra

Tables 5.2 and 5.3 show the effects of the various tuning stages described in Chapter 4 on overall event rate, for the unoscillated and oscillated predictions. The effects of the flux tuning described in Section 4.1 on the expected spectrum can be seen in Figure 5.1. The flux tuning increases unoscillated event rate by approximately 4% and oscillated

event rate by approximately 10%.

The external MiniBooNE and MINER $\nu$ A data tune described in Section 4.3 reduces the expected event rate significantly, but the use of the T2K near-detector data fit described in Section 4.4 returns the spectrum to within 3% of the flux-tuned prediction. The effect of the near-detector tuning on the spectrum can be seen in Figure 5.2.

The final selected event rate predicted for the no-oscillation hypothesis is  $103.6 \pm 10.5$  (syst), while using the oscillation parameter values from Table 5.1, the expected numbers of events are  $34.58 \pm 3.59$  (normal) and  $35.21 \pm 3.65$  (inverted). The expected Super-K  $E_{\text{reco}}$  spectra without oscillation can be seen in Figures 5.3 and 5.4, with and without the near-detector tune respectively. Similar spectra with typical oscillations applied can be seen in Figures 5.5 and 5.6.

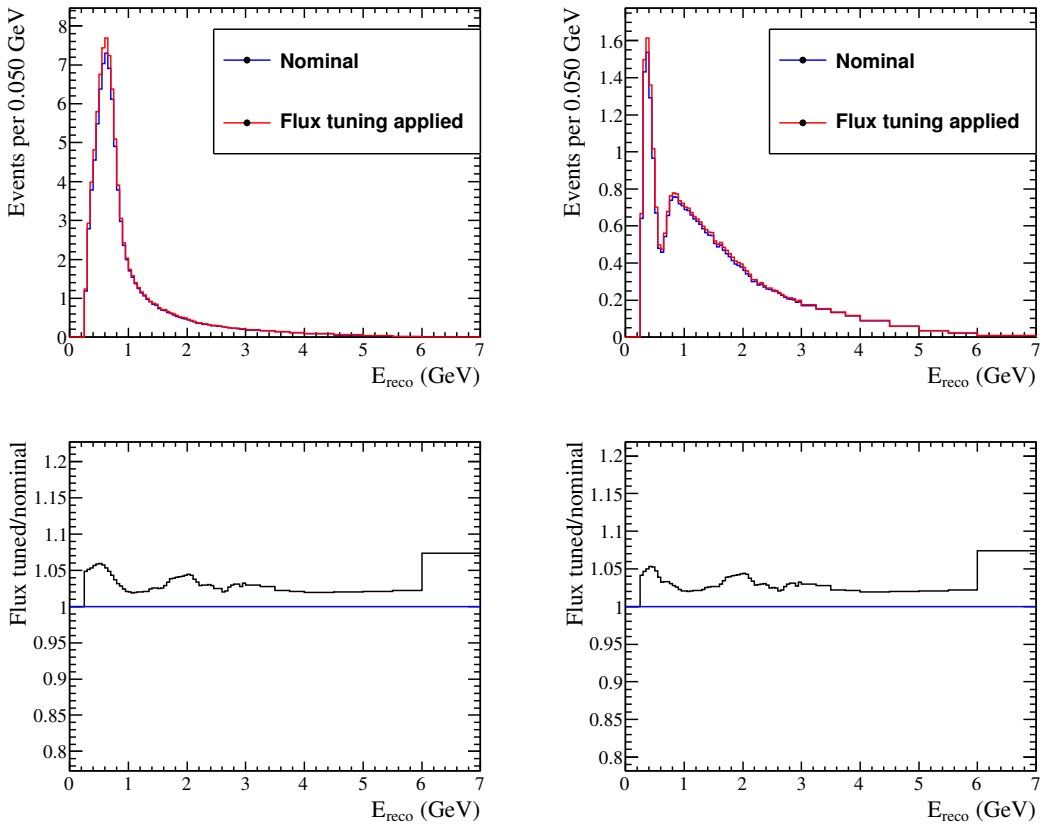


Figure 5.1: Top: Reconstructed-energy spectrum of 1  $\mu$ -like ring events, for an exposure of  $4.011 \times 10^{20}$  POT in antineutrino beam mode both with and without the effect of the flux tuning of the nominal MC templates. The spectra are shown both for no oscillations (left) and for oscillations assuming the normal hierarchy with the oscillation parameters shown in Table 5.1. Bottom: Ratio of flux-tuned spectrum to the nominal MC spectrum.

	Nominal MC	Flux-tuned MC	BANFF prefit MC (flux + CCQE tune)	BANFF postfit MC
Total	96.434	100.439	87.615	103.604
$\nu_\mu$ CCQE	14.186	14.493	14.250	15.405
$\nu_\mu$ CC $1\pi$	4.792	5.019	5.019	3.666
$\nu_\mu$ CC coherent	0.201	0.212	0.212	0.244
$\nu_\mu$ CC MEC	2.630	2.707	0.731	3.022
$\nu_\mu$ CC other	1.198	1.307	1.307	1.393
$\nu_\mu/\nu_\tau$ NC $1\pi^{+/-}$	0.495	0.523	0.523	0.340
$\nu_\mu/\nu_\tau$ NC $1\pi^0$	0.081	0.086	0.086	0.051
$\nu_\mu/\nu_\tau$ NC coherent	0.001	0.001	0.001	0.001
$\nu_\mu/\nu_\tau$ NC other	0.434	0.470	0.470	0.705
$\bar{\nu}_\mu$ CCQE	53.188	55.834	50.852	57.962
$\bar{\nu}_\mu$ CC $1\pi$	7.506	7.658	7.658	6.746
$\bar{\nu}_\mu$ CC coherent	2.409	2.515	2.515	3.082
$\bar{\nu}_\mu$ CC MEC	7.382	7.699	2.079	9.037
$\bar{\nu}_\mu$ CC other	0.914	0.891	0.891	1.005
$\bar{\nu}_\mu/\bar{\nu}_\tau$ NC $1\pi^{+/-}$	0.571	0.581	0.581	0.381
$\bar{\nu}_\mu/\bar{\nu}_\tau$ NC $1\pi^0$	0.081	0.082	0.082	0.048
$\bar{\nu}_\mu/\bar{\nu}_\tau$ NC coherent	0.006	0.006	0.006	0.007
$\bar{\nu}_\mu/\bar{\nu}_\tau$ NC other	0.265	0.260	0.260	0.410
$\nu_e$ CCQE	0.003	0.004	0.003	0.004
$\nu_e$ CC $1\pi$	0.003	0.003	0.003	0.003
$\nu_e$ CC coherent	0.000	0.000	0.000	0.000
$\nu_e$ CC MEC	0.001	0.001	0.000	0.001
$\nu_e$ CC other	0.001	0.001	0.001	0.001
$\nu_e$ NC $1\pi^{+/-}$	0.021	0.021	0.021	0.014
$\nu_e$ NC $1\pi^0$	0.003	0.004	0.004	0.002
$\nu_e$ NC coherent	0.000	0.000	0.000	0.000
$\nu_e$ NC other	0.022	0.022	0.022	0.035
$\bar{\nu}_e$ CCQE	0.005	0.005	0.004	0.005
$\bar{\nu}_e$ CC $1\pi$	0.002	0.002	0.002	0.002
$\bar{\nu}_e$ CC coherent	0.000	0.000	0.000	0.001
$\bar{\nu}_e$ CC MEC	0.001	0.001	0.000	0.001
$\bar{\nu}_e$ CC other	0.000	0.000	0.000	0.000
$\bar{\nu}_e$ NC $1\pi^{+/-}$	0.016	0.016	0.016	0.010
$\bar{\nu}_e$ NC $1\pi^0$	0.002	0.002	0.002	0.001
$\bar{\nu}_e$ NC coherent	0.000	0.000	0.000	0.000
$\bar{\nu}_e$ NC other	0.011	0.011	0.011	0.017

Table 5.2: Calculated predicted numbers of 1-ring  $\mu$ -like events in antineutrino beam mode without oscillations using the nominal MC templates, the NA61-tuned MC templates, the CCQE-tuned MC templates and the BANFF-tuned MC templates. The BANFF prefit column is the NA61 tuned data, with the CCQE samples reweighted according to the external data fits described in Section 4.3. The total numbers of events and the numbers of events from each mode considered in this analysis are shown. These numbers were calculated for an exposure of  $4.011 \times 10^{20}$  POT.

	$N_{SK}$ Nominal MC	$N_{SK}$ Flux-tuned MC	$N_{SK}$ BANFF prefit MC (flux + CCQE tune)	$N_{SK}$ BANFF postfit MC
Total	33.161	34.240	30.715	34.584
$\nu_\mu$ CCQE	6.269	6.525	6.447	6.871
$\nu_\mu$ CC $1\pi$	3.155	3.349	3.349	2.415
$\nu_\mu$ CC coherent	0.136	0.146	0.146	0.167
$\nu_\mu$ CC MEC	1.365	1.428	0.386	1.578
$\nu_\mu$ CC other	1.049	1.150	1.150	1.223
$\nu_\mu/\nu_\tau$ NC $1\pi^{+/-}$	0.495	0.523	0.523	0.340
$\nu_\mu/\nu_\tau$ NC $1\pi^0$	0.081	0.086	0.086	0.051
$\nu_\mu/\nu_\tau$ NC coherent	0.001	0.001	0.001	0.001
$\nu_\mu/\nu_\tau$ NC other	0.434	0.470	0.470	0.705
$\bar{\nu}_\mu$ CCQE	12.222	12.584	11.656	13.278
$\bar{\nu}_\mu$ CC $1\pi$	3.556	3.552	3.552	3.048
$\bar{\nu}_\mu$ CC coherent	0.565	0.574	0.574	0.697
$\bar{\nu}_\mu$ CC MEC	1.978	2.015	0.544	2.350
$\bar{\nu}_\mu$ CC other	0.805	0.782	0.782	0.881
$\bar{\nu}_\mu/\bar{\nu}_\tau$ NC $1\pi^{+/-}$	0.571	0.581	0.581	0.381
$\bar{\nu}_\mu/\bar{\nu}_\tau$ NC $1\pi^0$	0.081	0.082	0.082	0.048
$\bar{\nu}_\mu/\bar{\nu}_\tau$ NC coherent	0.006	0.006	0.006	0.007
$\bar{\nu}_\mu/\bar{\nu}_\tau$ NC other	0.265	0.260	0.260	0.410
$\nu_e$ CCQE	0.003	0.003	0.003	0.004
$\nu_e$ CC $1\pi$	0.003	0.003	0.003	0.003
$\nu_e$ CC coherent	0.000	0.000	0.000	0.000
$\nu_e$ CC MEC	0.001	0.001	0.000	0.001
$\nu_e$ CC other	0.001	0.001	0.001	0.001
$\nu_e$ NC $1\pi^{+/-}$	0.021	0.021	0.021	0.014
$\nu_e$ NC $1\pi^0$	0.003	0.004	0.004	0.002
$\nu_e$ NC coherent	0.000	0.000	0.000	0.000
$\nu_e$ NC other	0.022	0.022	0.022	0.035
Osc. $\nu_e$ CCQE	0.007	0.007	0.006	0.007
Osc. $\nu_e$ CC $1\pi$	0.003	0.003	0.003	0.003
Osc. $\nu_e$ CC coherent	0.000	0.000	0.000	0.000
Osc. $\nu_e$ CC MEC	0.001	0.001	0.000	0.001
Osc. $\nu_e$ CC other	0.000	0.000	0.000	0.000
$\bar{\nu}_e$ CCQE	0.005	0.005	0.004	0.005
$\bar{\nu}_e$ CC $1\pi$	0.002	0.002	0.002	0.002
$\bar{\nu}_e$ CC coherent	0.000	0.000	0.000	0.000
$\bar{\nu}_e$ CC MEC	0.001	0.001	0.000	0.001
$\bar{\nu}_e$ CC other	0.000	0.000	0.000	0.000
$\bar{\nu}_e$ NC $1\pi^{+/-}$	0.016	0.016	0.016	0.010
$\bar{\nu}_e$ NC $1\pi^0$	0.002	0.002	0.002	0.001
$\bar{\nu}_e$ NC coherent	0.000	0.000	0.000	0.000
$\bar{\nu}_e$ NC other	0.011	0.011	0.011	0.017
Osc. $\bar{\nu}_e$ CCQE	0.015	0.016	0.015	0.017
Osc. $\bar{\nu}_e$ CC $1\pi$	0.003	0.004	0.004	0.003
Osc. $\bar{\nu}_e$ CC coherent	0.001	0.001	0.001	0.002
Osc. $\bar{\nu}_e$ CC MEC	0.002	0.002	0.001	0.003
Osc. $\bar{\nu}_e$ CC other	0.000	0.000	0.000	0.000

Table 5.3: Calculated predicted numbers of 1-ring  $\mu$ -like events in antineutrino beam mode with oscillations using the nominal MC templates, the NA61-tuned MC templates, the CCQE-tuned MC templates and the BANFF-tuned MC templates. The BANFF prefit column is the NA61 tuned data, with the CCQE samples reweighted according to the external data fits described in Section 4.3. The total numbers of events and the numbers of events from each mode considered in this analysis are shown. The normal hierarchy was assumed, with oscillation parameters give the values listed in Table 5.1. These numbers were calculated for an exposure of  $4.011 \times 10^{20}$  POT.

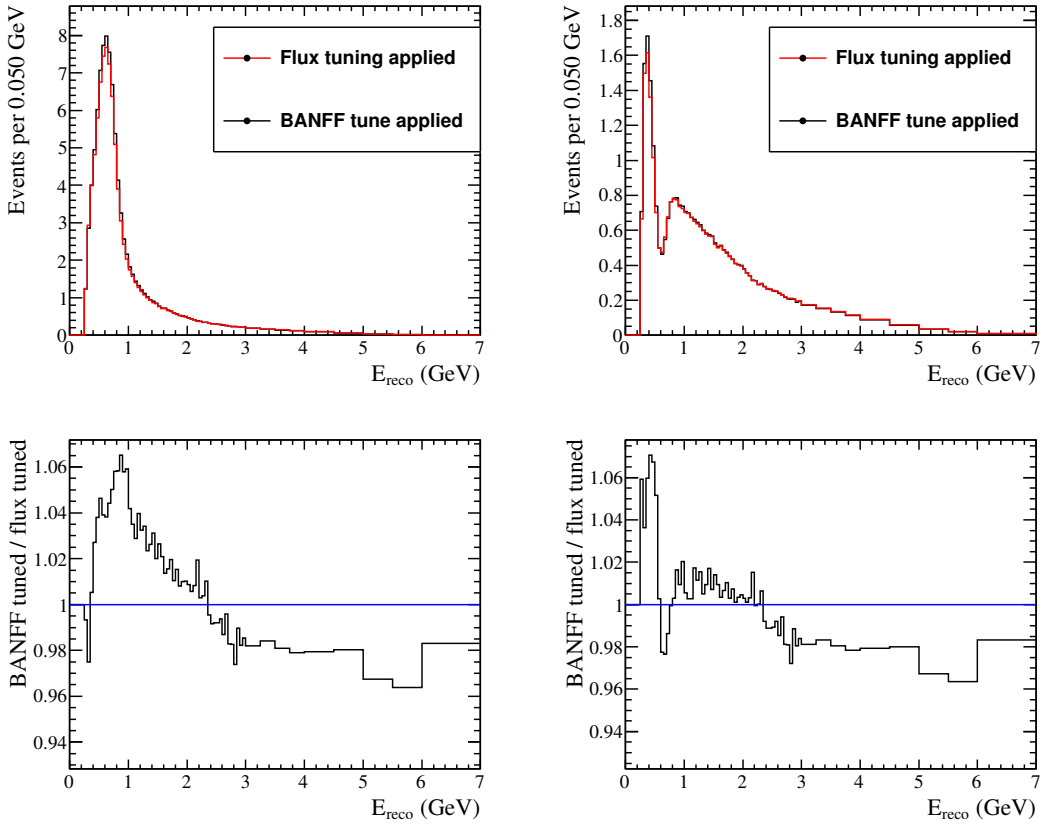


Figure 5.2: Top: Reconstructed-energy spectrum of 1  $\mu$ -like ring events, for an exposure of  $4.011 \times 10^{20}$  POT in antineutrino beam mode both with and without the effect of BANFF postfit tuning on the flux-tuned MC templates. The spectra are shown both for no oscillations (left) and for oscillations assuming the normal hierarchy, and the oscillation parameters shown in Table 5.1. Bottom: Ratio of BANFF-tuned spectrum to the flux-tuned spectrum.

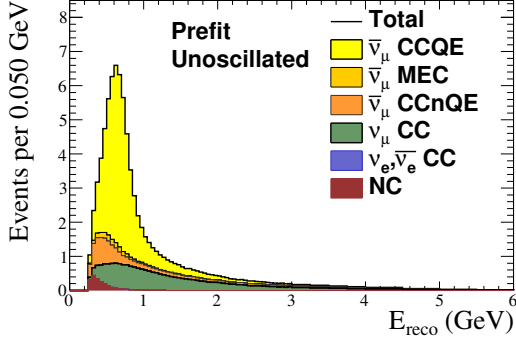


Figure 5.3: Predicted reconstructed-energy spectrum of  $1 \mu$ -like ring events, and contributions from various grouped true neutrino reaction modes, for no oscillations and for an exposure of  $4.011 \times 10^{20}$  POT in antineutrino beam mode. The spectrum was generated using the BANFF prefit MC templates.

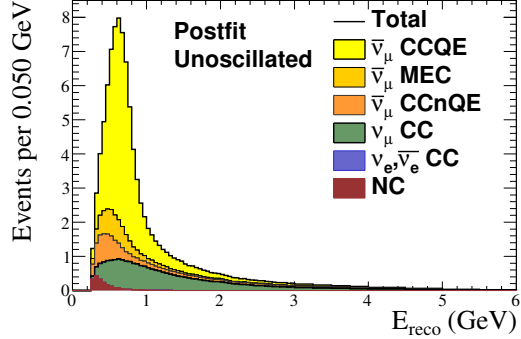


Figure 5.4: Predicted reconstructed-energy spectrum of  $1 \mu$ -like ring events, and contributions from various grouped true neutrino reaction modes, for no oscillations and for an exposure of  $4.011 \times 10^{20}$  POT in antineutrino beam mode. The spectrum was generated using the BANFF postfit-tuned MC templates.

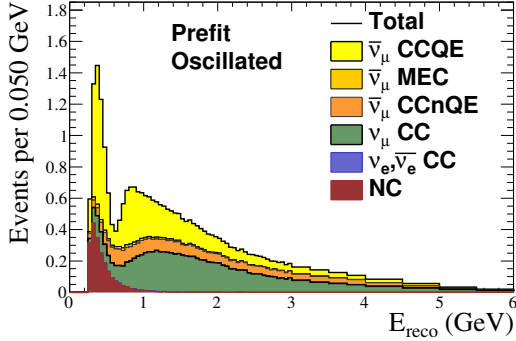


Figure 5.5: Predicted reconstructed-energy spectrum of  $1 \mu$ -like ring events, and contributions from various grouped true neutrino reaction modes, with oscillations for an exposure of  $4.011 \times 10^{20}$  POT in antineutrino beam mode. The spectrum was generated using the BANFF prefit MC templates. The spectrum shown was generated assuming the normal hierarchy, and the oscillation parameters shown in Table 5.1. Note that the vertical axis is zoomed in by a factor of more than 4 compared with Figure 5.3.

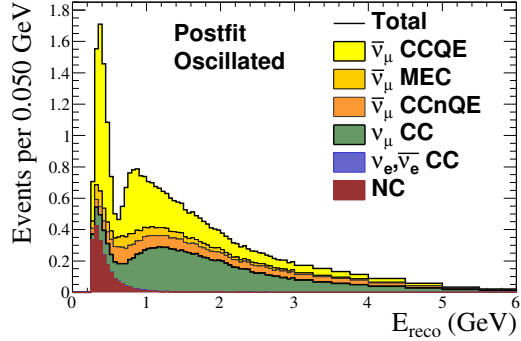


Figure 5.6: Predicted reconstructed-energy spectrum of  $1 \mu$ -like ring events, and contributions from various grouped true neutrino reaction modes, with oscillations for an exposure of  $4.011 \times 10^{20}$  POT in antineutrino beam mode. The spectrum was generated using the BANFF postfit-tuned MC templates. The spectrum shown was generated assuming the normal hierarchy, and the oscillation parameters shown in Table 5.1. Note that the vertical axis is zoomed in by a factor of more than 4 compared with Figure 5.4.

## 5.4 Effects of Systematics on the Spectrum

It is important to examine the effects of the 44 systematics described in Chapter 4 on the predicted  $\nu_\mu$ -like reconstructed energy spectrum at Super-K. These effects are shown both without oscillation and with oscillations applied assuming the normal mass hierarchy with the parameter values shown in Table 5.1. All results are generated for an integrated exposure of  $4.011 \times 10^{20}$  POT and tuned Monte Carlo templates are used.

The effects of systematic uncertainties on the predicted number of events are summarised in Table 5.4. In this table, systematic parameters are grouped into five categories and all parameter correlations are taken into account using the Cholesky decomposition [118] of the parameter covariance matrices. Percentage uncertainties are given both with and without the near detector constraint (BANFF) described in Section 4.4, described as ‘postfit’ and ‘prefit’. The effects of BANFF postfit errors from each individual systematic is shown in Table 5.5.

A number of representative error envelopes have been produced. These are the  $\pm 1\sigma$  spreads of each bin’s content over  $10^5$  toy Monte Carlo experiments generated with randomised systematic parameters. All correlations were taken into account. Figure 5.7 shows the combined effect of the BANFF tune and all systematics on the unoscillated  $E_{reco}$  spectrum’s error envelopes, while Figure 5.8 shows the same for the oscillated spectrum. The envelopes for the oscillated spectrum are shown as a ratio to their nominal value in order to demonstrate the relative size of the prefit and postfit uncertainties due to Super-K, flux and cross-section systematics respectively in Figures 5.9, 5.10 and 5.11. A similar envelope with all systematics included can be seen in Figure 5.12. It can be seen that the largest relative reduction in uncertainty is applied to the flux systematics, and that the reduction in relative error size does not vary significantly with the value of  $E_{reco}$ .

The individual effect of each systematic parameter on the best-fit values of  $\overline{\sin^2 \theta_{23}}$  and  $\overline{|\Delta m_{32}^2|}$  was quantified by generating the expected Super-K spectrum after applying a  $+1\sigma$  tweak of a single systematic parameter. This spectrum was fitted for  $\overline{\sin^2 \theta_{23}}$  and  $\overline{|\Delta m_{32}^2|}$  with all nuisance parameters fixed at their nominal values. The difference between the best-fit values of  $\overline{\sin^2 \theta_{23}}$  and  $\overline{|\Delta m_{32}^2|}$  for the tweaked toy experiment and those of an untweaked spectrum was taken as the  $+1\sigma$  effect of that systematic parameter on the oscillation parameters. Effects from a  $-1\sigma$  tweak were similarly evaluated. The study was repeated at 12 true points in the  $\overline{\sin^2 \theta_{23}} - \overline{|\Delta m_{32}^2|}$  plane, giving a total of 24 fits per systematic parameter.  $\overline{|\Delta m_{32}^2|}$  values of  $2.0 \times 10^{-3}$  eV<sup>2</sup>,  $2.5 \times 10^{-3}$  eV<sup>2</sup>, and  $3.0 \times 10^{-3}$  eV<sup>2</sup> were used with each of  $\overline{\sin^2 \theta_{23}} = 0.370, 0.500, 0.524, 0.650$ .

The results of these fits are used to produce an estimate of the size of the effect from each systematic, which are shown in Table 5.6 ordered by the size of effect on

$\sin^2 \overline{\theta_{23}}$ . To make this estimate, the systematic effect is compared with the statistical error for the specific values of  $\sin^2 \overline{\theta_{23}}$  and  $|\overline{\Delta m_{32}^2}|$ . For each systematic, the tables contain the largest observed effect on each of  $\sin^2 \overline{\theta_{23}}$  and  $|\overline{\Delta m_{32}^2}|$  from any of the 24 fits. These demonstrate the largest possible shift of the best-fit point by varying a parameter, and do not necessarily correspond to the marginal effect of the parameter at the edge of the contour, which can be expected to be small for a statistics-dominated analysis.

The largest uncertainty is the SuperK detector efficiency/FSI parameter for NC events. The uncertainty on this efficiency has a large effect on the oscillation parameters since the uncertainty itself is large (59.7% as listed in Table 4.10) and NC events constitute a significant fraction of the number of events near the oscillation maximum as shown in Figure 5.6. The second largest uncertainty is the MEC normalisation parameter on Oxygen. This has a large effect on the oscillation parameters since the uncertainty itself is large at 101% (as listed in Table 4.4), due to the fact that the ND280 data (with carbon as the signal target) does not constrain the uncertainty on the rate of MEC events on oxygen.

Source of uncertainty	$\delta N_{SK}/N_{SK}$ (Unoscillated)	$\delta N_{SK}/N_{SK}$ (Oscillated)
SuperK detector + FSI + SI	2.38%	4.23%
BANFF (prefit)	13.13%	13.04%
BANFF (postfit)	9.77%	9.47%
BANFF (Non-oxygen, postfit)	2.93%	2.95%
BANFF (Oxygen-specific postfit)	9.48%	9.12%
Total (BANFF prefit)	13.35%	13.71%
Total (BANFF postfit)	10.06%	10.37%

Table 5.4: Effect of  $1\sigma$  variations of the groups of systematics parameters on total number of 1-ring muon-like events in the reverse-horn current sample. The BANFF parameters considered to be oxygen-specific are Oxygen MEC normalisation, Fermi momentum, Binding energy, CC coherent normalisation and the  $\nu_e/\nu_\mu$  normalisation. The oscillation parameters used are those from Table 5.1.

Parameter	BANFF tuned +1 $\sigma$	BANFF tuned -1 $\sigma$	BANFF tuned +1 $\sigma$	BANFF tuned -1 $\sigma$
$f_{0;t,r}^{BANFF} RHC$	34.621	0.106 %	34.547	-0.106 %
$f_{1;t,r}^{BANFF} RHC$	34.630	0.132 %	34.538	-0.132 %
$f_{2;t,r}^{BANFF} RHC$	34.726	0.412 %	34.441	-0.412 %
$f_{3;t,r}^{BANFF} RHC$	34.829	0.708 %	34.339	-0.708 %
$f_{4;t,r}^{BANFF} RHC$	34.808	0.648 %	34.360	-0.648 %
$f_{5;t,r}^{BANFF} RHC$	34.728	0.417 %	34.440	-0.417 %
$f_{6;t,r}^{BANFF} RHC$	34.668	0.243 %	34.500	-0.243 %
$f_{7;t,r}^{BANFF} RHC$	34.602	0.051 %	34.566	-0.051 %
$f_{8;t,r}^{BANFF} RHC$	34.596	0.035 %	34.572	-0.035 %
$f_{9;t,r}^{BANFF} RHC$	34.812	0.659 %	34.356	-0.659 %
$f_{10;t,r}^{BANFF} RHC$	34.811	0.656 %	34.357	-0.656 %
$f_{11;t,r}^{BANFF} RHC$	34.785	0.581 %	34.383	-0.581 %
$f_{12;t,r}^{BANFF} RHC$	34.685	0.292 %	34.483	-0.292 %
$f_{13;t,r}^{BANFF} RHC$	34.697	0.326 %	34.471	-0.326 %
$f_{14;t,r}^{BANFF} RHC$	34.613	0.083 %	34.555	-0.083 %
$f_{15;t,r}^{BANFF} RHC$	34.590	0.018 %	34.578	-0.018 %
$f_{16;t,r}^{BANFF} RHC$	34.585	0.004 %	34.583	-0.004 %
$f_{17;t,r}^{BANFF} RHC$	34.586	0.005 %	34.582	-0.005 %
$f_{18;t,r}^{BANFF} RHC$	34.584	0.000 %	34.584	-0.000 %
$f_{19;t,r}^{BANFF} RHC$	34.584	0.000 %	34.584	-0.000 %
$f_{20;t,r}^{BANFF} RHC$	34.584	0.000 %	34.584	-0.000 %
$f_{21;t,r}^{BANFF} RHC$	34.584	0.001 %	34.584	-0.001 %
$f_{22;t,r}^{BANFF} RHC$	34.584	0.001 %	34.583	-0.001 %
$f_{23;t,r}^{BANFF} RHC$	34.584	0.002 %	34.583	-0.002 %
$f_{24;t,r}^{BANFF} RHC$	34.585	0.002 %	34.583	-0.002 %
$f_{Norm_{MEC}}^{BANFF} RHC$	38.456	11.196 %	30.712	-11.196 %
$f_{C_5^A}^{BANFF} RHC$	35.145	1.624 %	34.084	-1.446 %
$f_{B_{GRES}}^{BANFF} RHC$	34.943	1.039 %	34.268	-0.914 %
$f_{M_Q^A}^{BANFF} RHC$	35.021	1.264 %	34.149	-1.258 %
$f_{M_{RES}^A}^{BANFF} RHC$	34.925	0.987 %	34.270	-0.907 %
$f_{p_f}^{BANFF} RHC$	34.268	-0.915 %	34.896	0.903 %
$f_{Shape_{CC}^{Coh}}^{BANFF} RHC$	34.711	0.368 %	34.456	-0.368 %
$f_{E_B}^{BANFF} RHC$	34.591	0.020 %	34.578	-0.018 %
$f_{Norm_{CC}^{Coh}}^{BANFF} RHC$	35.366	2.260 %	33.802	-2.260 %
$f_{Norm_{NC}^{Coh}}^{BANFF} RHC$	34.586	0.007 %	34.581	-0.007 %
$f_{Norm_{NC}^{Other}}^{BANFF} RHC$	34.737	0.444 %	34.430	-0.444 %
$f_{Norm_{\nu_e \rightarrow \nu_\mu}}^{BANFF} RHC$	34.585	0.003 %	34.583	-0.003 %
$f_{E,r}^{SK} RHC$	34.584	0.000 %	34.584	0.000 %
$f_{0;t,r}^{SK+FSI} RHC$	34.631	0.137 %	34.536	-0.137 %
$f_{1;t,r}^{SK+FSI} RHC$	34.709	0.363 %	34.458	-0.363 %
$f_{2;t,r}^{SK+FSI} RHC$	34.802	0.630 %	34.366	-0.630 %
$f_{3;t,r}^{SK+FSI} RHC$	35.366	2.262 %	33.802	-2.262 %
$f_{4;t,r}^{SK+FSI} RHC$	34.638	0.156 %	34.530	-0.156 %
$f_{5;t,r}^{SK+FSI} RHC$	35.791	3.492 %	33.376	-3.492 %

Table 5.5:  $\pm 1\sigma$  effect of the systematic parameters on the total number of SuperK events in antineutrino beam mode, using  $4.011 \times 10^{20}$  POT, and the oscillation parameters in Table 5.1. The variations are shown both as the total event rate, and as a percentage change from the event rate with the systematic at its central value (34.584). The effects of these variations on  $E_{reco}$  spectrum shape can be seen in Appendix B.

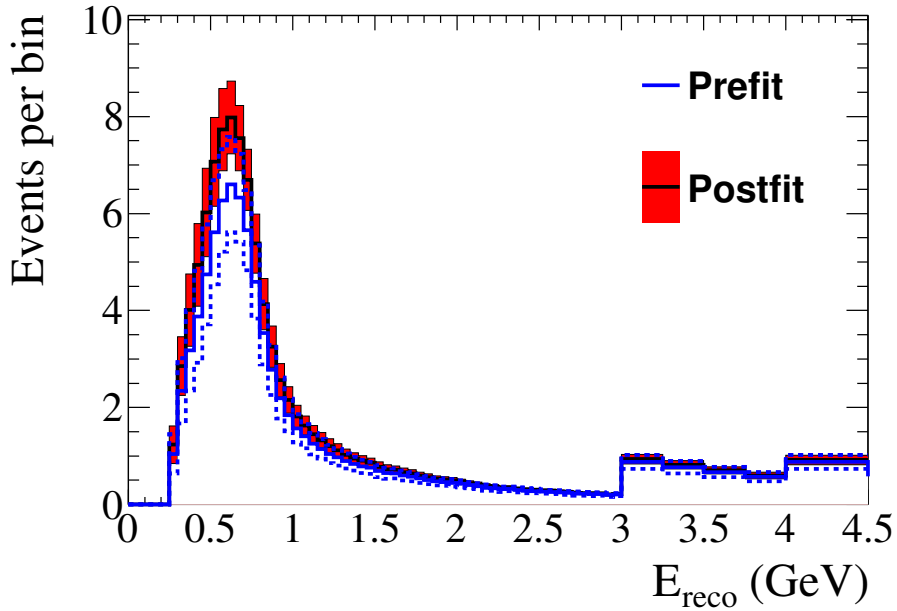


Figure 5.7: Error envelopes for the energy spectrum of selected RHC 1-ring muon-like events as a result of all systematic parameters. The ‘postfit’ envelope uses the ND280 constraint described in Section 4.4, while the ‘prefit’ envelope (blue dotted lines) does not. 100k toy MC experiments were generated with randomised systematic parameters and the  $1\sigma$  spread of bin contents was calculated. Correlations were taken into account. No oscillations were applied.

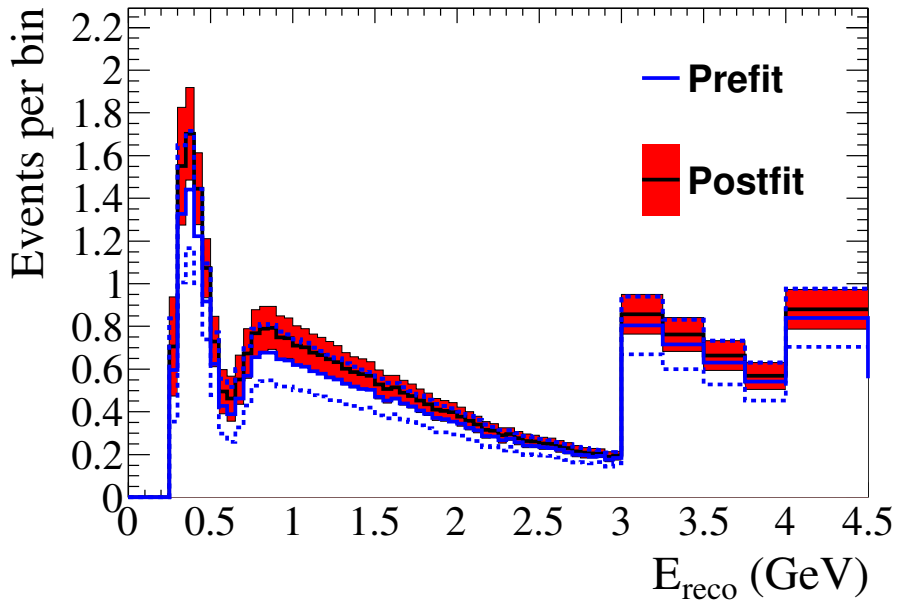


Figure 5.8: Error envelopes for the energy spectrum of selected RHC 1-ring muon-like events as a result of all systematic parameters. The ‘postfit’ envelope uses the ND280 constraint described in Section 4.4, while the ‘prefit’ envelope (blue dotted lines) does not. 100k toy MC experiments were generated with randomised systematic parameters and the  $1\sigma$  spread of bin contents was calculated. Correlations were taken into account. Oscillations were applied with the parameter values shown in Table 5.1.

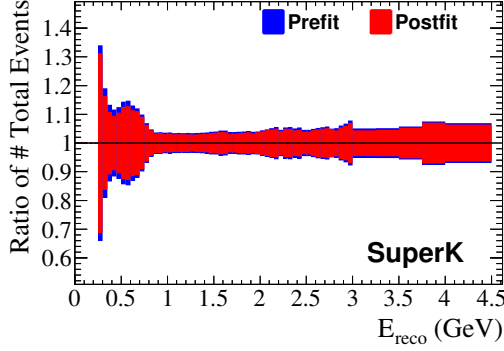


Figure 5.9: Antineutrino mode error envelopes, expressed as a fraction of event count, for the energy spectrum as a result of Super-K detector and FSI/SI systematics. 100k toy MC experiments were generated with randomised systematic parameters and the  $1\sigma$  spread of bin contents was calculated. Correlations were taken into account. Oscillations were applied with the parameter values shown in Table 5.1. The near-detector fit does not reduce the size of the uncertainties on these systematics, but the changes in the spectrum shape and composition lead to a small reduction in relative uncertainty.

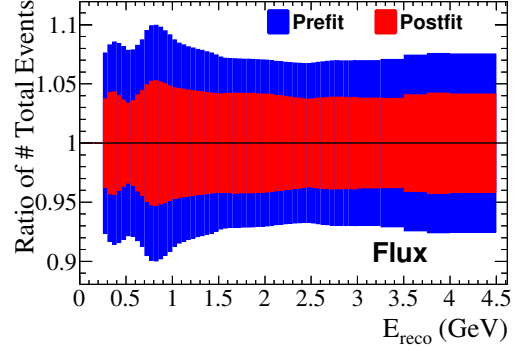


Figure 5.10: Antineutrino mode error envelopes, expressed as a fraction of event count, for the energy spectrum as a result of the BANFF flux systematics. 100k toy MC experiments were generated with randomised systematic parameters and the  $1\sigma$  spread of bin contents was calculated. Correlations were taken into account. Oscillations were applied with the parameter values shown in Table 5.1.

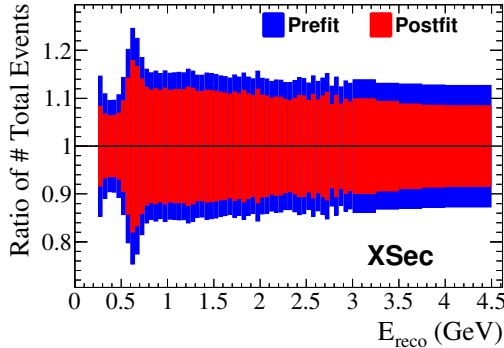


Figure 5.11: Antineutrino mode error envelopes, expressed as a fraction of event count, for the energy spectrum as a result of the BANFF cross-section systematics. 100k toy MC experiments were generated with randomised systematic parameters and the  $1\sigma$  spread of bin contents was calculated. Correlations were taken into account. Oscillations were applied with the parameter values shown in Table 5.1.

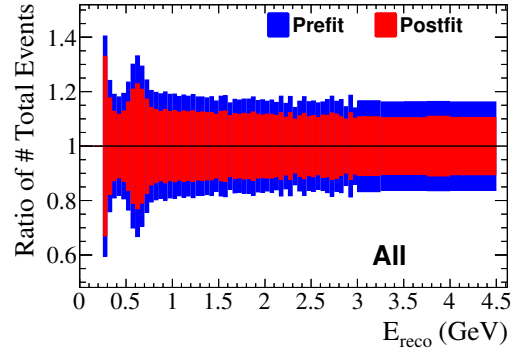


Figure 5.12: Antineutrino mode error envelopes, expressed as a fraction of event count, for the energy spectrum as a result of all systematics. 100k toy MC experiments were generated with randomised systematic parameters and the  $1\sigma$  spread of bin contents was calculated. Correlations were taken into account. Oscillations were applied with the parameter values shown in Table 5.1.

Parameter	$\frac{\delta_{syst} \sin^2 \theta_{23}}{\delta_{stat} \sin^2 \theta_{23}}$	$\frac{\delta_{syst}  \Delta m_{32}^2  (\text{eV}^2)}{\delta_{stat}  \Delta m_{32}^2  (\text{eV}^2)}$
SKDet + FSI/SI ; Ereco range 0.00 - 30.00 GeV; all NC	1.101	0.296
Meson exchange current normalisation for $^{16}\text{O}$	0.920	0.154
CC coherent for $^{16}\text{O}$ normalisation	0.517	0.034
$C_5^A$ nucleon to $\Delta$ transition axial form factor	0.439	0.034
SK energy scale; RHC	0.417	0.133
CCQE axial-mass scaling factor	0.416	0.032
NC other normalisation	0.367	0.039
RHC $\bar{\nu}_\mu$ flux normalisation, E = 0.7 - 1.0 GeV	0.347	0.066
Scale of isospin 1/2 nonresonant background	0.330	0.018
SKDet + FSI/SI ; Ereco range 0.00 - 30.00 GeV; $\bar{\nu}_\mu$ CCnQE	0.315	0.029
Resonance-production axial-mass scaling factor	0.250	0.016
RHC $\bar{\nu}_\mu$ flux normalisation, E = 0.0 - 0.4 GeV	0.242	0.026
SKDet + FSI/SI ; Ereco range 0.40 - 1.10 GeV; $\bar{\nu}_\mu$ CCQE	0.238	0.031
SKDet + FSI/SI ; Ereco range 0.00 - 30.00 GeV; $\bar{\nu}_e$ CC	0.224	0.012
RHC $\bar{\nu}_\mu$ flux normalisation, E = 1.0 - 1.5 GeV	0.210	0.021
Fermi momentum for $^{16}\text{O}$	0.202	0.034
RHC $\bar{\nu}_\mu$ flux normalisation, E = 0.4 - 0.5 GeV	0.201	0.039
RHC $\nu_\mu$ flux normalisation, E = 1.0 - 1.5 GeV	0.154	0.012
RHC $\bar{\nu}_\mu$ flux normalisation, E = 0.6 - 0.7 GeV	0.149	0.014
RHC $\bar{\nu}_\mu$ flux normalisation, E = 0.5 - 0.6 GeV	0.124	0.033
SKDet + FSI/SI ; Ereco range 1.10 - 30.00 GeV; $\bar{\nu}_\mu$ CCQE	0.122	0.008
SKDet + FSI/SI ; Ereco range 0.00 - 0.40 GeV; $\bar{\nu}_\mu$ CCQE	0.118	0.010
RHC $\nu_\mu$ flux normalisation, E = 0.7 - 1.0 GeV	0.118	0.008
RHC $\nu_\mu$ flux normalisation, E = 0.0 - 0.7 GeV	0.111	0.012
RHC $\nu_\mu$ flux normalisation, E = 1.5 - 2.5 GeV	0.110	0.009
CC other shape	0.095	0.005
RHC $\bar{\nu}_\mu$ flux normalisation, E = 3.5 - 5.0 GeV	0.087	0.003
RHC $\bar{\nu}_\mu$ flux normalisation, E = 1.5 - 2.5 GeV	0.071	0.008
RHC $\nu_\mu$ flux normalisation, E = 2.5 - 30.0 GeV	0.070	0.007
Binding energy for $^{16}\text{O}$	0.067	0.011
RHC $\bar{\nu}_\mu$ flux normalisation, E = 2.5 - 3.5 GeV	0.064	0.002
NC coherent normalisation	0.020	0.000
RHC $\bar{\nu}_\mu$ flux normalisation, E = 5.0 - 7.0 GeV	0.016	0.001
RHC $\bar{\nu}_\mu$ flux normalisation, E = 7.0 - 30.0 GeV	0.009	0.000
CC $\nu_e$ normalisation	0.008	0.000
RHC $\nu_e$ flux normalisation, E = 2.5 - 30.0 GeV	0.006	0.000
RHC $\nu_e$ flux normalisation, E = 0.0 - 2.5 GeV	0.004	0.000
RHC $\bar{\nu}_e$ flux normalisation, E = 4.0 - 30.0 GeV	0.003	0.000
RHC $\bar{\nu}_e$ flux normalisation, E = 2.5 - 4.0 GeV	0.002	0.000
RHC $\bar{\nu}_e$ flux normalisation, E = 1.5 - 2.5 GeV	0.001	0.000
RHC $\bar{\nu}_e$ flux normalisation, E = 0.8 - 1.5 GeV	0.000	0.000
RHC $\bar{\nu}_e$ flux normalisation, E = 0.0 - 0.5 GeV	0.000	0.000
RHC $\bar{\nu}_e$ flux normalisation, E = 0.5 - 0.7 GeV	0.000	0.000
RHC $\bar{\nu}_e$ flux normalisation, E = 0.7 - 0.8 GeV	0.000	0.000

Table 5.6: Maximum deviations, as a fraction of statistical error at the oscillation parameter grid point, from the input values of fits for only  $\sin^2 \theta_{23}$  and  $|\Delta m_{32}^2|$  to datasets with  $\pm 1$  sigma individual systematic variations at a range of 23-sector oscillation points.  $|\Delta m_{32}^2|$  values of  $2.0 \times 10^{-3}$  eV $^2$ ,  $2.5 \times 10^{-3}$  eV $^2$ , and  $3.0 \times 10^{-3}$  eV $^2$  are used with each of  $\sin^2 \theta_{23} = 0.370$ , 0.500, 0.524, 0.650. All other oscillation parameters are fixed at the values in Table 5.1. These maximum deviations usually occur at maximum disappearance, where the statistical error is smaller, as explained in Section 5.6. The values are sorted by the size of the deviation in  $\sin^2 \theta_{23}$ .

## 5.5 Method for Goodness-of-fit Tests

When fitting data to a model, it is important not just to extract the parameter values that offer the best agreement, but to consider how well the model and data agree. The binned likelihood ratio function shown in Equation 5.2 tends to a  $\chi^2$  distribution as the number of events increases, so it can be used as a goodness-of-fit test[119]. A very coarse binning scheme in  $E_{reco}$  is used to ensure that there are approximately four or more expected events in each bin; this scheme has 5 bins from 0-0.4, 0.4-0.7, 0.7-1.0, 1.0-2.0 and  $> 2.0$  GeV. The  $E_{true}$  binning is the same as described in Section 5.2. The expected spectrum using this binning can be seen in Figure 5.13. 1000 toy experiments are generated for each mass hierarchy, with both statistical fluctuations and systematics thrown according to their priors. All 44 systematic parameters are profiled in the fits to these toy datasets. The fraction of fits for which  $\chi^2_{toy} > \chi^2_{data}$  is used as a representative P-value. Additionally, the resulting  $\chi^2$  distribution can be fitted varying the number of degrees of freedom, demonstrating that the fit is working as intended.

## 5.6 Validation of the Oscillation Fitter

Validation of the fitting software was performed using ensembles of 5000 toy Monte Carlo datasets, created to mimic real results of the experiment. Statistical fluctuations were applied, and the true values of the systematic parameters were thrown according to their Gaussian prior, with correlations calculated using the Cholesky decomposition of the covariance matrix.

Toy ensembles were generated for each of the normal and inverted mass hierarchies, and for both the original expected POT for this analysis ( $2.5 \times 10^{20}$ ) and the T2K final goal POT ( $7.8 \times 10^{21}$ ). For the purposes of calculating pulls, the MINUIT best-fit point and HESSE error were calculated for each dataset. Nine sets of oscillation parameters are used: the combinations of  $\sin^2 \overline{\theta_{23}} = 0.35$ ,  $\sin^2 \overline{\theta_{23}} = 0.527$  and  $\sin^2 \overline{\theta_{23}} = 0.65$ , and  $|\Delta m_{32}^2| = 2.2$ ,  $|\Delta m_{32}^2| = 2.5$  and  $|\Delta m_{32}^2| = 2.8 \times 10^{-3}$  eV $^2$ . All other oscillation parameters are fixed at their values in Table 5.7.

For each toy experiment  $i$  and parameter  $f$  with true value  $x_{f,i,true}$ , fitted value  $x_{f,i,fitted}$  and HESSE uncertainty  $\sigma_{f,i,Hesse}$ , the pull  $P_{f,i}$  is calculated according the following formula:

$$P_{f,i} = \frac{x_{f,i,fitted} - x_{f,i,true}}{\sigma_{f,i,Hesse}} \quad (5.8)$$

For a parameter behaving as a Gaussian in the fit, the mean of the pull over many toys should be 0, and the RMS should be 1.

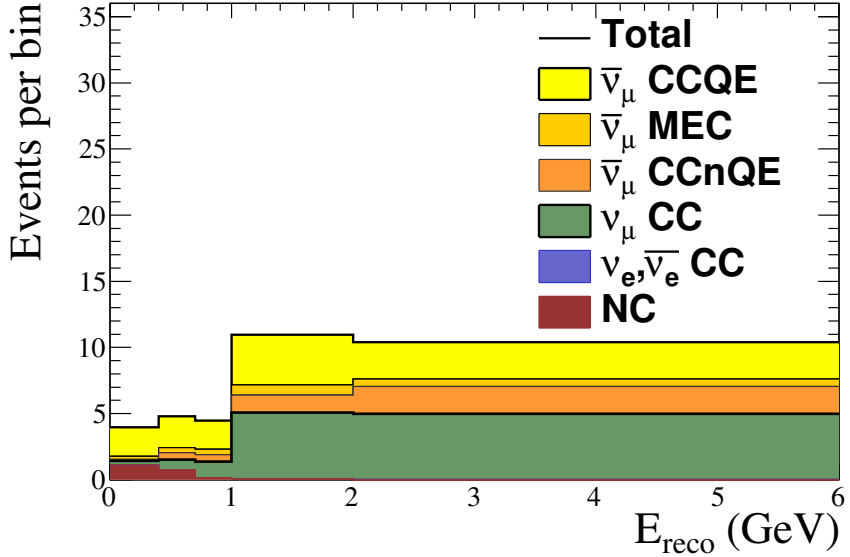


Figure 5.13: Predicted reconstructed-energy spectrum of 1  $\mu$ -like ring events, using ND280 postfit systematic values and using the goodness-of-fit binning, for an exposure of  $4.011 \times 10^{20}$  POT in antineutrino beam mode. Event counts are shown as total per bin, without accounting for bin width. Oscillations are applied at the values from Table 5.1. Note that the highest bin here, from 2.0 GeV onwards, contains all events with energies greater than 2.0 GeV.

Parameter(s)	Fixed value in fits (NH)	Fixed value in fits (IH)
$\sin^2 \theta_{23}$	0.524	0.534
$\sin^2 \bar{\theta}_{13}$ and $\sin^2 \theta_{13}$	0.0422	0.0491
$\sin^2 \bar{\theta}_{12}$ and $\sin^2 \theta_{12}$	0.304	0.304
$ \Delta m_{32}^2 $ (NH only)	$2.51 \times 10^{-3}$ eV $^2$	-
$ \Delta m_{31}^2 $ (IH only)	-	$2.49 \times 10^{-3}$ eV $^2$
$\overline{\Delta m_{21}^2}$ and $\Delta m_{21}^2$	$7.53 \times 10^{-5}$ eV $^2$	$7.53 \times 10^{-5}$ eV $^2$
$\delta_{CP}$	1.91	1.01

Table 5.7: Values of oscillation parameters that are fixed in validation fits (NH = normal mass hierarchy, IH = inverted mass hierarchy). These are the results of the T2K Run1-4 oscillation fit performed without the reactor constraint [41], and are used for certain validation plots. These validations were performed before the decision to use the reactor-constrained measurements in Table 5.7, and are computationally expensive to repeat.

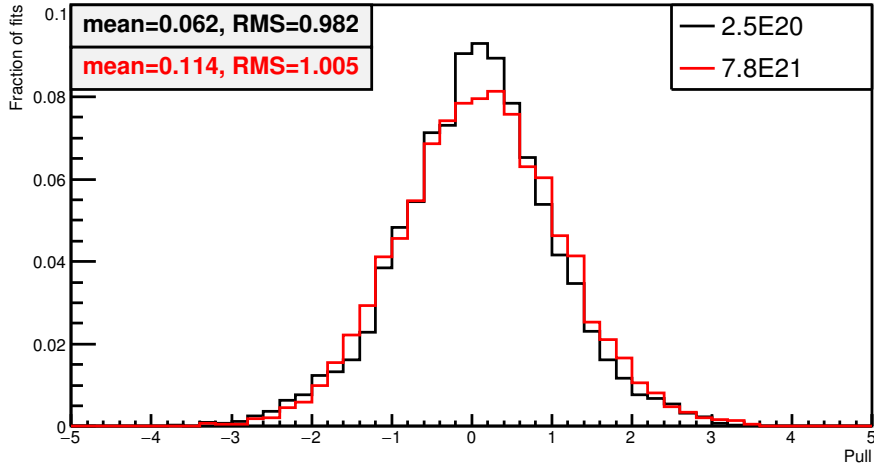


Figure 5.14: Distributions of the pulls of  $|\overline{\Delta m^2_{32}}|$  from 5k toy MC experiments generated at  $\sin^2 \overline{\theta_{23}} = 0.527$  and  $|\overline{\Delta m^2_{32}}| = 2.51 \times 10^{-3}$  eV $^2$ , including statistical fluctuations and randomised systematics. The other parameters are fixed at their values in Table 5.1, and the normal mass hierarchy is assumed. Distributions are shown for both  $2.5 \times 10^{20}$  and  $7.8 \times 10^{21}$  POT.

### 5.6.1 Oscillation Parameter Biases

$|\overline{\Delta m^2_{32}}|$  behaves mostly as desired, as can be seen in Figure 5.14, although a small bias of approximately 0.1 sigma can be seen at high POT due to the effect of the energy scale systematic discussed in the next section. In  $\sin^2 \overline{\theta_{23}}$ , we see a bias towards maximum disappearance. This is due to the presence of the physical boundary of the disappearance probability at 1, as described in Section 2.2.6. If the number of events has a statistical fluctuation down in the oscillation region, the number of events can be below the number expected with maximum disappearance. All datasets in which this happens will get the same best-fit point in  $\sin^2 \overline{\theta_{23}}$ , leading to a spike in the pull distribution.

This effect (and its reduction with increased statistics) can be seen in Figure 5.15 with a true  $\sin^2 \overline{\theta_{23}}$  value at maximum disappearance, leading to a large spike at 0. Figure 5.16 shows the best-fit value distribution for a true value of  $\sin^2 \overline{\theta_{23}} = 0.35$ , with a similar but smaller spike at maximum disappearance for the lower statistics fits, and no obvious spike in the high statistics fits. The pull distribution this leads to can be seen in Figure 5.17.

### 5.6.2 Systematic Parameter Biases

A check was also made of the pull distributions of the systematic parameters using two different methods to select random values of the parameters. In both methods, the true systematic parameter values were thrown according to a Gaussian with their

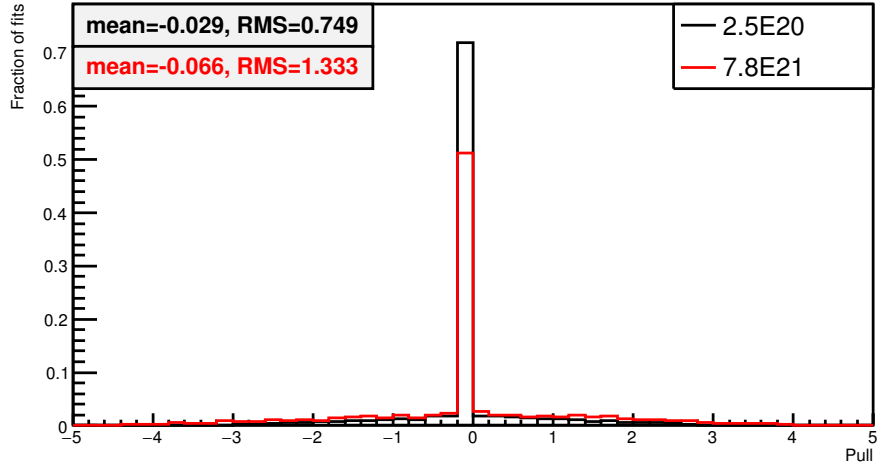


Figure 5.15: Distributions of the pulls of  $\sin^2 \bar{\theta}_{23}$  from 5k toy MC experiments generated at  $\sin^2 \bar{\theta}_{23} = 0.527$  and  $|\Delta m_{32}^2| = 2.51 \times 10^{-3} \text{ eV}^2$ , including statistical fluctuations and randomised systematics. The other parameters are fixed at their values in Table 5.1, and the normal mass hierarchy is assumed. Distributions are shown for both  $2.5 \times 10^{20}$  and  $7.8 \times 10^{21}$  POT.

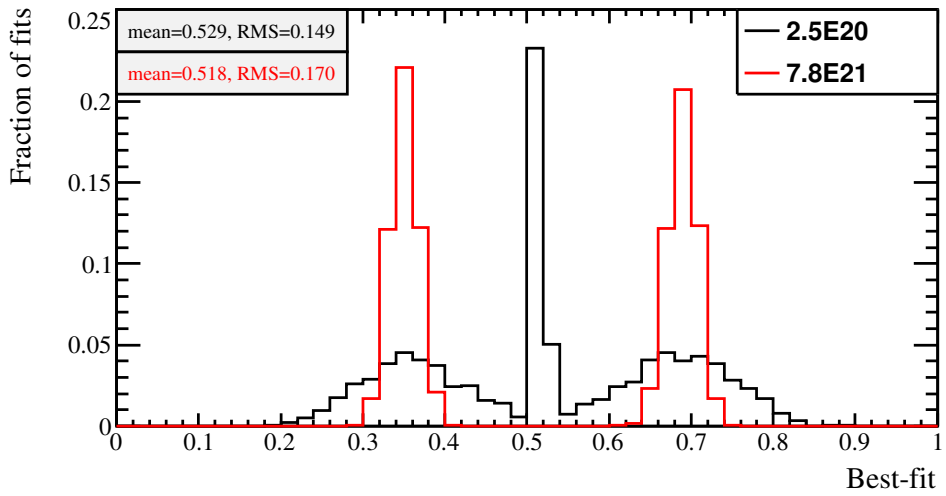


Figure 5.16: Distributions of the best-fit values of  $\sin^2 \bar{\theta}_{23}$  from 5k toy MC experiments generated at  $\sin^2 \bar{\theta}_{23} = 0.35$  and  $|\Delta m_{32}^2| = 2.51 \times 10^{-3} \text{ eV}^2$ , including statistical fluctuations and randomised systematics. The other parameters are fixed at their values in Table 5.1, and the normal mass hierarchy is assumed. Distributions are shown for both  $2.5 \times 10^{20}$  and  $7.8 \times 10^{21}$  POT.

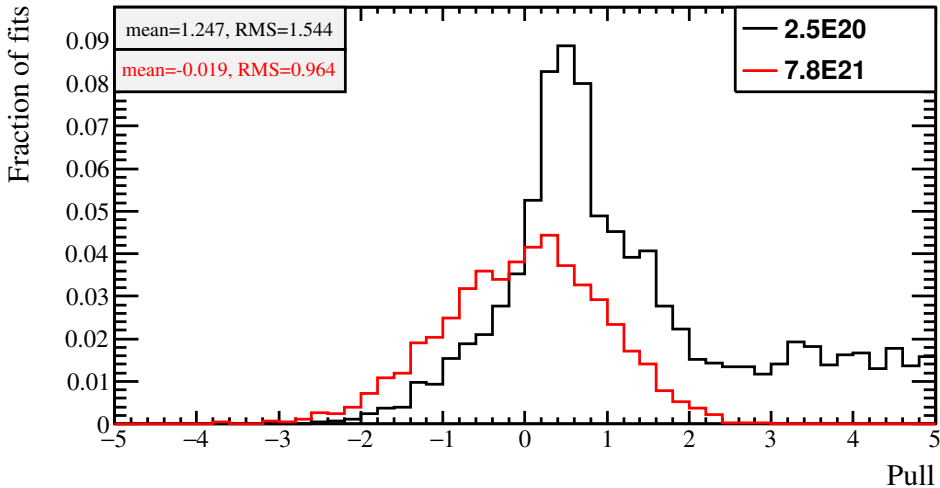


Figure 5.17: Distributions of the pulls of  $\sin^2 \overline{\theta_{23}}$  from 5k toy MC experiments generated at  $\overline{\sin^2 \theta_{23}} = 0.35$  and  $|\Delta m_{32}^2| = 2.51 \times 10^{-3}$  eV<sup>2</sup>, including statistical fluctuations and randomised systematics. The other parameters are fixed at their values in Table 5.1, and the normal mass hierarchy is assumed. Distributions are shown for both  $2.5 \times 10^{20}$  and  $7.8 \times 10^{21}$  POT.

central value as mean, and their input uncertainty as sigma. In the first study, throws of systematic parameters were allowed to vary outside their physical limits, leading to a full Gaussian distribution of thrown values. For the second method, parameters were restricted to their allowed values, and all parameters were rethrown if any extracted value was outside these limits. Thus the throw distribution formed a truncated Gaussian.

The physical limits imposed are a lower limit of zero for all normalisations,  $C_5^A$ ,  $M_A^{QE}$  and  $M_A^{RES}$ . Two additional limits are applied; the Fermi momentum of Oxygen is constrained to the range 200 MeV - 275 MeV, while binding energy has limits at 12 MeV and 42 MeV due to NEUT validity [86].

A summary of the mean and RMS of pulls from the unrestricted fits can be seen in Figures 5.18 and 5.19 for the normal and inverted hierarchy respectively. No problems were identified with the fitter, which performed as expected, and there are only small deviations from the expected mean of 0 and RMS of 1.

Pulls for the restricted fits can be seen in Figure 5.20 and 5.21 for the normal and inverted hierarchy respectively. These pulls are Gaussian with mean 1 and RMS 0 for most systematic parameters, but show small differences from this for a few parameters. Pull distributions for these parameters can be seen in Figure 5.22. The differences from a Gaussian with mean 0 and RMS 1 for these parameters are understood:

- **Super-K energy scale ( $f_{E;r}^{SK}$ )**. This systematic is different from the others in that it migrates events from bin to bin instead of increasing or decreasing the numbers of events in the bins of reconstructed energy. Its pull is not expected

to be a Gaussian with zero mean since a positive tweak of this parameter has a different effect on the spectrum shape than a negative tweak. This leads to a different shaped  $\chi^2$  for values of the parameter above and below zero, preventing the expected Gaussian behaviour. The differing distributions also increase the chance of the minimum  $\chi^2$  existing at the zero point, which contributes to a small spike in the number of fits with this best-fit point. An example of this discontinuity can be seen in Figure 5.23.

- **Fermi Momentum** ( $f_{P_f}^{banff}$ ). This systematic has a limit between 200 MeV and 275 MeV due to NEUT validity. The unconstrained parameter value is 225 MeV and the  $1\sigma$  error is 31 MeV. Consequently, the parameter has physical limits at around -1 and  $+2\sigma$ . The fitter cannot reach the true values when the parameter is thrown beyond these limits. The asymmetry of the allowed region around the central value results in a small downward bias in the pulls.
- **MEC Normalisation** ( $f_{Norm_{MEC}}^{banff}$ ). The MEC normalisation on  $^{16}\text{O}$  has a nominal value of 1.0 and a prefit error of 73.3%. This means that some unrestricted throws of this parameter are  $< 0$ , which is unphysical. Hence, the restricted throws have a Gaussian distribution that is truncated at its lower end. The throw values that are truncated are the lowest values, and these would be expected to have positive pulls due to the penalty term pulling them towards the nominal value. This leads to a pull distribution that is narrower on the plus side than on the minus side.
- **CC Coherent Normalisation** ( $f_{Norm_{CCcoh}}^{banff}$ ). The CC coherent normalisation has a nominal value of 1.0 and a prefit error of 100%. This means that some unrestricted throws of this parameter are  $< 0$ , which is unphysical. Hence, the restricted throws have a Gaussian distribution that is truncated at its lower end. The throw values that are truncated are the lowest values, and these would be expected to have positive pulls due to the penalty term pulling them towards the nominal value. This leads to a pull distribution that is narrower on the plus side than on the minus side.
- **Super-K Detector + FSI + SI Parameter 6 - all NC events** ( $f_{5;t;r}^{SK+FSI}$ ). The bias in this parameter comes from a statistical effect combined with the limit of the fitted normalisation at zero. When Poisson fluctuations are made of the bin contents of the  $E_{reco}$  distributions, a downward fluctuation is more likely than an upward fluctuation. For example, a Poisson distribution with mean 3 has  $P(1) = 0.149$  and  $P(2) = 0.224$ , whereas  $P(4) = 0.168$  and  $P(5) = 0.101$ . The NC events are mainly around the oscillation maximum where there are few events,

and downward Poisson fluctuations are more likely than upward ones. Fitting these downward fluctuations involves moving this parameter down from zero, and this explains the negative bias in its pull.

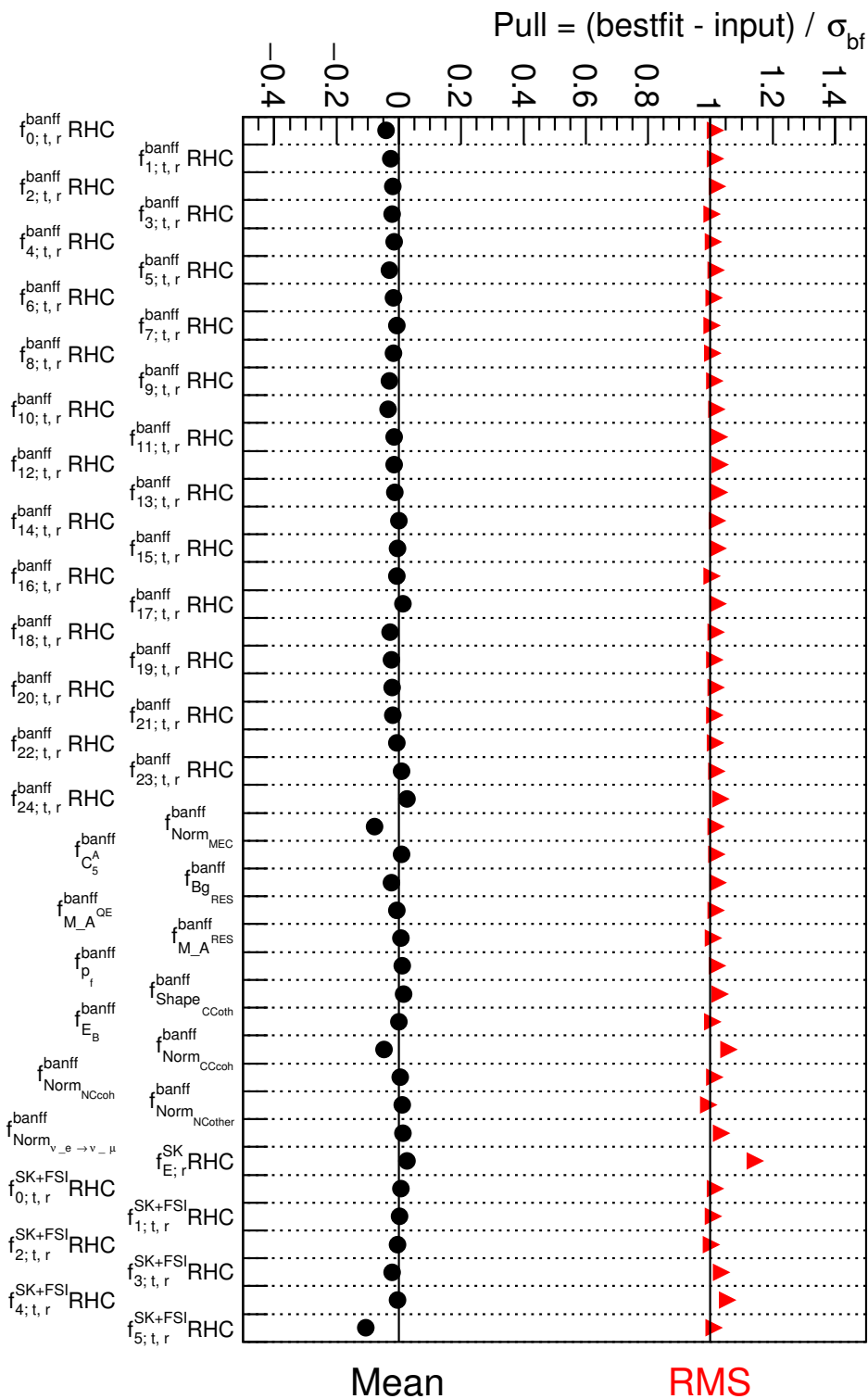


Figure 5.18: Summary of systematic pull distributions for all systematic parameters for 5k toy MC experiments at  $2.5 \times 10^{20}$  POT including statistical fluctuations and with randomised systematic parameters. Black circles show the mean of the pull, while red triangles show the RMS. Throws of systematic parameters were allowed to be thrown outside the physical region.  $|\Delta m_{32}^2|$  and  $\sin^2 \theta_{23}$  were fitted. All other oscillation parameters were fixed at their values from Table 5.7. The normal mass hierarchy is assumed.

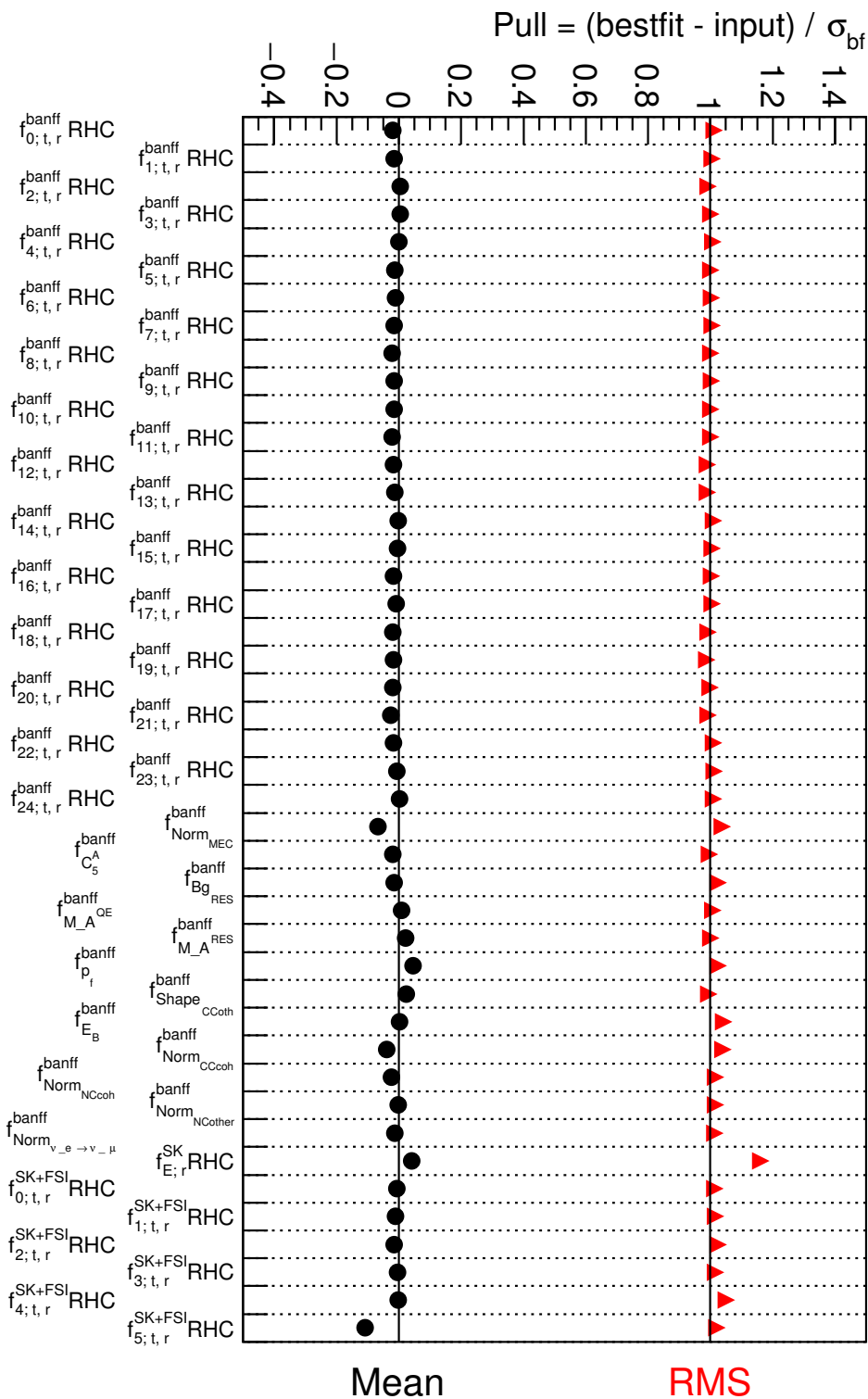


Figure 5.19: Summary of systematic pull distributions for all systematic parameters for 5k toy MC experiments at  $2.5 \times 10^{20}$  POT including statistical fluctuations and with randomised systematic parameters. Black circles show the mean of the pull, while red triangles show the RMS. Throws of systematic parameters were allowed to be thrown outside the physical region.  $|\Delta m_{32}^2|$  and  $\sin^2 \theta_{23}$  were fitted. All other oscillation parameters were fixed at their values from Table 5.7. The inverted mass hierarchy is assumed.

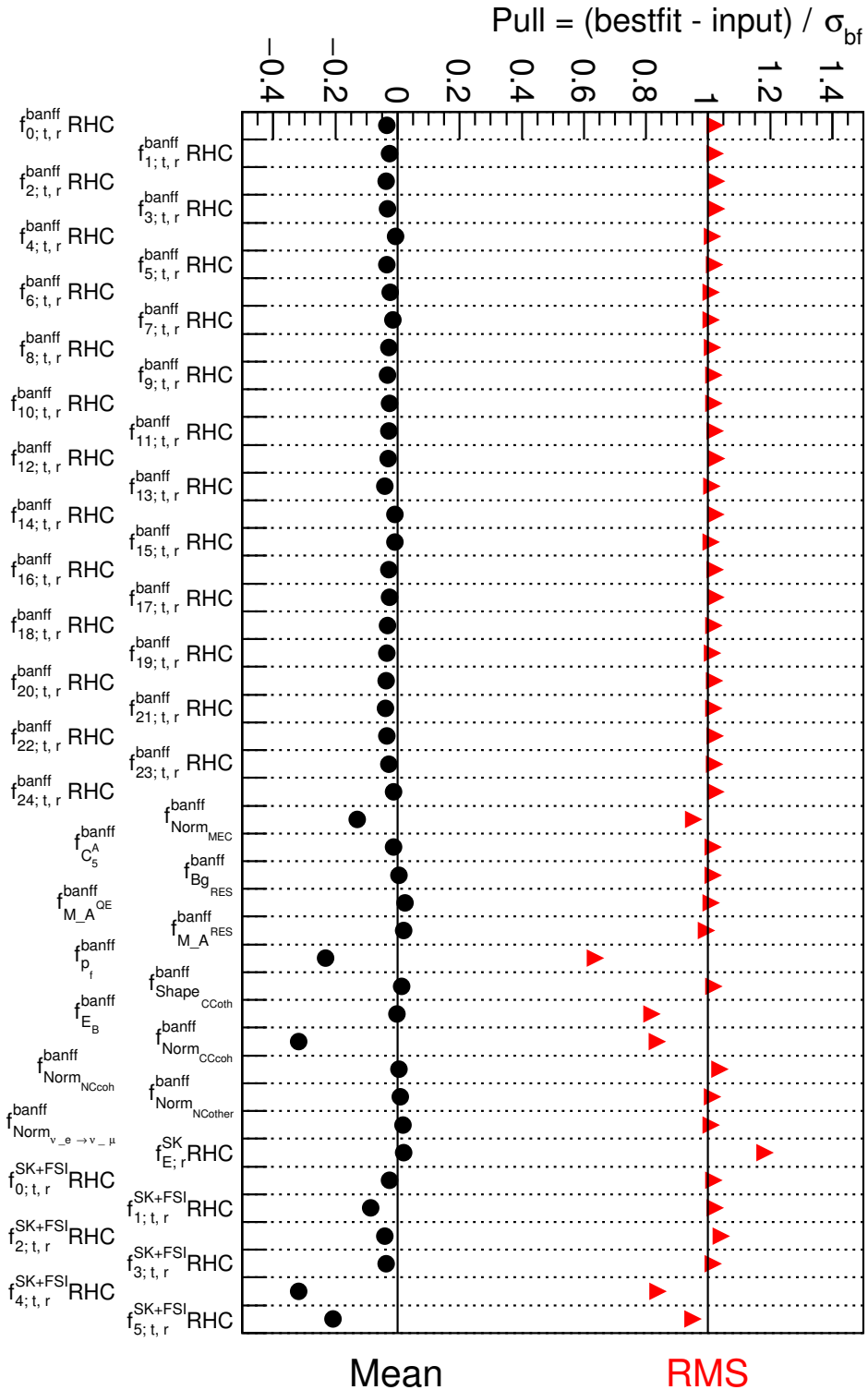


Figure 5.20: Summary of systematic pull distributions for all systematic parameters for 5k toy MC experiments at  $2.5 \times 10^{20}$  POT including statistical fluctuations and with randomised systematic parameters. Black circles show the mean of the pull, while red triangles show the RMS. Systematic parameters were rethrown if an unphysical thrown value was obtained.  $|\Delta m_{32}^2|$  and  $\sin^2 \theta_{23}$  were fitted. All other oscillation parameters were fixed at their values from Table 5.7. The normal mass hierarchy is assumed.

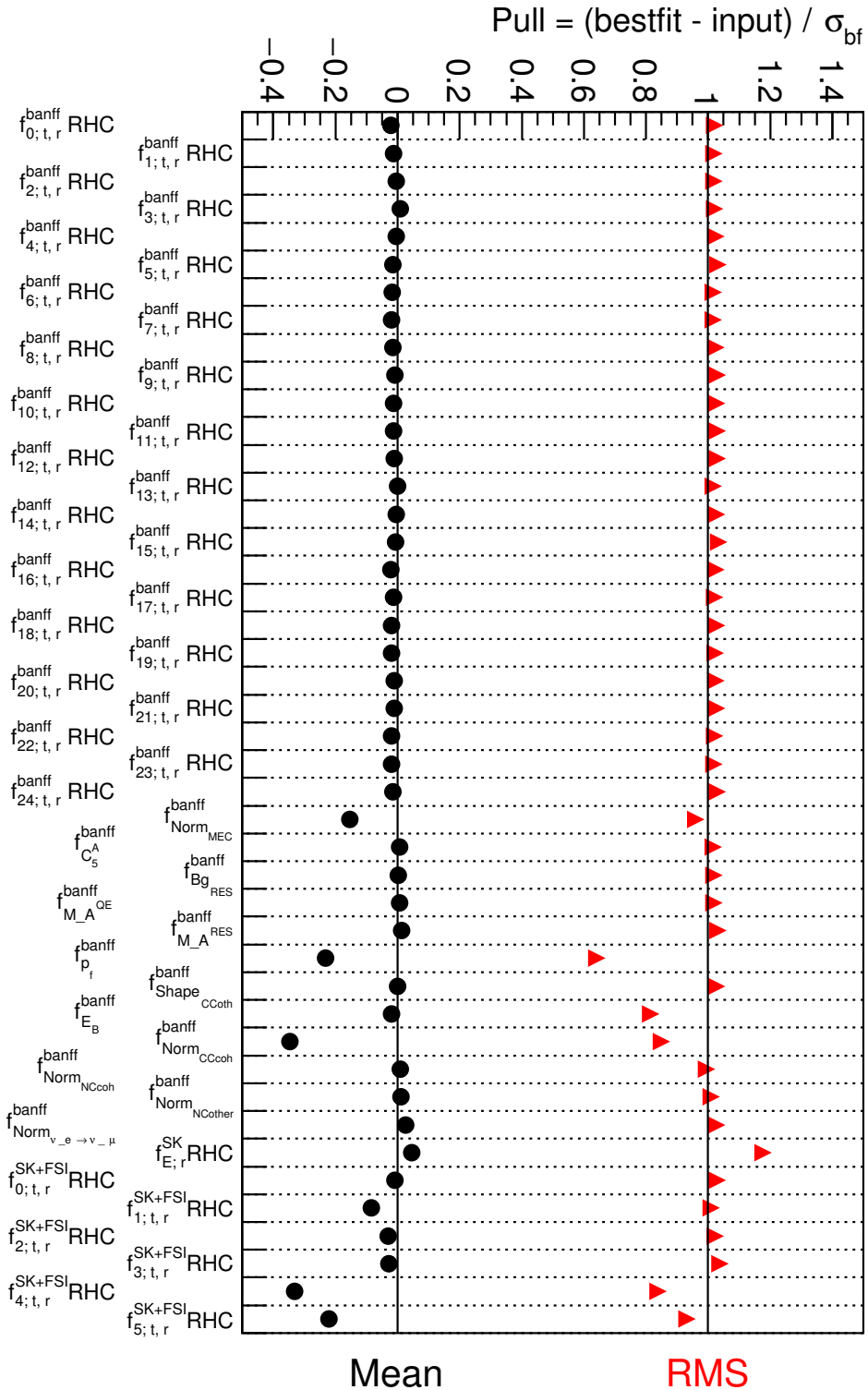


Figure 5.21: Summary of systematic pull distributions for all systematic parameters for 5k toy MC experiments at  $2.5 \times 10^{20}$  POT including statistical fluctuations and with randomised systematic parameters. Black circles show the mean of the pull, while red triangles show the RMS. Systematic parameters were rethrown if an unphysical thrown value was obtained.  $|\Delta m_{32}^2|$  and  $\sin^2 \theta_{23}$  were fitted. All other oscillation parameters were fixed at their values from Table 5.7. The inverted mass hierarchy is assumed.

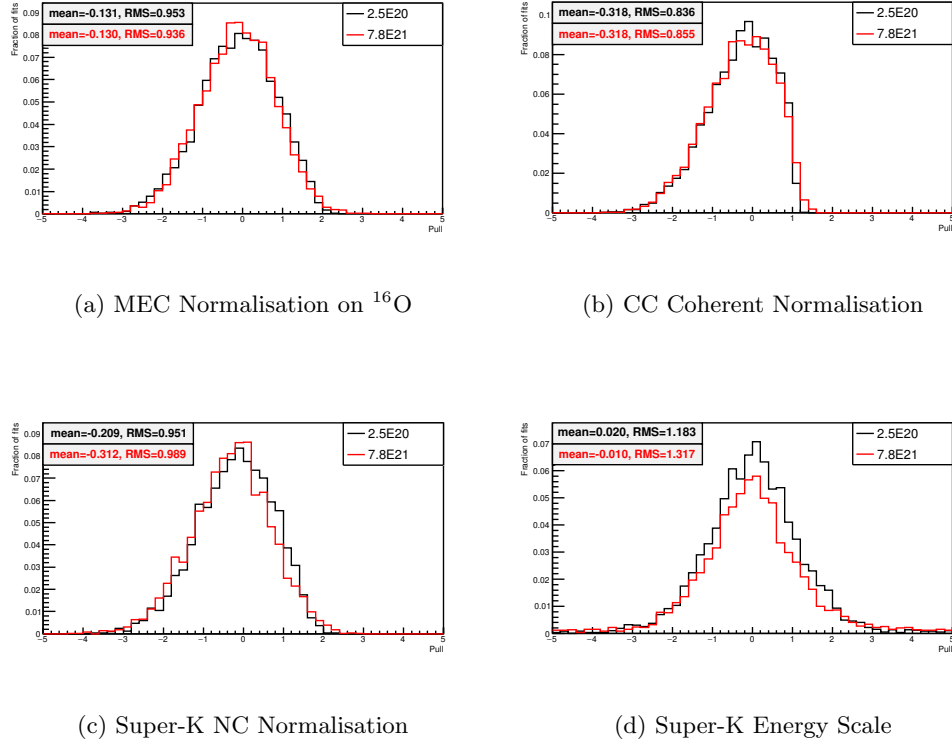


Figure 5.22: Distributions of pulls for four systematic parameters that have small biases. These distributions are shown for both  $2.5 \times 10^{20}$  POT (Runs 5 and 6, black histograms) and  $7.8 \times 10^{21}$  POT (the T2K ultimate goal).

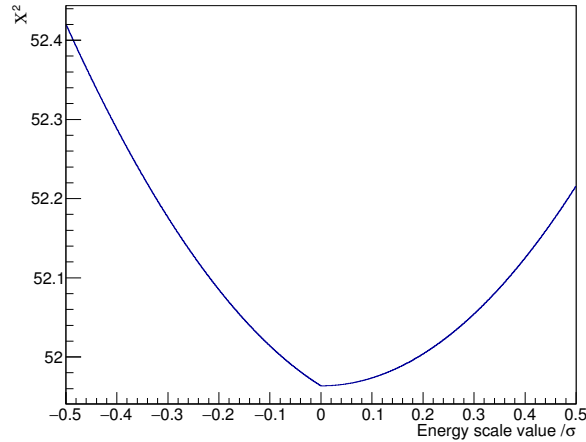


Figure 5.23: The chi-square distribution when varying Super-K energy scale for a single randomised toy experiment. Note that the distribution is different on the two sides of the zero point, leading to a kink in the plot at zero. In the vast majority of datasets, this kink is imperceptible; the toy plotted here was selected specifically from our validation toys as a clear demonstration of the effect.

## 5.7 Method for Construction of Confidence Regions

In order to produce confidence regions, the ‘constant- $\Delta\chi^2$ ’ method is used. First, the data is fitted with both the parameters of interest and the nuisance parameters free, in order to find the unbinned best-fit point (using MINUIT [106]), which has a  $\chi^2$  of  $\chi_{min}^2$ . After this, the parameter space in the parameters of interest is binned, and the fit is re-run with these parameters fixed at the values in that bin, and the nuisance parameters left free. For each fit, MINUIT is run twice, first in the upper octant in mixing angle (starting at  $\sin^2\overline{\theta_{23}} = 0.6$ ) and then in the lower octant (starting at  $\sin^2\overline{\theta_{23}} = 0.4$ ). The lower  $\chi^2$  of these two fits is used.

For this analysis, 201 bins were used in each of  $\sin^2\overline{\theta_{23}}$  and  $|\overline{\Delta m_{32}^2}|$ , requiring 40401 independent fits. The limits used were  $0 < \sin^2\overline{\theta_{23}} < 1$  and  $0.0002 \text{ eV}^2 < |\overline{\Delta m_{32}^2}| < 0.02 \text{ eV}^2$ . This information is summarised in Table 5.8. By performing the fit with the physics parameters of interest fixed at the grid point and the nuisance parameters free, a value for  $\chi_{i,j}^2$  can be calculated, which is dependent on the two parameters of interest, but has had the nuisance parameters profiled out. The value  $\Delta\chi^2$  is then calculated at each point  $(i,j)$  in the parameter space:

$$\Delta\chi_{i,j}^2 = \chi_{i,j}^2 - \chi_{min}^2 \quad (5.9)$$

Reference values  $\Delta\chi_{crit}^2$  are then used to define the edge of the contour for a region of given confidence level. Any point in the  $\sin^2\overline{\theta_{23}} - |\overline{\Delta m_{32}^2}|$  plane for which  $\Delta\chi_{i,j}^2 < \Delta\chi_{crit}^2$  is considered to be inside the confidence region. The  $\Delta\chi_{crit}^2$  values used are shown in Table 5.9.

## 5.8 Expected Sensitivity

Sensitivities were calculated for the oscillation analysis using the so-called ‘Asimov dataset’ [120]. A more traditional method of calculating the expected sensitivity of an experiment involves the production and fitting of many toy experiments, requiring a

	$\sin^2\overline{\theta_{23}}$	$ \overline{\Delta m_{32}^2} $
Number of Bins	201	201
Min Value	0	$2 \times 10^{-4} \text{ eV}^2$
Max Value	1	$2 \times 10^{-2} \text{ eV}^2$
Step Value	0.005	$9.9 \times 10^{-5} \text{ eV}^2$

Table 5.8: The binning used for the calculation of confidence regions. Note that the minimum and maximum value quoted are the centres of the first and last bin - the points at which the likelihood for those bins is evaluated.

	$N_P = 1$	$N_P = 2$	$N_P = 3$
68.3% confidence	1.00	2.30	3.53
90.0% confidence	2.71	4.61	6.25
99.7% confidence	9.00	11.83	15.16

Table 5.9: The critical values  $\Delta\chi^2_{crit}$  used for construction of confidence regions using the constant- $\Delta\chi^2$  method for a contour with  $N_P$  free parameters [44].

great deal of processing. In order to avoid such a computationally expensive method, we use the Asimov dataset as a substitute.

The Asimov dataset is selected as the single ‘most representative’ dataset, allowing a median sensitivity to be calculated without fitting large numbers of toys. In this analysis, the Asimov dataset is the expected Super-K  $E_{reco}$  spectrum with all parameters at their prior central values, and without any statistical fluctuations applied. Figure 5.24 shows the expected sensitivity for the Asimov dataset using the prior oscillation values from Table 5.1.

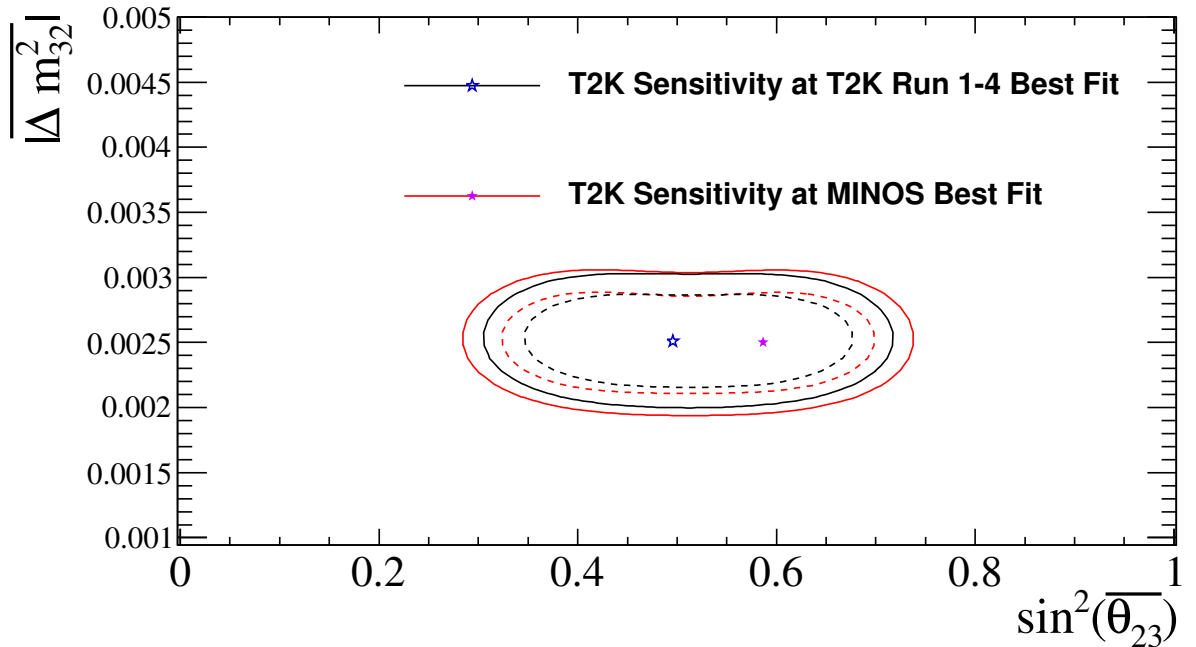


Figure 5.24: 68% CL (red) and 90% CL (black) allowed regions, constructed with the constant- $\Delta\chi^2$  method, from the fit of the  $4.011 \times 10^{20}$  Asimov dataset, with the effects of statistical fluctuations and postfit systematic variations being included. Contours are shown for both the T2K run 1-4 best-fit oscillation parameters shown in Table 5.1, and with the MINOS  $\bar{\nu}_\mu$ -only best-fit parameters converted to the single-angle convention and using the upper octant ( $\sin^2\bar{\theta}_{23} = 0.587$ ,  $|\Delta m_{32}^2| = 2.5 \times 10^{-3}$  eV $^2$ ) [39].

## 5.9 Results of the $\overline{\nu_\mu}$ Disappearance Analysis

### 5.9.1 Best-fit Oscillation Parameters and Spectra

Two 3-flavour  $\overline{\nu_\mu}$  disappearance fits were performed on the combined  $4.011 \times 10^{20}$  POT Run 5+6 dataset, using the method described in Section 5.2. In the first fit, the normal mass hierarchy was assumed, and  $\sin^2 \overline{\theta_{23}}$  and  $|\overline{\Delta m_{32}^2}|$  were allowed to float. In the second fit, the inverted mass hierarchy was assumed and  $\sin^2 \overline{\theta_{23}}$  and  $|\overline{\Delta m_{31}^2}|$  were allowed to float. In both fits, all 44 systematic parameters considered in this analysis were allowed to float.

The reconstructed energy distribution of the Run 5+6 single  $\mu$ -like ring  $4.011 \times 10^{20}$  POT dataset is shown in Figure 5.25 along with the best-fit energy spectrum assuming the normal mass hierarchy. The same Run 5+6 data spectrum is also shown with the best-fit energy spectrum assuming the inverted mass hierarchy in Figure 5.26. A summary is given of the best-fit oscillation parameters,  $\chi^2$ , p-values and event rates in Table 5.10.

A set of comparative best-fit spectra are also included, which use a coarser binning in reconstructed energy. The bin edges used are  $\{0.0, 0.4, 0.7, 1.0, 1.5, 2.0, 3.0, 4.0, 5.0, 30.0 \text{ GeV}\}$ . Figures 5.27 and 5.28 show a comparison between the best-fit spectrum from this analysis and the spectrum given by the T2K run 1-4 joint fit result.

Hierarchy	$\sin^2 \overline{\theta_{23}}$	$ \overline{\Delta m_{32}^2} $ or $ \overline{\Delta m_{31}^2} $	$N_{obs}$	$N_{exp}$	$\chi^2_{bf}/NDOF$	p-value
Normal	0.450	$2.518 \times 10^{-3}$	34	34.985	57.727/71	0.42
Inverted	0.453	$2.490 \times 10^{-3}$	34	35.727	57.726/71	0.42

Table 5.10: Summary of best-fit parameters from the fits of the combined Run 5+6 dataset. The quoted best-fit  $\chi^2$  values ( $\chi^2_{bf}$ ) were computed from Equation 5.2 using the reconstructed energy binning scheme given in Section 5.2. The table also shows the p-values obtained from the goodness-of-fit test described in Section 5.9.2. As described in that section, these p-values do not necessarily correspond to the  $\chi^2/NDOF$  values in this table.

### 5.9.2 Goodness-of-fit Tests

Goodness-of-fit tests were performed for the fits of the real data as described in Section 5.5, and the results are shown in Figures 5.29 and 5.30. The p-values are 0.42 for the normal hierarchy fit, and 0.42 for the inverted hierarchy, indicating that both results are plausible. The fitted number of degrees of freedom is approximately 3.6, which is reasonable given five bins and two correlated free parameters.

### 5.9.3 Confidence Regions

$\Delta\chi^2$  surfaces are shown in Figure 5.31 for the normal mass hierarchy and in Figure 5.32 for the inverted mass hierarchy. The 68% and 90% allowed regions calculated according to the constant- $\Delta\chi^2$  method in Section 5.7 are shown in Figure 5.33. These figures show the difference between statistics-only fits and fits with the systematic parameters profiled away. Figure 5.34 shows a comparison between the allowed regions from the fits of the combined run 5+6 dataset with those from the fits of the Asimov dataset. This Asimov contour was produced at the best-fit oscillation parameter values from this fit for  $\sin^2\overline{\theta_{23}}$  and  $|\Delta m_{32}^2|$ , with other values fixed at values from the T2K run 1-4 joint fit with reactor constraint, which can be seen in Table 5.1. In Figure 5.35, the T2K result is compared with the MINOS muon antineutrino disappearance result [39]. In Figure 5.36, the T2K run 5-6  $\overline{\nu_\mu}$  result is compared with the T2K run 1-4  $\nu_\mu$  result. The confidence region from this analysis is consistent with these other contours. A comparison between the contours produced using systematic profiling and the marginalisation method described in Section 5.2.2 can be seen in Figure 5.37. The contour produced using the marginalised likelihood has a best-fit point closer to maximum disappearance, leading to a somewhat smaller overall contour than the profiled measurement as described in Section 2.2.6.

One dimensional  $\Delta\chi^2$  surfaces and confidence intervals are shown for each of  $\sin^2\overline{\theta_{23}}$  and  $|\Delta m_{32}^2|$  separately in Figures 5.38 and 5.39 respectively. These figures were made independently, using fits of the Run 5+6 dataset in which the oscillation parameter not shown was profiled without a penalty term. Similar fits were performed where this parameter was fixed at its best-fit position, and these gave extremely similar results. These results rule out  $\sin^2\overline{\theta_{23}} = 0$  at  $7.3\sigma$ .

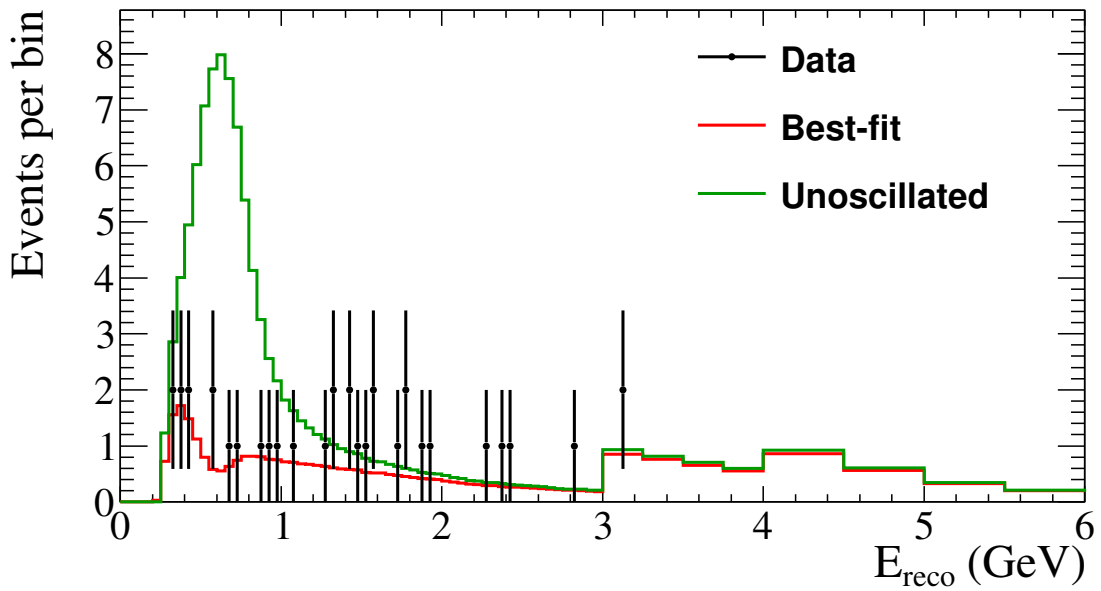


Figure 5.25: The Run 5+6 single  $\mu$ -like ring  $4.011 \times 10^{20}$  POT dataset and the best-fit reconstructed energy spectrum. The normal mass hierarchy result is shown, and is compared with the event rate prediction in the absence of oscillation.

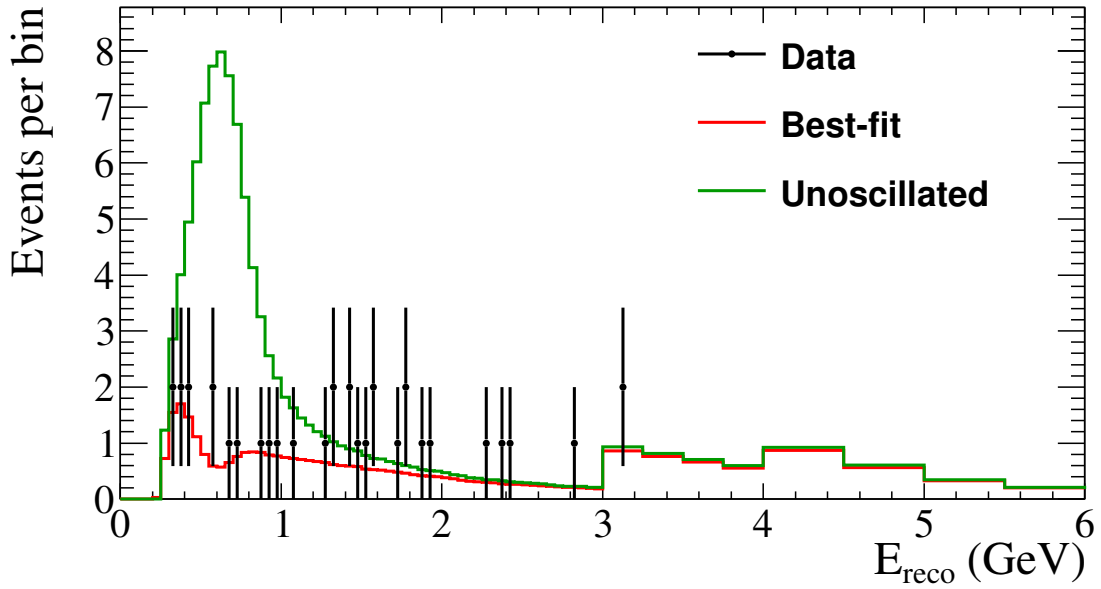


Figure 5.26: The Run 5+6 single  $\mu$ -like ring  $4.011 \times 10^{20}$  POT dataset and the best-fit reconstructed energy spectrum. The inverted mass hierarchy result is shown, and is compared with the event rate prediction in the absence of oscillation.

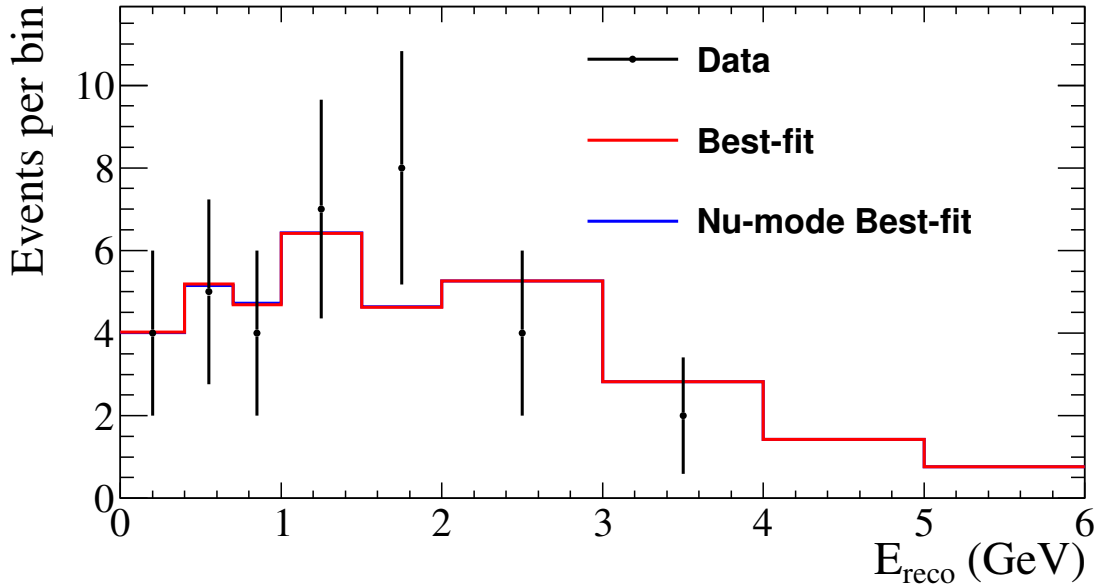


Figure 5.27: The Run 5+6 single  $\mu$ -like ring  $4.011 \times 10^{20}$  POT dataset and the best-fit spectrum. The binning is coarser than that used in the actual analysis (0.0, 0.4, 0.7, 1.0, 1.5, 2.0, 3.0, 4.0, 5.0, 30.0 GeV) and event counts are shown per bin. The normal mass hierarchy result is shown, and is compared with the best-fit spectrum from the  $\bar{\nu}_\mu$  dataset fixing all the  $\nu$  and  $\bar{\nu}$  oscillation parameters to the T2K best-fit values from the Run 1-4 joint analysis as shown in Table 5.1, while still profiling the systematics.

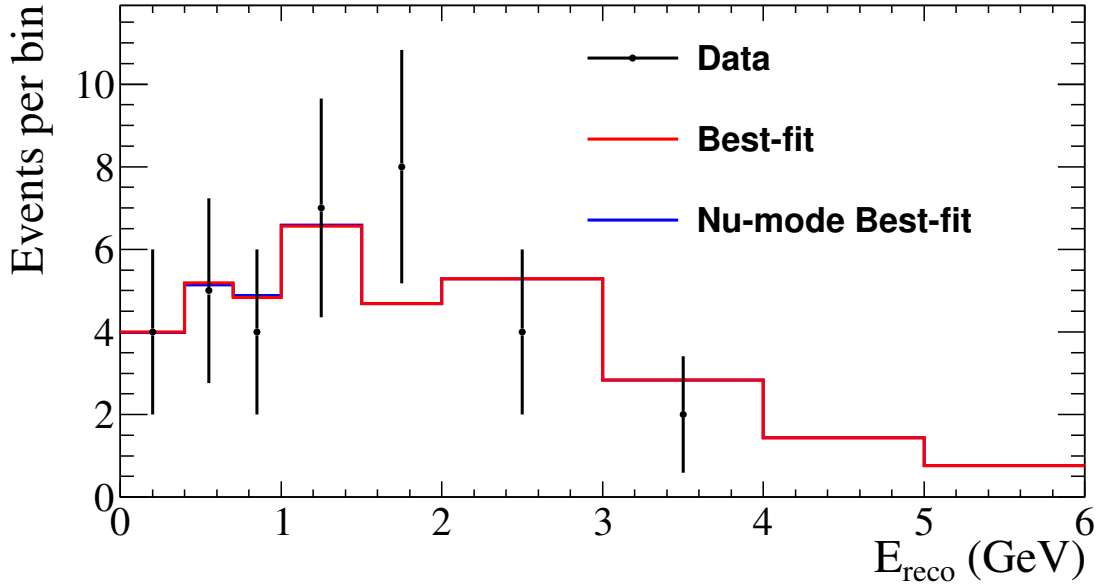


Figure 5.28: The Run 5+6 single  $\mu$ -like ring  $4.011 \times 10^{20}$  POT dataset and the best-fit spectrum. The binning is coarser than that used in the actual analysis (0.0, 0.4, 0.7, 1.0, 1.5, 2.0, 3.0, 4.0, 5.0, 30.0 GeV) and event counts are shown per bin. The inverted mass hierarchy result is shown, and is compared with the best-fit spectrum from the  $\bar{\nu}_\mu$  dataset fixing all the  $\nu$  and  $\bar{\nu}$  oscillation parameters to the T2K best-fit values from the Run 1-4 joint analysis as shown in Table 5.1, while still profiling the systematics.

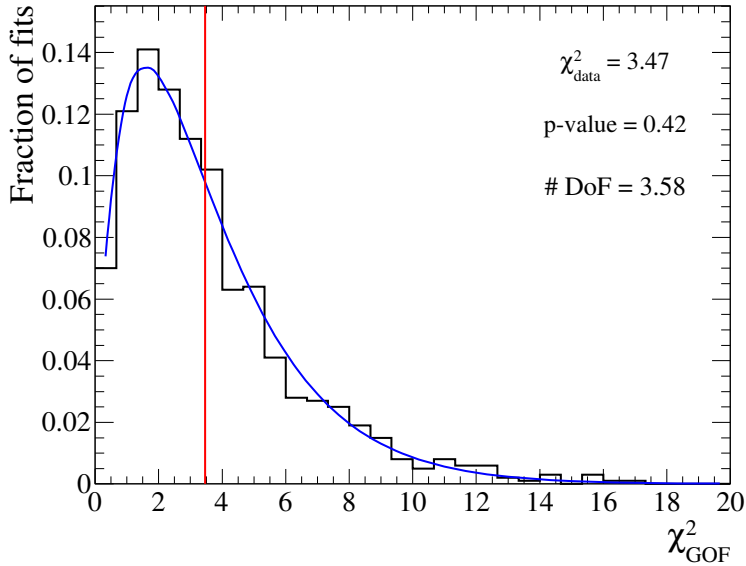


Figure 5.29: Distribution of  $\chi^2_{gof}$ , the goodness-of-fit (gof)  $\chi^2$ , from 1k toy MC experiments whose true input values are the best-fit oscillation parameters from the fit of the real data ( $\sin^2 \theta_{23} = 0.450$ ,  $|\Delta m^2_{32}| = 2.518 \times 10^{-3} \text{ eV}^2$ ). Systematic variations and statistical fluctuations are applied to the toy datasets, and all 44 systematic parameters are included in the fits. The toy experiments are generated for  $4.011 \times 10^{20}$  POT and the normal mass hierarchy is assumed. The  $\chi^2$  value from the fit of the real data assuming the normal mass hierarchy (with all 44 systematic parameters included in the fit) is shown as a red line. A  $\chi^2$  distribution with a fitted number of degrees of freedom is shown in blue.

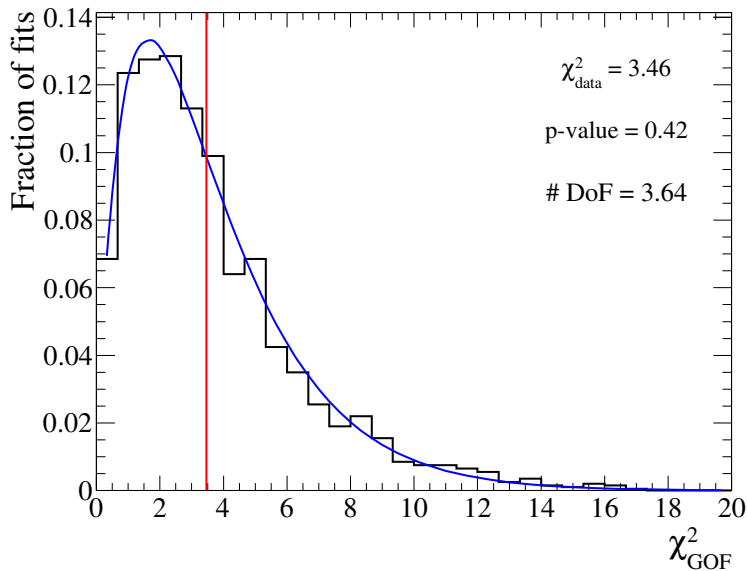


Figure 5.30: Distribution of  $\chi^2_{gof}$ , the goodness-of-fit (gof)  $\chi^2$ , from 1k toy MC experiments whose true input values are the best-fit oscillation parameters from the fit of the real data ( $\sin^2 \theta_{23} = 0.453$ ,  $|\Delta m^2_{31}| = 2.490 \times 10^{-3} \text{ eV}^2$ ). Systematic variations and statistical fluctuations are applied to the toy datasets, and all 44 systematic parameters are included in the fits. The toy experiments are generated for  $4.011 \times 10^{20}$  POT and the inverted mass hierarchy is assumed. The  $\chi^2$  value from the fit of the real data assuming the inverted mass hierarchy (with all 44 systematic parameters included in the fit) is shown as a red line. A  $\chi^2$  distribution with a fitted number of degrees of freedom is shown in blue.

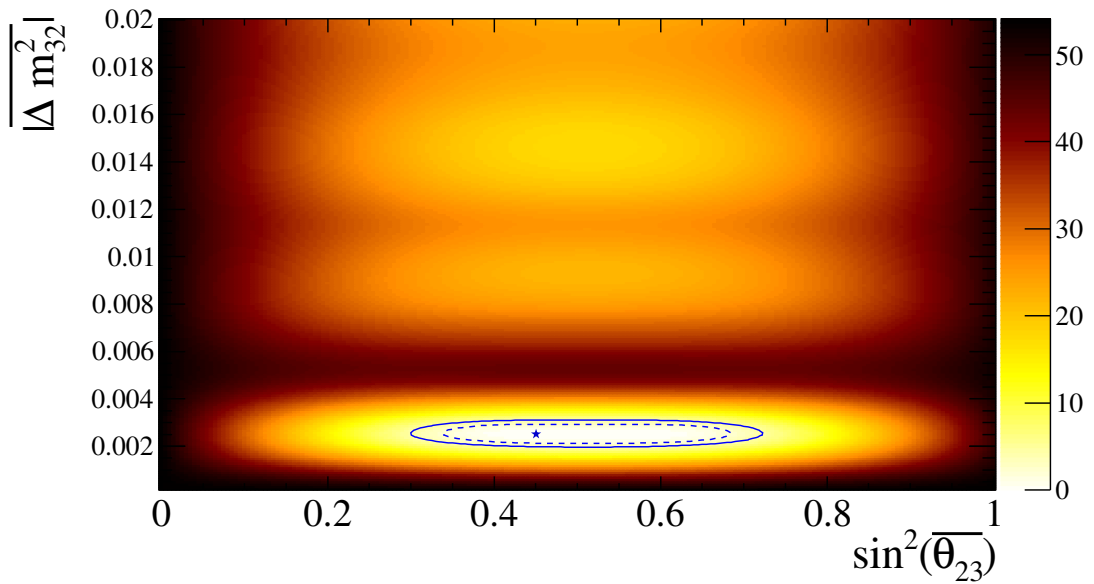


Figure 5.31:  $\Delta\chi^2$  surface from the fit of the  $4.011 \times 10^{20}$  POT run 5+6 dataset. The  $\Delta\chi^2$  values are calculated relative to the minimum at  $\chi^2 = 57.727$ . The normal mass hierarchy is assumed. 68% and 90% confidence contours are shown.

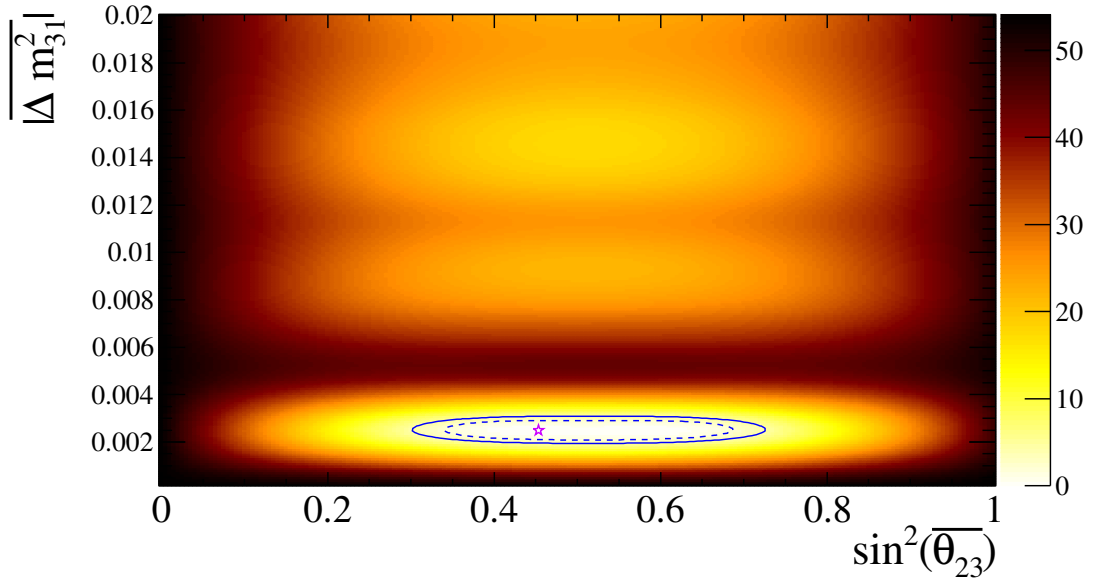


Figure 5.32:  $\Delta\chi^2$  surface from the fit of the  $4.011 \times 10^{20}$  POT Run 5+6 dataset. The  $\Delta\chi^2$  values are calculated relative to the minimum at  $\chi^2 = 57.726$ . The inverted mass hierarchy is assumed. 68% and 90% confidence contours are shown.

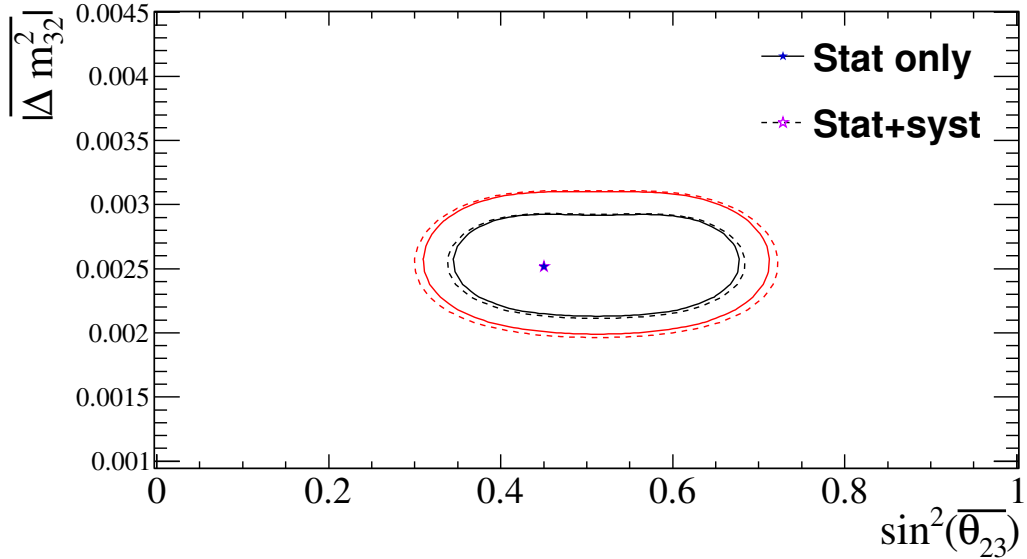


Figure 5.33: 68% (black) and 90% (red) confidence regions, constructed with the constant- $\Delta\chi^2$  method, from the fit to the T2K run 5 and 6 RHC dataset. A comparison is shown between the full contour with systematics profiled and the contour with the systematic parameters fixed at their best-fit values. It can be seen that the fit is statistically limited. The normal hierarchy is assumed.

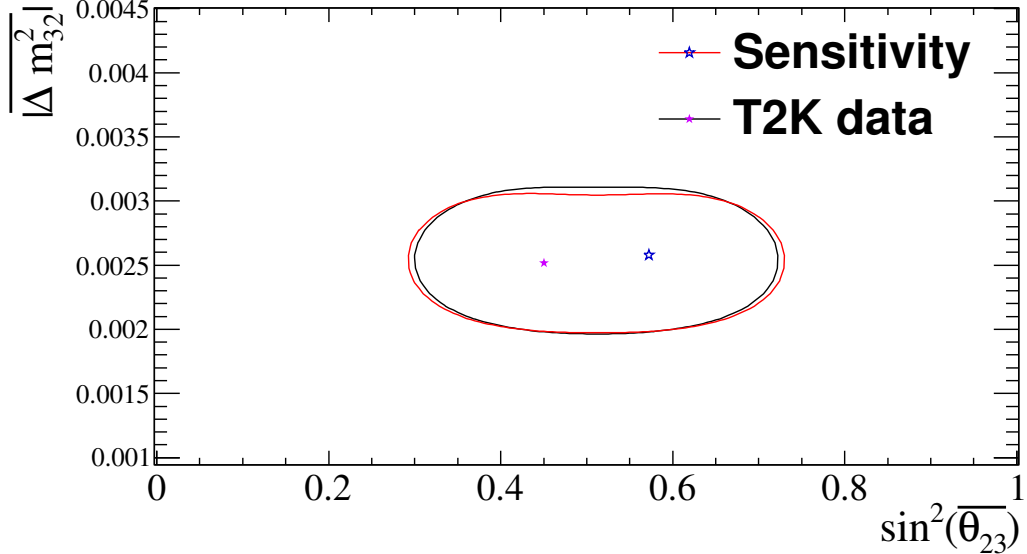


Figure 5.34: 90% CL allowed regions, constructed with the constant- $\Delta\chi^2$  method, from the fit to the Run 5+6 dataset, with the effects of statistical fluctuations and profiled systematic variations being included. These contours compare a fit to the Asimov dataset with the fit to the real data. The normal hierarchy is assumed, and the data best-fit values of  $\sin^2\theta_{23} = 0.450$  and  $|\Delta m_{32}^2| = 2.518 \times 10^{-3}$  are used. Other oscillation parameters are fixed at their values from the T2K run 1-4 joint fit with reactor constraint (Table 5.1).

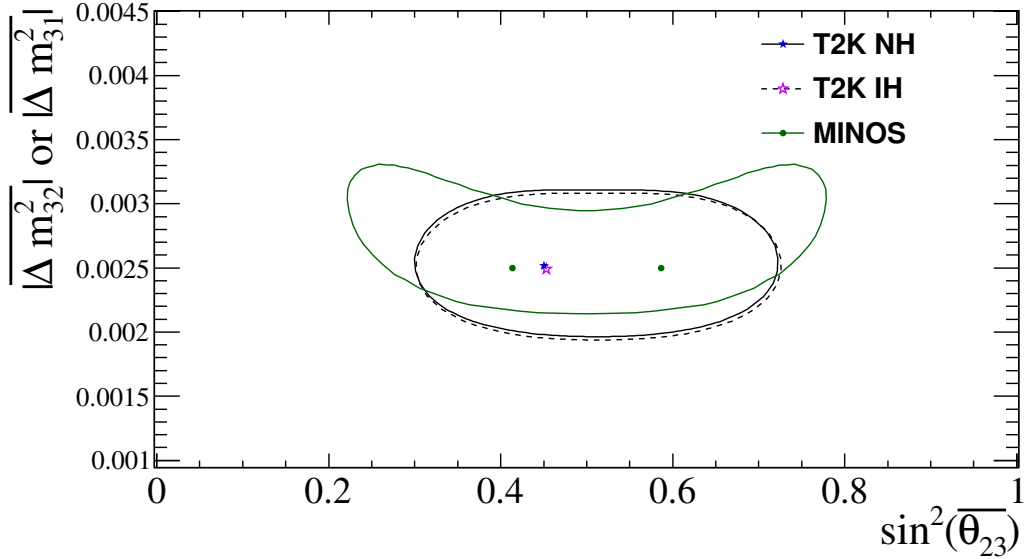


Figure 5.35: 90% confidence regions, constructed with the constant- $\Delta\chi^2$  method, from the fit to the T2K run 5 and 6 RHC dataset. A comparison is shown between the T2K fit result, and the MINOS antineutrino beam  $\bar{\nu}_\mu$  disappearance result [39]. The MINOS result was published in  $\sin^2 2\theta_{23}$ , and has been converted to  $\sin^2 \theta_{23}$  for this figure, yielding two best-fit points.

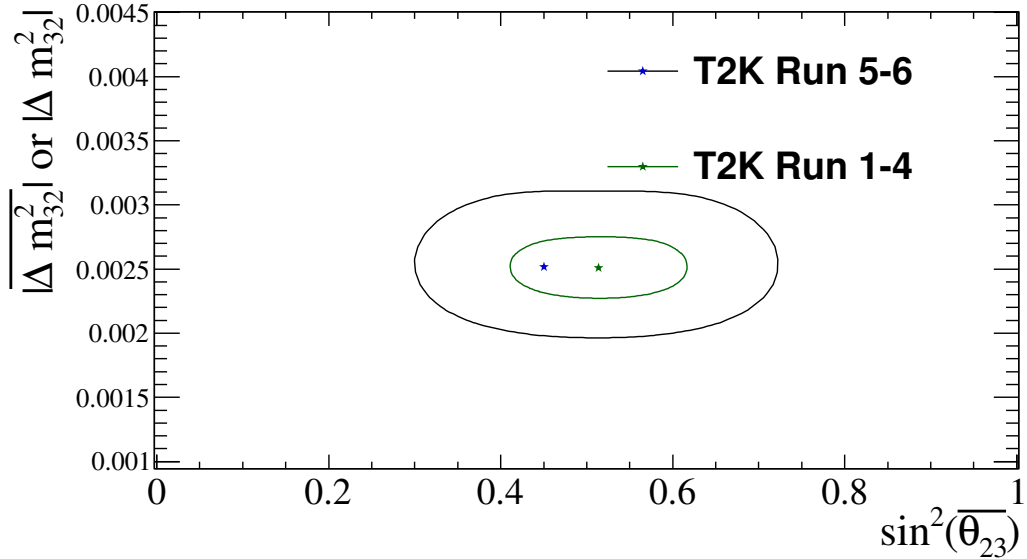


Figure 5.36: 90% CL allowed regions, comparing the T2K run 5+6  $\bar{\nu}_\mu$  disappearance result with the T2K published run 1-4  $\nu_\mu$  disappearance contour, produced with  $6.57 \times 10^{20}$  POT [39].

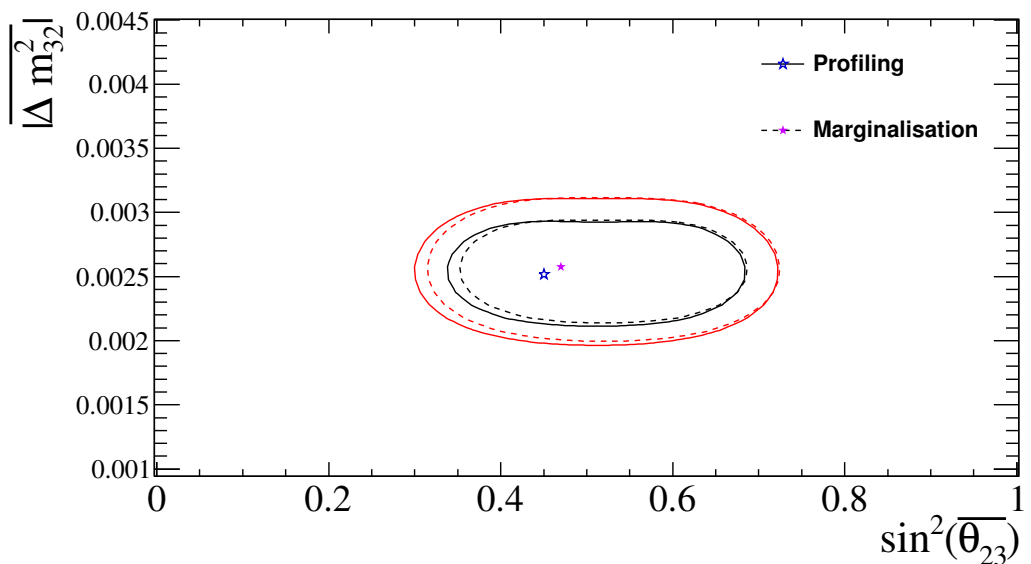


Figure 5.37: 90% confidence regions, constructed with the constant- $\Delta\chi^2$  method, from the fit to the T2K run 5 and 6 RHC dataset. A comparison is shown between the profiling the systematics as described in Section 5.2.1 and marginalising them as described in Section 5.2.2. The normal hierarchy is assumed.

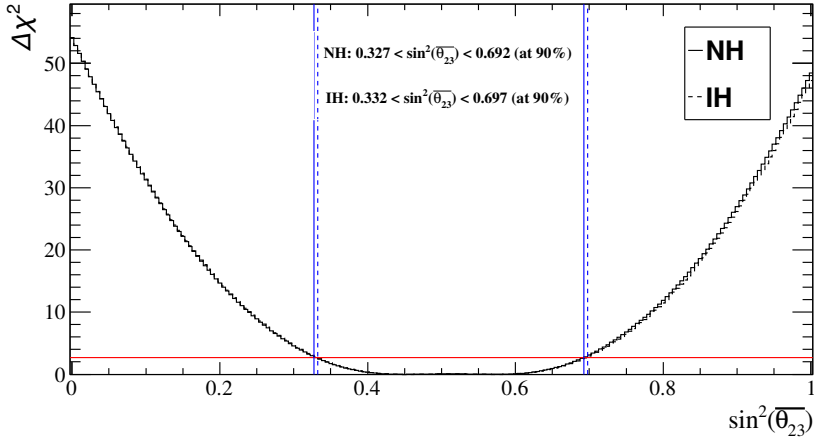


Figure 5.38: Plots of 1D  $\Delta\chi^2$  for  $\sin^2 \overline{\theta_{23}}$  with  $|\overline{\Delta m_{32}^2}|$  (normal hierarchy) or  $|\overline{\Delta m_{31}^2}|$  (inverted hierarchy) being profiled. These are from the fit of the  $4.011 \times 10^{20}$  real data with the effects of statistical fluctuations and postfit systematic variations being included. Using the constant- $\Delta\chi^2$  method, the 1D 90% CL allowed intervals are  $0.327 < \sin^2 \overline{\theta_{23}} < 0.692$  (normal hierarchy) and  $0.332 < \sin^2 \overline{\theta_{23}} < 0.697$  (inverted hierarchy).

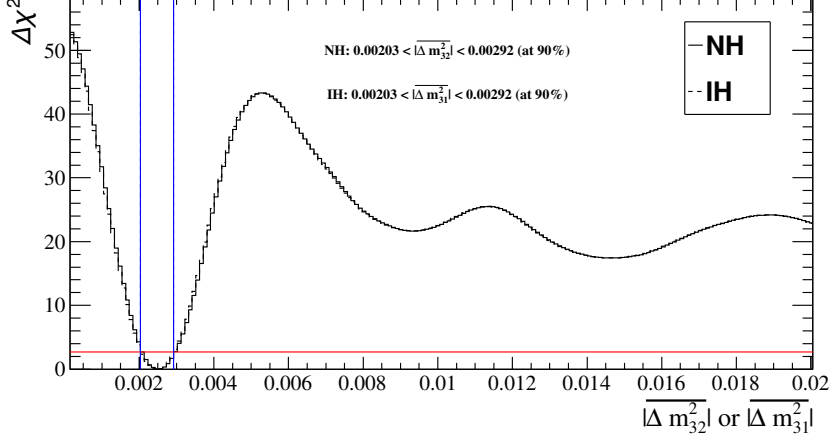


Figure 5.39: Plots of 1D  $\Delta\chi^2$  for  $|\overline{\Delta m_{32}^2}|$  (normal hierarchy) and  $|\overline{\Delta m_{31}^2}|$  (inverted hierarchy), with  $\sin^2 \overline{\theta_{23}}$  being profiled. These are from the fit of the  $4.011 \times 10^{20}$  real data with the effects of statistical fluctuations and postfit systematic variations being included. Using the constant- $\Delta\chi^2$  method, the 1D 90% CL allowed intervals are  $2.03 \times 10^{-3} \text{ eV}^2 < |\overline{\Delta m_{32}^2}| < 2.92 \times 10^{-3} \text{ eV}^2$  (normal hierarchy) and  $2.03 \times 10^{-3} \text{ eV}^2 < |\overline{\Delta m_{31}^2}| < 2.92 \times 10^{-3} \text{ eV}^2$  (inverted hierarchy).

## 5.10 Summary

The T2K run 5+6 antineutrino beam mode dataset corresponds to an integrated J-PARC neutrino beam exposure of  $4.011 \times 10^{20}$  POT. This dataset has been studied to measure  $\overline{\nu_\mu}$  disappearance.

This analysis predicts  $103.6 \pm 10.5$  (syst) single  $\mu$ -like ring events in Super K in the absence of any oscillation, but only 34 were observed. The observed deficit exhibits a strong energy dependence: the ratio of the number of observed events to the number expected under the no-oscillation hypothesis is  $\sim 31.48\% < 0.5$  GeV,  $\sim 12.84\%$  between 0.5 and 1 GeV and  $\sim 69.94\% > 1$  GeV.

A  $\overline{\nu_\mu}$ -disappearance analysis was performed in a framework of 3-flavour oscillations including matter effects in constant-density matter. The observed reconstructed energy spectrum of single  $\mu$ -like ring events was fitted, and separate fits were made for the normal and the inverted mass hierarchies. In these fits,  $\sin^2 \overline{\theta_{23}}$  and either  $|\overline{\Delta m_{32}^2}|$  (normal hierarchy) or  $|\overline{\Delta m_{31}^2}|$  (inverted hierarchy) were allowed to float, while all other oscillation parameters in both sets were fixed to T2K best-fit or PDG 2014 values. All 44 systematic parameters considered in this analysis were also allowed to float in the fits.

For the normal mass hierarchy, the 3-flavour  $\overline{\nu_\mu}$ -disappearance fit of the combined Run 5+6 dataset gives  $\sin^2 \overline{\theta_{23}} = 0.450$  and  $|\overline{\Delta m_{32}^2}| = 2.518 \times 10^{-3}$  eV<sup>2</sup> as the best-fit values (p-value = 0.42). The fit for the inverted mass hierarchy yields  $\sin^2 \overline{\theta_{23}} = 0.453$  and  $|\overline{\Delta m_{31}^2}| = 2.490 \times 10^{-3}$  eV<sup>2</sup> as the best-fit values (p-value = 0.42). The p-value for the normal hierarchy antineutrino-mode dataset given a null hypothesis of the normal hierarchy best-fit values of the equivalent parameters from the official Run 1-4 neutrino-mode analysis is 0.60; thus the results of this analysis considered together with the Run 1-4 neutrino-mode results are consistent with CPT being conserved.

Confidence regions in the parameter space  $\sin^2 \overline{\theta_{23}} - |\overline{\Delta m_{32}^2}|$  (normal hierarchy) and  $\sin^2 \overline{\theta_{23}} - |\overline{\Delta m_{31}^2}|$  (inverted hierarchy) are shown using the constant- $\Delta\chi^2$  method. Each parameter was also fitted individually and 1-dimensional confidence regions produced. The 90% CL allowed values for mass splitting are  $2.03 \times 10^{-3}$  eV<sup>2</sup>  $< |\overline{\Delta m_{32}^2}| < 2.92 \times 10^{-3}$  eV<sup>2</sup> (normal hierarchy) and  $2.03 \times 10^{-3}$  eV<sup>2</sup>  $< |\overline{\Delta m_{31}^2}| < 2.92 \times 10^{-3}$  eV<sup>2</sup> (inverted hierarchy). The 90% CL allowed values for mixing angle are  $0.327 < \sin^2 \overline{\theta_{23}} < 0.692$  (normal hierarchy) and  $0.332 < \sin^2 \overline{\theta_{23}} < 0.697$  (inverted hierarchy). These contours rule out  $\sin^2 \overline{\theta_{23}} = 0$  at  $7.3\sigma$ .

The confidence regions were compared with the current best results produced by MINOS. T2K provides the world's best measurement of  $\sin^2 \overline{\theta_{23}}$ .

# Chapter 6

# Non-standard Neutrino-Matter Interactions

## 6.1 Introduction

Neutrino oscillation probabilities are modified by interactions with electrons in the matter they propagate through. As described in Section 2.2.7, these only have an effect on the electron flavour component due to the negligible muon and tau content of normal matter.

It has been theorised that there could exist additional flavour-dependent matter interactions beyond this, which can lead to new flavour changing behaviour [121]. For the purposes of this document, these will be called Non-standard Interactions (NSI). Charged current NSI could affect neutrino source and detector processes, allowing a charged lepton to produce a neutrino of a different flavour or vice versa. They could also produce a charged lepton somewhere along the baseline which would not be detected. Data from short-baseline experiments such as NOMAD [122] and KARMEN [123] can be used to constrain these effects [124], and they would not have an observable effect at T2K. As a result, this analysis will only consider neutral current NSI. If the neutrino undergoes NC NSI between the source and detector the flavour of the final neutrino could change, leading to a different flavour content being observed at the far detector.

The matter NSI are described by an addition to the Standard Model Lagrangian density [124]:

$$\mathcal{L}_{\text{NSI}}^M = -2\sqrt{2}G_F \varepsilon_{\alpha\beta}^{fc} [\bar{f}\gamma^\mu P_c f][\bar{\nu}_\alpha \gamma_\mu P_L \nu_\beta], \quad (6.1)$$

Here  $f$  represents the Fermion types in normal matter (electron, up quark, down quark), and  $\varepsilon_{\alpha\beta}^{fc}$  are parameters scaling the size of deviation from standard interactions for neutrino flavours  $\alpha$  and  $\beta$  and chirality  $c$ . For the purposes of a phenomenological study searching for the existence of any NSI at all, it is useful to reduce the large parameter

space to effective parameters, summed over chirality and fermion flavour in the medium:

$$\varepsilon_{\alpha\beta} = \sum_{f,c} \varepsilon_{\alpha\beta}^{fc} \frac{N_f}{N_e}, \quad (6.2)$$

$N_f$  represents the number density of fermion  $f$ , with  $N_e$  representing the electron number density.

In a neutrino oscillation experiment, NSI effects with this parameterisation appear as an additional contribution to the standard matter Hamiltonian shown in Equation 2.44. The new matter contribution is given in terms of the 6 new free parameters:

$$\mathbf{A}_{matter} = 2E_\nu V \begin{pmatrix} 1 + \varepsilon_{ee} & \varepsilon_{e\mu}^* & \varepsilon_{e\tau}^* \\ \varepsilon_{e\mu} & \varepsilon_{\mu\mu} & \varepsilon_{\mu\tau}^* \\ \varepsilon_{e\tau} & \varepsilon_{\mu\tau} & \varepsilon_{\tau\tau} \end{pmatrix} \quad (6.3)$$

The factor of 1 in the first diagonal matrix element represents normal matter effects. As in Section 2.2.7,  $V$  is defined as:

$$V = \pm \sqrt{2} G_F N_e \quad (6.4)$$

Assuming the Earth's crust has an equal number of protons and neutrons, the electron number density is:

$$N_e = \frac{\rho N_A}{2} \quad (6.5)$$

where  $N_A$  is the Avogadro constant. The matter density  $\rho$  used is  $2.6 \text{ g cm}^{-3}$ , based on a geological survey of the T2K baseline [117], leading to a value  $V = 9.9 \times 10^{-14} \text{ eV}$ .

This is a phenomenological model, independent of the underlying physics which would cause the new interactions. Many beyond-the-Standard-Model theories can add interactions of this form, such as introducing additional scalar exchange bosons or leptoquarks [125].

The parameters  $\varepsilon_{\alpha\beta}$  could be complex, and can be either flavour-changing or flavour-conserving, but for the purposes of this study we will examine the real part of the flavour-changing  $\varepsilon_{\mu\tau}$ , which leads to a difference in muon neutrino and muon antineutrino disappearance probability. The other parameters  $\varepsilon_{\alpha\beta}$  have a negligible effect on the probability of muon neutrino survival at T2K. All other components, real and complex are set to zero. If we make a similar two-flavour oscillation approximation to the one used for Equation 2.38 for muon survival only, we get the following expressions:

$$P(\bar{\nu}_\mu \rightarrow \bar{\nu}_\mu) = 1 - \mathcal{F} \sin^2 \phi \quad (6.6)$$

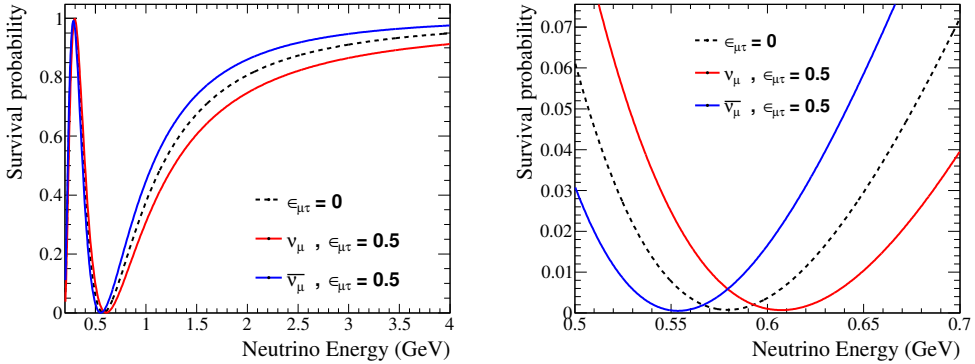


Figure 6.1: Survival probabilities of muon neutrinos for different values of the NSI parameter  $\varepsilon_{\mu\tau}$ , given the T2K baseline of 295 km. The probabilities are shown both over a wide energy range, and close to the oscillation maximum.

$$\phi = L \sqrt{\left( \frac{\Delta m_{32}^2}{4E_\nu} \right)^2 \mp 2\sin(2\theta_{23}) \frac{\Delta m_{32}^2}{4E_\nu} \varepsilon_{\mu\tau} |V| + (\varepsilon_{\mu\tau} V)^2} \quad (6.7)$$

$$\mathcal{F} = 1 - \frac{\cos^2 2\theta_{23}}{1 \mp 2\sin(2\theta_{23}) \frac{4\varepsilon_{\mu\tau}|V|}{\Delta m_{32}^2} E_\nu + \left( \frac{4\varepsilon_{\mu\tau} V}{\Delta m_{32}^2} E_\nu \right)^2} \quad (6.8)$$

For the purposes of all studies in this thesis, the full three-flavour calculation is performed numerically, without the use of such approximations. Muon neutrino survival probabilities at the T2K baseline can be seen in Figure 6.1. It can be observed that a positive value of  $\varepsilon_{\mu\tau}$  leads to the oscillation peak energy being slightly higher for  $\nu_\mu$  and more disappearance in the tail of the distribution, with the opposite effect on  $\bar{\nu}_\mu$ .

A comprehensive review of available data in 2009 for all of these parameters assuming matter with an equal number of protons and neutrons gives the upper bounds [124]:

$$|\varepsilon_{\alpha\beta}| < \begin{pmatrix} 4.2 & 0.33 & 3.0 \\ 0.33 & 0.068 & 0.33 \\ 3.0 & 0.33 & 21 \end{pmatrix} \quad (6.9)$$

The relevant limit for this analysis is  $|\varepsilon_{\mu\tau}| < 0.33$  at 90%. More recently, the MINOS experiment has published a long-baseline limit using a combined neutrino-antineutrino fit similar to the one described in this chapter. The MINOS data gives a 90% confidence region  $-0.20 < \varepsilon_{\mu\tau} < 0.07$  [126]. Finally, the Super-K experiment performed an analysis on their atmospheric neutrino sample giving a 90% limit of  $|\varepsilon_{\mu\tau}| < 0.011$  [127]. The SK measurement used atmospheric data binned in energy and zenith angle allowing the study to be performed at many different values of  $L/E$ , where the relative effects of normal disappearance parameters and NSI could be separated. This method is comple-

mentary to the method of studying possible differences in oscillation probability between neutrinos and antineutrinos in an accelerator driven experiment.

## 6.2 Analysis Strategy

In general, the NSI analysis strategy mirrors the methods used for the normal disappearance analysis as described in Section 5.2, using MINUIT to minimise the likelihood function given in Equation 5.2. The most important differences are the introduction of the neutrino beam mode event sample, and the modification of the fit hypothesis. We now consider a single set of oscillation parameters affecting both neutrinos and antineutrinos: the six oscillation parameters used in a normal three-flavour fit, and the NSI parameter  $\varepsilon_{\mu\tau}$ . No limits are set on the range of the NSI parameter. The neutrino and antineutrino beam-mode datasets are fitted simultaneously. Identical Super-K binning is used for the two datasets in both  $E_{reco}$  and  $E_{true}$ , giving a total of 146 observable bins.

The addition of the neutrino mode dataset introduces another 25 flux systematic parameters, and another 6 Super-K efficiency systematics. The FHC systematics are correlated with their RHC counterparts. The values of the new flux parameters used are listed in Table 4.5, while the values of the detector efficiencies are listed in Table 4.10. The correlations between the neutrino and antineutrino parameters can be seen in Figures 4.25 and 4.38. Note that the CCQE-like and NC efficiencies at Super-K are strongly correlated between beam modes. Similarly, the FHC  $\nu_\mu$  flux is strongly correlated with the RHC  $\bar{\nu}_\mu$  flux. In order to obtain results in terms of  $\varepsilon_{\mu\tau}$ , all systematic parameters as well as  $\sin^2 \theta_{23}$  and  $|\Delta m_{32}^2|$  are profiled in these fits, according to the method described in Section 5.2.1.

## 6.3 Predicted Event Rates and Spectra

The NSI analysis uses a combined fit to both forward horn current and reverse horn current data. The spectrum predictions for RHC are described in detail in Section 5.3. This section describes equivalent spectra for the forward horn current data.

Tables 6.1 and 6.2 show the effects of the various tuning stages described in Chapter 4 on the overall event rate, for the unoscillated and oscillated prediction. The effects of the flux tuning described in Section 4.1 on the expected spectrum can be seen in Figure 6.2. The effect of the BANFF tuning described in Section 4.4 can be seen in Figure 6.3. It should be observed that the BANFF tuning increases both the unoscillated event rate and the event rate with expected oscillations by around 14%.

The final selected event rate predicted for the no-oscillation hypothesis is 460.4

$\pm 45.9$  (syst), while for the oscillated hypothesis using the numbers from Table 5.1, the expected numbers of events are 125.8 (normal) and 128.5 (inverted). The expected Super-K  $E_{\text{reco}}$  spectra without oscillation can be seen in Figures 6.4 and 6.5, with and without the near-detector tune respectively. Similar spectra with oscillations applied can be seen in Figures 6.6 and 6.7. These plots use a POT of  $6.91 \times 10^{20}$ , the T2K collected POT in neutrino beam mode to date.

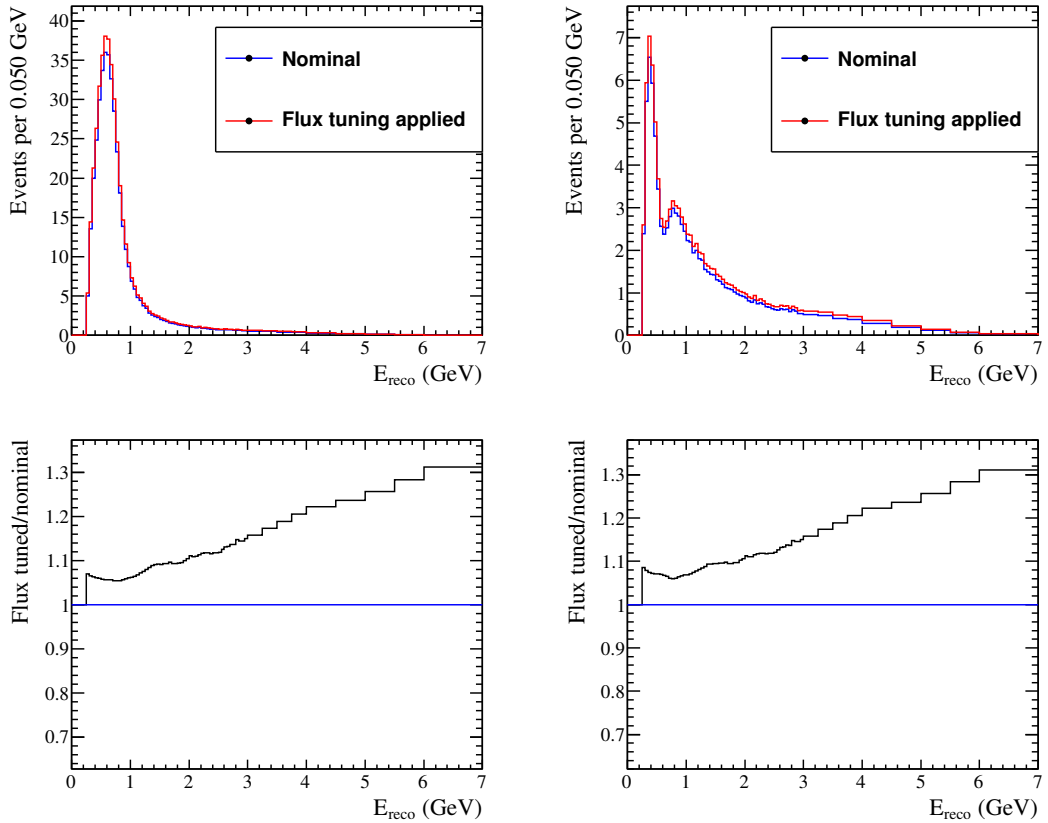


Figure 6.2: Top: Reconstructed-energy spectrum of 1  $\mu$ -like ring events, for an exposure of  $6.91 \times 10^{20}$  POT in neutrino beam mode both with and without the effect of the flux tuning of the nominal MC templates. The spectra are shown both for no oscillations (left) and for oscillations assuming the normal hierarchy with the oscillation parameters shown in Table 5.1. Bottom: Ratio of flux-tuned spectrum to the nominal MC spectrum.

	$N_{SK}$ Nominal MC	$N_{SK}$ Flux-tuned MC	$N_{SK}$ BANFF prefit MC (flux + CCQE tune)	$N_{SK}$ BANFF postfit MC
Total	421.230	450.235	404.951	460.434
$\nu_\mu$ CCQE	304.816	324.495	312.478	337.776
$\nu_\mu$ CC $1\pi$	44.769	49.110	49.110	38.272
$\nu_\mu$ CC coherent	2.033	2.231	2.231	2.684
$\nu_\mu$ CC MEC	40.210	43.087	11.634	48.817
$\nu_\mu$ CC other	6.573	7.923	7.923	9.216
$\nu_\mu/\nu_\tau$ NC $1\pi^{+/-}$	4.778	5.251	5.251	3.846
$\nu_\mu/\nu_\tau$ NC $1\pi^0$	0.670	0.747	0.747	0.495
$\nu_\mu/\nu_\tau$ NC coherent	0.014	0.015	0.015	0.017
$\nu_\mu/\nu_\tau$ NC other	2.292	2.695	2.695	4.438
$\bar{\nu}_\mu$ CCQE	8.926	8.727	8.047	8.915
$\bar{\nu}_\mu$ CC $1\pi$	2.817	2.694	2.694	2.300
$\bar{\nu}_\mu$ CC coherent	0.494	0.481	0.481	0.576
$\bar{\nu}_\mu$ CC MEC	1.592	1.547	0.418	1.778
$\bar{\nu}_\mu$ CC other	0.522	0.491	0.491	0.544
$\bar{\nu}_\mu/\bar{\nu}_\tau$ NC $1\pi^{+/-}$	0.224	0.214	0.214	0.138
$\bar{\nu}_\mu/\bar{\nu}_\tau$ NC $1\pi^0$	0.029	0.028	0.028	0.016
$\bar{\nu}_\mu/\bar{\nu}_\tau$ NC coherent	0.001	0.001	0.001	0.001
$\bar{\nu}_\mu/\bar{\nu}_\tau$ NC other	0.153	0.144	0.144	0.225
$\nu_e$ CCQE	0.031	0.034	0.034	0.038
$\nu_e$ CC $1\pi$	0.019	0.021	0.021	0.018
$\nu_e$ CC coherent	0.001	0.001	0.001	0.001
$\nu_e$ CC MEC	0.006	0.006	0.002	0.007
$\nu_e$ CC other	0.007	0.008	0.008	0.009
$\nu_e$ NC $1\pi^{+/-}$	0.109	0.123	0.123	0.088
$\nu_e$ NC $1\pi^0$	0.021	0.023	0.023	0.015
$\nu_e$ NC coherent	0.000	0.000	0.000	0.000
$\nu_e$ NC other	0.094	0.108	0.108	0.176
$\bar{\nu}_e$ CCQE	0.002	0.002	0.002	0.002
$\bar{\nu}_e$ CC $1\pi$	0.001	0.001	0.001	0.001
$\bar{\nu}_e$ CC coherent	0.000	0.000	0.000	0.000
$\bar{\nu}_e$ CC MEC	0.000	0.000	0.000	0.000
$\bar{\nu}_e$ CC other	0.001	0.000	0.000	0.001
$\bar{\nu}_e$ NC $1\pi^{+/-}$	0.013	0.012	0.012	0.008
$\bar{\nu}_e$ NC $1\pi^0$	0.002	0.002	0.002	0.001
$\bar{\nu}_e$ NC coherent	0.012	0.011	0.011	0.012
$\bar{\nu}_e$ NC other	0.000	0.000	0.000	0.000

Table 6.1: Calculated predicted numbers of 1-ring  $\mu$ -like events in neutrino beam mode without oscillations using the nominal MC templates, the NA61-tuned MC templates, the CCQE-tuned MC templates and the BANFF-tuned MC templates. The BANFF prefit column is the NA61 tuned data, with the CCQE samples reweighted according to the external data fits described in Section 4.3. The total numbers of events and the numbers of events from each mode considered in this analysis are shown. These numbers were calculated for an exposure of  $6.91 \times 10^{20}$  POT.

	$N_{SK}$ Nominal MC	$N_{SK}$ Flux-tuned MC	$N_{SK}$ BANFF prefit MC (flux + CCQE tune)	$N_{SK}$ BANFF postfit MC
Total	110.201	121.340	109.941	125.767
$\nu_\mu$ CCQE	58.367	63.780	61.350	69.147
$\nu_\mu$ CC 1 $\pi$	18.568	21.217	21.217	16.738
$\nu_\mu$ CC coherent	0.780	0.898	0.898	1.122
$\nu_\mu$ CC MEC	9.930	11.011	2.973	13.057
$\nu_\mu$ CC other	5.775	7.017	7.017	8.137
$\nu_\mu/\nu_\tau$ NC 1 $\pi^{+/-}$	4.778	5.251	5.251	3.846
$\nu_\mu/\nu_\tau$ NC 1 $\pi^0$	0.670	0.747	0.747	0.495
$\nu_\mu/\nu_\tau$ NC coherent	0.014	0.015	0.015	0.017
$\nu_\mu/\nu_\tau$ NC other	2.292	2.695	2.695	4.438
$\bar{\nu}_\mu$ CCQE	4.407	4.234	3.951	4.358
$\bar{\nu}_\mu$ CC 1 $\pi$	1.956	1.852	1.852	1.555
$\bar{\nu}_\mu$ CC coherent	0.264	0.252	0.252	0.301
$\bar{\nu}_\mu$ CC MEC	0.876	0.838	0.226	0.960
$\bar{\nu}_\mu$ CC other	0.460	0.432	0.432	0.478
$\bar{\nu}_\mu/\bar{\nu}_\tau$ NC 1 $\pi^{+/-}$	0.224	0.214	0.214	0.138
$\bar{\nu}_\mu/\bar{\nu}_\tau$ NC 1 $\pi^0$	0.029	0.028	0.028	0.016
$\bar{\nu}_\mu/\bar{\nu}_\tau$ NC coherent	0.001	0.001	0.001	0.001
$\bar{\nu}_\mu/\bar{\nu}_\tau$ NC other	0.153	0.144	0.144	0.225
$\nu_e$ CCQE	0.029	0.031	0.032	0.036
$\nu_e$ CC 1 $\pi$	0.018	0.020	0.020	0.017
$\nu_e$ CC coherent	0.001	0.001	0.001	0.001
$\nu_e$ CC MEC	0.005	0.006	0.002	0.007
$\nu_e$ CC other	0.007	0.008	0.008	0.009
$\nu_e$ NC 1 $\pi^{+/-}$	0.109	0.123	0.123	0.088
$\nu_e$ NC 1 $\pi^0$	0.021	0.023	0.023	0.015
$\nu_e$ NC coherent	0.000	0.000	0.000	0.000
$\nu_e$ NC other	0.094	0.108	0.108	0.176
Osc. $\nu_e$ CCQE	0.224	0.237	0.231	0.247
Osc. $\nu_e$ CC 1 $\pi$	0.082	0.087	0.087	0.072
Osc. $\nu_e$ CC coherent	0.003	0.003	0.003	0.004
Osc. $\nu_e$ CC MEC	0.031	0.032	0.009	0.036
Osc. $\nu_e$ CC other	0.002	0.002	0.002	0.002
$\bar{\nu}_e$ CCQE	0.002	0.002	0.002	0.002
$\bar{\nu}_e$ CC 1 $\pi$	0.001	0.001	0.001	0.001
$\bar{\nu}_e$ CC coherent	0.000	0.000	0.000	0.000
$\bar{\nu}_e$ CC MEC	0.000	0.000	0.000	0.000
$\bar{\nu}_e$ CC other	0.001	0.000	0.000	0.001
$\bar{\nu}_e$ NC 1 $\pi^{+/-}$	0.013	0.012	0.012	0.008
$\bar{\nu}_e$ NC 1 $\pi^0$	0.002	0.002	0.002	0.001
$\bar{\nu}_e$ NC coherent	0.012	0.011	0.011	0.012
$\bar{\nu}_e$ NC other	0.000	0.000	0.000	0.000
Osc. $\bar{\nu}_e$ CCQE	0.001	0.001	0.001	0.001
Osc. $\bar{\nu}_e$ CC 1 $\pi$	0.001	0.001	0.001	0.000
Osc. $\bar{\nu}_e$ CC coherent	0.000	0.000	0.000	0.000
Osc. $\bar{\nu}_e$ CC MEC	0.000	0.000	0.000	0.000
Osc. $\bar{\nu}_e$ CC other	0.000	0.000	0.000	0.000

Table 6.2: Calculated predicted numbers of 1-ring  $\mu$ -like events in neutrino beam mode with oscillations using the nominal MC templates, the NA61-tuned MC templates, the CCQE-tuned MC templates and the BANFF-tuned MC templates. The BANFF prefit column is the NA61 tuned data, with the CCQE samples reweighted according to the external data fits described in Section 4.3. The total numbers of events and the numbers of events from each mode considered in this analysis are shown. The normal hierarchy was assumed, with oscillation parameters give the values listed in Table 5.1. These numbers were calculated for an exposure of  $6.91 \times 10^{20}$  POT.

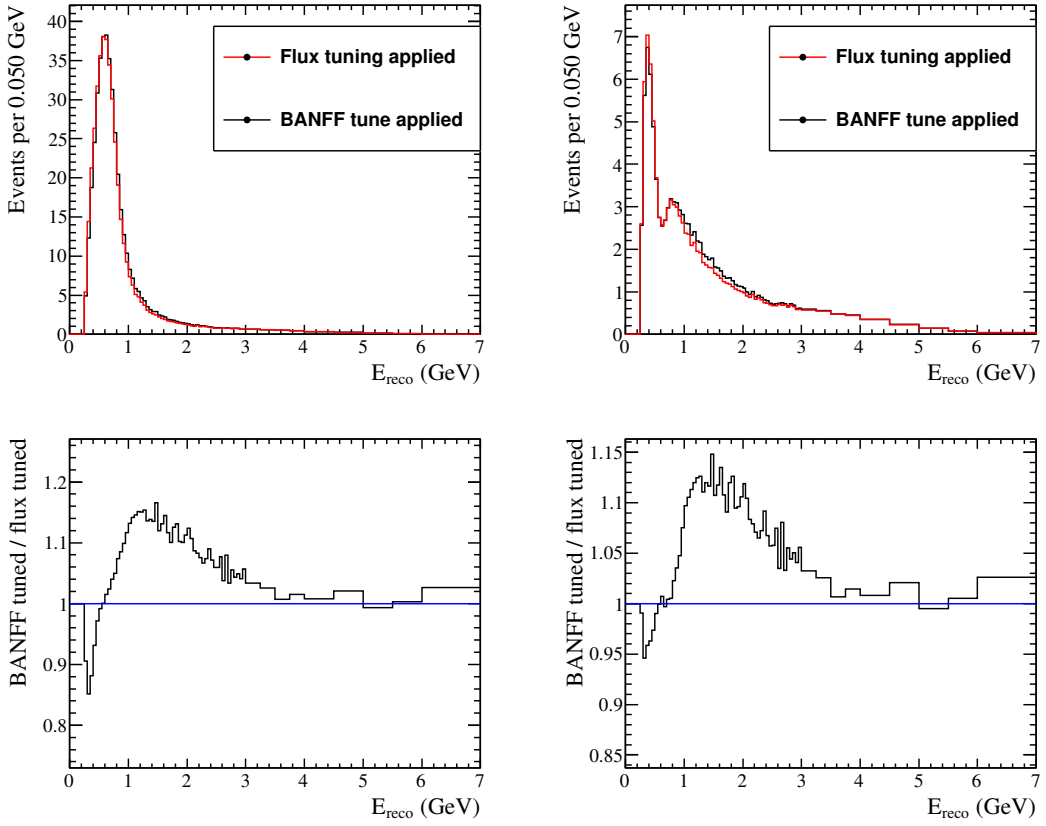


Figure 6.3: Top: Reconstructed-energy spectrum of 1  $\mu$ -like ring events, for an exposure of  $6.91 \times 10^{20}$  POT in neutrino beam mode both with and without the effect of postfit BANFF flux and cross-section tuning on the NA61-tuned flux MC templates. The spectra are shown both for no oscillations (left) and for oscillations assuming the normal hierarchy, and the oscillation parameters shown in Table 5.1. Bottom: Ratio of BANFF-tuned spectrum to the flux-tuned spectrum.

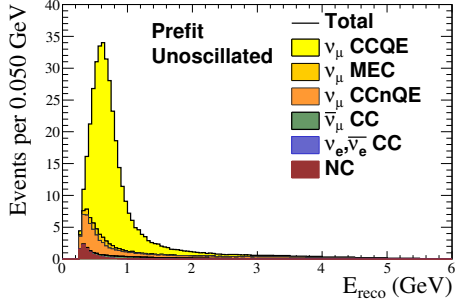


Figure 6.4: Predicted reconstructed-energy spectrum of  $1 \mu$ -like ring events, and contributions from various grouped true neutrino reaction modes, for no oscillations and for an exposure of  $6.91 \times 10^{20}$  POT in neutrino beam mode. The spectrum was generated using the BANFF prefit MC templates.

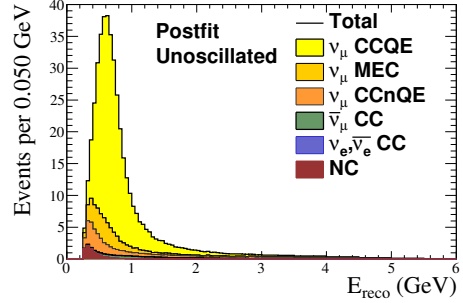


Figure 6.5: Predicted reconstructed-energy spectrum of  $1 \mu$ -like ring events, and contributions from various grouped true neutrino reaction modes, for no oscillations and for an exposure of  $6.91 \times 10^{20}$  POT in neutrino beam mode. The spectrum was generated using the BANFF postfit-tuned MC templates.

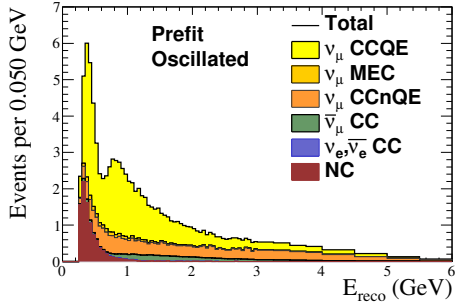


Figure 6.6: Predicted reconstructed-energy spectrum of  $1 \mu$ -like ring events, and contributions from various grouped true neutrino reaction modes, with oscillations for an exposure of  $6.91 \times 10^{20}$  POT in neutrino beam mode. The spectrum was generated using the BANFF prefit MC templates. The spectrum shown was generated assuming the normal hierarchy, and the oscillation parameters shown in Table 5.1. Note that the vertical axis is zoomed in by a factor of more than 4 compared with Figure 6.4.

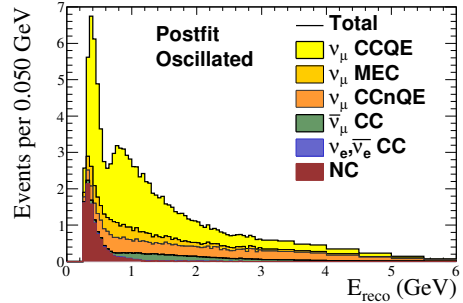


Figure 6.7: Predicted reconstructed-energy spectrum of  $1 \mu$ -like ring events, and contributions from various grouped true neutrino reaction modes, with oscillations for an exposure of  $6.91 \times 10^{20}$  POT in neutrino beam mode. The spectrum was generated using the BANFF postfit-tuned MC templates. The spectrum shown was generated assuming the normal hierarchy, and the oscillation parameters shown in Table 5.1. Note that the vertical axis is zoomed in by a factor of more than 4 compared with Figure 6.5.

## 6.4 Effects of Systematics on the Neutrino-Mode Spectrum

The addition of the neutrino mode muon-like event sample introduces 25 additional flux systematics and 6 extra Super-K efficiency systematics. The new FHC flux systematics are correlated with the RHC flux systematics and the cross-section systematics. The FHC Super-K detector efficiencies are correlated with the RHC efficiencies. The cross-section systematics and Super-K energy scale systematic are shared between the beam modes.

The effects of BANFF postfit errors from the individual systematics are shown in Table 6.3. Table 6.4 summarises the effects of groups of systematics on the final event rate in neutrino beam mode. Percentage uncertainties are given for both the BANFF prefit and postfit errors.

Representative error envelopes are shown in Figures 6.8 to 6.13. These are the  $\pm 1\sigma$  spreads of each bin's content over  $10^5$  toy Monte Carlo experiments generated with randomised systematic parameters. All correlations were taken into account. Figure 6.8 shows the combined effect of the BANFF tune and all systematics on the unoscillated  $E_{reco}$  spectrum's error envelopes, while Figure 6.9 shows the same for the oscillated spectrum. The envelopes for the oscillated spectrum are shown as a ratio to their nominal value in order to demonstrate the relative size of the prefit and postfit uncertainties due to Super-K, flux and cross-section systematics respectively in Figures 6.10, 6.11 and 6.12. A similar envelope with all systematics included can be seen in Figure 6.13. It can be seen that the largest relative reduction in uncertainty is applied to the flux systematics, and that the reduction in relative error size does not vary significantly with the value of  $E_{reco}$ . The equivalent envelopes for the RHC sample can be found in Section 5.4.

Parameter	BANFF tuned +1 $\sigma$	BANFF tuned -1 $\sigma$	BANFF tuned +1 $\sigma$	BANFF tuned -1 $\sigma$
$f_{0;t,r}^{BANFF}$	126.351	0.460 %	125.193	-0.460 %
$f_{1;t,r}^{BANFF}$	126.197	0.338 %	125.348	-0.338 %
$f_{2;t,r}^{BANFF}$	125.892	0.095 %	125.653	-0.095 %
$f_{3;t,r}^{BANFF}$	125.906	0.106 %	125.639	-0.106 %
$f_{4;t,r}^{BANFF}$	126.771	0.794 %	124.773	-0.794 %
$f_{5;t,r}^{BANFF}$	127.021	0.993 %	124.523	-0.993 %
$f_{6;t,r}^{BANFF}$	126.813	0.827 %	124.732	-0.827 %
$f_{7;t,r}^{BANFF}$	126.328	0.442 %	125.216	-0.442 %
$f_{8;t,r}^{BANFF}$	126.224	0.359 %	125.321	-0.359 %
$f_{9;t,r}^{BANFF}$	126.082	0.246 %	125.463	-0.246 %
$f_{10;t,r}^{BANFF}$	125.825	0.042 %	125.719	-0.042 %
$f_{11;t,r}^{BANFF}$	125.791	0.015 %	125.754	-0.015 %
$f_{12;t,r}^{BANFF}$	125.794	0.017 %	125.751	-0.017 %
$f_{13;t,r}^{BANFF}$	125.879	0.085 %	125.666	-0.085 %
$f_{14;t,r}^{BANFF}$	125.935	0.130 %	125.609	-0.130 %
$f_{15;t,r}^{BANFF}$	126.022	0.198 %	125.523	-0.198 %
$f_{16;t,r}^{BANFF}$	125.773	0.000 %	125.772	-0.000 %
$f_{17;t,r}^{BANFF}$	125.773	0.001 %	125.771	-0.001 %
$f_{18;t,r}^{BANFF}$	125.773	0.000 %	125.772	-0.000 %
$f_{19;t,r}^{BANFF}$	125.776	0.003 %	125.769	-0.003 %
$f_{20;t,r}^{BANFF}$	125.777	0.003 %	125.768	-0.003 %
$f_{21;t,r}^{BANFF}$	125.776	0.003 %	125.769	-0.003 %
$f_{22;t,r}^{BANFF}$	125.774	0.002 %	125.770	-0.002 %
$f_{23;t,r}^{BANFF}$	125.773	0.001 %	125.772	-0.001 %
$f_{24;t,r}^{BANFF}$	125.775	0.002 %	125.770	-0.002 %
$f_{Norm_{MEC}}^{BANFF}$	139.613	11.004 %	111.932	-11.004 %
$f_{C_5^A}^{BANFF}$	127.748	1.571 %	123.932	-1.463 %
$f_{Bg_{RES}}^{BANFF}$	126.991	0.969 %	124.700	-0.852 %
$f_{M^{QE}}^{BANFF}$	127.533	1.400 %	123.987	-1.420 %
$f_{M^{RES}}^{BANFF}$	127.376	1.275 %	124.224	-1.231 %
$f_{p_f}^{BANFF}$	124.611	-0.923 %	126.884	0.884 %
$f_{Shape_{CC}^{Coh}}^{BANFF}$	126.274	0.399 %	125.271	-0.399 %
$f_{E_B}^{BANFF}$	125.805	0.026 %	125.750	-0.018 %
$f_{Norm_{CC}^{Coh}}^{BANFF}$	127.062	1.025 %	124.483	-1.025 %
$f_{Norm_{NC}^{Coh}}^{BANFF}$	125.778	0.004 %	125.767	-0.004 %
$f_{Norm_{NC}^{Other}}^{BANFF}$	126.411	0.508 %	125.134	-0.508 %
$f_{Norm_{\nu_e \rightarrow \nu_\mu}}^{BANFF}$	125.781	0.007 %	125.764	-0.007 %
$f_{SK}^{E;r}$	125.772	0.000 %	125.772	-0.000 %
$f_{0;t,r}^{SK+FSI}$	125.927	0.123 %	125.618	-0.123 %
$f_{1;t,r}^{SK+FSI}$	126.374	0.478 %	125.171	-0.478 %
$f_{2;t,r}^{SK+FSI}$	126.534	0.606 %	125.010	-0.606 %
$f_{3;t,r}^{SK+FSI}$	127.961	1.740 %	123.583	-1.740 %
$f_{4;t,r}^{SK+FSI}$	126.210	0.348 %	125.334	-0.348 %
$f_{5;t,r}^{SK+FSI}$	131.439	4.505 %	120.106	-4.505 %

Table 6.3:  $\pm 1\sigma$  effect of the systematic parameters on the total number of SuperK events in neutrino beam mode, using  $4.011 \times 10^{20}$  POT, and the oscillation parameters in Table 5.1. The variations are shown both as the total event rate, and as a percentage change from the event rate with the systematic at its central value (125.772).

Source of uncertainty	$\delta N_{SK}/N_{SK}$ (Unoscillated)	$\delta N_{SK}/N_{SK}$ (Oscillated)
SuperK detector + FSI + SI	2.37%	5.40%
BANFF (prefit)	12.94%	13.15%
BANFF (postfit)	8.94%	8.77%
BANFF (Non-oxygen, postfit)	2.02%	1.94%
BANFF (Oxygen-specific, postfit)	8.58%	8.70%
Total (BANFF prefit)	13.25%	13.15%
Total (BANFF postfit)	8.65%	9.98%

Table 6.4: Effect of  $1\sigma$  variations of the groups of systematics parameters on total number of 1-ring muon-like events in the neutrino beam mode sample. The BANFF parameters considered to be oxygen-specific are Oxygen MEC normalisation, Fermi momentum, Binding energy, CC coherent normalisation and the  $\nu_e/\nu_\mu$  normalisation. The oscillation parameters used are those from Table 5.1.

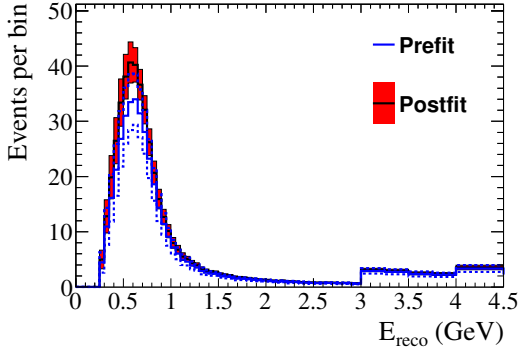


Figure 6.8: Neutrino mode error envelopes for the energy spectrum at SuperK as a result of all systematic parameters. 100k toy MC experiments were generated with randomised systematic parameters and the  $1\sigma$  spread of bin contents was calculated. Correlations were taken into account. No oscillations were applied. Absolute event numbers shown are for  $6.91 \times 10^{20}$  POT.

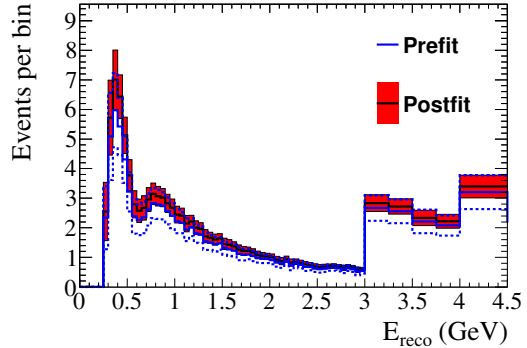


Figure 6.9: Neutrino mode error envelopes for the energy spectrum at SuperK as a result of all systematic parameters. 100k toy MC experiments were generated with randomised systematic parameters and the  $1\sigma$  spread of bin contents was calculated. Correlations were taken into account. Oscillations were applied with the parameter values shown in Table 5.1. Absolute event numbers shown are for  $6.91 \times 10^{20}$  POT.

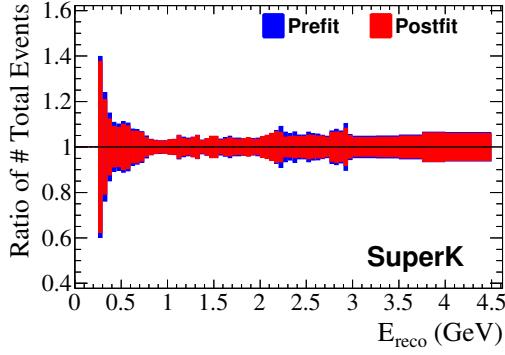


Figure 6.10: Neutrino mode error envelopes, expressed as a fraction of event count, for the energy spectrum as a result of Super-K detector and FSI/SI systematics. 100k toy MC experiments were generated with randomised systematic parameters and the  $1\sigma$  spread of bin contents was calculated. Correlations were taken into account. Oscillations were applied with the parameter values shown in Table 5.1. The near-detector fit does not reduce the size of the uncertainties on these systematics, but the changes in the spectrum shape and composition lead to a small reduction in relative uncertainty.

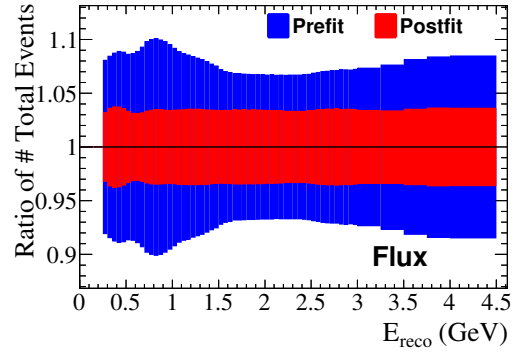


Figure 6.11: Neutrino mode error envelopes, expressed as a fraction of event count, for the energy spectrum as a result of the BANFF flux systematics. 100k toy MC experiments were generated with randomised systematic parameters and the  $1\sigma$  spread of bin contents was calculated. Correlations were taken into account. Oscillations were applied with the parameter values shown in Table 5.1.

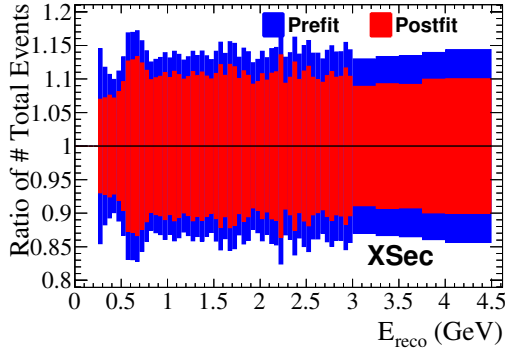


Figure 6.12: Neutrino mode error envelopes, expressed as a fraction of event count, for the energy spectrum as a result of the BANFF cross-section systematics. 100k toy MC experiments were generated with randomised systematic parameters and the  $1\sigma$  spread of bin contents was calculated. Correlations were taken into account. Oscillations were applied with the parameter values shown in Table 5.1.

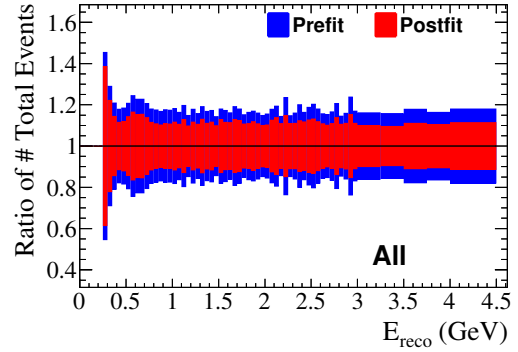


Figure 6.13: Neutrino mode error envelopes, expressed as a fraction of event count, for the energy spectrum as a result of all systematics. 100k toy MC experiments were generated with randomised systematic parameters and the  $1\sigma$  spread of bin contents was calculated. Correlations were taken into account. Oscillations were applied with the parameter values shown in Table 5.1.

## 6.5 Validation of the Oscillation Fitter for the NSI Hypothesis

The fits for NSI were performed using the fitting software package developed for the  $\overline{\nu}_\mu$  disappearance analysis, and validation of the software for that analysis can be seen in Section 5.6. However, the joint neutrino-mode and antineutrino-mode NSI fit adds 25 flux systematics, 6 detector systematics and the NSI parameter  $\varepsilon_{\mu\tau}$  itself.

Similarly to the validation of the disappearance analysis, ensembles of 5000 toy experiments were generated with statistical fluctuations and systematic parameters randomised according to their priors. These were generated at 27 points in the oscillation parameter space, using all the combinations of three values for each of the oscillation parameters. The parameter values used were  $\sin^2 \theta_{23} = 0.35$ ,  $\sin^2 \theta_{23} = 0.527$  and  $\sin^2 \theta_{23} = 0.65$ ,  $|\Delta m_{32}^2| = 2.2$ ,  $|\Delta m_{32}^2| = 2.5$  and  $|\Delta m_{32}^2| = 2.8 \times 10^{-3}$  eV<sup>2</sup> and  $\varepsilon_{\mu\tau} = -0.5$ ,  $\varepsilon_{\mu\tau} = 0.0$  and  $\varepsilon_{\mu\tau} = 0.5$ . These were fitted using MINUIT and HESSE errors were calculated. The parameter  $\varepsilon_{\mu\tau}$  behaved as desired. Three sets of best-fit parameter values can be seen in Figure 6.14, while Figure 6.15 shows the distribution of their pull values. For each toy experiment  $i$  and parameter  $f$  with true value  $x_{f,i,true}$ , fitted value  $x_{f,i,fitted}$  and HESSE uncertainty  $\sigma_{f,i,Hesse}$ , the pull  $P_{f,i}$  is calculated according the following formula:

$$P_{f,i} = \frac{x_{f,i,fitted} - x_{f,i,true}}{\sigma_{f,i,Hesse}} \quad (6.10)$$

The new flux and Super-K parameters also behaved as expected. A summary of their pull distributions can be seen in Figure 6.16. The systematic parameters behave as expected, with the pull distributions forming a Gaussian with a mean of 0 with the exception of a slightly biased mean in the Super-K NC systematic ( $f_{5;t;r}^{SK+FSI}$ ). This effect is explained in Section 5.6.2. The  $\nu_e$  CC systematic  $f_{5;t;r}^{SK+FSI}$  has a low pull RMS due to the full correlation with the equivalent RHC parameter, which can be seen in Figure 4.38. This parameter was fixed as it adds no additional freedom to the fit.

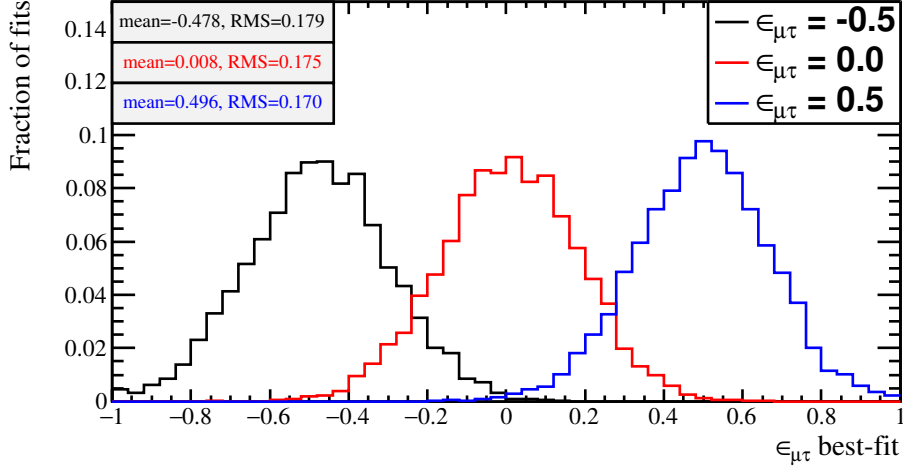


Figure 6.14: Distributions of the best-fit values of  $\epsilon_{\mu\tau}$  from 5k toy MC experiments generated at  $\epsilon_{\mu\tau} = 0$  and  $\epsilon_{\mu\tau} \pm 0.5$  including statistical fluctuations and randomised systematics. The other oscillation parameters are fixed at their values in Table 5.1, and the normal mass hierarchy is assumed. The fits were performed with the T2K target POT ( $7.8 \times 10^{21}$ ) divided equally between neutrino and antineutrino mode.

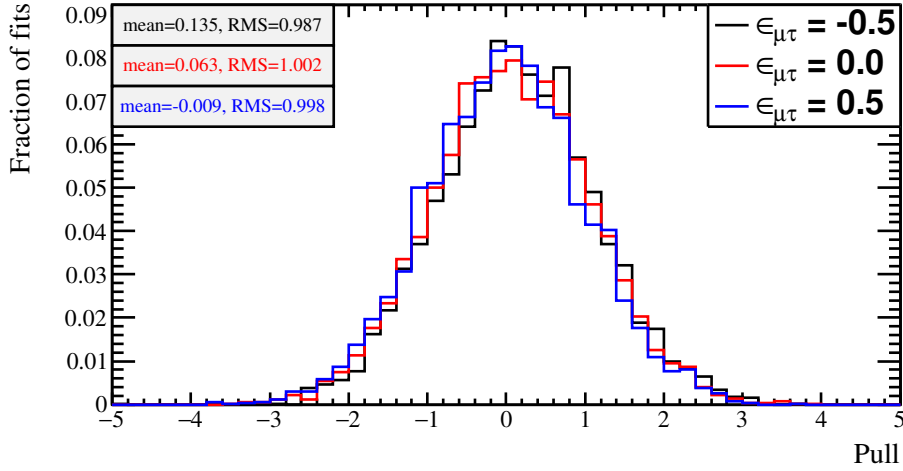


Figure 6.15: Distributions of the pulls of  $\epsilon_{\mu\tau}$  from 5k toy MC experiments generated at  $\epsilon_{\mu\tau} = 0$  and  $\epsilon_{\mu\tau} \pm 0.5$  including statistical fluctuations and randomised systematics. The other oscillation parameters are fixed at their values in Table 5.1, and the normal mass hierarchy is assumed. The fits were performed with the T2K target POT ( $7.8 \times 10^{21}$ ) divided equally between neutrino and antineutrino mode.

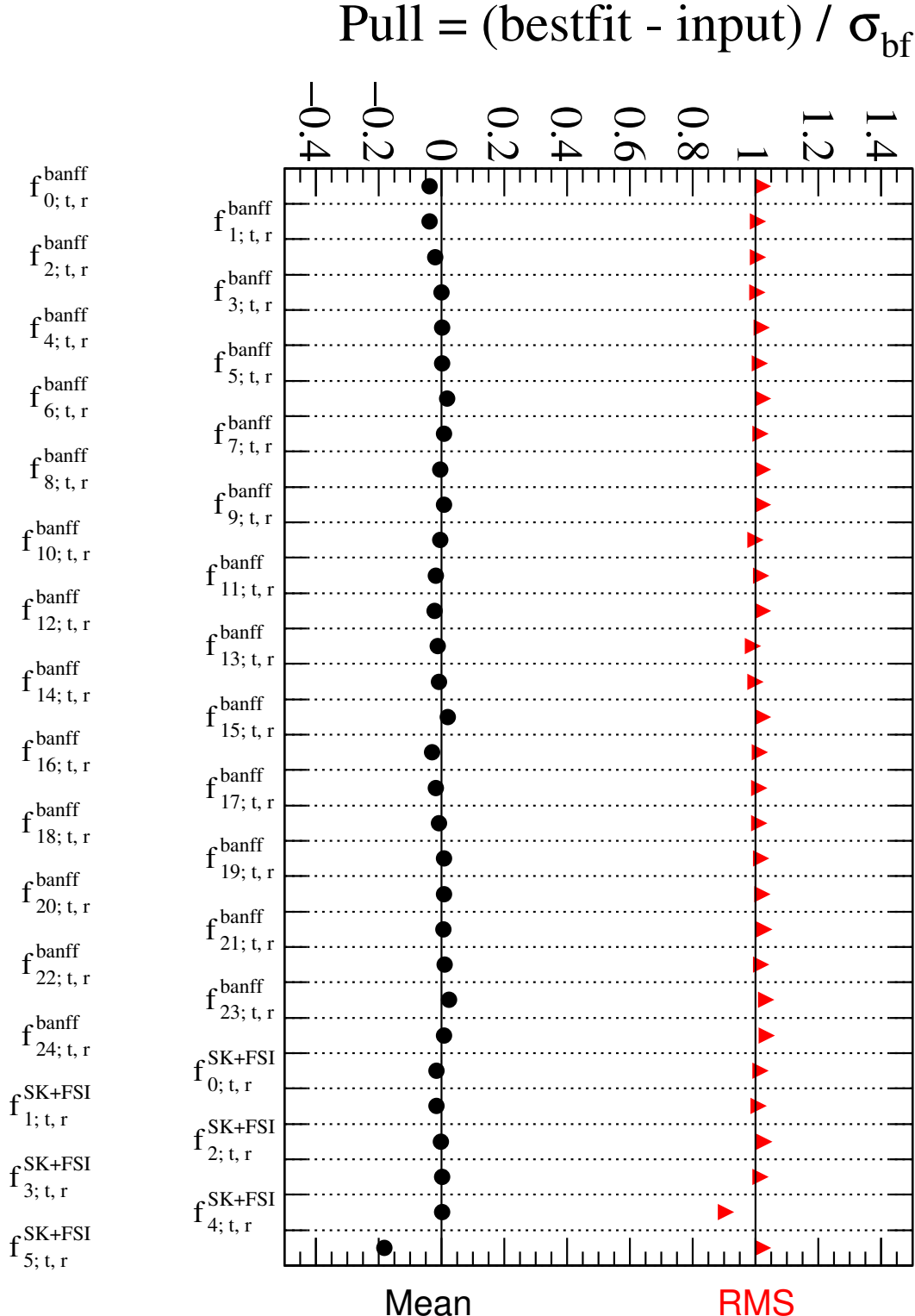


Figure 6.16: Summary of systematic pull distributions for FHC-specific systematic parameters for 5k toy MC experiments with the current T2K data POT:  $6.91 \times 10^{20}$  in neutrino mode and  $4.011 \times 10^{20}$  in antineutrino mode. The RHC and common parameters all appear similar to their distributions in Figure 5.18 and have been left out for clarity. Statistical fluctuations are included, and systematic parameters are randomised according to their priors. Black circles show the mean of the pull, while red triangles show the RMS.  $|\Delta m_{32}^2|$ ,  $\sin^2 \theta_{23}$  and  $\varepsilon_{\mu\tau}$  were fitted. All other oscillation parameters were fixed at their true values. The normal mass hierarchy is assumed.

## 6.6 Method for Construction of Confidence Regions

The method used for the construction of confidence regions for the NSI parameter  $\varepsilon_{\mu\tau}$  is similar to the method used for the muon antineutrino disappearance study described in Section 5.7. For the NSI parameter, the primary result is a 1d confidence region in the range  $-1 \leq \varepsilon_{\mu\tau} \leq 1$  with 201 evenly spaced bins. The fit is performed with  $\varepsilon_{\mu\tau}$  free, to find the unbinned best-fit point with a  $\chi^2$  of  $\chi^2_{min}$ . The fit is then re-run with  $\varepsilon_{\mu\tau}$  fixed to the value of every bin  $i$ , giving a value for  $\chi^2_i$ .

For each fit, MINUIT is run twice, first in the upper octant in mixing angle (starting at  $\sin^2 \theta_{23} = 0.6$ ) and then in the lower octant (starting at  $\sin^2 \theta_{23} = 0.4$ ). The lower  $\chi^2$  of these two fits is used. This means that a hypothetical dataset could have  $\sin^2 \theta_{23}$  best-fit points in different octants in neighbouring  $\varepsilon_{\mu\tau}$  bins, although this has never been observed in any fitted dataset.

For the NSI analysis, two different results are measured. The first is a T2K-only data fit, in which  $|\Delta m^2_{32}|$  and  $\sin^2 \theta_{23}$  are profiled with no prior constraint, and all systematics are profiled according to their prior constraint. For the remainder of this document, this fit will be referred to ‘flat prior’. The second fit uses a constraint on the values of the standard muon-neutrino disappearance parameters from the MINOS experiment [39]. A penalty term is added to the  $\chi^2$  described in Equation 5.2, according to a Gaussian with  $\sin^2 2\theta_{23} = 0.950 \pm 0.036$  and  $|\Delta m^2_{32}| = 2.41 \pm 0.10$ . Note that while we fit the single angle parameter  $\sin^2 \theta_{23}$ , the constraint is calculated based on a Gaussian in  $\sin^2 2\theta_{23}$ , as this is the measurement published by MINOS. This fit will be referred to as the ‘MINOS prior’. It should be noted that the MINOS data was fitted assuming standard oscillations. If NSI effects are real, they would also have an effect on this measurement, altering the prior probability. The fit with the MINOS prior should be interpreted as an indication of the result a combined MINOS/T2K fit would achieve, rather than a completely robust measurement of  $\varepsilon_{\mu\tau}$ .

By performing the fit with  $\varepsilon_{\mu\tau}$  fixed and the nuisance parameters free, a value for  $\chi^2_i$  can be calculated, which is dependent only on  $\varepsilon_{\mu\tau}$ . The value of  $\Delta\chi^2$  is calculated at each point ( $i$ ) in the parameter space:

$$\Delta\chi^2_i = \chi^2_i - \chi^2_{min} \quad (6.11)$$

Reference values  $\Delta\chi^2_{crit}$  are then used to define the edge of the region of given confidence level. Any point in  $\varepsilon_{\mu\tau}$  for which  $\Delta\chi^2_i < \Delta\chi^2_{crit}$  is considered to be inside the confidence region. The  $\Delta\chi^2_{crit}$  values used are the same as those in the used in the muon antineutrino disappearance analysis, shown in Table 5.9.

## 6.7 Expected Sensitivity for Current and Future Datasets

As described in Section 6.7, sensitivities were calculated using the Asimov dataset method.

In this analysis, the Asimov dataset is the expected Super-K  $E_{reco}$  spectrum with all parameters at their prior central values, and without any statistical fluctuations applied. The standard oscillation values from Table 5.1 are used. Figure 6.17 and Figure 6.18 shows the expected sensitivity using the prior oscillation values for T2K’s current accumulated POT, and projected final POT respectively.

The expected sensitivity at 90% confidence with current data was calculated as  $-0.825 < \varepsilon_{\mu\tau} < 0.775$  using a T2K only fit, and  $-0.645 < \varepsilon_{\mu\tau} < 0.725$  using MINOS constraints on  $\sin^2 \theta_{23}$  and  $|\Delta m_{32}^2|$ . At T2K’s projected final POT, the sensitivity with current systematic uncertainties was calculated to be  $-0.285 < \varepsilon_{\mu\tau} < 0.285$ , with little added sensitivity from the MINOS prior. Removing the systematic uncertainties, this sensitivity is improved to  $-0.265 < \varepsilon_{\mu\tau} < 0.265$ .

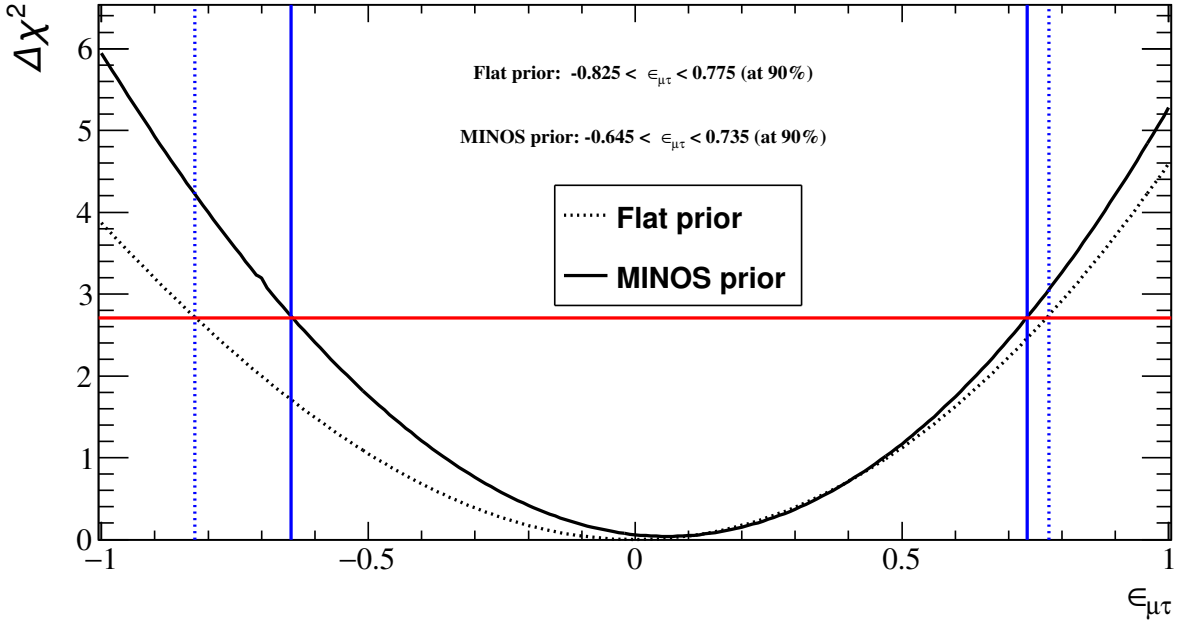


Figure 6.17: T2K expected sensitivity to  $\epsilon_{\mu\tau}$  for a true value of  $\epsilon_{\mu\tau} = 0$ , using T2K's current POT ( $6.91 \times 10^{20}$  FHC POT,  $4.011 \times 10^{20}$  RHC POT). The normal hierarchy is assumed, as are the oscillation parameters in Table 5.1. The 90% confidence regions constructed using the constant  $\Delta\chi^2$  technique are shown for a T2K only fit with free  $\sin^2 \theta_{23}$  and  $|\Delta m_{32}^2|$ , and for a fit using the MINOS constraint on  $\sin^2 \theta_{23}$  and  $|\Delta m_{32}^2|$ .

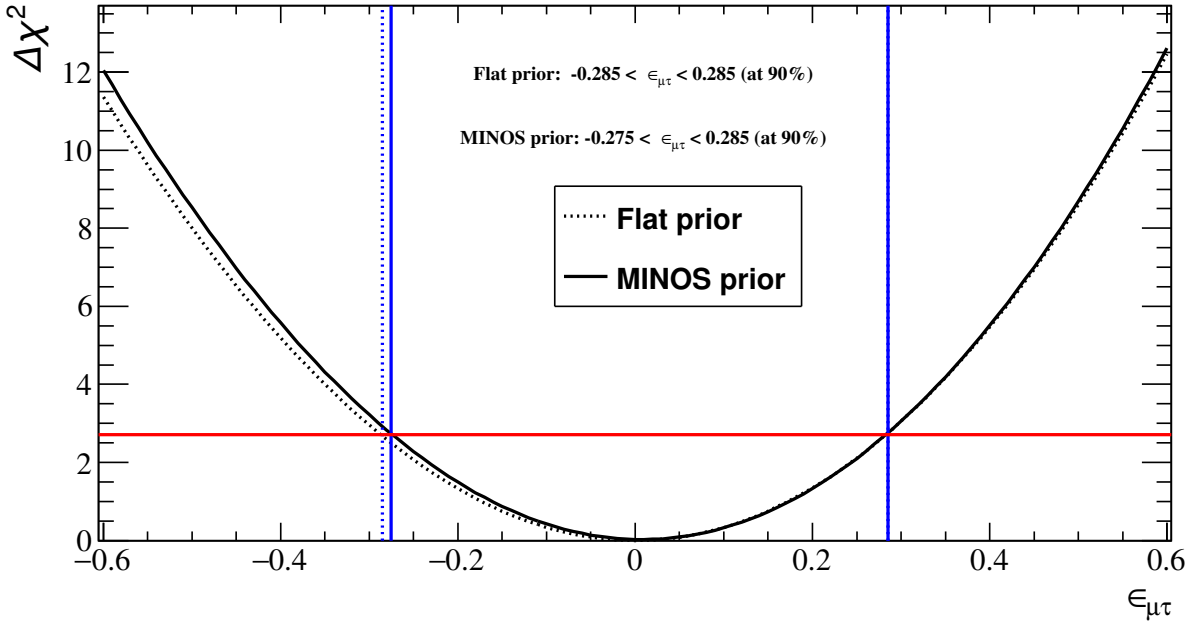


Figure 6.18: T2K expected sensitivity to  $\epsilon_{\mu\tau}$  for a true value of  $\epsilon_{\mu\tau} = 0$ , using T2K's projected final POT ( $7.8 \times 10^{21}$ ) divided equally between FHC and RHC beam mode. The normal hierarchy is assumed, as are the oscillation parameters in Table 5.1. The 90% confidence regions constructed using the constant  $\Delta\chi^2$  technique are shown for a T2K only fit with free  $\sin^2 \theta_{23}$  and  $|\Delta m_{32}^2|$ , and for a fit using the MINOS constraint on  $\sin^2 \theta_{23}$  and  $|\Delta m_{32}^2|$ .  
 140

## 6.8 Results of the Non-standard Matter Interactions Analysis

### 6.8.1 Best-fit Oscillation Parameters

T2K’s entire Run 1-6 dataset was analysed using the method described in Section 6.2, totalling  $6.91 \times 10^{20}$  POT in neutrino beam mode and  $4.011 \times 10^{20}$  POT in antineutrino beam mode. Two different sets of fits were performed, one applying an external constraint from MINOS to the parameters  $\sin^2 \theta_{23}$  and  $|\Delta m_{32}^2|$ , and another with these parameters left unconstrained.

A summary is given of the best-fit oscillation parameters,  $\chi^2$  and p-values in Table 6.5. All of the fit results are compatible with  $\varepsilon_{\mu\tau} = 0$ . The data and best-fit spectra are shown in Figures 6.19 and 6.20 for neutrino mode and antineutrino mode respectively.

Fit	$\sin^2 \theta_{23}$	$ \Delta m_{32}^2 $ or $ \overline{\Delta m_{31}^2} $	$\varepsilon_{\mu\tau}$	$\chi^2_{bf}/NDOF$	p-value
Flat prior (normal)	0.514	$2.506 \times 10^{-3}$	0.021	122.57 / 143	0.90
Flat prior (inverted)	0.511	$2.553 \times 10^{-3}$	-0.019	122.57 / 143	0.87
MINOS prior (normal)	0.556	$2.508 \times 10^{-3}$	0.041	124.11 / 145	0.75
MINOS prior (inverted)	0.554	$2.525 \times 10^{-3}$	-0.128	124.24 / 145	0.73

Table 6.5: Summary of best-fit parameters from the fits of the combined full T2K Run 1-6 dataset. The quoted best-fit  $\chi^2$  values ( $\chi^2_{bf}$ ) were computed from Equation 5.2. The table also shows the p-values obtained from the goodness-of-fit test described in Section 6.8.2. As described in that section, these p-values do not necessarily correspond to the  $\chi^2/NDOF$  values in this table.

### 6.8.2 Goodness-of-fit Tests

Goodness-of-fit tests were performed for the fits of the real data as described in Section 5.5. The results for the fit using the MINOS constraint are shown in Figures 6.21 and 6.22. The p-values are 0.75 for the normal hierarchy fit, and 0.73 for the inverted hierarchy, indicating that both results are plausible. The fitted number of degrees of freedom is 9, as expected given 10 bins and a single unconstrained parameter. For the fits performed without the MINOS constraint, the p-values are 0.90 and 0.87 for normal and inverted hierarchy respectively.

### 6.8.3 Confidence regions

Confidence regions for the data fit are shown in Figure 6.23 and Figure 6.24 for the normal hierarchy and inverted hierarchy respectively. The confidence regions are consistent

with a value for  $\varepsilon_{\mu\tau}$  of zero, and there is a clear improvement in sensitivity using the external constraint on  $\sin^2 \theta_{23}$  and  $|\Delta m_{32}^2|$ . A comparison between the fitted normal hierarchy data result and the expected sensitivity can be seen in Figures 6.25 and 6.26 for the fits with and without the MINOS constraint. The data is very similar to the predicted sensitivity, as would be expected given that the oscillation parameters used for this sensitivity study come from a fit to the FHC component of the data being fitted here.

## 6.9 Summary

Using the combined neutrino and antineutrino beam mode datasets from T2K, it is possible to perform fits to non-standard neutrino interaction models. Studies were performed evaluating the sensitivity of the T2K experiment to matter effects on muon neutrino and antineutrino disappearance which would lead to a difference in survival probability, in terms of a parameter  $\varepsilon_{\mu\tau}$ .

The expected sensitivity at 90% confidence with current data was calculated as  $-0.825 < \varepsilon_{\mu\tau} < 0.775$  using a T2K-only data, and  $-0.645 < \varepsilon_{\mu\tau} < 0.725$  using a constraint on  $\sin^2 \theta_{23}$  and  $|\Delta m_{32}^2|$  from the MINOS experiment. Given the T2K projected final POT, T2K can achieve a sensitivity of  $-0.285 < \varepsilon_{\mu\tau} < 0.285$  with current systematic parameters, or  $-0.265 < \varepsilon_{\mu\tau} < 0.265$  in a statistics-only fit. These studies demonstrated that T2K is less sensitive to these effects than MINOS, which used a wide-band beam and thus had access to more events in the tail of the  $E_{reco}$  spectrum, as well as a significantly longer baseline leading to stronger matter effects, and a magnetised far detector allowing separation of events caused by neutrinos and antineutrinos, which Super-K is currently not capable of.

The T2K run 1 to 6 data was fitted, and set a limit at 90% confidence of  $-0.925 < \varepsilon_{\mu\tau} < 0.825$  with no external constraint on the disappearance parameters, and  $-0.695 < \varepsilon_{\mu\tau} < 0.725$  using the MINOS constraint on  $\sin^2 \theta_{23}$  and  $|\Delta m_{32}^2|$ . These values are consistent with no non-standard matter interactions, as well as consistent with other experiments [126, 127].

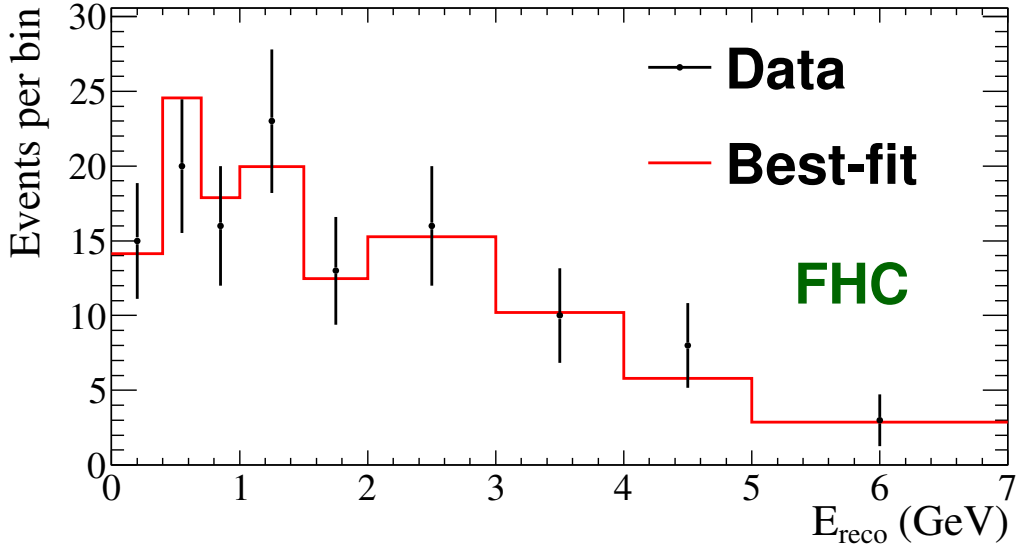


Figure 6.19: The Run 5+6 single  $\mu$ -like ring  $6.91 \times 10^{20}$  POT neutrino-mode dataset and the best-fit reconstructed energy spectrum when fitting the NSI hypothesis with the MINOS prior. For clarity, a coarser binning is used in this figure than in the fit. The normal mass hierarchy is assumed.

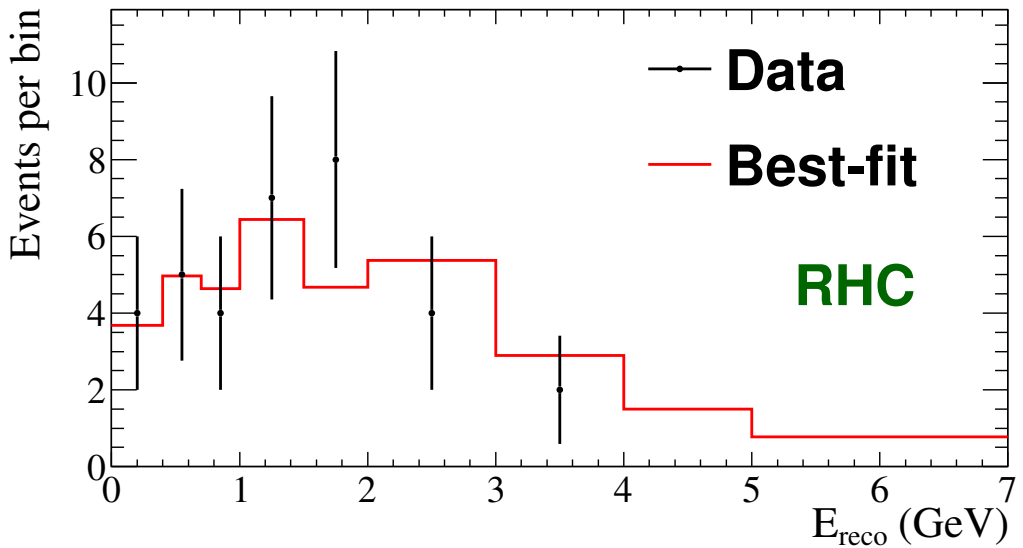


Figure 6.20: The Run 5+6 single  $\mu$ -like ring  $4.011 \times 10^{20}$  POT antineutrino-mode dataset and the best-fit reconstructed energy spectrum when fitting the NSI hypothesis with the MINOS prior. For clarity, a coarser binning is used in this figure than in the fit. The normal mass hierarchy is assumed.

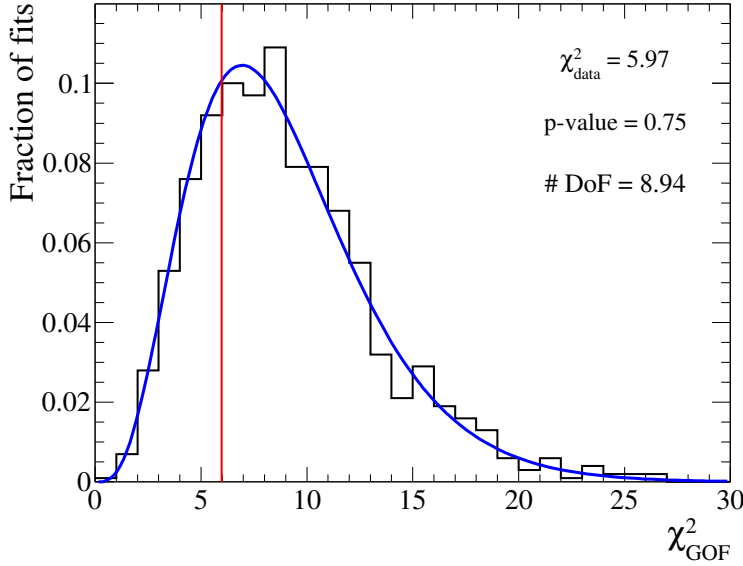


Figure 6.21: Distribution of  $\chi^2_{\text{gof}}$ , the goodness-of-fit (gof)  $\chi^2$ , from 1k toy MC experiments whose true input values are the best-fit oscillation parameters from the fit of the real data for the normal hierarchy ( $\varepsilon_{\mu\tau} = 0.041$ ,  $\sin^2 \theta_{23} = 0.556$ ,  $|\Delta m_{32}^2| = 2.508 \times 10^{-3} \text{ eV}^2$ ). The MINOS constraint was used. Systematic variations and statistical fluctuations are applied to the toy datasets, and all 44 systematic parameters are included in the fits. The  $\chi^2$  value from the fit of the real data assuming the normal mass hierarchy (with all 44 systematic parameters included in the fit) is shown as a red line. A  $\chi^2$  distribution with a fitted number of degrees of freedom is shown in blue.

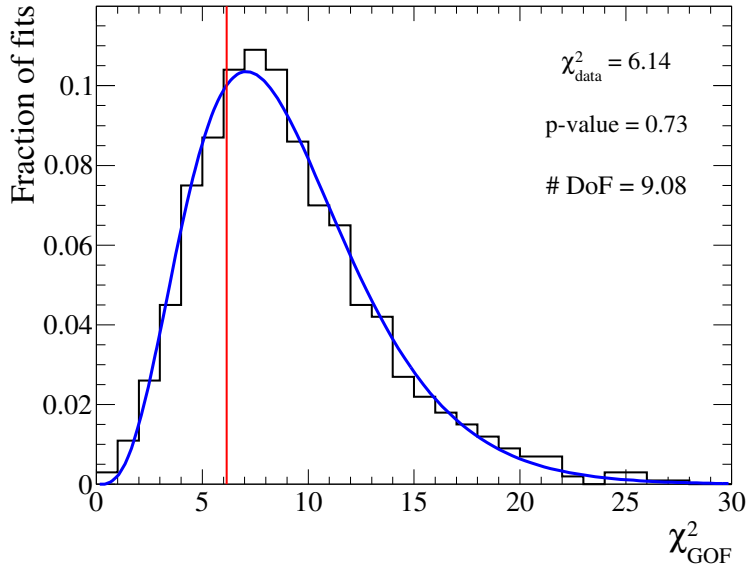


Figure 6.22: Distribution of  $\chi^2_{\text{gof}}$ , the goodness-of-fit (gof)  $\chi^2$ , from 1k toy MC experiments whose true input values are the best-fit oscillation parameters from the fit of the real data for the inverted hierarchy ( $\varepsilon_{\mu\tau} = -0.128$ ,  $\sin^2 \theta_{23} = 0.554$ ,  $|\Delta m_{32}^2| = 2.525 \times 10^{-3} \text{ eV}^2$ ). The MINOS constraint was used. Systematic variations and statistical fluctuations are applied to the toy datasets, and all 44 systematic parameters are included in the fits. The  $\chi^2$  value from the fit of the real data assuming the inverted mass hierarchy (with all 44 systematic parameters included in the fit) is shown as a red line. A  $\chi^2$  distribution with a fitted number of degrees of freedom is shown in blue.

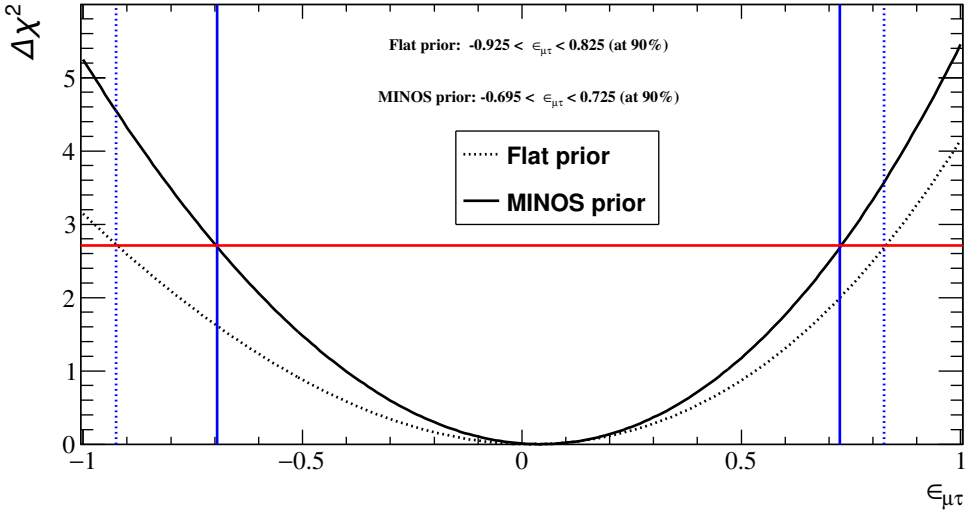


Figure 6.23: Results of the T2K Run 1 to 6 data fit for the NSI parameter  $\epsilon_{\mu\tau}$ , in the normal mass hierarchy. Results are shown both with and without a MINOS constraint on  $\sin^2 \theta_{23}$  and  $|\Delta m_{32}^2|$ . The single parameter 90% CL allowed intervals are  $-0.925 < \epsilon_{\mu\tau} < 0.825$  (with flat prior) and  $-0.695 < \epsilon_{\mu\tau} < 0.725$  (with MINOS prior).

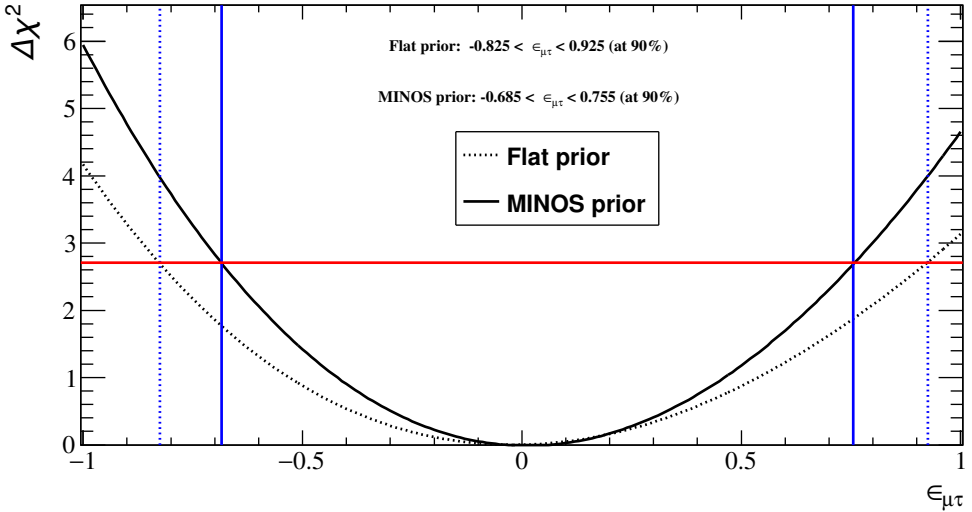


Figure 6.24: Results of the T2K Run 1 to 6 data fit for the NSI parameter  $\epsilon_{\mu\tau}$ , in the inverted mass hierarchy. Results are shown both with and without a MINOS constraint on  $\sin^2 \theta_{23}$  and  $|\Delta m_{32}^2|$ . The single parameter 90% CL allowed intervals are  $0.825 < \epsilon_{\mu\tau} < 0.925$  (with flat prior) and  $-0.685 < \epsilon_{\mu\tau} < 0.755$  (with MINOS prior).

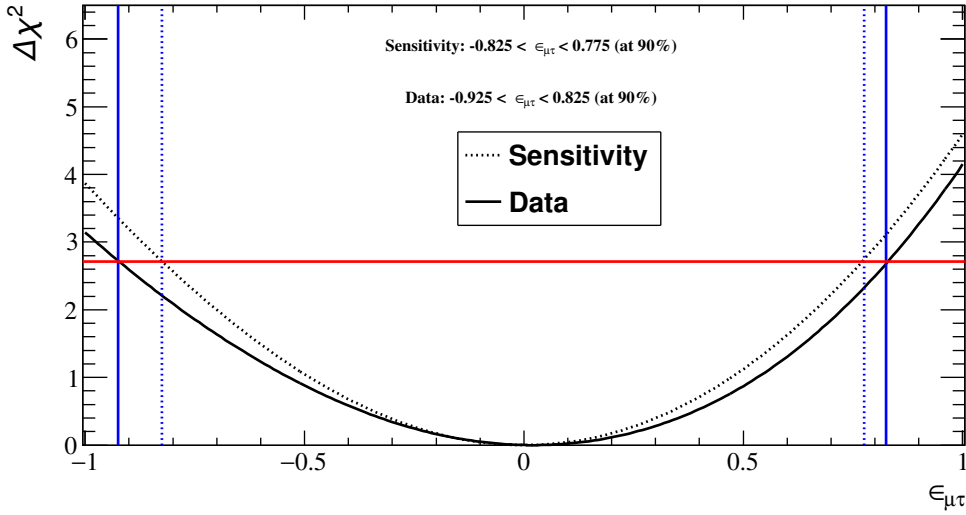


Figure 6.25: Results of the T2K Run 1 to 6 data fit for the NSI parameter  $\varepsilon_{\mu\tau}$ , in the normal mass hierarchy, compared to the expected sensitivity. No constraint was put on  $\sin^2 \theta_{23}$  and  $|\Delta m_{32}^2|$ .

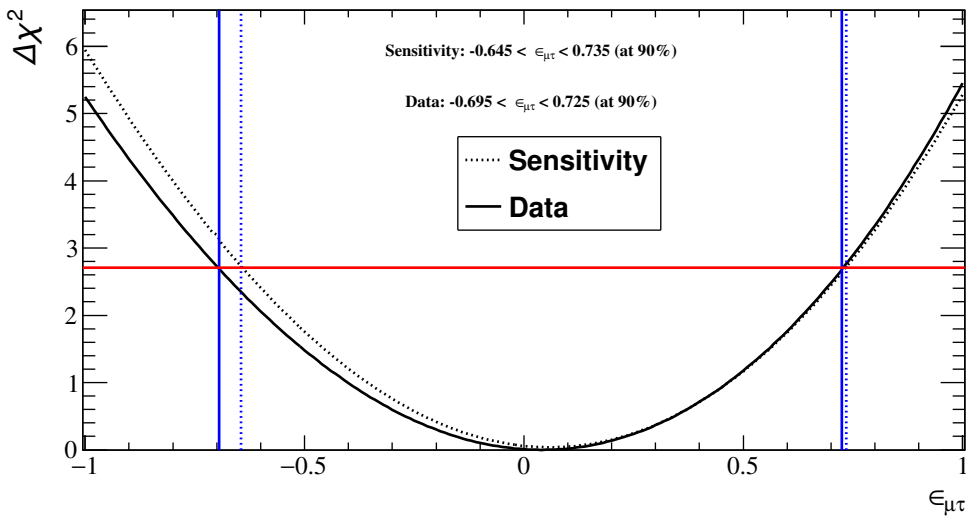


Figure 6.26: Results of the T2K Run 1 to 6 data fit for the NSI parameter  $\varepsilon_{\mu\tau}$ , in the normal mass hierarchy, compared to the expected sensitivity.  $\sin^2 \theta_{23}$  and  $|\Delta m_{32}^2|$  were constrained using the published results from MINOS, as described in Section 6.6.

## Chapter 7

# Conclusions and Outlook

This thesis presents two analyses of the T2K beam data, both of which fit the muon-like reconstructed energy spectrum at Super-K. The first uses only the antineutrino beam mode dataset collected by June 2015, totalling  $4.011 \times 10^{20}$  protons on target. With an unoscillated expectation of 103.6 events and an observation of 34 events, the antineutrino oscillation parameters were measured to be  $0.327 < \overline{\sin^2 \theta_{23}} < 0.692$  ( $0.332 < \overline{\sin^2 \theta_{23}} < 0.697$ ) and  $2.03 \times 10^{-3} \text{ eV}^2 < \overline{|\Delta m_{32}^2|} < 2.92 \times 10^{-3} \text{ eV}^2$  and ( $2.03 \times 10^{-3} \text{ eV}^2 < \overline{|\Delta m_{31}^2|} < 2.92 \times 10^{-3} \text{ eV}^2$ ) for the normal (inverted) hierarchy. The T2K data gives a world leading measurement on  $\overline{\sin^2 \theta_{23}}$ , and rules out  $\overline{\sin^2 \theta_{23}} = 0$  at  $7.3\sigma$ .

The second analysis uses similar techniques to test the hypothesis of nonstandard neutrino-matter interactions (NSI), which could lead to a difference between the survival probabilities  $P(\nu_\mu \rightarrow \nu_\mu)$  and  $P(\overline{\nu}_\mu \rightarrow \overline{\nu}_\mu)$ . This analysis simultaneously fits the  $6.91 \times 10^{20}$  POT neutrino-mode sample and the  $4.011 \times 10^{20}$  anti-neutrino mode sample. We find no evidence for NSI. The future sensitivity of T2K to NSI has been evaluated, showing that with the expected final POT delivered, we expect to be able to set limits of  $-0.925 < \varepsilon_{\mu\tau} < 0.825$  at 90% confidence without an external constraint.

T2K will continue to collect data toward a final goal of  $7.8 \times 10^{21}$  POT, and will perform measurements of  $\nu_\mu$  disappearance and  $\nu_e$  appearance to even greater precision. With  $7.8 \times 10^{21}$  POT divided equally between neutrino and antineutrino beam modes, T2K should achieve a  $1\sigma$  resolution of 0.054 on  $\overline{\sin^2 \theta_{23}}$  and  $0.045 \times 10^{-3} \text{ eV}^2$  on  $\overline{|\Delta m_{32}^2|}$  [63]. The methods and software developed for this analysis will be used to constrain  $\delta_{CP}$  at T2K. Joint analysis using the T2K and NO $\nu$ A datasets will allow improved limits to be set on the  $\delta_{CP}$  and stronger hints about the neutrino mass hierarchy. The combination of the two datasets can exclude  $\delta_{CP} = 0$  at 90% confidence for an approximately  $60^\circ$  range of true  $\delta_{CP}$  values, although the exact range which can be excluded is dependent on the other oscillation parameters and the hierarchy. The next generation of neutrino experiments including DUNE and HyperKamiokande experiments are currently in development, and will provide ever more data to resolve these open questions.

## Appendix A

# Interaction Modes in the Analysis

- **$\nu_\mu$  CCQE.** A muon neutrino interacts with a neutron, producing a proton and a negatively charged muon. This interaction is the main signal mode for T2K FHC disappearance studies.
- **$\nu_\mu$  CC MEC.** A muon neutrino interacts with multiple nucleons in the nucleus, producing a negatively charged muon and other nucleons which are not seen by Super-K. These events are considered CCQE-like.
- **$\nu_\mu$  CC1 $\pi$ .** A muon neutrino interacts with a nucleon, to produce a final state with a negatively charged muon and a pion. This category includes three different interactions:
  - ★  $\nu_\mu + p \rightarrow \mu^- + p + \pi^+$
  - ★  $\nu_\mu + n \rightarrow \mu^- + p + \pi^0$
  - ★  $\nu_\mu + n \rightarrow \mu^- + n + \pi^+$
- **$\nu_\mu$  CC coherent.** A muon neutrino interacts coherently with the entire nucleus, producing a negative muon and a positive pion, leaving the original nucleus intact.
- **$\nu_\mu$  CC other.** Other interactions where a muon neutrino produces a negative muon.
- **$\nu_\alpha$  NC1 $\pi^\pm$ .** A neutrino interacts with a nucleon, changing the nucleon type and producing a charged pion.
- **$\nu_\alpha$  NC1 $\pi^0$ .** A neutrino interacts with a nucleon, producing a neutral pion.
- **$\nu_\alpha$  NC other.** Other neutral current neutrino interactions.

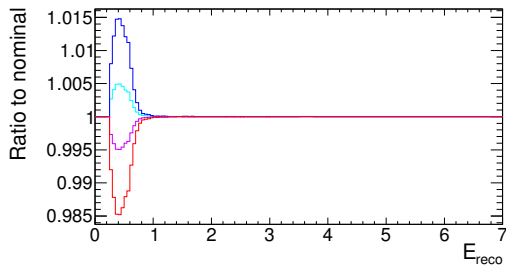
- **$\overline{\nu}_\mu$  CCQE.** A muon antineutrino interacts with a proton, producing a neutron and a positively charged muon. This interaction is the main signal mode for the RHC disappearance study in this thesis.
- **$\overline{\nu}_\mu$  CC MEC.** A muon antineutrino interacts with multiple nucleons in the nucleus, producing a positively charged muon and other nucleons which are not seen by Super-K. These events are considered CCQE-like.
- **$\overline{\nu}_\mu$  CC1 $\pi$ .** A muon antineutrino interacts with a nucleon, to produce a final state with a positively charged muon and a pion. This category includes three different interactions:
  - ★  $\overline{\nu}_\mu + n \rightarrow \mu^+ + n + \pi^-$
  - ★  $\overline{\nu}_\mu + p \rightarrow \mu^+ + n + \pi^0$
  - ★  $\overline{\nu}_\mu + p \rightarrow \mu^+ + p + \pi^-$
- **$\overline{\nu}_\mu$  CC coherent.** A muon antineutrino interacts coherently with the entire nucleus, producing a positively charged muon and a negative pion.
- **$\overline{\nu}_\mu$  CC other.** Other muon antineutrino interactions which produce a positive muon.
- **$\overline{\nu}_\alpha$  NC1 $\pi^\pm$ .** An antineutrino interacts with a nucleon, changing the nucleon type and producing a charged pion.
- **$\overline{\nu}_\alpha$  NC1 $\pi^0$ .** An antineutrino interacts with a nucleon, producing a neutral pion.
- **$\overline{\nu}_\alpha$  NC other.** Other neutral current antineutrino interactions.
- **$\nu_e$  CCQE.** An electron neutrino interacts with a neutron, producing a proton and an electron. This interaction is the main signal mode for T2K FHC appearance studies.
- **$\nu_e$  CC MEC.** An electron neutrino interacts with multiple nucleons in the nucleus, producing an electron and other nucleons which are not seen by Super-K. These events are considered CCQE-like.
- **$\nu_e$  CC1 $\pi$ .** An electron neutrino interacts with a nucleon, to produce a final state with an electron, any pion and a nucleon.
- **$\nu_e$  CC coherent.** An electron neutrino interacts coherently with the entire nucleus, producing an electron and a positive pion, leaving the original nucleus intact.
- **$\nu_e$  CC other.** Other interactions where an electron neutrino produces an electron.

- **$\bar{\nu}_e$  CCQE.** An electron antineutrino interacts with a proton, producing a neutron and a positron. This interaction is the main signal mode for the T2K appearance studies.
- **$\bar{\nu}_e$  CC MEC.** An electron neutrino interacts with multiple nucleons in the nucleus, producing a positron and other nucleons which are not seen by Super-K. These events are considered CCQE-like.
- **$\bar{\nu}_e$  CC1 $\pi$ .** An electron antineutrino interacts with a nucleon, to produce a final state with a positron, any pion and a nucleon.
- **$\bar{\nu}_e$  CC coherent.** An electron antineutrino interacts coherently with the entire nucleus, producing a positron and a negative pion.
- **$\bar{\nu}_e$  CC other.** Other electron antineutrino interactions which produce a positron.
- **Oscillated  $\nu_e$  CCQE.**
- **Oscillated  $\nu_e$  CC MEC.**
- **Oscillated  $\nu_e$  CC1 $\pi$ .**
- **Oscillated  $\nu_e$  CC coherent.**
- **Oscillated  $\nu_e$  CC other.**
- **Oscillated  $\bar{\nu}_e$  CCQE.**
- **Oscillated  $\bar{\nu}_e$  CC MEC.**
- **Oscillated  $\bar{\nu}_e$  CC1 $\pi$ .**
- **Oscillated  $\bar{\nu}_e$  CC coherent.**
- **Oscillated  $\bar{\nu}_e$  CC other.**

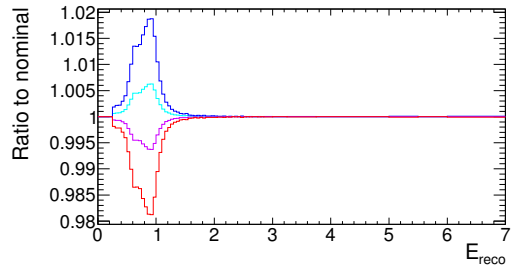
## Appendix B

# Effects of Systematics on the Spectrum

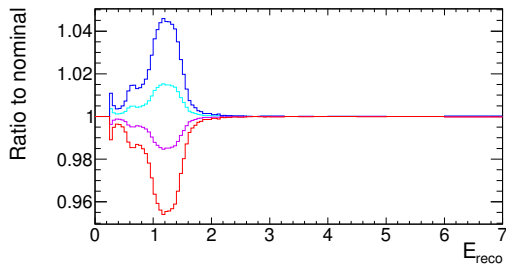
This appendix contains plots showing the effects of varying the T2K Super-K systematics listed in Table 4.8 to the single ring  $\nu_\mu$ -like sample in RHC mode. The values are presented as a ratio to spectrum shown in Figure 6.7. The lines are shown for  $+1\sigma$  (cyan),  $+3\sigma$  (blue),  $-1\sigma$  (violet) and  $-3\sigma$  (red).



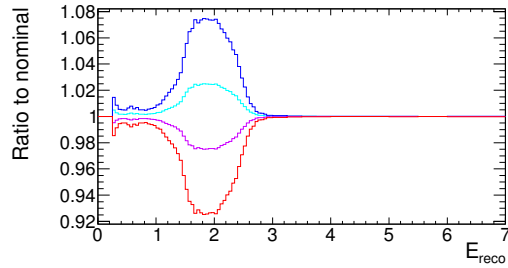
$+1, +3, -1$  and  $-3 \sigma$  variations of the RHC  $\nu_\mu$  flux normalisation,  $E = 0.0 - 0.7$  GeV systematic.



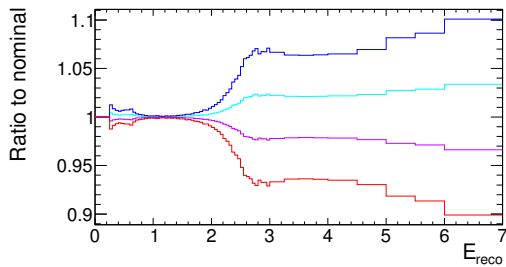
$+1, +3, -1$  and  $-3 \sigma$  variations of the RHC  $\nu_\mu$  flux normalisation,  $E = 0.7 - 1.0$  GeV systematic.



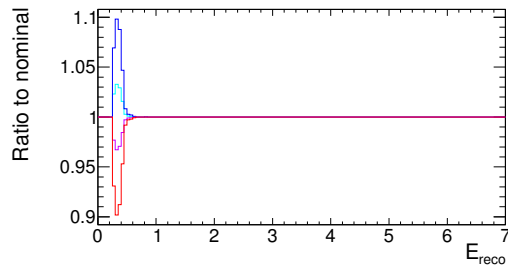
$+1, +3, -1$  and  $-3 \sigma$  variations of the RHC  $\nu_\mu$  flux normalisation,  $E = 1.0 - 1.5$  GeV systematic.



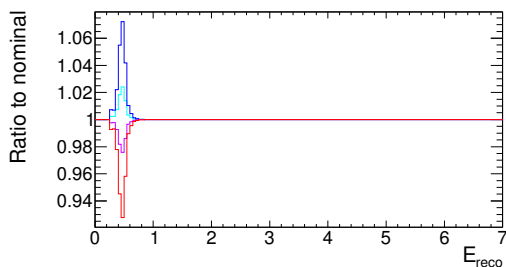
$+1, +3, -1$  and  $-3 \sigma$  variations of the RHC  $\nu_\mu$  flux normalisation,  $E = 1.5 - 2.5$  GeV systematic.



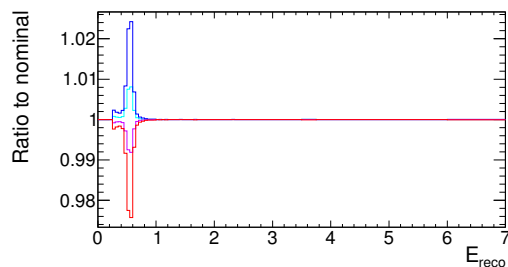
$+1, +3, -1$  and  $-3 \sigma$  variations of the RHC  $\nu_\mu$  flux normalisation,  $E = 2.5 - 30.0$  GeV systematic.



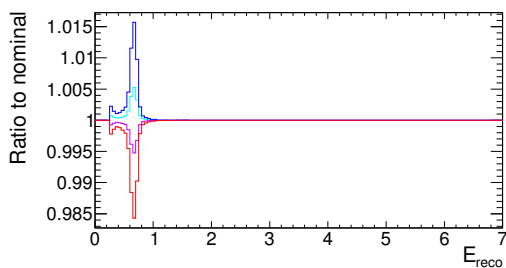
$+1, +3, -1$  and  $-3 \sigma$  variations of the RHC  $\bar{\nu}_\mu$  flux normalisation,  $E = 0.0 - 0.4$  GeV systematic.



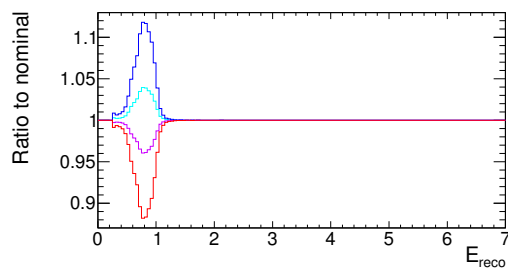
$+1, +3, -1$  and  $-3 \sigma$  variations of the RHC  $\bar{\nu}_\mu$  flux normalisation,  $E = 0.4 - 0.5$  GeV systematic.



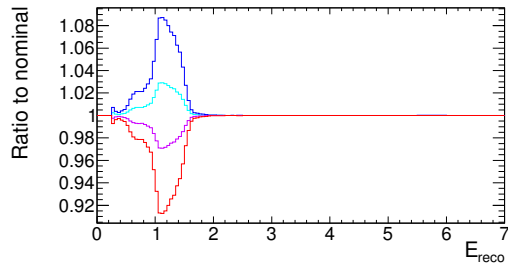
$+1, +3, -1$  and  $-3 \sigma$  variations of the RHC  $\bar{\nu}_\mu$  flux normalisation,  $E = 0.5 - 0.6$  GeV systematic.



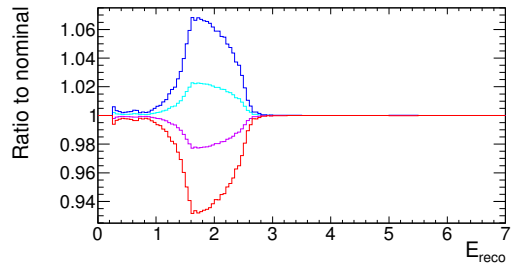
$+1, +3, -1$  and  $-3 \sigma$  variations of the RHC  $\bar{\nu}_\mu$  flux normalisation,  $E = 0.6 - 0.7$  GeV systematic.



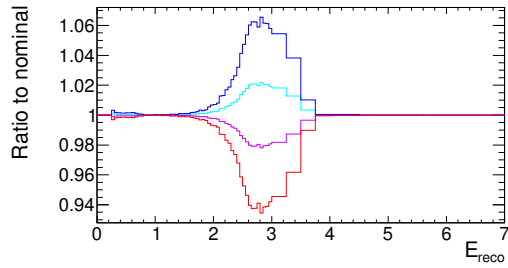
$+1, +3, -1$  and  $-3 \sigma$  variations of the RHC  $\bar{\nu}_\mu$  flux normalisation,  $E = 0.7 - 1.0$  GeV systematic.



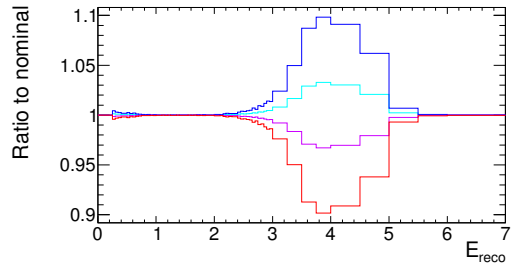
+1, +3, -1 and -3  $\sigma$  variations of the RHC  $\overline{\nu}_\mu$  flux normalisation,  $E = 1.0 - 1.5$  GeV systematic.



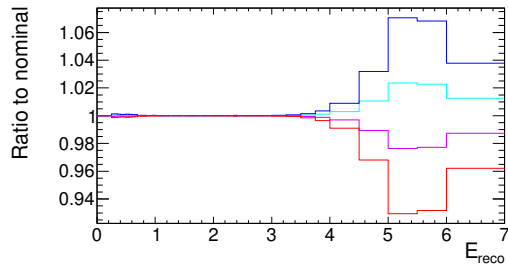
+1, +3, -1 and -3  $\sigma$  variations of the RHC  $\overline{\nu}_\mu$  flux normalisation,  $E = 1.5 - 2.5$  GeV systematic.



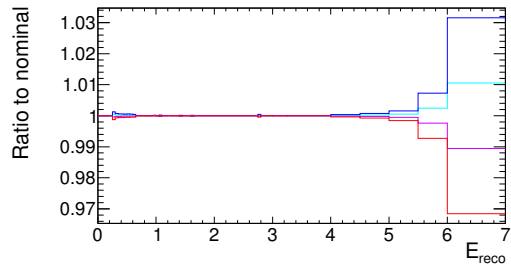
+1, +3, -1 and -3  $\sigma$  variations of the RHC  $\overline{\nu}_\mu$  flux normalisation,  $E = 2.5 - 3.5$  GeV systematic.



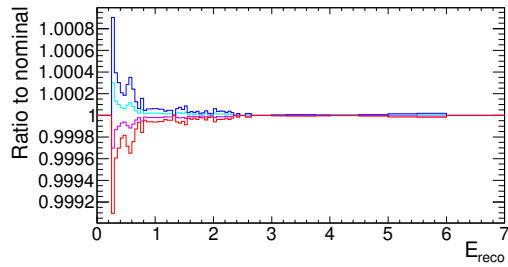
+1, +3, -1 and -3  $\sigma$  variations of the RHC  $\overline{\nu}_\mu$  flux normalisation,  $E = 3.5 - 5.0$  GeV systematic.



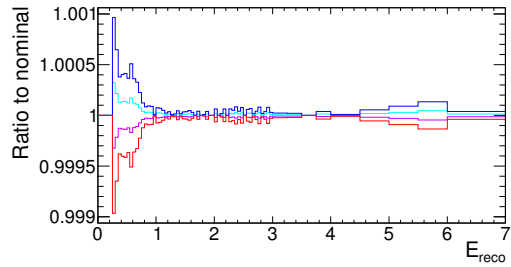
+1, +3, -1 and -3  $\sigma$  variations of the RHC  $\overline{\nu}_\mu$  flux normalisation,  $E = 5.0 - 7.0$  GeV systematic.



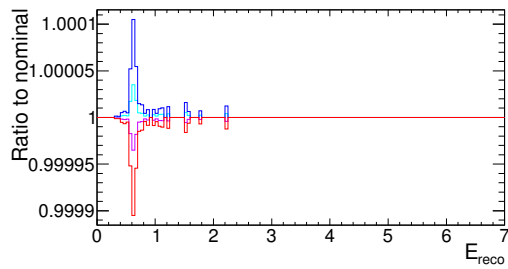
+1, +3, -1 and -3  $\sigma$  variations of the RHC  $\overline{\nu}_\mu$  flux normalisation,  $E = 7.0 - 30.0$  GeV systematic.



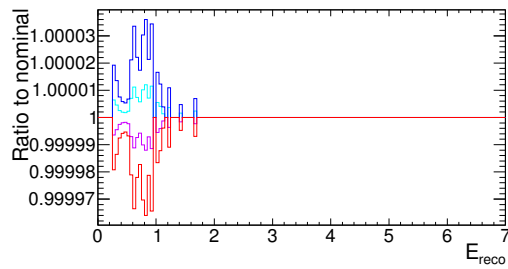
+1, +3, -1 and -3  $\sigma$  variations of the RHC  $\nu_e$  flux normalisation,  $E = 0.0 - 2.5$  GeV systematic.



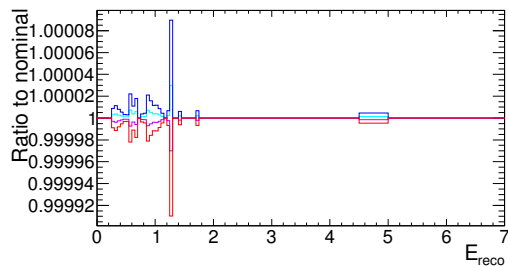
+1, +3, -1 and -3  $\sigma$  variations of the RHC  $\nu_e$  flux normalisation,  $E = 2.5 - 30.0$  GeV systematic.



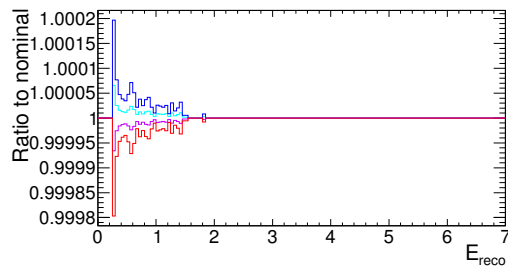
+1, +3, -1 and -3  $\sigma$  variations of the RHC  $\bar{\nu}_e$  flux normalisation,  $E = 0.0 - 0.5$  GeV systematic.



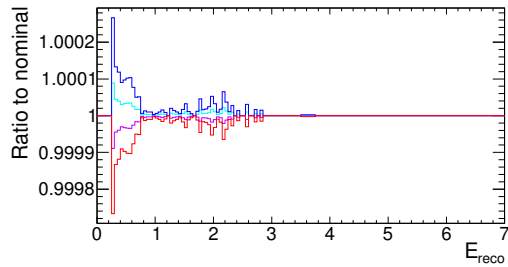
+1, +3, -1 and -3  $\sigma$  variations of the RHC  $\bar{\nu}_e$  flux normalisation,  $E = 0.5 - 0.7$  GeV systematic.



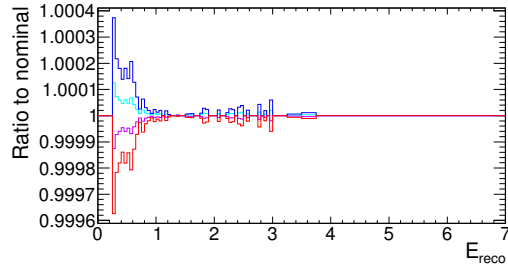
+1, +3, -1 and -3  $\sigma$  variations of the RHC  $\bar{\nu}_e$  flux normalisation,  $E = 0.7 - 0.8$  GeV systematic.



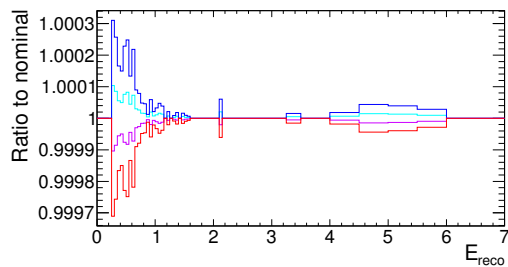
+1, +3, -1 and -3  $\sigma$  variations of the RHC  $\bar{\nu}_e$  flux normalisation,  $E = 0.8 - 1.5$  GeV systematic.



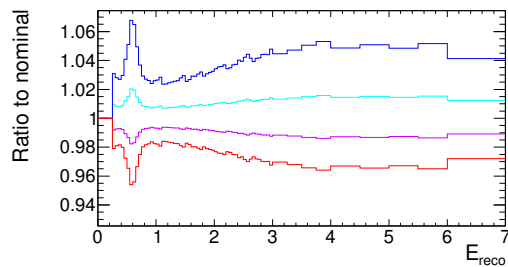
+1, +3, -1 and -3  $\sigma$  variations of the RHC  $\bar{\nu}_e$  flux normalisation,  $E = 1.5 - 2.5$  GeV systematic.



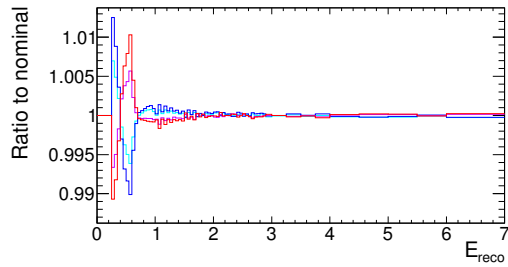
+1, +3, -1 and -3  $\sigma$  variations of the RHC  $\bar{\nu}_e$  flux normalisation,  $E = 2.5 - 4.0$  GeV systematic.



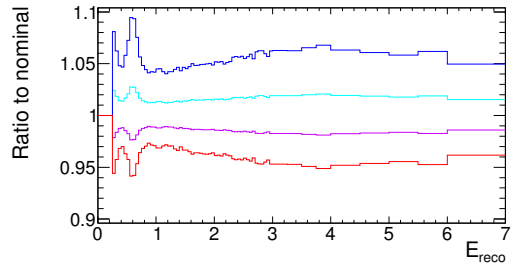
+1, +3, -1 and -3  $\sigma$  variations of the RHC  $\bar{\nu}_e$  flux normalisation,  $E = 4.0 - 30.0$  GeV systematic.



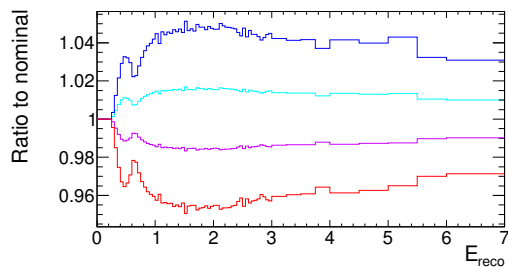
+1, +3, -1 and -3  $\sigma$  variations of the Scale of isospin 1/2 nonresonant background systematic.



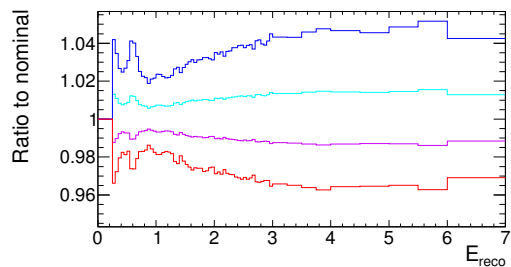
$+1$ ,  $+3$ ,  $-1$  and  $-3 \sigma$  variations of the Binding energy for  $^{16}\text{O}$  systematic.



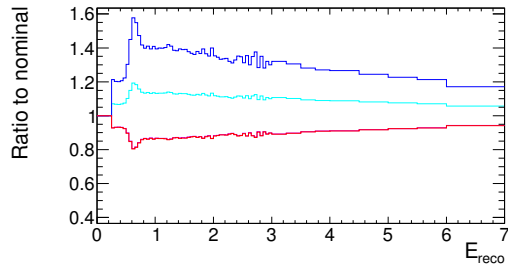
$+1$ ,  $+3$ ,  $-1$  and  $-3 \sigma$  variations of the  $C_5^A$  nucleon to  $\Delta$  transition axial form factor systematic.



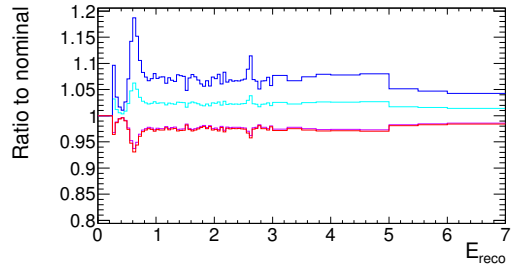
$+1$ ,  $+3$ ,  $-1$  and  $-3 \sigma$  variations of the CCQE axial-mass scaling factor systematic.



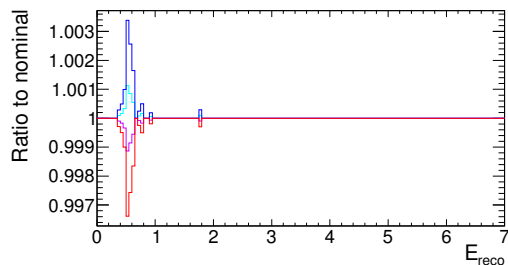
$+1$ ,  $+3$ ,  $-1$  and  $-3 \sigma$  variations of the Resonance-production axial-mass scaling factor systematic.



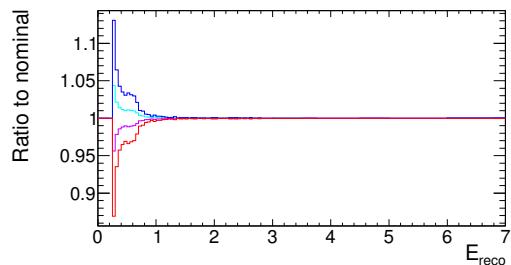
$+1$ ,  $+3$ ,  $-1$  and  $-3 \sigma$  variations of the Meson exchange current normalisation for  $^{16}\text{O}$  systematic.



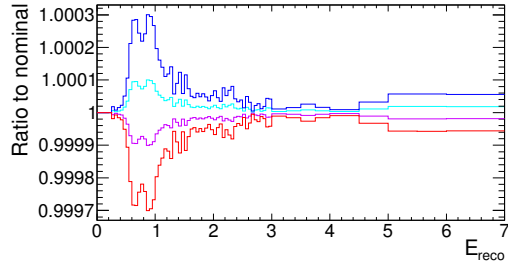
$+1$ ,  $+3$ ,  $-1$  and  $-3 \sigma$  variations of the CC coherent for  $^{16}\text{O}$  normalisation systematic.



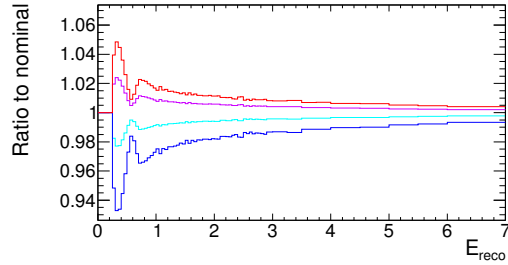
$+1$ ,  $+3$ ,  $-1$  and  $-3 \sigma$  variations of the NC coherent normalisation systematic.



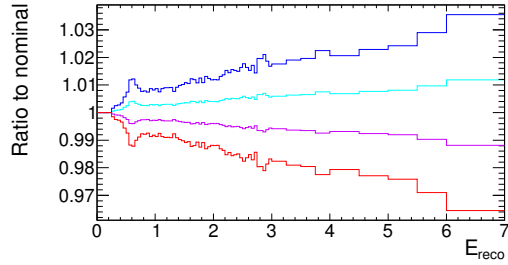
$+1$ ,  $+3$ ,  $-1$  and  $-3 \sigma$  variations of the NC other normalisation systematic.



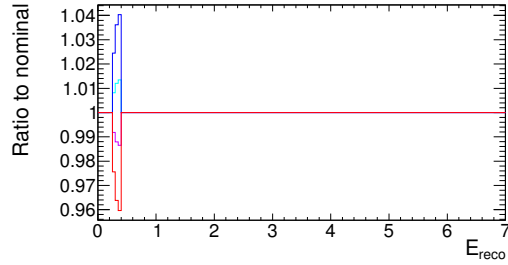
+1, +3, -1 and -3  $\sigma$  variations of the CC  $\nu_e$  normalisation systematic.



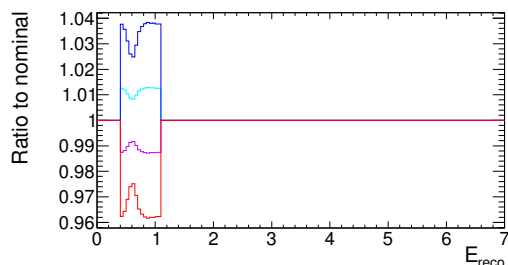
+1, +3, -1 and -3  $\sigma$  variations of the Fermi momentum for  $^{16}\text{O}$  systematic.



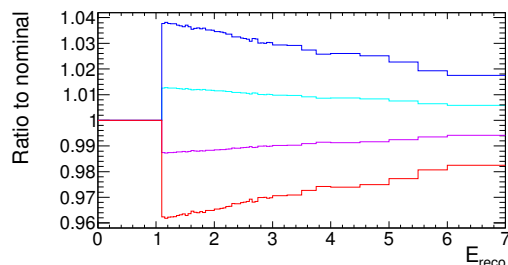
+1, +3, -1 and -3  $\sigma$  variations of the CC other shape systematic.



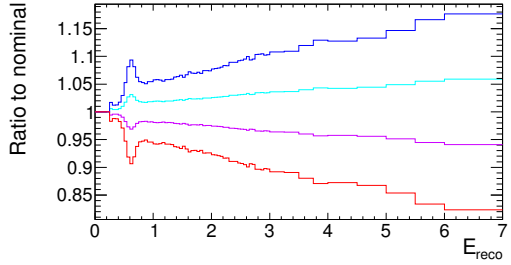
+1, +3, -1 and -3  $\sigma$  variations of the SKDet + FSI/SI 0; Ereco range 0.00 - 0.40 GeV; numu/numubar CCQE (1Rmu); RHC systematic.



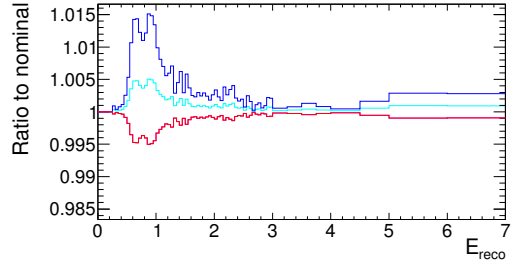
+1, +3, -1 and -3  $\sigma$  variations of the SKDet + FSI/SI 1; Ereco range 0.40 - 1.10 GeV; numu/numubar CCQE (1Rmu); RHC systematic.



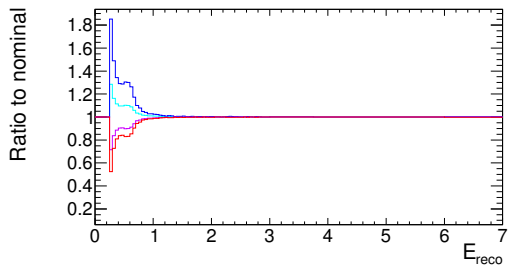
+1, +3, -1 and -3  $\sigma$  variations of the SKDet + FSI/SI 2; Ereco range 1.10 - 30.00 GeV; numu/numubar CCQE (1Rmu); RHC systematic.



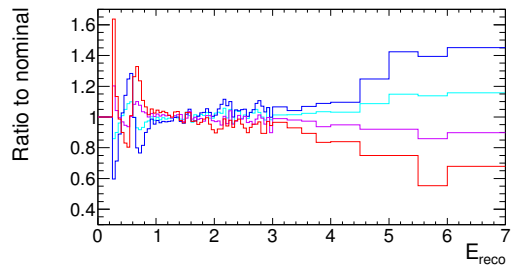
+1, +3, -1 and -3  $\sigma$  variations of the SKDet + FSI/SI 3; Ereco range 0.00 - 30.00 GeV; numu/numubar CCnQE (1Rmu); RHC systematic.



+1, +3, -1 and -3  $\sigma$  variations of the SKDet + FSI/SI 4; Ereco range 0.00 - 30.00 GeV; nue/nuebar/signue CC (1Rmu); RHC systematic.



+1, +3, -1 and -3  $\sigma$  variations of the SKDet + FSI/SI 5; Ereco range 0.00 - 30.00 GeV; all NC (1Rmu); RHC systematic.



+1, +3, -1 and -3  $\sigma$  variations of the SK energy scale; RHC systematic.

# Bibliography

- [1] C. Cowan, F. Reines, F. Harrison, H. Kruse, and A. McGuire, Science **124**, 103 (1956).
- [2] G. Danby, J. Gaillard, K. A. Goulian, L. Lederman, N. B. Mistry, *et al.*, Phys.Rev.Lett. **9**, 36 (1962).
- [3] M. Acciarri *et al.* (L3 Collaboration), Phys.Lett. **B431**, 199 (1998).
- [4] K. Kodama *et al.* (DONUT Collaboration), Phys.Lett. **B504**, 218 (2001), arXiv:hep-ex/0012035 [hep-ex] .
- [5] R. Davis, D. S. Harmer, and K. C. Hoffman, Phys. Rev. Lett. **20**, 1205 (1968).
- [6] J. N. Bahcall, N. A. Bahcall, and G. Shaviv, Phys. Rev. Lett. **20**, 1209 (1968).
- [7] J. N. Abdurashitov *et al.* (SAGE), Phys. Rev. **C60**, 055801 (1999), arXiv:astro-ph/9907113 [astro-ph] .
- [8] W. Hampel *et al.* (GALLEX), Phys. Lett. **B447**, 127 (1999).
- [9] G. Bellini *et al.* (BOREXINO Collaboration), Nature **512**, 383 (2014).
- [10] Y. Fukuda *et al.* (Super-Kamiokande Collaboration), Phys.Lett. **B436**, 33 (1998), arXiv:hep-ex/9805006 [hep-ex] .
- [11] Y. Fukuda *et al.* (Super-Kamiokande Collaboration), Phys.Rev.Lett. **81**, 1562 (1998), arXiv:hep-ex/9807003 [hep-ex] .
- [12] Q. Ahmad *et al.* (SNO Collaboration), Phys.Rev.Lett. **89**, 011301 (2002), arXiv:nucl-ex/0204008 [nucl-ex] .
- [13] Q. Ahmad *et al.* (SNO Collaboration), Phys.Rev.Lett. **87**, 071301 (2001), arXiv:nucl-ex/0106015 [nucl-ex] .
- [14] J. Beringer *et al.* (Particle Data Group), Phys.Rev. **D86**, 010001 (2012).

- [15] S. Riemer-Sorensen, C. Blake, D. Parkinson, T. M. Davis, S. Brough, *et al.*, Phys.Rev. **D85**, 081101 (2012), arXiv:1112.4940 [astro-ph.CO] .
- [16] A. Aguilar-Arevalo *et al.* (LSND Collaboration), Phys.Rev. **D64**, 112007 (2001), arXiv:hep-ex/0104049 [hep-ex] .
- [17] M. Goldhaber, L. Grodzins, and A. W. Sunyar, Phys. Rev. **109**, 1015 (1958).
- [18] C. Giunti and C. W. Kim, *Fundamentals of Neutrino Physics and Astrophysics* (Oxford University Press, Oxford, UK, 2007) pp. 1–728.
- [19] A. D. Sakharov, Pisma Zh. Eksp. Teor. Fiz. **5**, 32 (1967), [Usp. Fiz. Nauk161,61(1991)].
- [20] C. Wu, E. Ambler, R. Hayward, D. Hoppes, and R. Hudson, Phys.Rev. **105**, 1413 (1957).
- [21] D. Griffiths, *Introduction to elementary particles*, 2nd ed. (2008).
- [22] J. Horstkotte *et al.*, Phys. Rev. **D25**, 2743 (1982).
- [23] B. Kayser, eConf **C040802**, L004 (2004), arXiv:hep-ph/0506165 [hep-ph] .
- [24] S. Mikheyev and A. Smirnov, Il Nuovo Cimento C **9**, 17 (1986).
- [25] L. Wolfenstein, Phys. Rev. D **17**, 2369 (1978).
- [26] H. Bethe, Phys.Rev.Lett. **56**, 1305 (1986).
- [27] R. Wendell (Super-Kamiokande), *Proceedings, 26th International Conference on Neutrino Physics and Astrophysics (Neutrino 2014)*, AIP Conf. Proc. **1666**, 100001 (2015), arXiv:1412.5234 [hep-ex] .
- [28] M. Aartsen *et al.* (IceCube), Phys. Rev. **D91**, 072004 (2015), arXiv:1410.7227 [hep-ex] .
- [29] W. Winter, Phys.Rev. **D88**, 013013 (2013), arXiv:1305.5539 [hep-ph] .
- [30] D. A. Dwyer and T. J. Langford, Phys. Rev. Lett. **114**, 012502 (2015), arXiv:1407.1281 [nucl-ex] .
- [31] S.-H. Seo (RENO), *Proceedings, 26th International Conference on Neutrino Physics and Astrophysics (Neutrino 2014)*, AIP Conf. Proc. **1666**, 080002 (2015), arXiv:1410.7987 [hep-ex] .
- [32] M. Apollonio *et al.* (CHOOZ), Eur. Phys. J. **C27**, 331 (2003), arXiv:hep-ex/0301017 [hep-ex] .

- [33] Y. Abe *et al.* (Double Chooz), JHEP **10**, 086 (2014), [Erratum: JHEP02,074(2015)], arXiv:1406.7763 [hep-ex].
- [34] F. An *et al.* (Daya Bay), Phys.Rev.Lett. **108**, 171803 (2012), arXiv:1203.1669 [hep-ex].
- [35] F. P. An *et al.* (Daya Bay), (2015), arXiv:1505.03456 [hep-ex].
- [36] S.-H. Seo (RENO), *Proceedings, 26th International Conference on Neutrino Physics and Astrophysics (Neutrino 2014)*, AIP Conf. Proc. **1666**, 080002 (2015), arXiv:1410.7987 [hep-ex].
- [37] A. Gando *et al.* (KamLAND), Phys. Rev. **D83**, 052002 (2011), arXiv:1009.4771 [hep-ex].
- [38] M. Ahn *et al.* (K2K Collaboration), Phys.Rev. **D74**, 072003 (2006), arXiv:hep-ex/0606032 [hep-ex].
- [39] P. Adamson *et al.* (MINOS), Phys.Rev.Lett. **110**, 251801 (2013), arXiv:1304.6335 [hep-ex].
- [40] K. Abe *et al.* (T2K), Phys.Rev.Lett. **112**, 061802 (2014), arXiv:1311.4750 [hep-ex]
- .
- [41] K. Abe *et al.* (T2K), Phys.Rev. **D91**, 072010 (2015), arXiv:1502.01550 [hep-ex].
- [42] A. Aguilar-Arevalo *et al.* (MiniBooNE Collaboration), Phys.Rev.Lett. **110**, 161801 (2013), arXiv:1303.2588 [hep-ex].
- [43] F. Capozzi, G. Fogli, E. Lisi, A. Marrone, D. Montanino, *et al.*, Phys.Rev. **D89**, 093018 (2014), arXiv:1312.2878 [hep-ph].
- [44] K. Olive *et al.* (Particle Data Group), Chin.Phys. **C38**, 090001 (2014).
- [45] T. T. Collaboration, Nuclear Instruments and Methods in Physics Research Section A: Accelerators, Spectrometers, Detectors and Associated Equipment **659**, 106 (2011).
- [46] K. Matsuoka, A. Ichikawa, H. Kubo, K. Maeda, T. Maruyama, *et al.*, Nucl.Instrum.Meth. **A624**, 591 (2010), arXiv:1008.4077 [physics.ins-det].
- [47] A. Para and M. Szleper, (2001), arXiv:hep-ex/0110032 [hep-ex].
- [48] D. Allan *et al.* (T2K UK), JINST **8**, P10019 (2013), arXiv:1308.3445 [physics.ins-det].

- [49] K. Gilje *et al.* (T2K), T2K-TN-144v2.1 (2014).
- [50] P. A. Amaudruz *et al.* (T2K ND280 FGD), Nucl. Instrum. Meth. **A696**, 1 (2012), arXiv:1204.3666 [physics.ins-det].
- [51] D. Renker and E. Lorenz, JINST **4**, P04004 (2009).
- [52] N. Abgrall *et al.* (T2K ND280 TPC), Nucl.Instrum.Meth. **A637**, 25 (2011), arXiv:1012.0865 [physics.ins-det].
- [53] Y. Hayato, Acta Phys.Polon. **B40**, 2477 (2009).
- [54] C. Andreopoulos *et al.*, Nucl. Instrum. Meth. **A614**, 87 (2010), arXiv:0905.2517 [hep-ph].
- [55] S. Agostinelli *et al.* (GEANT4), Nucl. Instrum. Meth. **A506**, 250 (2003).
- [56] S. W. Li and J. F. Beacom, Phys.Rev. **C89**, 045801 (2014), arXiv:1402.4687 [hep-ph].
- [57] E. R. Davies, *Machine Vision: Theory, Algorithms, Practicalities*, 4th ed. (Academic Press, Oxford, 2012).
- [58] M. Shiozawa (Super-Kamiokande), Nucl.Instrum.Meth. **A433**, 240 (1999).
- [59] J. Hignight *et al.* (T2K), T2K-TN-148v4 (2014).
- [60] R. Wendell *et al.* (T2K), T2K-TN-219 (2014).
- [61] R. Patterson, E. Laird, Y. Liu, P. Meyers, I. Stancu, *et al.*, Nucl.Instrum.Meth. **A608**, 206 (2009), arXiv:0902.2222 [hep-ex].
- [62] K. Abe *et al.* (T2K), Phys.Rev.Lett. **112**, 181801 (2014), arXiv:1403.1532 [hep-ex].
- [63] K. Abe *et al.* (T2K), PTEP **2015**, 043C01 (2015), arXiv:1409.7469 [hep-ex].
- [64] K. Abe *et al.* (T2K), Phys.Rev. **D91**, 051102 (2015), arXiv:1410.8811 [hep-ex].
- [65] K. Abe *et al.* (T2K), Phys.Rev. **D87**, 092003 (2013), arXiv:1302.4908 [hep-ex].
- [66] K. Abe *et al.* (T2K), Phys.Rev.Lett. **113**, 241803 (2014), arXiv:1407.7389 [hep-ex].
- [67] K. Abe *et al.* (T2K), (2014), arXiv:1411.6264 [hep-ex].
- [68] K. Abe *et al.* (T2K), Phys.Rev. **D90**, 052010 (2014), arXiv:1407.4256 [hep-ex].

- [69] K. Abe *et al.* (T2K), Phys.Rev. **D91**, 112002 (2015), arXiv:1503.07452 [hep-ex] .
- [70] K. Abe *et al.* (T2K), (2015), arXiv:1503.08815 [hep-ex] .
- [71] K. Abe *et al.* (T2K), Phys.Rev. **D90**, 072012 (2014), arXiv:1403.3140 [hep-ex] .
- [72] G. Battistoni, S. Muraro, P. R. Sala, F. Cerutti, A. Ferrari, *et al.*, AIP Conf.Proc. **896**, 31 (2007).
- [73] C. Zeitnitz and T. Gabriel, Nucl.Instrum.Meth. **A349**, 106 (1994).
- [74] N. Abgrall *et al.* (NA61/SHINE Collaboration), Phys.Rev. **C84**, 034604 (2011), arXiv:1102.0983 [hep-ex] .
- [75] N. Abgrall *et al.* (NA61/SHINE Collaboration), Phys.Rev. **C85**, 035210 (2012), arXiv:1112.0150 [hep-ex] .
- [76] N. Abgrall *et al.* (NA61 collaboration), JINST **9**, P06005 (2014), arXiv:1401.4699 [physics.ins-det] .
- [77] T. Eichten, D. Haidt, J. Pattison, W. Venus, H. Wachsmuth, *et al.*, Nucl.Phys. **B44**, 333 (1972).
- [78] J. Allaby *et al.*, CERN Tech. Rep **70**, 12 (1970).
- [79] I. Chemakin *et al.* (E910 Collaboration), Phys.Rev. **C77**, 015209 (2008), arXiv:0707.2375 [nucl-ex] .
- [80] N. Abgrall *et al.* (NA61/SHINE), Nucl. Instrum. Meth. **A701**, 99 (2013), arXiv:1207.2114 [hep-ex] .
- [81] K. Abe *et al.* (T2K Collaboration), Phys.Rev. **D87**, 012001 (2013), arXiv:1211.0469 [hep-ex] .
- [82] M. Friend *et al.* (T2K), T2K-TN-217v5 (2015).
- [83] C. L. Smith, Physics Reports **3**, 261 (1972).
- [84] K. S. Kuzmin, V. V. Lyubushkin, and V. A. Naumov, Eur. Phys. J. **C54**, 517 (2008), arXiv:0712.4384 [hep-ph] .
- [85] R. Smith and E. Moniz, Nuclear Physics B **43**, 605 (1972).
- [86] A. Bercellie *et al.* (T2K), T2K-TN-192 (2015).
- [87] O. Benhar, D. Day, and I. Sick, Rev. Mod. Phys. **80**, 189 (2008).

- [88] J. Nieves, I. R. Simo, and M. J. V. Vacas, Phys. Rev. C **83**, 045501 (2011).
- [89] A. Bodek, H. Budd, and M. Christy, Eur.Phys.J. **C71**, 1726 (2011), arXiv:1106.0340 [hep-ph].
- [90] D. Rein and L. M. Sehgal, Annals Phys. **133**, 79 (1981).
- [91] K. M. Graczyk and J. T. Sobczyk, Phys.Rev. **D77**, 053001 (2008), arXiv:0707.3561 [hep-ph].
- [92] D. Rein and L. M. Sehgal, Nucl.Phys. **B223**, 29 (1983).
- [93] D. Rein and L. Sehgal, Phys.Lett. **B657**, 207 (2007), arXiv:hep-ph/0606185 [hep-ph].
- [94] M. Gluck, E. Reya, and A. Vogt, Eur.Phys.J. **C5**, 461 (1998), arXiv:hep-ph/9806404 [hep-ph].
- [95] A. Bodek and U.-K. Yang, PoS **ICHEP2010**, 292 (2010), arXiv:1012.0261 [hep-ph].
- [96] M. Derrick, P. Gregory, L. Hyman, K. Jaeger, D. Lissauer, *et al.*, Phys.Rev. **D17**, 1 (1978).
- [97] T. Sjostrand, S. Mrenna, and P. Z. Skands, JHEP **0605**, 026 (2006), arXiv:hep-ph/0603175 [hep-ph].
- [98] P. Musset and J. Vialle, Phys.Rept. **39**, 1 (1978).
- [99] J. E. Kim, P. Langacker, M. Levine, and H. Williams, Rev.Mod.Phys. **53**, 211 (1981).
- [100] M. Nakahata *et al.* (Kamiokande), J. Phys. Soc. Jap. **55**, 3786 (1986).
- [101] A. Aguilar-Arevalo *et al.* (MiniBooNE Collaboration), Phys.Rev. **D81**, 092005 (2010), arXiv:1002.2680 [hep-ex].
- [102] A. Aguilar-Arevalo *et al.* (MiniBooNE Collaboration), Phys.Rev. **D88**, 032001 (2013), arXiv:1301.7067 [hep-ex].
- [103] G. Fiorentini *et al.* (MINERvA Collaboration), Phys.Rev.Lett. **111**, 022502 (2013), arXiv:1305.2243 [hep-ex].
- [104] L. Fields *et al.* (MINERvA Collaboration), Phys.Rev.Lett. **111**, 022501 (2013), arXiv:1305.2234 [hep-ex].

- [105] O. Benhar, N. Farina, H. Nakamura, M. Sakuda, and R. Seki, Phys. Rev. D **72**, 053005 (2005).
- [106] F. James and M. Roos, Comput.Phys.Commun. **10**, 343 (1975).
- [107] M. Maltoni and T. Schwetz, Phys. Rev. **D68**, 033020 (2003), arXiv:hep-ph/0304176 [hep-ph] .
- [108] P. Bartet *et al.* (T2K), T2K-TN-212v1 (2015).
- [109] V. Berardi *et al.* (T2K), T2K-TN-224v5.2 (2015).
- [110] V. Berardi *et al.* (T2K), T2K-TN-227v3.6 (2015).
- [111] C. Bojeckho *et al.* (T2K), T2K-TN-152v4.2 (2013).
- [112] M. Hartz *et al.* (T2K), T2K-TN-220 (2015).
- [113] P. De Perio *et al.* (T2K), T2K-TN-033v2 (2012).
- [114] J. Kameda (T2K), T2K-TN-159v2 (2013).
- [115] J. Kopp, Int. J. Mod. Phys. **C19**, 523 (2008), arXiv:physics/0610206 [physics] .
- [116] R. Wendell, “Prob3++,” (2012).
- [117] K. Hagiwara, N. Okamura, and K.-i. Senda, JHEP **09**, 082 (2011), arXiv:1107.5857 [hep-ph] .
- [118] W. H. Press, S. A. Teukolsky, W. T. Vetterling, and B. P. Flannery, *Numerical Recipes 3rd Edition: The Art of Scientific Computing*, 3rd ed. (Cambridge University Press, New York, NY, USA, 2007).
- [119] S. Baker and R. D. Cousins, Nucl. Instrum. Meth. **221**, 437 (1984).
- [120] G. Cowan, K. Cranmer, E. Gross, and O. Vitells, Eur.Phys.J. **C71**, 1554 (2011), arXiv:1007.1727 [physics.data-an] .
- [121] Y. Grossman, Phys.Lett. **B359**, 141 (1995), arXiv:hep-ph/9507344 [hep-ph] .
- [122] P. Astier *et al.* (NOMAD), Nucl. Phys. **B611**, 3 (2001), arXiv:hep-ex/0106102 [hep-ex] .
- [123] K. Eitel (KARMEN), *Neutrino physics and astrophysics. Proceedings, 19th International Conference, Neutrino 2000, Sudbury, Canada, June 16-21, 2000*, Nucl. Phys. Proc. Suppl. **91**, 191 (2001), [,191(2000)], arXiv:hep-ex/0008002 [hep-ex] .

- [124] C. Biggio, M. Blennow, and E. Fernandez-Martinez, JHEP **08**, 090 (2009), arXiv:0907.0097 [hep-ph] .
- [125] S. Davidson and V. Sanz, Phys. Rev. **D84**, 113011 (2011), arXiv:1108.5320 [hep-ph] .
- [126] P. Adamson *et al.* (MINOS), Phys.Rev. **D88**, 072011 (2013), arXiv:1303.5314 [hep-ex] .
- [127] G. Mitsuka *et al.* (Super-Kamiokande), Phys. Rev. **D84**, 113008 (2011), arXiv:1109.1889 [hep-ex] .